

**Charged-Current Double-Differential Cross Section Measurement of Electron  
Neutrinos in Low Recoil Region on Hydrocarbon at  $\langle E_\nu \rangle \sim 7$  GeV**

by

**Hang Su**

B.E., Shanghai Jiaotong University, 2013

M.S.E., University of Pennsylvania, 2014

Submitted to the Graduate Faculty of  
the Dietrich School of Arts and Science in partial fulfillment  
of the requirements for the degree of  
**Doctor of Philosophy**

University of Pittsburgh

2022

UNIVERSITY OF PITTSBURGH  
DIETRICH SCHOOL OF ARTS AND SCIENCE

This dissertation was presented

by

Hang Su

It was defended on

September 2nd 2022

and approved by

Vittorio Paolone, Professor of Physics

Donna Naples, Professor of Physics

Brian Batell, Professor of Physics

Andrew Zentner, Professor of Physics

Manfred Paulini, Professor of Physics

Copyright © by Hang Su  
2022

# **Charged-Current Double-Differential Cross Section Measurement of Electron Neutrinos in Low Recoil Region on Hydrocarbon at $\langle E_\nu \rangle \sim 7$ GeV**

Hang Su, PhD

University of Pittsburgh, 2022

Measuring neutrino mixing angles, especially the CP violation phase and mass hierarchy, is one of the priorities of the neutrino community and long baseline neutrino oscillation programs, such as T2K and NOvA, provided the most precise measurements to date. One of the dominating uncertainties of the measurements is the neutrino interaction model due to the difficulty of modeling the nuclear effects from first principles. As a result, neutrino scattering experiments such as MINERvA were conducted to provide data as input to reduce this uncertainty. This thesis presents a charged-current double-differential cross section measurement of electron neutrinos using the MINERvA detector in terms of available energy (a proxy of energy transfer), three-momentum transfer, and/or transverse momentum of the final state electron. This measurement focuses on the transition region between quasi-elastic and resonance processes, where the multi-nucleon knockout process dominates. The result is compared to a modified GENIE model and similar measurements using muon neutrino samples. In addition, this measurement reproduces the photon-like excess seen by previous MINERvA electron neutrino measurements.



## Table of Contents

|   |     |
|---|-----|
| <b>Preface</b> . . . . .  | xiv |
| <b>1.0 Introduction</b> . . . . .   | 1   |
| 1.1 The Standard Model . . . . .  | 4   |
| 1.1.1 Fields, Principle of Least Action, and Canonical Quantization . . . . | 4   |
| 1.1.2 Interacting Fields and Gauge Theory . . . . .                         | 5   |
| 1.1.3 Standard Model Lagrangian . . . . .                                   | 7   |
| 1.1.3.1 Gauge Boson Dynamics Terms . . . . .                                | 8   |
| 1.1.3.2 Lepton Dynamics Terms . . . . .                                     | 8   |
| 1.1.3.3 Quark Dynamics Terms . . . . .                                      | 9   |
| 1.1.3.4 Higgs Field Terms . . . . .   | 9   |
| 1.1.3.5 Lepton and Quark Mass Terms (Yukawa Coupling) . . . . .             | 10  |
| 1.1.4 Spontaneous Symmetry Breaking and Electroweak Interaction . . . .     | 10  |
| 1.1.5 Flavor Mixing and CKM Matrix . . . . .                                | 12  |
| 1.2 Beyond Standard Model: Neutrino Oscillation . . . . .                   | 13  |
| 1.2.1 History of Neutrino Mass and Oscillations . . . . .                   | 13  |
| 1.2.2 Neutrino Oscillation Formalism . . . . .                              | 14  |
| 1.2.3 Current Status of Neutrino Oscillation Parameter Measurements . .     | 15  |
| 1.2.4 Beyond 3 Neutrino Paradigm . . . . .                                  | 17  |
| 1.3 Motivation of Neutrino Scattering Cross Section Measurements . . . . .  | 18  |
| 1.3.1 Neutrino Cross Section as Input to Oscillation Measurements . . . .   | 18  |
| 1.3.2 Modeling of Neutrino Scattering and Its Challenges . . . . .          | 19  |
| 1.3.2.1 Elastic and Quasi-elastic Scattering . . . . .                      | 21  |
| 1.3.2.2 Resonance Production . . . . .                                      | 22  |
| 1.3.2.3 Coherent Pion Production . . . . .                                  | 24  |
| 1.3.2.4 Deep Inelastic Scattering . . . . .                                 | 24  |
| 1.3.2.5 Nuclear Effects . . . . .   | 25  |

|            |  |           |
|------------|--|-----------|
| 1.3.3      | Previous Measurements of $\nu_e$ Cross Section . . . . .               | 27        |
| <b>2.0</b> | <b>The Main Injector Experiment for <math>\nu - A</math> . . . . .</b> | <b>28</b> |
| 2.1        | The NuMI Beam Line . . . . .   | 28        |
| 2.1.1      | Main Injector Proton Beam . . . . .                                    | 28        |
| 2.1.2      | Targets and Magnetic Focusing Horns . . . . .                          | 29        |
| 2.1.3      | Decay Pipe and Absorbers . . . . .                                     | 30        |
| 2.2        | The Minerva Detector . . . . .   | 32        |
| 2.2.1      | Tracking Modules . . . . .   | 33        |
| 2.2.2      | Passive Nuclear Target Modules . . . . .                               | 34        |
| 2.2.3      | ECAL and HCAL modules . . . . .  | 34        |
| 2.2.4      | MINOS Near Detector . . . . .  | 35        |
| 2.2.5      | Optical System and Readout Electronics . . . . .                       | 36        |
| 2.3        | Calibration Chain . . . . .  | 39        |
| 2.3.1      | Energy Calibration . . . . .   | 39        |
| 2.3.1.1    | FEB Response . . . . .   | 39        |
| 2.3.1.2    | PMT Response . . . . .   | 40        |
| 2.3.1.3    | Scintillator Strip Response . . . . .                                  | 42        |
| 2.3.1.4    | Rock Muon Sample . . . . .   | 43        |
| 2.3.1.5    | Strip-to-Strip Correction . . . . .                                    | 43        |
| 2.3.1.6    | Absolute Energy Scale . . . . .  | 44        |
| 2.3.2      | Timing Calibration . . . . .   | 45        |
| 2.3.3      | Alignment Calibration . . . . .  | 48        |
| 2.3.4      | Cross-talk Measurements . . . . .                                      | 48        |
| <b>3.0</b> | <b>Simulation in MINERvA . . . . .</b>                                 | <b>52</b> |
| 3.1        | Flux Simulation . . . . .  | 52        |
| 3.2        | Neutrino Interaction Simulation . . . . .                              | 53        |
| 3.3        | Detector and Readout Simulation . . . . .                              | 54        |
| 3.4        | Post-simulation Reweighting . . . . .                                  | 55        |
| 3.4.1      | Flux Reweighting . . . . .   | 56        |
| 3.4.2      | Interaction Model Reweighting . . . . .                                | 56        |

|            |  |           |
|------------|--|-----------|
| 3.4.2.1    | RPA Reweighting . . . . .  | 57        |
| 3.4.2.2    | 2p2h Reweighting . . . . .   | 57        |
| 3.4.2.3    | Non-Resonant Pion Reweighting . . . . .                                    | 58        |
| 3.4.2.4    | Resonant Pion Reweighting . . . . .  | 58        |
| 3.4.3      | Calorimetry Tuning . . . . .   | 58        |
| <b>4.0</b> | <b>Reconstruction in MINERvA . . . . .</b>                                 | <b>60</b> |
| 4.1        | Generic Reconstruction . . . . .   | 60        |
| 4.1.1      | Time Slicing . . . . .   | 61        |
| 4.1.2      | Cluster Formation . . . . .  | 61        |
| 4.1.3      | Track Reconstruction . . . . .   | 62        |
| 4.1.4      | Rock Muon Identification and Removal . . . . .                             | 64        |
| 4.2        | Final State Electron Identification . . . . .                              | 66        |
| 4.2.1      | Characteristics of Electron in MINERvA Detector . . . . .                  | 66        |
| 4.2.2      | EM Shower Candidate Formation . . . . .                                    | 67        |
| 4.2.3      | Electron Candidate Kinematics Reconstruction . . . . .                     | 68        |
| 4.2.4      | kNN Classification . . . . .   | 69        |
| 4.2.4.1    | Mean $dE/dX$ . . . . .   | 70        |
| 4.2.4.2    | Endpoint Energy Fraction . . . . .   | 70        |
| 4.2.4.3    | Median Transverse Width . . . . .  | 71        |
| 4.2.5      | Choice of The Best Electron Candidate . . . . .                            | 71        |
| 4.3        | Hadron Reconstruction . . . . .  | 72        |
| 4.3.1      | Calorimetry Segmented by Subdetectors . . . . .                            | 72        |
| 4.3.2      | Calorimetry Segmented by Relative Location . . . . .                       | 72        |
| 4.3.3      | Hadron Reconstructions as By-product of Data Preservation Effort . . . . . | 73        |
| 4.4        | Truth Plausibility Veto . . . . .  | 73        |
| <b>5.0</b> | <b>Electron Neutrino Differential Cross Section Measurement . . . . .</b>  | <b>75</b> |
| 5.1        | Definition of Signal . . . . .   | 75        |
| 5.2        | Sample Selection . . . . .   | 76        |
| 5.2.1      | Selection Cuts . . . . .   | 76        |
| 5.2.1.1    | Pre-selection Cuts . . . . .   | 76        |

|         |   |     |
|---------|---|-----|
| 5.2.1.2 | Reconstruction Quality Cuts . . . . .                                       | 77  |
| 5.2.1.3 | Electron Selection Cuts . . . . .   | 78  |
| 5.2.1.4 | Phase Space Cuts . . . . .  | 79  |
| 5.3     | Definition of Analysis Variables and Selected Sample Distribution . . . . . | 81  |
| 5.3.1   | Available Energy . . . . .  | 81  |
| 5.3.2   | Lepton Transverse Momentum . . . . .  | 82  |
| 5.3.3   | Three Momentum Transfer . . . . .   | 83  |
| 5.3.4   | Leakage Correction . . . . .  | 83  |
| 5.3.5   | Selected Data and MC Samples . . . . .                                      | 85  |
| 5.4     | Background Constraint . . . . .   | 87  |
| 5.4.1   | $\pi^0$ Background Constraint with Sideband . . . . .                       | 88  |
| 5.4.2   | Wrong Sign Background Constraint . . . . .                                  | 94  |
| 5.4.3   | Constrained Background Predictions . . . . .                                | 96  |
| 5.5     | Unfolding . . . . .   | 96  |
| 5.6     | Acceptance and Target Normalization . . . . .                               | 103 |
| 5.7     | Cross Section Result . . . . .  | 105 |
| 5.8     | Uncertainties . . . . .   | 105 |
| 5.8.1   | Interaction Model Uncertainties . . . . .                                   | 108 |
| 5.8.1.1 | MINERvA Tune Uncertainties . . . . .  | 108 |
| 5.8.2   | Detector Model Uncertainties . . . . .                                      | 111 |
| 5.8.2.1 | Angular Resolution . . . . .  | 111 |
| 5.8.2.2 | Beam Angle . . . . .  | 111 |
| 5.8.2.3 | EM Energy Scale . . . . .   | 111 |
| 5.8.2.4 | Calorimetry Responses . . . . .   | 112 |
| 5.8.2.5 | Hadron Re-interaction Rate . . . . .  | 112 |
| 5.8.2.6 | Leakage Estimation . . . . .  | 113 |
| 5.8.2.7 | Target Mass . . . . .   | 113 |
| 5.8.3   | Flux Uncertainty . . . . .  | 113 |
| 5.8.4   | Background Constraint Method . . . . .                                      | 114 |
| 5.9     | Direct Comparison with Published $\nu_\mu$ Measurements . . . . .           | 114 |

|  |     |
|--|-----|
| <b>6.0 Conclusion</b> . . . . .                  | 123 |
| <b>Appendix A. Closure Tests</b> . . . . .       | 124 |
| <b>Appendix B. Warping Tests</b> . . . . .       | 127 |
| <b>Appendix C. Data Excess Studies</b> . . . . . | 130 |
| C.1 Excess Characterization . . . . .            | 131 |
| C.2 Creating an Excess Model . . . . .           | 133 |
| <b>Bibliography</b> . . . . .                    | 135 |

## List of Tables

|     |   |     |
|-----|---|-----|
| 1.1 | Well-known representations and corresponding free field lagrangians . . . . .       | 5   |
| 1.2 | Experiments contributing to the present determination of the oscillation parameters | 16  |
| 1.3 | Best-fit values of neutrino oscillation parameters . . . . .                        | 16  |
| 3.1 | Elemental Composition of Scintillator and Nuclear Targets . . . . .                 | 55  |
| 3.2 | 2p2h Reweighting Function Parameters . . . . .                                      | 58  |
| 4.1 | Electron Energy Calorimetry Constants and Variables . . . . .                       | 70  |
| 4.2 | Hadronic Energy Calorimetry Constants . . . . .                                     | 73  |
| 5.1 | Selection Cut Performance . . . . .   | 80  |
| 5.2 | correction factors for energy reconstruction . . . . .                              | 82  |
| 5.3 | Anchor points of $q_0$ spline function . . . . .                                    | 83  |
| 5.4 | Scale factors applied to $\pi^0$ production processes . . . . .                     | 93  |
| 5.5 | GENIE uncertainties: primary interactions . . . . .                                 | 109 |
| 5.6 | GENIE uncertainties: final state interactions . . . . .                             | 110 |
| 5.7 | Calorimetry uncertainties . . . . .   | 112 |

## List of Figures

|      |  |    |
|------|--|----|
| 1.1  | Standard Model Particles . . . . .   | 2  |
| 1.2  | Cartoon illustrating the configuration of DUNE Experiment . . . . .                                      | 17 |
| 1.3  | Aerial view of SBN program . . . . .   | 18 |
| 1.4  | Expected sensitivity of DUNE as a function of exposure and signal normalization<br>uncertainty . . . . . | 19 |
| 1.5  | Feynman diagram of neutrino scattering and flux . . . . .  | 21 |
| 1.6  | Feynman Diagrams of Single Pion Production . . . . .   | 23 |
| 1.7  | Cartoon of Nuclear Effects . . . . .   | 25 |
| 2.1  | Schematic view of NuMI beam line . . . . .   | 29 |
| 2.2  | Schematic view of target and horns . . . . .   | 30 |
| 2.3  | Schematic view of monitors and absorbers downstream of decay pipe . . . . .                              | 31 |
| 2.4  | MINERvA detector configuration . . . . .   | 32 |
| 2.5  | MINERvA scintillator strips . . . . .  | 34 |
| 2.6  | Arrangement of passive nuclear target modules . . . . .  | 35 |
| 2.7  | Configuration of passive nuclear target module . . . . .   | 36 |
| 2.8  | MINOS near detector . . . . .  | 37 |
| 2.9  | Optical box and schematic view of readout channel . . . . .  | 38 |
| 2.10 | FEB response . . . . .   | 40 |
| 2.11 | PMT responses . . . . .  | 41 |
| 2.12 | Peak Energy Deposition among Planes . . . . .  | 45 |
| 2.13 | Absolution Energy Scale Calibration. . . . .   | 46 |
| 2.14 | Timing Calibration . . . . .   | 47 |
| 2.15 | Alignment Calibration . . . . .  | 49 |
| 2.16 | PMT Weaving Pattern . . . . .  | 50 |
| 2.17 | Simulated and Measured Cross-talk strength . . . . .   | 51 |
| 3.1  | Simulated Neutrino Flux at MINERvA . . . . .   | 53 |

|      |   |     |
|------|---|-----|
| 3.2  | Constrained Flux . . . . .  | 57  |
| 3.3  | RPA and Resonant Pion Reweight . . . . .  | 59  |
| 4.1  | Time Structure of a Typical Gate . . . . .  | 61  |
| 4.2  | Examples of various types of cluster . . . . .  | 63  |
| 4.3  | Example of Tracking Algorithm . . . . .   | 65  |
| 4.4  | Electron Fractional Energy Loss per Radiation Length . . . . .                        | 67  |
| 4.5  | illustration of EM Shower region . . . . .  | 69  |
| 5.1  | Available energy distribution sliced by lepton energy of $\nu + e$ sub-sample . . . . | 84  |
| 5.2  | Selected sample distributions . . . . .   | 86  |
| 5.3  | Illustration of sideband definition . . . . .   | 88  |
| 5.4  | Non-coherent sideband sample distributions before constraint . . . . .                | 90  |
| 5.5  | Coherent sideband sample distributions before constraint . . . . .                    | 91  |
| 5.6  | Diffraction sideband sample distributions before constraint . . . . .                 | 92  |
| 5.7  | Wrong sign prediction in signal region . . . . .                                      | 95  |
| 5.8  | Non-coherent sideband sample distributions after constraint . . . . .                 | 97  |
| 5.9  | Coherent sideband sample distributions after constraint . . . . .                     | 98  |
| 5.10 | Diffraction sideband sample distributions after constraint . . . . .                  | 99  |
| 5.11 | Selected sample distributions after background constraint . . . . .                   | 100 |
| 5.12 | Migration matrices . . . . .  | 102 |
| 5.13 | Estimated acceptance . . . . .  | 104 |
| 5.14 | Measured differential cross section . . . . .   | 106 |
| 5.15 | Fractional uncertainties of measured differential cross section . . . . .             | 107 |
| 5.16 | Non-coherent sideband sample distributions constrained by alternative method 1        | 115 |
| 5.17 | Coherent sideband sample distributions constrained by alternative method 1 . .        | 116 |
| 5.18 | Diffraction sideband sample distributions constrained by alternative method 1 .       | 117 |
| 5.19 | Non-coherent sideband sample distributions constrained by alternative method 2        | 118 |
| 5.20 | Coherent sideband sample distributions constrained by alternative method 2 . .        | 119 |
| 5.21 | Diffraction sideband sample distributions constrained by alternative method 2 .       | 120 |
| 5.22 | Comparison with published MINERvA $\nu_\mu$ measurements . . . . .                    | 122 |
| A1   | Conventional Closure Test . . . . .   | 125 |



|    |   |     |
|----|---|-----|
| A2 | Second Closure Test . . . . .   | 126 |
| B1 | Warping Tests Results . . . . .   | 129 |
| C1 | Excess Plots . . . . .  | 130 |
| C2 | Shower Shape Particle Cannon Study . . . . .                                    | 131 |
| C3 | $E_{\pi^0}\theta_{\pi^0}^2$ and $\Psi$ Distributions in Excess Region . . . . . | 132 |
| C4 | Upstream Inline Energy in bins of $E_{EM}$ in excess Region . . . . .           | 133 |

## Preface

I would like to dedicate this space to thank everyone helped me through my journey in earning the degree.

First, I want to thank the professors, staffs, and students in Physics department of University of Pittsburgh for giving me the opportunity and support to complete the Ph.D. program. Special thanks to Vittorio Paolone, my advisor, for supporting my free exploration in the physics world; To Donna Naples, for providing detailed and insightful feed backs for this work.

Second, I want to thank everyone in the MINERvA collaboration. This thesis could not possibly be completed without the hard work of everyone in the collaboration. Special thanks to Sarah Henry, who helped shape the final result of this work.

Third, thank you my parents. Thank you for giving me the opportunity to study aboard, which is a game-changer of my life. Thank you for your faith, patient, and support over the years.

Last but not least, thank you Xintong. I enjoyed the time we spent together and I am looking forward to spend my life with you. Love you.

## 1.0 Introduction

Physics was revolutionized in the 20th century. Longstanding classical mechanics, which successfully explained everything in life except “two clouds”[59], was superseded during the first two decades. Absolute spacetime concept was undermined by special and general relativity, while quantum mechanics revealed a non-continuous non-deterministic microscopic world. Physicists spend the next 50 years piecing together the theoretical framework and experimental evidence, leading to a theory of (almost) everything: the standard model, which is still the standard today.

The standard model is a quantum field theory, which is a theory compatible with special relativity and quantum mechanics, constrained by experimental inputs. It describes the structure of the world by 12 matter particles (fermions) and 5 force mediators (bosons), capable of explaining 3 out of 4 known fundamental forces<sup>1</sup>. The standard model is remarkably successful, as it predicts particles that have never been seen before, such as the top quark, tau neutrino, and Higgs boson, and makes the most accurate prediction in history: the prediction of the anomalous magnetic moment of the electron agrees with the measurement at an order of 10 significant figures[56].

However, it is known that the standard model is not complete. The major inadequacies include:

- Quantum field theory is incompatible with general relativity, another incredibly successful theory.
- Standard model doesn’t include dark matter and dark energy, which account for a large portion of energy in the universe[37].
- There are tens of free parameters that are completely determined by measurements, which is considered ad-hoc by some physicists.

Enormous number of theories have been proposed to extend the standard model to overcome the shortcomings, and it boils down to experimental evidence to confirm or rule out

---

<sup>1</sup>Strong, weak, and electromagnetic forces. Gravity is explained by general relativity

those theories. Hence searching for beyond standard model phenomena is the main topic of experimental particle physics today.

Neutrino oscillation, which means neutrinos created in one flavor ( $\nu_e, \nu_\mu$ , or  $\nu_\tau$ ) transform into another after traveling some distance in spacetime, is the first widely verified beyond standard model phenomenon. It was first observed in the 1960s as a deficit of solar neutrino flux and confirmed by multiple experiments later. The minimal modification of the standard model required to explain neutrino oscillation introduces 7 additional free parameters[90], while more complex models such as seesaw mechanism[106] are proposed to explain the origins of neutrino mass. As a result, the current frontier of experimental neutrino physics is the measurement of the oscillation parameters, especially the CP violating phase ( $\delta_{CP}$ ) and mass hierarchy, and ruling out models that are inconsistent with oscillation data. Neutrino

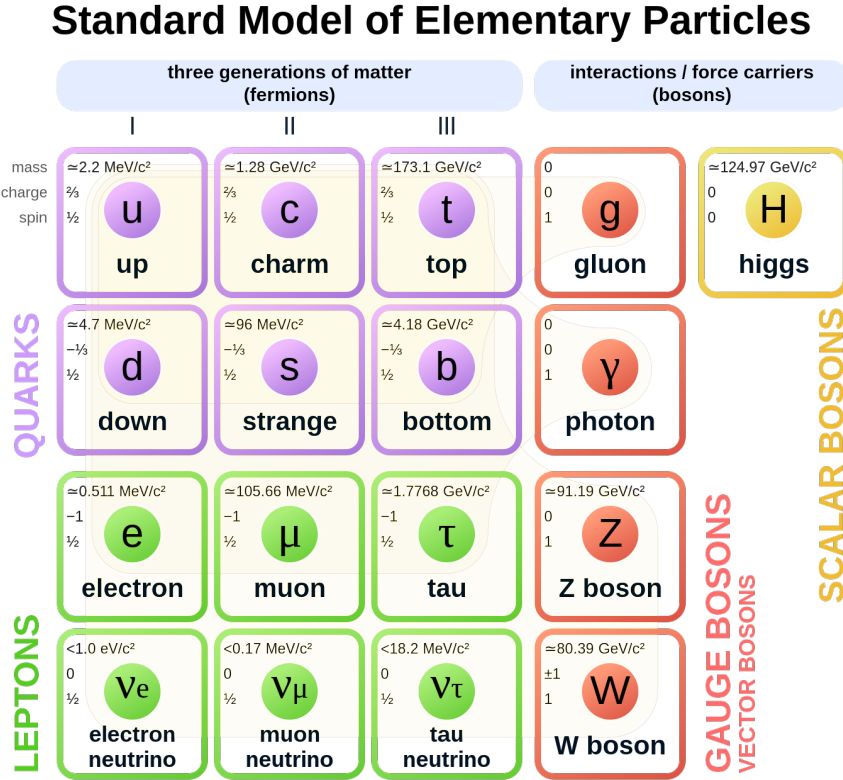


Figure 1.1: Particle contents of the standard model. Figure from[70]

oscillation experiments demand huge exposure to explore the parameter space because the neutrino interactions are “weak” and not well understood in the few GeV region. Therefore,  $\delta_{CP}$  and mass hierarchy are only weakly constrained by current data today, more than a half-century after the first observation of neutrino oscillations.

The Main Injector Experiment for  $\nu - A$  (MINERvA)[34], a neutrino scattering experiment located at Fermi National Accelerator Laboratory (Fermilab) in Batavia, IL, was conducted to improve our understanding of few GeV neutrino interactions. While the majority of MINERvA measurements focused on muon neutrinos, it is important to measure the electron neutrino cross section as well. The accelerator-based neutrino oscillation programs rely on the knowledge of electron neutrino cross section to make precise measurements of electron neutrino appearance probability, which is sensitive to  $\delta_{CP}$ . This thesis presents the first-ever double-differential cross section measurement of electron neutrino interaction in the low recoil region, using the hydrocarbon target in the MINERvA detector and  $\langle E_\nu \rangle \sim 7$  GeV neutrino beam.

Chapter 1 discusses the theoretical background and motivation of the measurement. Chapter 2 describes the data collection setup of the experiment, including the neutrino beam, the detector, and the calibration method. Chapter 3 describes the simulation we used to make a theoretical prediction of neutrino interactions in the detector. Chapter 4 discusses the reconstruction algorithm this analysis uses and chapter 5 describes the procedure this analysis used to extract cross section, the cross section results, and the uncertainties. Chapter 6 discusses the results and conclusion.

In this chapter, we’ll give a brief introduction to the standard model in section 1.1, and describe the neutrino oscillation phenomenon in section 1.2. Finally, the motivation of this analysis is presented in section 1.3. We’ll use natural units,  $\hbar = c = 1$ , through this chapter.

## 1.1 The Standard Model

### 1.1.1 Fields, Principle of Least Action, and Canonical Quantization

In the standard model, or quantum field theory in general, all particles are described by the *field*  $\psi(x^\mu)$ , which is a function of spacetime  $x^\mu = (t, \vec{x})$ , having one or multiple components depending on the objects it describes. The dynamics of the field are governed by the Lagrangian density  $\mathcal{L}(\partial_\mu\psi, \psi)$ , which is a functional of  $\psi$  and its spacetime derivative  $\partial_\mu\psi = \frac{\partial\psi}{\partial x^\mu}$ , and the principle of least action. The principle of least action states that the action is stationary to first order:

$$\delta S = \delta\left(\int d^4x \mathcal{L}\right) = 0 \quad (1)$$

such that the equation of motion is the Euler-Lagrange equation:

$$\partial_\mu\left(\frac{\partial\mathcal{L}}{\partial(\partial_\mu\psi)}\right) - \frac{\partial\mathcal{L}}{\partial\psi} = 0 \quad (2)$$

The formalism does not put a constraint on the form of  $\psi$  nor  $\mathcal{L}$  except that they have to transform properly under Lorentz group<sup>2</sup> in order to be compatible with special relativity. As a result,  $\psi$  must be a representation of the Lorentz group, and  $\mathcal{L}$  must be a Lorentz invariant. The well-known representations are scalar (scalar boson), spinor (fermion), and vector (vector boson) representations, each describing a type of elemental particle found in the real world, and a multiple particle field can be represented by the direct product of these representations. The corresponding free field lagrangians, which represent non-interacting particles traversing the spacetime, are listed in table 1.1.

The free fields can be quantized by canonical quantization, a.k.a second quantization, which is achieved by interpreting the fields as operators that obey canonical commutation relations, an interpretation of Heisenberg's uncertainty principle:

$$[\phi(\vec{x}), \pi(\vec{y})] = i\delta^{(3)}(\vec{x} - \vec{y}), \quad \pi(\vec{y}) = \frac{\partial\mathcal{L}}{\partial\dot{\phi}(\vec{y})} \quad (3)$$

---

<sup>2</sup>More precisely, Poincaré group

| Representation | Field     | Components | Free Field Lagrangian   | Equation of Motion                           |
|----------------|-----------|------------|---|--|
| Scalar         | $\phi$    | 1          | $\frac{1}{2}\partial^\mu\phi\partial_\mu\phi - \frac{1}{2}m^2\phi^2$  | $\partial^\mu\partial_\mu\phi + m^2\phi = 0$ |
| Spinor (Dirac) | $\psi$    | 4          | $i\bar{\psi}\gamma^\mu\partial_\mu\psi - m\bar{\psi}\psi$   | $i\gamma^\mu\partial_\mu\psi - m\psi = 0$    |
| Spinor (Weyl)  | $u_{L,R}$ | 2          | $iu_R^\dagger\sigma^\mu\partial_\mu u_R$  | $\sigma^\mu\partial_\mu u_R = 0$             |
|                |           |            | or $iu_L^\dagger\tilde{\sigma}^\mu\partial_\mu u_L$   | or $\tilde{\sigma}^\mu\partial_\mu u_L = 0$  |
| Vector         | $A^\mu$   | 4          | $-\frac{1}{4}F^{\mu\nu}F_{\mu\nu} + \frac{m^2}{2}A^\nu A_\nu$<br>where $F_{\mu\nu} = \partial_\mu A_\nu - \partial_\nu A_\mu$ | $\partial_\mu F^{\mu\nu} + m^2 A^\nu = 0$    |

Table 1.1: Well-known representations and corresponding free field lagrangians, from [78]

where the square bracket  $[A, B]$  is (anti-)commutator for (fermion) boson fields. This eventually leads to energy eigenstates given by:

$$H|\phi\rangle = \int d^3x (\pi(\vec{x})\dot{\phi}(\vec{x}) - \mathcal{L})|\phi\rangle = \int \frac{d^3p}{(2\pi)^3} \sqrt{|\vec{p}|^2 + m^2} N_{\vec{p}} |\phi\rangle \quad (4)$$

where  $N_{\vec{p}}$  is a non-negative integer. The energy eigenstates are interpreted as a collection of particles with various momentum  $\vec{p}$ , each has  $N_{\vec{p}}$  particles that share the same state.

### 1.1.2 Interacting Fields and Gauge Theory

So far, the particles freely move in the universe, but we know real-life particles interact. Hence additional interaction terms (coupling terms) have to be added to the lagrangian to create a practical theory. At first glance, there are many possible coupling terms, but most of them suffer from non-physical states or ultraviolet divergence (non-renormalizable). Yang and Mills finally came up with a consistent way to introduce coupling terms without those problems, and such a theory was later known as a gauge theory.

The method they introduced generates coupling terms by requiring the lagrangian to be invariant under local transformations of a symmetry group (gauge transformations). As an example, we can start with gauge transformations of Dirac fields:

$$\psi \rightarrow e^{i\alpha_a(x)T^a}\psi \quad (5)$$

where  $\psi$  is a multiplet of Dirac fields,  $T^a$  are the generators of the symmetry group, and  $\alpha_a(x)$  are spacetime-dependent transformation parameters (hence local transformations). As a result, the free field lagrangian transforms like:

$$\begin{aligned}\mathcal{L} &= i\bar{\psi}\gamma^\mu\partial_\mu\psi - m\bar{\psi}\psi \\ &\rightarrow i\bar{\psi}\gamma^\mu e^{-i\alpha_a(x)T^a}\partial_\mu(e^{i\alpha_a(x)T^a}\psi) - m\bar{\psi}e^{-i\alpha_a(x)T^a}e^{i\alpha_a(x)T^a}\psi \\ &= i\bar{\psi}\gamma^\mu\partial_\mu\psi - m\bar{\psi}\psi + i\bar{\psi}\gamma^\mu e^{-i\alpha_a(x)T^a}(\partial_\mu e^{i\alpha_a(x)T^a})\psi\end{aligned}\tag{6}$$

Obviously, the lagrangian is not invariant under such transformations. it is necessary to replace derivative  $\partial_\mu$  by covariant derivative  $D_\mu$  to keep lagrangian invariant, which transforms in the following way:

$$D_\mu \rightarrow e^{i\alpha_a(x)T^a} D_\mu e^{-i\alpha_a(x)T^a}\tag{7}$$

which can be achieved by introducing additional vector fields,  $A_{a\mu}T^a$ , that transform in a particular way under the gauge transformations:

$$\begin{aligned}D_\mu &= \partial_\mu - igA_{a\mu}T^a \\ A_{a\mu}T^a &\rightarrow A_{a\mu}T^a + \frac{1}{g}\partial_\mu\alpha_a(x)T^a + i[\alpha_b(x)T^b, A_{c\mu}T^c]\end{aligned}\tag{8}$$

where  $g$  is a free parameter interpreted as coupling strength constant. As a result, the coupling term is introduced into the lagrangian naturally:

$$\begin{aligned}\mathcal{L} &= i\bar{\psi}\gamma^\mu D_\mu\psi - m\bar{\psi}\psi \\ &= i\bar{\psi}\gamma^\mu\partial_\mu\psi - m\bar{\psi}\psi + g\bar{\psi}\gamma^\mu A_{a\mu}T^a\partial_\mu\psi\end{aligned}\tag{9}$$

The last piece of the theory is adding free field dynamics terms of  $A_{a\mu}$  to the lagrangian, which turns out to be:

$$\begin{aligned}\mathcal{L}_A &= -\frac{1}{2}\text{tr}(F_{a\mu\nu}T^a F_b^{\mu\nu}T^b) = -\frac{1}{4}F_{a\mu\nu}F^{a\mu\nu} \\ F_{a\mu\nu}T^a &= \partial_\mu A_{a\nu}T^a - \partial_\nu A_{a\mu}T^a - ig[A_{b\mu}T^b, A_{c\nu}T^c]\end{aligned}\tag{10}$$

where square bracket  $[A, B]$  is the commutator. Notice that the free field lagrangian here is different from what listed in table 1.1, because of the additional gauge invariance constraint.



The gauge theory is a built-in feature of quantum electrodynamics, and the work done by Yang and Mills generalizes the idea to non-abelian cases, leading to a successful explanation of the strong force (quantum chromodynamics) with  $SU(3)$  gauge symmetry constraint. However, the gauge theory had difficulty explaining the weak interaction because experimental evidence suggested that the vector boson mediator of the weak force is massive. In contrast, gauge theory forbids vector boson mass term due to gauge invariance constraint. This problem was solved later by Higgs mechanism, giving the standard model its modern form.

We'll introduce the standard model lagrangian before exploring the Higgs mechanism, such that we can derive the weak interaction lagrangian that this analysis measures.

### 1.1.3 Standard Model Lagrangian

The standard model is a gauge theory with symmetry group  $SU(3) \times SU(2) \times U(1)$ , plus additional Higgs field and Yukawa couplings to give particles masses.

The standard model lagrangian can be written as[39]<sup>3</sup>:

$$\begin{aligned}
\mathcal{L} = & -\frac{1}{4}B_{\mu\nu}B^{\mu\nu} - \frac{1}{8}W_{a\mu\nu}W^{a\mu\nu} - \frac{1}{2}T_{a\mu\nu}T^{a\mu\nu} && \text{gauge boson dynamics} \\
& +(\nu_L^\dagger, e_L^\dagger)\tilde{\sigma}^\mu iD_\mu \begin{pmatrix} \nu_L \\ e_L \end{pmatrix} + e_R^\dagger \sigma^\mu iD_\mu e_R + \text{h.c.} && \text{lepton dynamics} \\
& +(u_L^\dagger, d_L^\dagger)\tilde{\sigma}^\mu iD_\mu \begin{pmatrix} u_L \\ d_L \end{pmatrix} + u_R^\dagger \sigma^\mu iD_\mu u_R + d_R^\dagger \sigma^\mu iD_\mu d_R + \text{h.c.} && \text{quark dynamics} \\
& +(D_\mu \phi)^\dagger D^\mu \phi - \frac{m_h^2}{2v^2}[\phi^\dagger \phi - v^2/2]^2 && \text{Higgs field} \\
& -\frac{\sqrt{2}}{v} \left[ (\nu_L^\dagger, e_L^\dagger)\phi M^e e_R + e_R^\dagger (M^e)^\dagger \phi^\dagger \begin{pmatrix} \nu_L \\ e_L \end{pmatrix} \right] && \text{charged-lepton mass} \\
& -\frac{\sqrt{2}}{v} \left[ (u_L^\dagger, d_L^\dagger)\phi M^d d_R + d_R^\dagger (M^d)^\dagger \phi^\dagger \begin{pmatrix} u_L \\ d_L \end{pmatrix} \right] && \text{down-type quark mass} \\
& -\frac{\sqrt{2}}{v} \left[ (-d_L^\dagger, u_L^\dagger)\phi^* M^u u_R + u_R^\dagger (M^u)^\dagger \phi^T \begin{pmatrix} -d_L \\ u_L \end{pmatrix} \right] && \text{up-type quark mass}
\end{aligned} \tag{11}$$

where h.c. means hermitian conjugate of preceding terms. We'll explain each terms in the following context.

---

<sup>3</sup>Written in chiral basis and explicit  $SU(2)$  doublet, assuming massless neutrino. Righted neutrinos are omitted because they are completely isolated with other particles in this case

### 1.1.3.1 Gauge Boson Dynamics Terms

There are three gauge boson fields whose vector potentials are  $G_{a\mu}T^a$ ,  $W_{a\mu}t^a$ , and  $B_\mu$ , corresponding to SU(3), SU(2), and U(1) gauge symmetries, respectively, adding up to  $8 + 3 + 1$  vector fields<sup>4</sup>. It is common to choose the explicit form of  $T^a$  and  $t^a$  to be Gell-Mann matrices  $\frac{\lambda^a}{2}$  and Pauli matrices  $\frac{\sigma^a}{2}$ , such that the field strength tensors ( $G_{a\mu\nu}$ ,  $W_{a\mu\nu}$ , and  $B_{\mu\nu}$ ) given by equation 10 can be simplified to:

$$\begin{aligned} G_{a\mu\nu} &= \partial_\mu G_{a\nu} - \partial_\nu G_{a\mu} + g_3 f_a^{bc} G_{b\mu} G_{c\nu} \\ W_{a\mu\nu} &= \partial_\mu W_{a\nu} - \partial_\nu W_{a\mu} + g_2 \epsilon_a^{bc} W_{b\mu} W_{c\nu} \\ B_{\mu\nu} &= \partial_\mu B_\nu - \partial_\nu B_\mu \end{aligned} \tag{12}$$

Where  $g_3$  and  $g_2$  are coupling constants of SU(3) and SU(2),  $f_a^{bc}$  and  $\epsilon_a^{bc}$  are completely anti-symmetric structure constants of SU(3) and SU(2)<sup>5</sup>.

### 1.1.3.2 Lepton Dynamics Terms

There are 3 lepton fields,  $e_L$ ,  $e_R$  and  $\nu_L$ , in standard model. Each of them has implicit 3-component generation indices,  $e_i = (e, \mu, \tau)$  and  $\nu_i = (\nu_e, \nu_\mu, \nu_\tau)$ , adding up to  $3 \times 3$  Weyl spinor fields. The covariant derivative is given by:

$$D_\mu = \partial_\mu - ig_1 B_\mu Y - ig_2 W_{a\mu} t^a \tag{13}$$

with

$$\begin{aligned} t^a &= 0 & Y &= -1 & \text{for } e_R \\ t^a &= \frac{\sigma^a}{2} & Y &= -\frac{1}{2} & \text{for } (\nu_L, e_L) \end{aligned} \tag{14}$$

where  $g_1$  is U(1) coupling constant. The values of  $Y$  and  $t^a$  for different fields are required by experimental inputs, the electric charge and maximal parity violation feature of weak interactions.

---

<sup>4</sup>The W, Z, and gamma bosons are linear combinations of  $W_{a\mu}t^a$  and  $B_\mu$  fields, discussed in section 1.1.4.

<sup>5</sup> $\epsilon_a^{bc}$  is Levi-Civita symbol.  $f^{123} = 1, f^{147} = f^{165} = f^{246} = f^{257} = f^{345} = f^{376} = \frac{1}{2}, f^{458} = f^{678} = \frac{\sqrt{3}}{2}$

### 1.1.3.3 Quark Dynamics Terms

There are four quark fields,  $u_{L,R}$  and  $d_{L,R}$ , which have implicit generation indices like lepton fields:  $u_i = (u, c, t)$  and  $d_i = (d, s, b)$ . In addition, quark fields have 3-component color indices that contract with SU(3) gauge field  $G_{a\mu} \frac{\lambda^a}{2}$  through covariant derivative:

$$D_\mu = \partial_\mu - ig_1 B_\mu Y - ig_2 W_{a\mu} t^a - ig_s G_{a\mu} \frac{\lambda^a}{2} \quad (15)$$

with

$$\begin{array}{lll} t^a = 0 & Y = \frac{2}{3} & \text{for } u_R \\ t^a = 0 & Y = -\frac{1}{3} & \text{for } d_R \\ t^a = \frac{\sigma^a}{2} & Y = \frac{1}{6} & \text{for } (u_L, d_L) \end{array} \quad (16)$$

There are  $4 \times 3 \times 8$  Weyl spinor fields for quarks.

### 1.1.3.4 Higgs Field Terms

The Higgs field is a SU(2) doublet scalar field in the standard model:

$$\phi = \frac{1}{\sqrt{2}} \begin{pmatrix} \phi^+ \\ \phi^0 \end{pmatrix} \quad (17)$$

The covariant derivative is:

$$\begin{aligned} D_\mu &= \partial_\mu - ig_1 B_\mu Y - ig_2 W_{a\mu} t^a \\ t^a &= \frac{\sigma^a}{2} \quad Y = \frac{1}{2} \end{aligned} \quad (18)$$

$m_h$  and  $\nu$  are Higgs mass and Higgs vacuum expectation value (VEV) respectively. Assuming the Higgs field has non-zero VEV, the interaction terms of ground state Higgs field and vector fields become the forbidden mass terms for vector fields. This is known as Higgs mechanism, and we'll discuss how this works in section 1.1.4. The standard model assumes the Higgs potential takes a double well form like equation 11, leading to VEV given by:

$$\langle \phi \rangle = e^{i\alpha_i \sigma^i} \frac{1}{\sqrt{2}} \begin{pmatrix} 0 \\ \nu \end{pmatrix} \quad (19)$$

where  $\alpha_i$  is an arbitrary SU(2) phase.

### 1.1.3.5 Lepton and Quark Mass Terms (Yukawa Coupling)

While Higgs mechanism makes gauge theory capable of generating massive vector bosons, the weak interaction poses another challenge to the theory because of the parity violation. The naive fermion mass term in Weyl spinor form is  $-m(u_L^\dagger u_R + \text{h.c.})$ , which is not invariant under  $SU(2)$  gauge transformation because  $u_L$  transforms as a part of doublet while  $u_R$  transforms as singlet. The solution is generating mass terms by coupling with the Higgs field, known as Yukawa coupling. The Higgs field transforms as a doublet under  $SU(2)$  gauge transformation, which cancels the left-handed spinor doublet transformation. The Yukawa coupling constants are not constrained by gauge theory, hence the gauge interaction eigenstates are not necessarily the mass eigenstates. Experimental evidence suggests that the  $SU(2)$  gauge interaction eigenstates are not mass eigenstates indeed, but there is no evidence that the  $SU(3)$  interaction eigenstates are different from mass eigenstates<sup>6</sup>. As a result, the Yukawa coupling terms in the standard model are written in the forms of 3 mass matrices,  $M^{e,u,d}$ , that contract with implicit generation indices, as shown in equation 11. By redefining the fermion fields by mass eigenstates, the  $SU(2)$  gauge bosons couple to all three generations of quarks, leading to flavor mixing discussed in section 1.1.5.

### 1.1.4 Spontaneous Symmetry Breaking and Electroweak Interaction

As mentioned above, Higgs field has non-vanishing VEV, hence we can redefine the Higgs field by the sum of the VEV and residual field:

$$\phi = \langle \phi \rangle + h \quad (20)$$

Taking the arbitrary phase of  $\langle \phi \rangle$  to be 0 without loss of generality, the Higgs terms of lagrangian can be rewritten as:

$$\mathcal{L}_{Higgs} = \frac{\nu^2}{8} [g_2^2 (W_\mu^1 W^{1\mu} + W_\mu^2 W^{2\mu}) + (g_2 W_\mu^3 - g_1 B_\mu)(g_2 W^{3\mu} - g_1 B^\mu)] + \mathcal{O}(h, \partial_\mu h) \quad (21)$$

---

<sup>6</sup>Why does strong interaction behaves this way is another question by itself, which is known as the strong CP problem.

which are terms quadratic in  $W_{a\mu}$  and  $B_\mu$ , i.e. mass terms. The mass eigenstates of electroweak gauge bosons (W boson  $W_\mu^\pm$ , Z boson  $Z_\mu$ , and photon  $A_\mu$ ) are linear combinations of  $W_{a\mu}$  and  $B_\mu$ :

$$\begin{aligned} W_\mu^\pm &= \frac{1}{\sqrt{2}}(W_\mu^1 \mp iW_\mu^2) & m_w &= g_2 \frac{\nu}{2} \\ Z_\mu &= \frac{1}{\sqrt{g_1^2 + g_2^2}}(g_2 W_\mu^3 - g_1 B_\mu) & m_Z &= \frac{\nu}{2} \sqrt{g_1^2 + g_2^2} \\ A_\mu &= \frac{1}{\sqrt{g_1^2 + g_2^2}}(g_1 W_\mu^3 + g_2 B_\mu) & m_A &= 0 \end{aligned} \quad (22)$$

Consequently, the electroweak part of the covariant derivative can be written in terms of massive vector fields:

$$D_\mu = \partial_\mu - i \frac{g_2}{\sqrt{2}}(W_\mu^+ t^+ + W_\mu^- t^-) - i \frac{g_2}{\cos \theta_w} Z_\mu(t^3 - \sin^2 \theta_w Q) - ie A_\mu Q \quad (23)$$

where

$$\begin{aligned} \cos \theta_w &= \frac{g_2}{g_1^2 + g_2^2} & e &= g_2 \sin \theta_w & Q &= t^3 + Y \\ t^\pm &= \frac{\sigma^1}{2} \pm i \frac{\sigma^2}{2} & t^3 &= \frac{\sigma^3}{2} & & \text{for } (u_L, d_L), (\nu_L, e_L) \\ & & t^\pm &= t^3 = 0 & & \text{for } u_R, d_R, e_R \end{aligned}$$

Finally, the electroweak interaction Lagrangian is:

$$\begin{aligned} \mathcal{L}_{EW} &= \frac{g_2}{\sqrt{2}}(\nu_L^\dagger \tilde{\sigma}^\mu W_\mu^+ e_L + e_L^\dagger \tilde{\sigma}^\mu W_\mu^- \nu_L + u_L^\dagger \tilde{\sigma}^\mu W_\mu^+ d_L + d_L^\dagger \tilde{\sigma}^\mu W_\mu^- u_L) & \text{charged-current} \\ &+ \frac{g_2}{\cos \theta_w} \left[ \sum_{u=\nu, u} \left( \frac{1}{2} + Q \sin^2 \theta_w \right) u_L^\dagger \tilde{\sigma}^\mu Z_\mu u_L \right. \\ &+ \sum_{u=e, d} \left( -\frac{1}{2} + Q \sin^2 \theta_w \right) u_L^\dagger \tilde{\sigma}^\mu Z_\mu u_L + \sum_{u=e, u, d} Q \sin^2 \theta_w u_R^\dagger \sigma^\mu Z_\mu u_R \left. \right] & \text{neutral-current} \\ &+ e \sum_{u=e, u, d} Q(u_L^\dagger \tilde{\sigma}^\mu A_\mu u_L + u_R^\dagger \sigma^\mu A_\mu u_R) & \text{electromagnetic} \end{aligned} \quad (24)$$

The W boson mediated interaction are usually referred as charged current (CC) interactions, while the Z boson mediated interactions are referred as neutral-current (NC) interactions. Notice that the left handed and right handed spinners couple to W and Z bosons differently,

especially the W boson, which only couples to left handed spinners (left handed particle or right handed anti-particle). This feature is known as parity-violation of the weak interaction, which is a result of complete decoupling of right handed spinner fields and the  $W_{a\mu}$  gauge field in the Lagrangian. The parity violation was first experimentally observed by Wu in 1957[105] and the V-A theory proposed by Feymann and Gell-Mann in 1958[44, 97] was the first theory successfully described this iconic characteristic of the weak interaction.

### 1.1.5 Flavor Mixing and CKM Matrix

The last but not least feature of the standard model is flavor mixing, as advertised in section 1.1.3. The fermion fields we have been discussing are eigenstates of SU(2) gauge interactions or flavor eigenstates, but the particles detected in detectors are usually mass eigenstates, which can be defined by:

$$u'_{L,R} = U_{L,R}^u u_{L,R} \quad u = u, d, e, \nu \quad (25)$$

where  $U_{L,R}^u$  are 3 by 3 unitary matrices contracted with generation indices. Rewriting the lagrangian in terms of mass eigenstate fermions, the  $U$  matrices cancel with each other except the W boson coupling term,  $u_L'^{\dagger} U_L^u \tilde{\sigma}^{\mu} W_{\mu}^{\pm} U_L^{d\dagger} d'_L$ , or  $u_L'^{\dagger} V^q \tilde{\sigma}^{\mu} W_{\mu}^{\pm} d'_L$  where  $V^q = U_L^u U_L^{d\dagger}$ . The  $V^q$  is known as Cabibbo-Kobayashi-Maskawa matrix (CKM matrix), which can be parameterized by 3 mixing angles and 1 CP violating phase by absorbing constants into fermion fields:

$$V^q = \begin{bmatrix} 1 & 0 & 0 \\ 0 & \cos \theta_{23} & \sin \theta_{23} \\ 0 & -\sin \theta_{23} & \cos \theta_{23} \end{bmatrix} \begin{bmatrix} \cos \theta_{13} & 0 & \sin \theta_{13} e^{-i\delta} \\ 0 & 1 & 0 \\ -\sin \theta_{13} e^{i\delta} & 0 & \cos \theta_{13} \end{bmatrix} \begin{bmatrix} \cos \theta_{12} & \sin \theta_{12} & 0 \\ -\sin \theta_{12} & \cos \theta_{12} & 0 \\ 0 & 0 & 1 \end{bmatrix} \quad (26)$$

The non-diagonal CKM matrix leads to couplings of all 3 mass eigenstates of up type quarks to all 3 down type quarks, in contrast with flavor eigenstates which only couples corresponding doublets (u and d, c and s, or t and b). Such phenomenon is known as flavor mixing.

## 1.2 Beyond Standard Model: Neutrino Oscillation

### 1.2.1 History of Neutrino Mass and Oscillations

The neutrino was assumed to be a particle lighter than an electron when Pauli introduced neutrinos in 1930 and early experiments put an upper bound of neutrino mass of 100-200 eV by beta decay[25]. The theory of massless neutrino was first proposed by Landau[60], Lee and Yang[62], and Salam[89], and further established in the V-A theory of weak interactions in 1958. Although these theories didn't require massless neutrinos, it was a popular assumption at the time the standard model matured, since there was no evidence of massive neutrinos.

The idea of the massless neutrino was challenged when Raymond Davis and collaborators measured solar neutrino flux and found a deficit of roughly two-thirds of what was expected[31]. Many subsequent experiments confirmed the deficit Davis found, and ruled out the possibility of experimental error, and gave rise to the solar neutrino problem.

Neutrino oscillation, first predicted by B. Pontecorvo[79] as a consequence of massive neutrino assumption, was one of the proposed solutions to the solar neutrino problem. It became the most convincing solution after Super-Kamiokande detector observed atmosphere neutrino oscillations by measuring electron and muon neutrino flux as functions of zenith angle in 1998[47]. In 2001, the Sudbury Neutrino Observatory (SNO) provided direct evidence of solar neutrino oscillations by making neutral-current measurement of solar neutrino flux[13], which confirmed that the neutrino flux of all flavors is consistent with the solar model, and rejected all solutions that modify the solar model. These two measurements dealt the fatal blow to the massless neutrino assumption and the 2015 Nobel Prize in Physics was awarded to Takaaki Kajita (Super-Kamiokande) and Arthur B. McDonald (SNO) for the discovery of neutrino oscillations.

Since then, the neutrino community has been working on determining the masses and mixing angles of neutrinos by measuring neutrino oscillation with all sources of neutrinos. As of today, neutrino oscillation measurements have entered the precision era, in which experiments are attempting to measure oscillation parameters at a few percent uncertainties. On the other hand, the source of neutrino mass (Majorana or Dirac, or both) is another

open question. There are ongoing experiments, such as KamLAND-Zen[48], looking for neutrinoless double beta decay, a signature of Majorana mass.

### 1.2.2 Neutrino Oscillation Formalism

A simple extension to the standard model can describe neutrino oscillation: adding right-handed neutrino fields  $\nu_R$  and its dynamic terms<sup>7</sup>, and assuming Yukawa coupling constants of neutrinos,  $M^\nu$ , has non-zero eigenvalue. As a result, neutrino mass eigenstates would be distinct from mass eigenstates, related by a matrix similar to the CKM matrix, which is known as the Pontecorvo-Maki-Nakagawa-Sakata matrix (PMNS matrix)  $U$ .

The elements of PMNS matrix and neutrino mass splittings can be measured by neutrino oscillation experiments, which measure CC neutrino interaction event rates at two different locations, or at one location and make assumptions about the initial state of neutrino. We can demonstrate this by assuming a neutrino beam in a flavor eigenstate with definite 3 momenta  $\vec{p}$ <sup>8</sup>:

$$|\nu_\alpha\rangle = \sum_i U_{\alpha i}^* |\nu_i\rangle \quad \alpha = e, \mu, \tau \quad (27)$$

According to the Schrödinger equation, the mass eigenstates evolve in time as plane waves:

$$|\nu_i(t)\rangle = e^{iE_i t} |\nu_i\rangle \quad (28)$$

Consequently, the flavor eigenstates evolve in time as:

$$|\nu_\alpha(t)\rangle = \sum_i U_{\alpha i}^* e^{iE_i t} |\nu_i\rangle = \sum_{\beta=e,\mu,\tau} \sum_i U_{\alpha i}^* e^{iE_i t} U_{\beta i} |\nu_\beta\rangle \quad (29)$$

The event rate of charged-current neutrino interactions, which produces a charged lepton  $\beta$ , is proportional to the transition probability  $P(\nu_\alpha \rightarrow \nu_\beta)$ , which is the probability of a

---

<sup>7</sup> $D_\mu = \partial_\mu$  since  $t^a = 0$  and  $Y = 0$  for  $\nu_R$

<sup>8</sup>This assumption is not realistic at all, because such state must have definite energy as well because of energy-momentum conservation in the production process, leading to a mixture rather than a superposition of mass eigenstates. However, this assumption is applicable to practical oscillation experiments as discussed in [49].



neutrino created in  $|\nu_\alpha\rangle$  state observed in  $|\nu_\beta\rangle$  state[49]:

$$\begin{aligned} N_\beta &\propto P(\nu_\alpha \rightarrow \nu_\beta) = |\langle \nu_\beta | \nu_\alpha(t) \rangle|^2 = \left| \sum_i U_{\alpha i}^* e^{iE_i t} U_{\beta i} \right|^2 \\ &= \sum_{i,j} U_{\alpha i}^* U_{\beta i} U_{\alpha j} U_{\beta j}^* e^{i(E_i - E_j)t} \end{aligned} \quad (30)$$

For practical neutrino oscillation experiments, we can make approximations in the ultra relativistic limit  $m_i \ll E = |\vec{p}|$ , such that the energy  $E_i$  can be approximate by  $E + \frac{m_i^2}{2E}$ , and the time between creation and detection can be approximated by the distance between the detector and source  $L$ . As a result, the transition probability is written as:

$$P(\nu_\alpha \rightarrow \nu_\beta, L, E) = \sum_{i,j} U_{\alpha i}^* U_{\beta i} U_{\alpha j} U_{\beta j}^* \exp\left(-i \frac{\Delta m_{ij}^2 L}{2E}\right) \quad (31)$$

where  $\Delta m_{ij}^2 = m_i^2 - m_j^2$ .

The formula we presented here is a simplified version of the complete story. A more accurate approach, including the MSW effect[93] that enables the sign measurement of  $\Delta m_{ij}^2$ , and/or wave package treatment, is employed by real neutrino oscillation analyses[43, 49].

### 1.2.3 Current Status of Neutrino Oscillation Parameter Measurements

The PMNS matrix is usually parameterized the same way as CKM matrix like quation 26, hence there are 6 measurable parameters (3 mixing angle  $\theta_{12,23,13}$ , 1 CP violating phase  $\delta_{CP}$ , and 2 mass splitting  $\Delta m_{21}^2, \Delta m_{13}^2$ ). There are four types of neutrino sources that are commonly used in oscillation experiments: solar, atmosphere, reactor, and accelerator neutrinos, each type has a unique practical constraint of energy and distance, leading to sensitivities to different parameters, summarized in table 1.2. The best fit of these parameters is listed in table 1.3. As shown in table 1.3, the sign of  $\Delta m_{13}^2$  (mass hierarchy) and  $\delta_{CP}$  are not well measured yet. Data favors normal ordering ( $m_3^2 > m_1^2$ ) by marginal  $\chi^2$ , and more than half of  $\delta_{CP}$  phase space is still allowed at  $3\sigma$ . Long baseline accelerator-based neutrino oscillation experiments, such as T2K,  $\text{No}\nu\text{A}$ , and next-generation flagship DUNE, are most sensitive to these two parameters. Both T2K and  $\text{No}\nu\text{A}$  are taking data and aim to determine mass hierarchy with full statistics and DUNE, which is in preparation, aims for covering more than 75% of  $\delta_{CP}$  by  $3\sigma$ [3].

On the other hand, there are on-going efforts in the neutrino community to refine the measurements of other oscillation parameters as well, such as reactor based experiment JUNO[19], atmospheric neutrino experiment IceCube[1], and standard solar model works[92].

| Experiment   | Dominant                            | Important   |
|--|-------------------------------------|---|
| Solar Experiments  | $\theta_{12}$                       | $\Delta m_{12}^2, \theta_{13}$                      |
| Reactor LBL (KamLAND)  | $\Delta m_{12}^2$                   | $\theta_{12}, \theta_{13}$                          |
| Reactor MBL (Daya-Bay, Reno, D-Chooz)                                | $\Delta  m_{12,13}^2 , \theta_{13}$ |   |
| Atmospheric Experiments (SK, IC-DC)                                  |                                     | $\Delta  m_{12,13}^2 , \theta_{13,23}, \delta_{CP}$ |
| Accel LBL $\nu_\mu, \bar{\nu}_\mu$ , Disapp (MINOS, T2K, NO $\nu$ A) | $\Delta  m_{12,13}^2 , \theta_{23}$ |   |
| Accel LBL $\nu_e, \bar{\nu}_e$ , App (MINOS T2K, NO $\nu$ A)         | $\delta_{CP}$                       | $\theta_{13}, \theta_{23}$                          |

Table 1.2: Experiments contributing to the present determination of the oscillation parameters, from [107]

| Parameters                             | Normal Ordering (best fit) |                           | Inverted Ordering ( $\Delta\chi^2 = 2.7$ ) |                             |
|--|----------------------------|---------------------------|--|-----------------------------|
|  | bfp $\pm 1\sigma$          | $3\sigma$ range           | bfp $\pm 1\sigma$                          | $3\sigma$ range             |
| $\theta_{12}/^\circ$                   | $33.44^{+0.78}_{-0.75}$    | $37.21 \rightarrow 35.86$ | $33.45^{+0.78}_{-0.75}$                    | $37.21 \rightarrow 35.87$   |
| $\theta_{23}/^\circ$                   | $49.0^{+1.1}_{-1.4}$       | $39.6 \rightarrow 51.8$   | $49.3^{+1.0}_{-1.2}$                       | $39.9 \rightarrow 52.0$     |
| $\theta_{13}/^\circ$                   | $8.57^{+0.13}_{-0.12}$     | $8.20 \rightarrow 8.97$   | $8.61^{+0.12}_{-0.12}$                     | $8.24 \rightarrow 8.98$     |
| $\delta_{CP}/^\circ$                   | $195^{+51}_{-25}$          | $107 \rightarrow 403$     | $286^{+27}_{-32}$                          | $192 \rightarrow 360$       |
| $\frac{\delta m_{21}^2}{10^{-5}} eV^2$ | $7.42^{+0.21}_{-0.20}$     | $6.82 \rightarrow 8.04$   | $7.42^{+0.21}_{-0.20}$                     | $6.82 \rightarrow 8.04$     |
| $\frac{\delta m_{31}^2}{10^{-3}} eV^2$ | $2.514^{+0.028}_{-0.027}$  | $2.431 \rightarrow 2.598$ | $-2.497^{+0.028}_{-0.028}$                 | $-2.583 \rightarrow -2.412$ |

Table 1.3: Best-fit values of neutrino oscillation parameters, without SK atmospheric data, from [43].

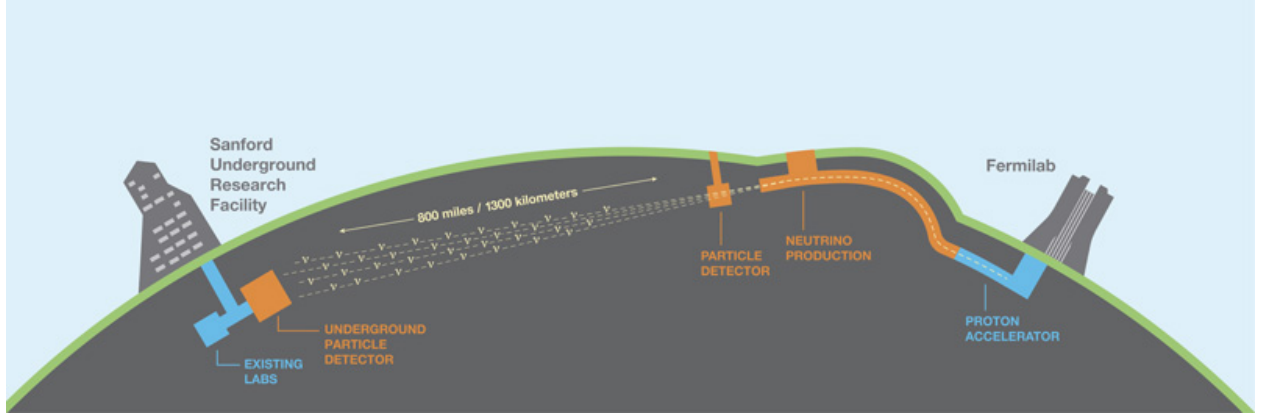


Figure 1.2: Cartoon illustrating the configuration of DUNE Experiment. Figure from [3]

#### 1.2.4 Beyond 3 Neutrino Paradigm

Despite the success of the 3 neutrino oscillation paradigm, there are several anomalies that can not be explained by this framework. LSND reported  $\bar{\nu}_\mu \rightarrow \bar{\nu}_e$  appearance at  $L/E \approx 1\text{eV}^2$  in 2001[12]. Subsequently, MiniBooNE observed an excess of electron neutrino and antineutrino at the low energy region (MiniBooNE LEE), which can be explained by neutrino oscillations using parameters consistent with LSND[36]. On the other hand, Gallium-based solar neutrino experiments, SAGE and GALLEX/GNO, observed an event rate lower than expected, which can be explained by neutrino oscillation with  $\Delta m^2 \gtrsim 1\text{eV}$ [7, 50].

The existence of more neutrinos with masses in the eV region is postulated to explain these anomalies, yet none of them consistently explained all anomalies. The Short-Baseline Neutrino (SBN) Program at Fermilab, which consists of three detectors, is built to search for neutrinos at eV scale[65].

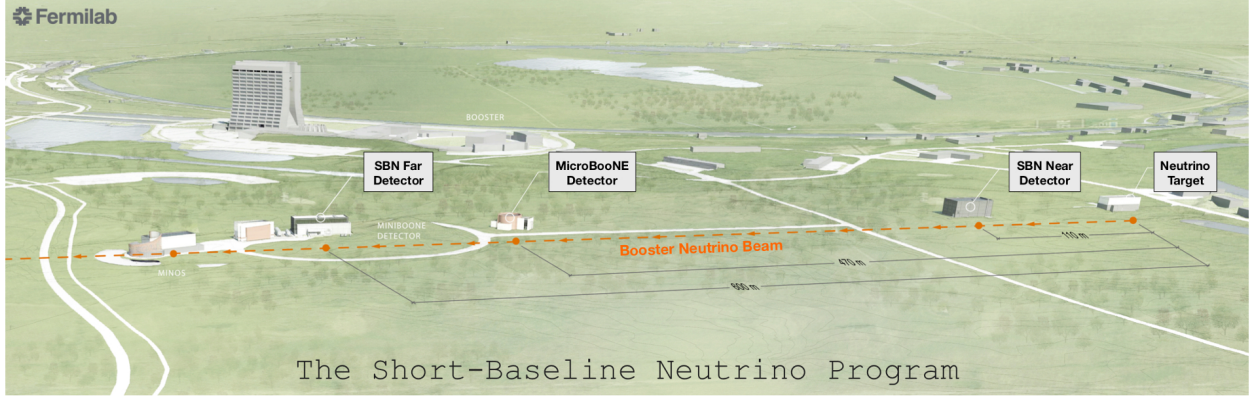


Figure 1.3: An Aerial view of SBN program. 8 GeV Booster proton beam interacts with the target on the right of the plot, creating a neutrino beam traveling to the left. SBN Near Detector, MicroBooNE, and SBN Far Detector are located downstream on the beamline (in this order). Figure from [65]

### 1.3 Motivation of Neutrino Scattering Cross Section Measurements

#### 1.3.1 Neutrino Cross Section as Input to Oscillation Measurements

Neutrino cross section uncertainty is one of the dominating systematical uncertainties for current long baseline accelerator neutrino oscillation measurements (T2K and  $\text{NO}\nu\text{A}$ ), and is expected to dominate DUNE uncertainty as well[33]. The neutrino oscillation amplitude is energy dependent, but current detectors can not measure neutrino energy without using interaction models. On one hand, the charged lepton kinematics can be measured precisely, but this alone can not determine neutrino energy without assumptions of hadronic final states. On the other hand, hadronic energy measurement is not reliable, because the calorimetry response depends on particle type, which is not trivial to determine, and the response doesn't strong correlated with the neutron kinematic energy.

Although all aforementioned experiments use a near detector to constrain the neutrino interaction model, the cross section uncertainty can not be avoided altogether. The near detector may use a different technology from the far detector, hence the cross section de-

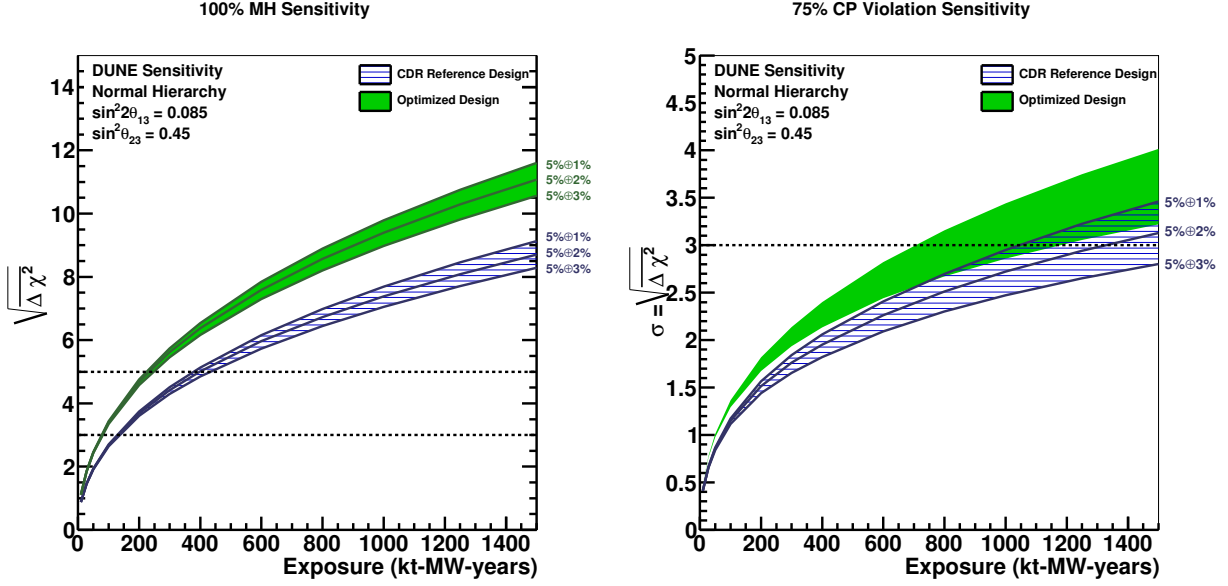


Figure 1.4: Expected sensitivity of DUNE as a function of exposure and signal normalization uncertainty. Figure from [33]

pendence doesn't cancel exactly, because of A-dependence and/or detector physics modeling differences. Even if the two detectors are identical, the interaction model has to be invoked to constrain the neutrino flux model. The neutrino flux as a function of energy is another significant uncertainty of oscillation measurements. The (unoscillated) neutrino flux is usually not the same at the near and the far detector, because of alignment error and/or physical constraints. As a result, the near detector has to constrain the flux model as well, by using an interaction model.

Consequently, improvements in neutrino interaction modeling will greatly help reduce the exposure required to meet goals of these experiments, as shown in figure 1.4.

### 1.3.2 Modeling of Neutrino Scattering and Its Challenges

We talked about why cross section uncertainty plays an important role in long baseline neutrino oscillation experiments, but we didn't discuss why the uncertainty of the interaction model is relatively large in the first place, given that we already understand the weak

interaction.

In the standard model, 2 particle scattering differential cross section is given by[78]:

$$d\sigma = \frac{1}{2E_A E_B |\nu_A - \nu_B|} \left( \prod_f \frac{d^3 p_f}{(2\pi)^3} \frac{1}{E_f} \right) \times |\mathcal{M}(p_A, p_B \rightarrow p_f)|^2 (2\pi)^3 \delta^4(p_A + p_B - \sum p_f) \quad (32)$$

where  $(E_A, p_A)$ ,  $(E_B, p_B)$ , and  $(E_f, p_f)$  are 4 momenta of incoming particles labeled A and B, and outgoing particles labeled  $f$ ,  $|\nu_A - \nu_B| = |\frac{p_A^z}{E_A} - \frac{p_B^z}{E_B}|$  is the relative velocity of beams viewed from lab frame, the delta function reflects energy-momentum conservation and  $\mathcal{M}$  is known as the transition matrix element. The calculation of the transition matrix is commonly summarized by Feynman diagrams and Feynman rules.

For example, the Feynman diagram for a Charged Current neutrino scattering off nucleus at leading order is shown in figure 1.5, and the corresponding matrix element, at the limit of small energies compared to W boson mass (about 80 GeV), can be written as:

$$\begin{aligned} i\mathcal{M}(\nu_e, A \rightarrow e^-, X) &= \frac{ig_2^2}{2m_w^2} j^\mu(p_\nu, p_l) J_\mu(p_A, p_X) \\ &= \frac{ig_2^2}{2m_w^2} \nu_L^\dagger(p_\nu) \tilde{\sigma}^\mu e_L(p_l) J_\mu(p_A, p_X) \end{aligned} \quad (33)$$

where  $j^\mu$  is lepton current that depends on lepton kinematics  $(p_\nu, p_e)$ , derived from the electron weak lagrangian term  $\nu_L^\dagger \tilde{\sigma}^\mu W_\mu^+ e_L$  and  $J_\mu$  is hadronic current, which is more complicated to calculate. The nucleus is a strong interacting many-body system, instead of elementary particles like the leptons, hence hadronic current can not be derived directly by the standard model lagrangian, yet. Consequently, the hadronic current is usually modeled by combinations of all possible terms allowed by conservation laws, such that the cross section can be expressed in terms of coefficients of the combination, or more concisely in terms of structure functions, which are functions of kinematic variables determined by experimental inputs. Due the lack of first principle description, the neutrino-nucleus interactions are artificially categorized to three main channels: elastic and quasi-elastic(QE), resonance production(RES), and deep inelastic scattering(DIS). There are a few sub-dominat channels, such as two-particle-two-hole(2p2h) process and coherent/diffractive pion production, which contribute a significant fraction for this measurement.

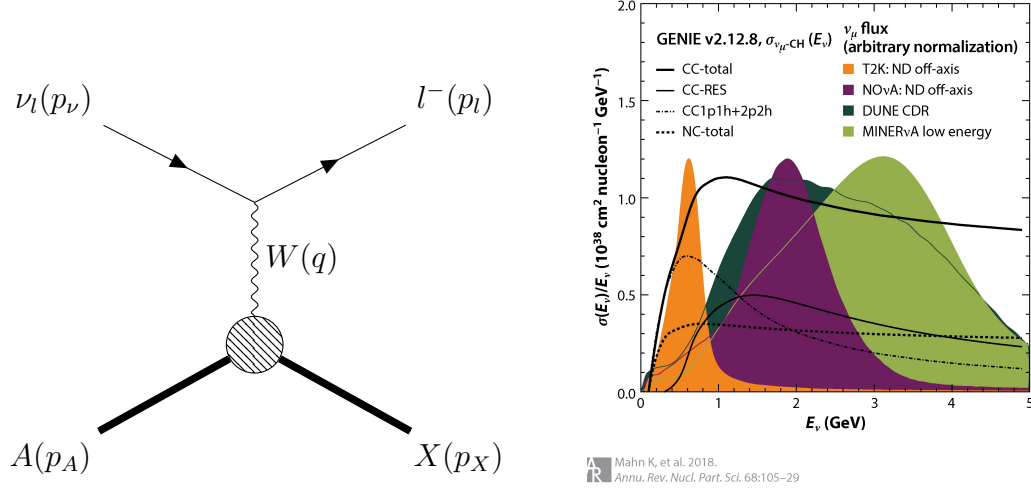


Figure 1.5: Left: Feynman diagram of charged current neutrino-nucleus scattering. Right: Long baseline neutrino program flux and relevant scattering cross section. All three channels are comparable in the energy range of long baseline neutrino programs. Figure from [66]

### 1.3.2.1 Elastic and Quasi-elastic Scattering

At lower energy ( $E_\nu \lesssim 1 \text{ GeV}$ ), the neutrino interaction is dominated by nucleon knock-out processes:

$$\nu_l + n \rightarrow l^- + p^+ \quad \nu_l + n(p) \rightarrow \nu_l + n(p) \quad (34)$$

The charged current process is usually referred to as charged-current quasi-elastic (CCQE) scattering while the neutral-current is traditionally referred to as elastic scattering. The scattering cross section of free nuclei is usually modeled by Llewellyn-Smith formalism[63].

In the case of charged-current, the cross section can be written as:

$$\frac{d\sigma}{dQ^2} = \frac{G_F^2 M^2}{8\pi E_\nu^2} \left[ A(Q^2) \pm \frac{s-u}{M^2} B(Q^2) + \frac{(s-u)^2}{M^4} C(Q^2) \right] \quad (35)$$

where  $s$ ,  $u$ , and  $Q^2 = -t$  are Mandelstam variables,  $M$  is nucleon mass, and  $(-)+$  applies to (anti)-neutrino scattering. The factors A,B,C are functions of form factors:

$$\begin{aligned}
A(Q^2) &= \frac{m^2 + Q^2}{M^2} [(1 + \eta)F_A^2 - (1 - \eta)F_1^2 + \eta(1 - \eta)F_2^2 + 4\eta F_1 F_2 \\
&\quad + \frac{m^2}{4M^2} \left( (F_1 + F_2)^2 + (F_A + F_p)^2 - \left( \frac{Q^2}{M^2} + 4 \right) F_p^2 \right)] \\
B(Q^2) &= \frac{Q^2}{M^2} F_A (F_1 + F_2) \\
C(Q^2) &= \frac{1}{4} (F_A^2 + F_1^2 + F_2^2) \\
\eta &= \frac{Q^2}{4M^2}
\end{aligned} \tag{36}$$

where  $m$  is lepton mass,  $F_1, F_2$  are vector,  $F_p$  is pseudo-scalar, and  $F_A$  is axial vector. The vector form factors are obtained from electron scattering data by assuming conserved vector current, while the pseudo-scalar term is typically neglected because of  $\frac{m^2}{M^2}$  suppression, leaving only axial form factor which needs neutrino scattering data to constrain. The axial form factor is commonly assumed to take the dipole form:

$$F_A(Q^2) = \frac{g_A}{(1 + Q^2/M_A^2)^2} \tag{37}$$

where  $g_A$ , and  $M_A$  are empirical parameters.  $g_A$  is determined precisely by beta decay, and early bubble chamber measurements consistently measured  $M_A \approx 1 \text{ GeV}$  [45]. However, modern long baseline oscillation experiments using heavy nuclear targets and few GeV neutrinos systematically measured higher values than 1 GeV. This disagreement is currently believed to be a result of poorly modeled nuclear effects, and we'll discuss this in section 1.3.2.5.

### 1.3.2.2 Resonance Production

At higher energy, neutrinos can excite the nucleon to an excited state ( $N^*$ ), which quickly decays, most likely to a pion and a nucleon:

$$\begin{aligned}
\nu_l + n(p) &\rightarrow l^- + N^* \\
N^* &\rightarrow \pi + N'
\end{aligned} \tag{38}$$



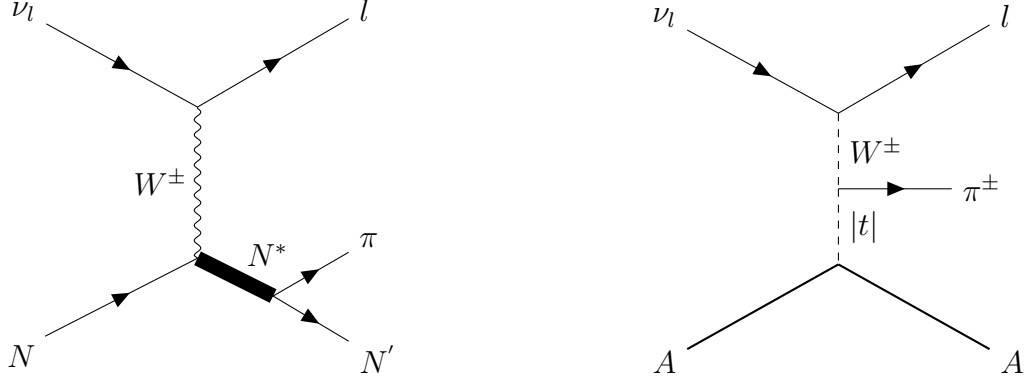


Figure 1.6: Feynman diagrams of charged-current resonance (left) and coherent (right) pion production

The most commonly used model for the resonance production processes is the Berger-Sehgal model[23], which considers all baryon resonance below 2GeV and their interference, as well as a simple non-interfering non-resonance single pion production. There is a similar vector and axial mass term in form factors like Llewellyn-Smith formalism and bubble chamber data suggest  $M_A \approx 1.1\text{GeV}$ , though the data is often limited in statistics[30]. In addition, the other decay modes of the excited nucleon contribute as well, leading to multiple pions or photon final states. The challenge of modeling resonance production is threefold. First, the nuclear effects play an important role, just like QE scattering. Second, the modeling of non-resonance background is an oversimplification in the Rein-Sehgal model, since the interference of resonance and non-resonance single pion production is not calculated. More recently, the MK model[57] attempted to calculate the interference of resonance and non-resonance single pion production, and the improvements remains to be seen. Third, the transition from higher resonance to DIS, or shallow inelastic scattering (SIS) region, is not modeled at all. Current theoretical models in the region were either a hard cut-off or a simple linear transition. The experimental data in the region is limited too, hence both theoretical and experimental efforts are required to study neutrino interactions in the SIS region.

### 1.3.2.3 Coherent Pion Production

In addition to resonance pion production, neutrinos can coherently interact with the entire nucleus, producing a single pion and negligible energy transfer to the nucleus.

$$\begin{aligned}\nu_l + A &\rightarrow l^- + \pi^+ + A \\ \nu_l + A &\rightarrow \nu_l + \pi^0 + A\end{aligned}\tag{39}$$

This process has been observed in both NC and CC interaction among a wide energy range, predicted to be relatively small compared to resonance production. The existing model is another Rein-Sehgal model[82] based on Adler's partially conserved axial current (PCAC) assumption[10], which relates the pion-nucleus scattering cross section to the coherent cross section.

### 1.3.2.4 Deep Inelastic Scattering

At very high energy, the nucleus can be approximated by free quarks and gluons, because of the asymptotic freedom property of QCD. The hadronic current can be replaced by elementary quark current in this case, and such a process is known as deep inelastic scattering.

$$\nu_l + q \rightarrow l^- + X\tag{40}$$

The DIS cross section is given by[45]:

$$\begin{aligned}\frac{d^2\sigma}{dxdy} &= \frac{G_F^2 M E_\nu}{\pi(1 + Q^2/M_{W,Z}^2)^2} \left\{ \left( xy + \frac{m^2}{2ME_\nu} \right) y F_1 + \left[ (1-y) - \left( \frac{Mxy}{2E_\nu} + \frac{m^2}{4E_\nu^2} \right) \right] F_2 \right. \\ &\quad \left. \pm \left[ xy(1 - \frac{1}{2}y) - \frac{m^2}{4ME_\nu} y \right] F_3 + \frac{m^2}{M^2} \left[ \left( \frac{M}{2E_\nu} xy + \frac{m^2}{4E_\nu^2} \right) F_4 - \frac{M}{2E_\nu} F_5 \right] \right\} \\ x &= \frac{Q^2}{2ME_\nu y} \quad y = E_{had}/E_\nu\end{aligned}\tag{41}$$

where  $M$  is nucleon mass,  $m$  is charged lepton mass,  $E_{had}$  is energy of hadronic system,  $(-)+$  sign applies to (anti)-neutrino, and  $F_1, F_2, F_3, F_4, F_5$  are structure functions determined by the parton distribution functions, which describe the flavor and kinematic distributions of initial state quarks in nucleon. The parton distribution functions of free nucleons in the high  $Q^2$  region have been measured using neutrinos and charged leptons scattering experiments

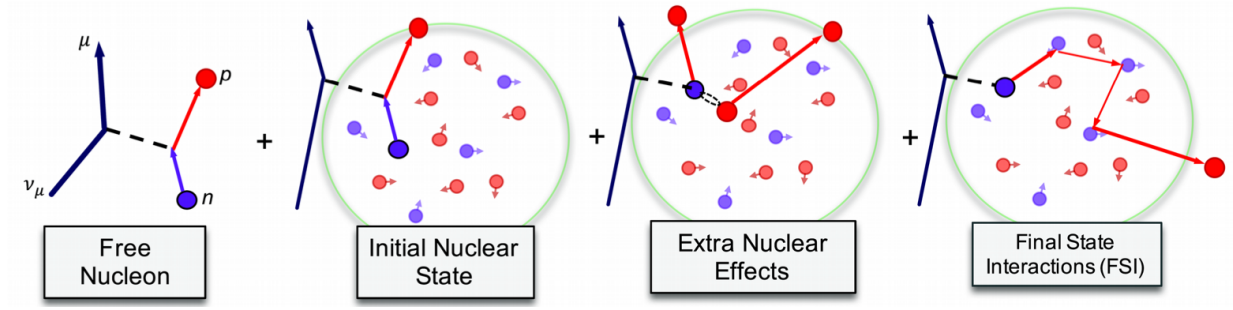


Figure 1.7: Cartoon of nuclear effects, including initial state (left), 2p2h (middle), and FSI (right). Figure from [101]

and well understood. However, the DIS interactions events observed in long baseline neutrino experiments are in the low  $Q^2$  region, because the neutrino energy is smaller than what used for measuring structure functions. There are two challenges for modeling DIS processes at low  $Q^2$  region. First, the extrapolation of structure functions remains to be validated experimentally. Second, the interference with resonance production can be sizable.

### 1.3.2.5 Nuclear Effects

The descriptions above only apply to free nuclei, but the nuclei are not free in the real world. Modern neutrino experiments use heavy nuclei to increase the event rate, leading to sizable nuclear effects. Currently modeling are developed using data from early experiments using light nuclei, and don't describe modern experiment data well. The nuclear effects are usually modeled in three ways: nucleon initial states, multi-nucleon knockouts, and final state interactions(FSI).

First, the nucleons inside the nucleus are not particles at rest but are bound by nuclear forces with a momentum distribution, described by the nucleon's initial state. A nucleus is commonly modeled by the relativistic Fermi gas model[94], which models nucleons as fermions confined in a spherical square well, leading to non-zero nucleon momentum because of the Pauli exclusion principle. This is a very simple model as it doesn't model the interac-

tions between nucleons, and it doesn't describe the electron scattering data. More sophisticated models have been proposed recently, such as spectral function[71], superscaling[18], and random phase approximation (RPA)[72]. These models remain to be tested by experiments.

Second, neutrinos can knock out multiple short-range correlated nucleons rather than just one, leading to the final states of multiple nucleons. Notice that this process is likely to be mis-reconstructed as a quasi-elastic event, especially when a proton-neutron pair is knocked out because most detectors are not efficient in detecting neutrons. Consequently, accounting for this multi-nucleon knockout process properly may be able to reconcile the disagreement in  $M_A$  measurements. Modeling of this process is being developed actively. For example, the Valencia group models the leading order contribution, 2-particle-2-hole (2p2h), by meson exchange current[73].

Finally, FSI is the re-interaction of final state particles inside the nuclear medium before detection. The nuclear medium is a dense strongly interacting many body system. Final state particles can scatter elastically or inelastically, or even be absorbed before being detected. FSI makes it difficult to measure the aforementioned free nucleon processes separately, since FSI mixes signatures of different channels<sup>9</sup>, hence modern experiments choose to measure exclusive cross sections defined by the particles that exit the nucleus: quasi-elastic-like (QE-like) for events without any meson,  $1\pi^{\pm,0}$ , for events with single pion, etc. Consequently, the theory has to describe all free nucleon scattering processes and FSI to be able to adequately describe the scattering data, which is a challenging goal even today.

There are two popular approaches to modeling FSI. The first one uses the nuclear scattering cross section of a particle to approximate the scattering of a given particle inside the nucleus[20]. Naturally, this approach is limited by the accurateness of the fundamental assumption, as the scattering inside the nuclear medium is not the same as scattering from outside of it. The other approach is a cascade approach, which simulates the fate of final state particles by stepping inside the nuclear medium[51]. At each step, the fate of a particle is determined by the probability, including various re-interactions or simply continued propagation. The interaction probabilities may be determined from data or derived from

---

<sup>9</sup>For example, a resonance pion production event can have the same final state particles as a QE event if the pion is absorbed in the nucleus, while a QE event can produce a pion if the final state proton re scattered with a pion before leaving the nucleus.

first principles.

### 1.3.3 Previous Measurements of $\nu_e$ Cross Section

The  $\nu_e$  cross section measurements are rare in the few GeV region because existing accelerator based neutrino sources can't produce them efficiently. On one hand, an accelerator-based neutrino source produces few GeV neutrinos but the majority are muon neutrinos. On the other hand, solar and reactor neutrinos are dominated by  $\nu_e$ , but their energies are mostly less than 1 GeV. Current  $\nu_e$  cross section predictions are extrapolated from  $\nu_\mu$  measurements by taking advantage of “lepton universality”, which is a standard model feature that all generations of leptons interact the same way under electroweak interactions. Lepton universality has been tested extensively using various methods, and no evidence of its violation was found[38, 32, 61, 24].

The first  $\nu_e$  cross section measurement in this energy range was done by the Gargamelle experiment using bubble chamber technology[26]. They found 200 and 60 candidates for electron neutrino and anti-neutrino interaction events, and the result was in good agreement with lepton universality. More recently, T2K collaboration measured  $\nu_e$  charged-current inclusive cross section using carbon target and  $\langle E_\nu \rangle = 1.3$  GeV beam[2], MINERvA collaboration measured CCQE-like cross section using hydrocarbon target and  $\langle E_\nu \rangle = 3.6$  GeV beam[103], and MicroBooNE collaboration measured  $\nu_e + \bar{\nu}_e$  charged-current inclusion cross section using argon target and  $\langle E_\nu \rangle = 837$  MeV beam[5]. All these results reported flux-integrated differential cross sections in electron momentum, electron scattering angle, while T2K and MINERvA result  $Q_{QE}^2$  in addition. The MINERvA result also reported the differential cross section ratio between electron and muon neutrino in  $Q_{QE}^2$ . All three results were consistent with lepton universality predictions.

## 2.0 The Main Injector Experiment for $\nu - A$

MINERvA was first planned in the 2000s, completed construction in 2013, and took data until 2019. The physics goal of MINERvA is to provide data to improve neutrino-nucleus scattering models, thus reducing the cross section uncertainty in neutrino oscillation experiments. In total, MINERvA collected about  $2 \times 10^{21}$  protons on target (P.O.T.)<sup>1</sup> data during two flux eras, low energy (L.E.) and medium energy (M.E.). MINERvA is in the “data preservation” era at the time of writing (2022), developing software to support long-term access to collected data and analysis software.

This chapter describes how the experiment was operated, including a description of the neutrino beam (section 2.1), the detector (section 2.3), and the calibration chain (section 2.3).

### 2.1 The NuMI Beam Line

The neutrino source of the MINERvA experiment is the Main Injector (NuMI) neutrino beam at Fermilab. The neutrino beam is created by colliding protons with fixed targets, which produce various mesons that subsequently decay into neutrinos. The technical details are briefly introduced in the following subsections, and more information in [9].

#### 2.1.1 Main Injector Proton Beam

NuMI beam uses Main Injector Proton Beam as a proton source. The start point of the beam is a magnetron emitting 35 keV  $H^-$  ions[58]. The ions are accelerated by R.F. quadrupole and linac to 400 MeV, converted to protons in the Booster, and further accelerated to 8 GeV as 1.6  $\mu s$  long batches with 54 MHz bunch spacing. These protons are

---

<sup>1</sup>The integrated luminosity is measured in the unit of the proton beam flux described in section 2.1.1 because there is no reliable way to measure neutrino flux, which is the reason for building MINERvA in the first place.

passed to the Main Injector synchrotron ring next, which accelerates the protons to desired 120 GeV. In addition, a “slip-stacking” technique is used to stack incoming proton batches, increasing the intensity of proton batches in the Main Injector. In the end, protons leave the Main Injector in spills, which have more than  $5 \times 10^{13}$  protons each, separated by 1.33 s apart.

### 2.1.2 Targets and Magnetic Focusing Horns

The Main Injector proton beam is directed 3.3 degrees downward, pointing to the underground target hall 350m downstream. The target hall contains the target, two focusing horns, and other supporting and shielding equipment. The target is made of graphite and consists of 47  $20 \text{ mm} \times 15 \text{ mm} \times 6.4 \text{ mm}$  fins, stacked along the beam direction 0.3 mm apart[4]. The material and structure of the target are chosen such that the main products of proton scatterings are pions and kaons, and the target is capable of withstanding the 400 kW proton beam.

The magnetic focusing horns create a toroidal magnetic field, acting as charged particle lens. Either positive or negative charged particles can be focused, depending on the current direction, while the oppositely charged particles are deflected. The forward horn current (F.H.C.) configuration focuses positively charged particles, leading to a neutrino-dominated beam, while the reverse horn current (R.H.C.) configuration focuses negatively charged particles, resulting in an anti-neutrino-dominated beam. In addition, the target is movable, such

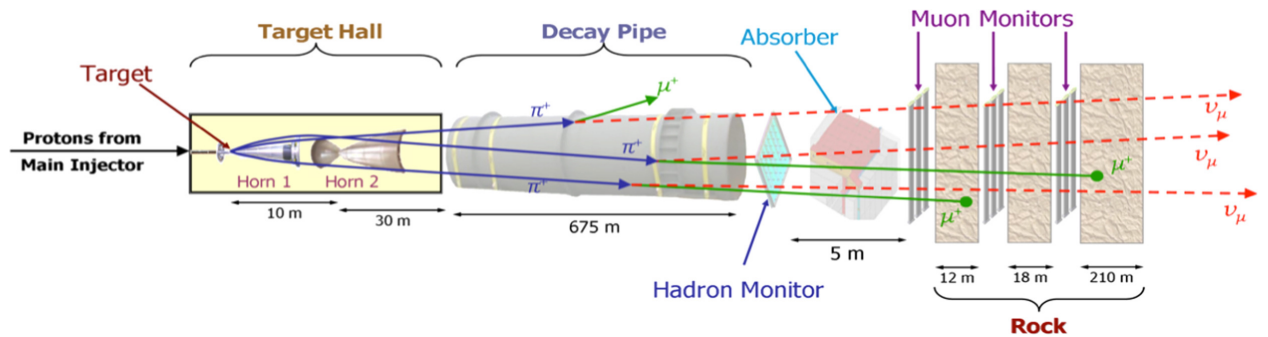


Figure 2.1: Schematic view of NuMI beamline, Figure from [9]

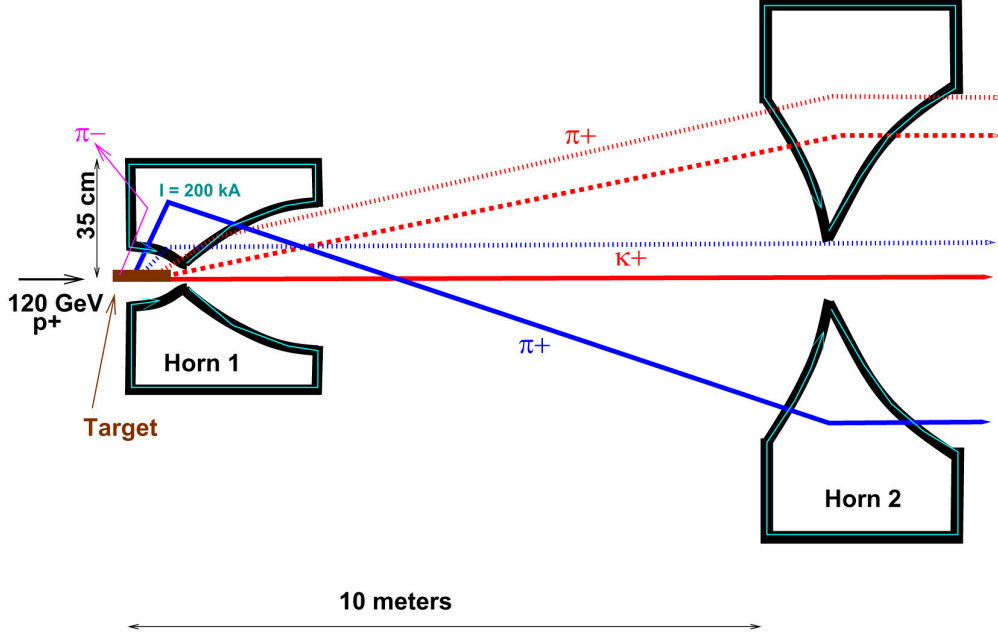


Figure 2.2: Schematic view of target and horns, as well as possible particle trajectories. The second horn further focuses particles that are under-focused (dotted-red trajectories) or over-focused (solid-blue trajectory) by the first horn. Wrong sign particles are de-focused (solid-pink trajectory). Figure from [9]

that the energy spectra of the neutrino beam can be tuned by moving the target. There were two major energy configurations, low energy (L.E.) and medium energy (M.E.), during the time MINERvA took data. The mean neutrino energies of L.E. and M.E. configurations are roughly 3 GeV and 6 GeV respectively.

### 2.1.3 Decay Pipe and Absorbers

Downstream of the target hall is a 675 m long, 2 m diameter decay pipe, 46 m apart from the graphite target. Most pions and kaons decay into neutrinos (and other particles) here, creating the neutrino beam. The decay pipe was evacuated to 0.5 Torr initially and filled with helium to 13.2 PSIA since 2007. A hadron monitor, a hadron absorber, and three muon monitors are installed downstream of the decay pipe. The hadron monitor is a square array



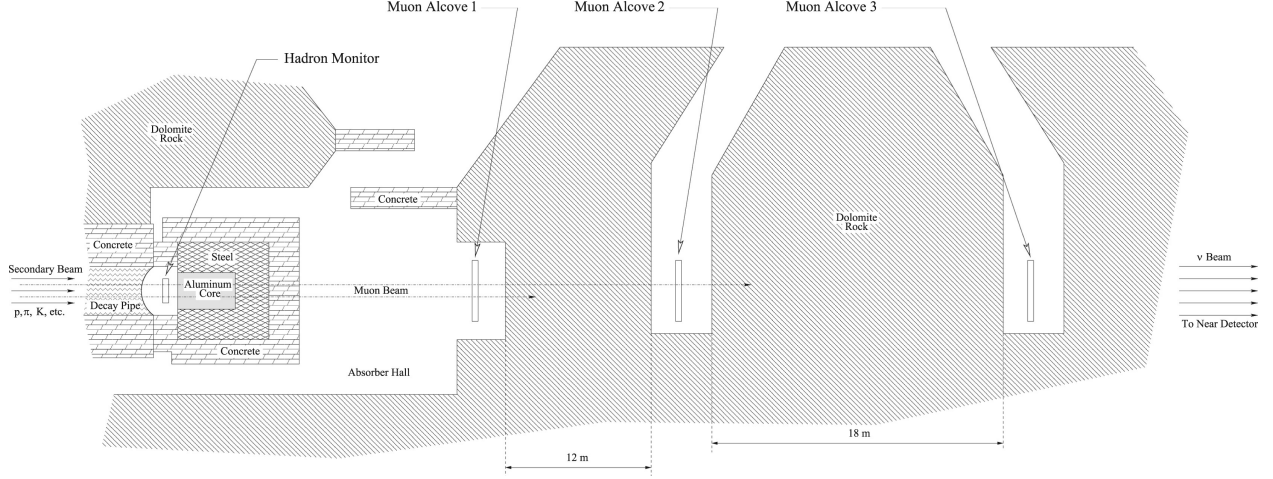


Figure 2.3: Schematic view of monitors and absorbers downstream of decay pipe. Figure from [9]

of 49 ionization chambers, providing in-situ beam alignment measurement by monitoring the hadronic flux (mainly uninteracted protons). The hadron absorber is a massive aluminum, steel, and concrete structure, approximately  $5.5 \text{ m} \times 5.6 \text{ m} \times 8.5 \text{ m}$  size. This absorber stops most beam particles except muons and neutrinos and protects groundwater and personnel from irradiation. The three muon monitors are installed in the muon alcoves, separated by rocks. They all have the same construction of  $9 \times 9$  orthogonal array of ionization chambers. The detection threshold for the muon monitors is 4 GeV, 10 GeV, and 20 GeV, respectively, because of muon range-out. The quality and intensity can be monitored on a pulse-to-pulse basis thanks to the 2D profiling of the muon beam. Finally, there are 240 m of rocks between the last muon monitor and MINERvA detector, serving as muon shield, such that the beam muons would range out before reaching MINERvA detector.

## 2.2 The Minerva Detector

The main detector of MINERvA is a 5m long, 1.7m apothem hexagonal prism shape scintillator-based detector[14]. A steel shield, a scintillator veto wall, and a liquid helium target are placed in front of the main detector, while MINOS near detector[68] is located at the back. The MINERvA coordinate system defines the z-axis as horizontal and points downstream along the central axis of the main detector. The y-axis is defined to point upward, while the x-axis is horizontal and points to the beam left. The steel shield is a passive absorber, and the veto wall consists of a 5cm thick steel plane, a 1.9cm thick scintillator plane, a 2.5cm thick steel plane, and a second 1.9cm thick scintillator plane. They provide shielding and tagging for non-neutrino components (mainly muons produced by upstream neutrino interactions) in the neutrino beam.

The main detector consists of 120 “modules” stacked along the z direction, subdivided into 5 subdetector regions: nuclear target region, active tracker region, downstream electromagnetic calorimetry (ECAL), downstream hadronic calorimetry (HCAL), and outer detector (OD). The first 4 subdetector regions are collectively referred to as the inner detector

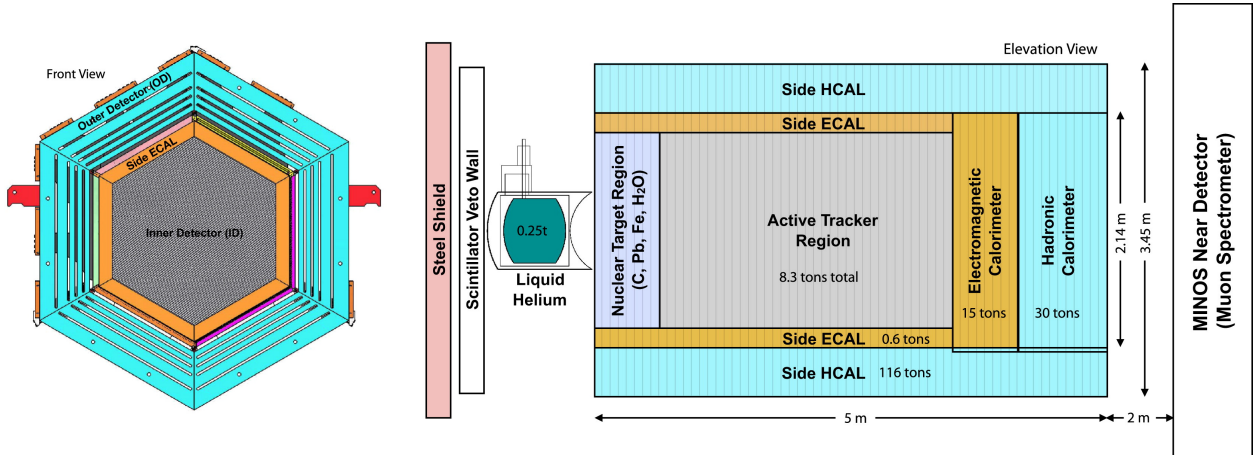


Figure 2.4: MINERvA detector configuration. Left: front view of a tracker module. Right: side view of the detector, neutrino beam direction is left to right. Figure from [14]

(ID) as well, since the OD surrounds the other subdetector regions. The OD portion of all modules is identical except for thickness, which are steels interleaved with scintillators. The OD provides structure support, side containment, and calorimetry for the MINERvA detector. The ID portion of modules is configured to fit the functionality of subdetector regions, leading to 4 basic types of modules: tracking modules, electromagnetic calorimeter modules (ECAL modules), hadronic calorimeter modules (HCAL modules), and passive nuclear target modules. The inner hexagon of corresponding types of modules, while the nuclear target region is made from passive nuclear target modules and tracking modules.

### 2.2.1 Tracking Modules

The tracking modules are fully active, hence providing the best tracking capability and calorimetry resolution among all modules. The inner part of the tracking module consists of two scintillator planes, each composed of 127 triangular prism shape scintillator strips. These strips are 1.7 cm in height and 3.3 cm in base, varied in length to fit in the inner hexagon, glued together by translucent epoxy. There is a 2.6 mm hole in the center of each strip, where a 1.2 mm diameter green Wavelength-shifting (WLS) fiber is inserted and connected to the readout electronics. In addition, the outer edges of the scintillator region (about 90 cm from the center) are wrapped by a 0.2cm thick lead collar, serving as side ECAL. Scintillator planes have 3 orientation configurations, referred to as X, U, and V planes. The scintillator strips are aligned vertically in X planes and rotated 60 degrees clockwise or counterclockwise in U or V planes. The downstream plane of the two scintillator planes in one module is always an X plane, while the upstream plane is either U or V plane, referred to as UX or VX configuration, respectively. The UX and VX configurations are arranged in alternating patterns throughout the detector.

The active tracker region is made of tracking modules alone, consisting of 62 modules. 22 tracking modules are used in nuclear target regions as well.

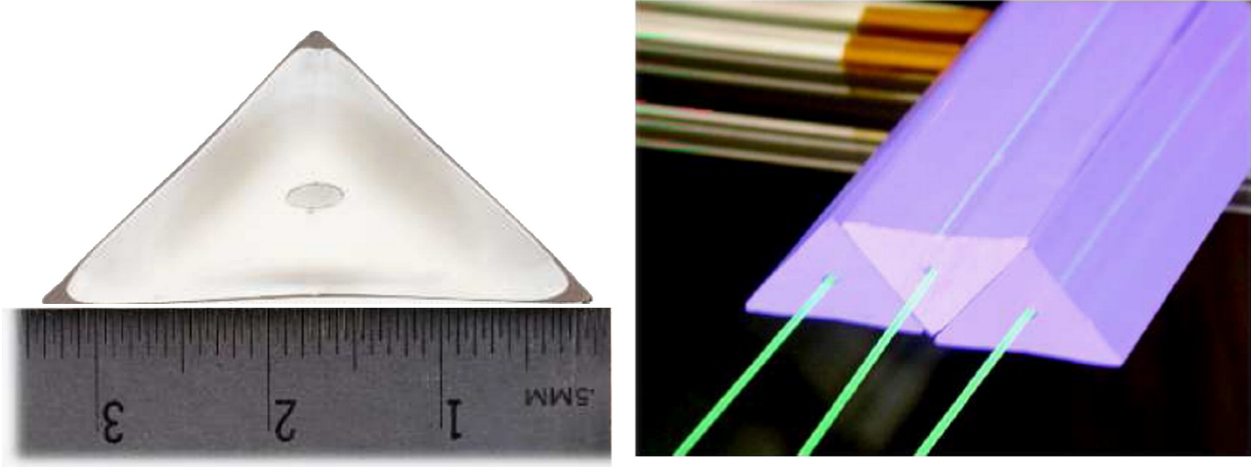


Figure 2.5: MINERvA scintillator strips. Left: cross-section of strips. Right: arrangement of strips in the scintillator plane. Figure from [14]

### 2.2.2 Passive Nuclear Target Modules

The passive nuclear target modules are modules with passive materials in the ID portion. MINERvA can measure the A-dependence of neutrino nuclear interaction thanks to these passive targets. Five different passive nuclear target modules and a water target are installed between every 4 tracking modules in the nuclear target region, except the most downstream target, which is 2 tracking modules apart from the upstream target. In addition, a liquid helium “module” is placed between the veto wall and the main detector. This passive/active interchanging pattern helps vertex reconstruction, and the configuration of target materials is optimized so that each target’s event rates are similar.

### 2.2.3 ECAL and HCAL modules

An ECAL module is similar to a tracking module, differing in that the 0.2cm thick sheet of lead covers the entire scintillator region rather than only the edges. A transition module, which is an ECAL module with a lead cover on the front instead of the back, is placed at the end of the tracker region. There are 10 ECAL modules in the ECAL region, arranged in

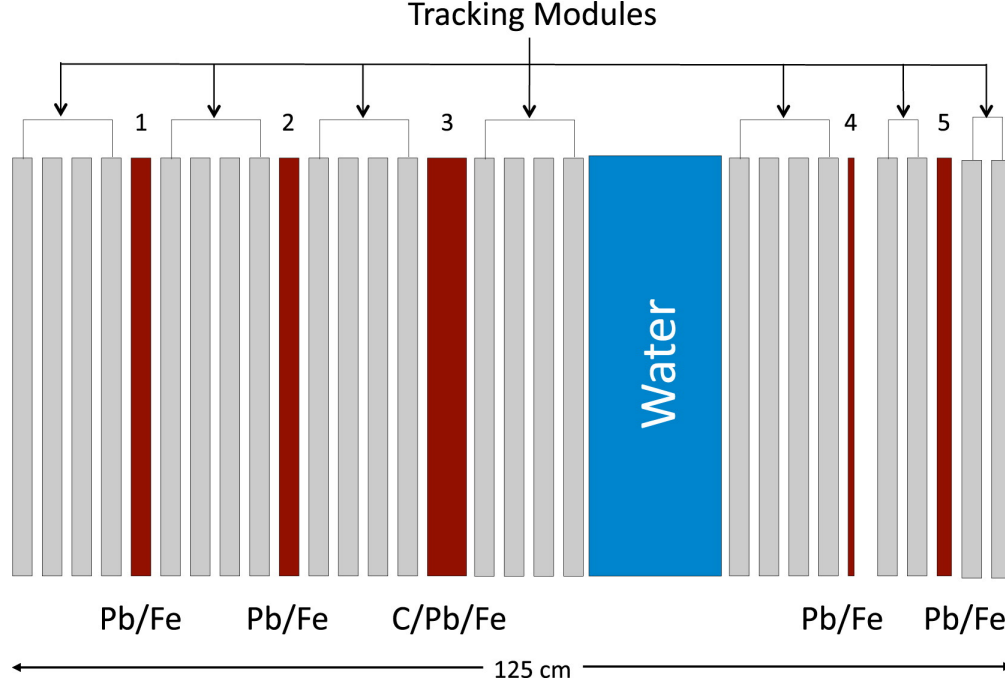


Figure 2.6: Arrangement of passive nuclear target modules. Figure from [14]

alternating UX and VX configurations like the active tracking region.

A hadronic calorimeter module has one plane of scintillator and one plane of 2.54 cm thick steel in the ID portion. 20 hadronic calorimeter modules make up the HCAL region, and the orientation configurations of scintillator planes are arranged in a repeating pattern of UXVX.

Both ECAL and HCAL modules provide better containment for the final state particles thanks to more high Z materials, at the cost of calorimetry resolution and tracking capability due to more passive materials.

#### 2.2.4 MINOS Near Detector

A magnetic field is necessary to distinguish positive and negative charged particles, but it is impractical to magnetize the MINERvA main detector. The workaround MINERvA implemented was to locate the MINERvA detector at 2.1 m upstream of MINOS near detector

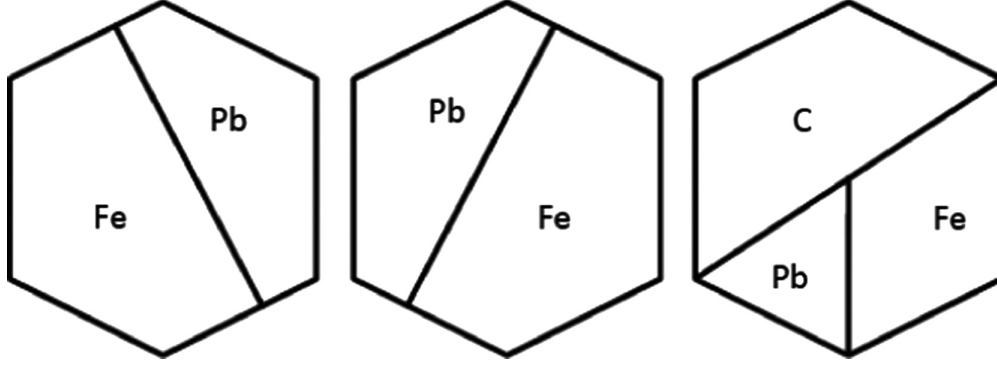


Figure 2.7: Configuration of passive nuclear target modules. Targets 1 and 5 use the left configuration, target 2 uses the middle, target 3 uses the right, and target 4 is pure lead. Figure from [14]

(MINOS) [68].

MINOS is a scintillator-based detector with a 1.3T toroidal magnetic field, capable of measuring curvature and range of charged particles. MINOS can recapture back escaping particles from MINERvA main detector, mostly muons, and measures the charge and momentum, hence acting as a muon spectrometer for MINERvA.

### 2.2.5 Optical System and Readout Electronics

The scintillator strips used in MINERvA are made of Dow Styron 663 W polystyrene pellets, doped with PPO<sup>2</sup> and POPOP<sup>3</sup>, using extruded plastic scintillator technology. The inserted Y-11 WLS fibers produced by Kuraray are mirrored on one end, and connected to Fujikura-DDK optical connector on the other end, transmitting and wavelength shifting the blue light emitted by the scintillators. The optical connectors connect WLS fibers to Hamamatsu H8804MOD-2 photo-multiplier tubes (PMT) by clear optical fibers, and the PMTs convert light to analog electric signal.

PMTs are hosted in cylindrical light-tight steel boxes, with an optical decoder unit (ODU)

---

<sup>2</sup>2,5-diphenyloxazole

<sup>3</sup>1,4-bis(5-phenyloxazol-2-yl) benzene

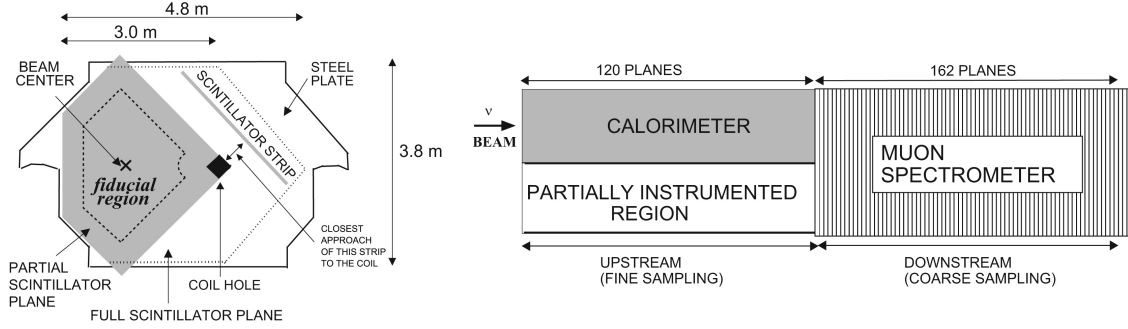


Figure 2.8: MINOS near detector configuration. Left: front view. Right: side view. Figure from [8]

on one end, and a front end board (FEB) connector board on the other end, collectively called optical box. The ODU exposes the 64 channels of each PMT in a  $8 \times 8$  arrays, connected to the clear fibers in a weave pattern, shown in figure 2.16, while the FEB connector board is the electrical interface of PMT, connected to FEB mounted directly outside the optical box. The optical system is essentially the same as MINOS[68], as both experiments use the same scintillator, WLS fiber, and PMT.

The FEBs provide high voltage for PMTs, communicate with readout controllers, and digitize timing and analog signal generated by the PMTs. The readout controller activates the readout electronics  $0.5 \mu\text{s}$  before the NuMI beam spill arrives, and stays active until  $5.5 \mu\text{s}$  after the end of the spill, such that delayed activities can be recorded.

The analog-to-digital converter functionality is performed by 6 TriP-t chips[87] mounted on each FEB, each has 32 channels. Two out of the six are configured to low gain (about  $15.6 \text{ fC/ADC}$ ), and the rest are configured half high gain ( $1.25 \text{ fC/ADC}$ ) half medium gain (about  $4 \text{ fC/ADC}$ ), such that one FEB provides all 3 ADC configurations to 64 PMT channels. The discriminator of a channel fires when the charge in the high gain channel exceeds the discriminator threshold (about  $70 \text{ fC}$ ). Once the discriminator fires, the charges in all channels on the same TriP-t are integrated for another  $150 \text{ ns}$ , then digitized and recorded. In addition, the corresponding low gain configuration TriP-t chip and the “parallel” high/medium gain configuration TriP-t chip that shares the same low gain chip are effectively

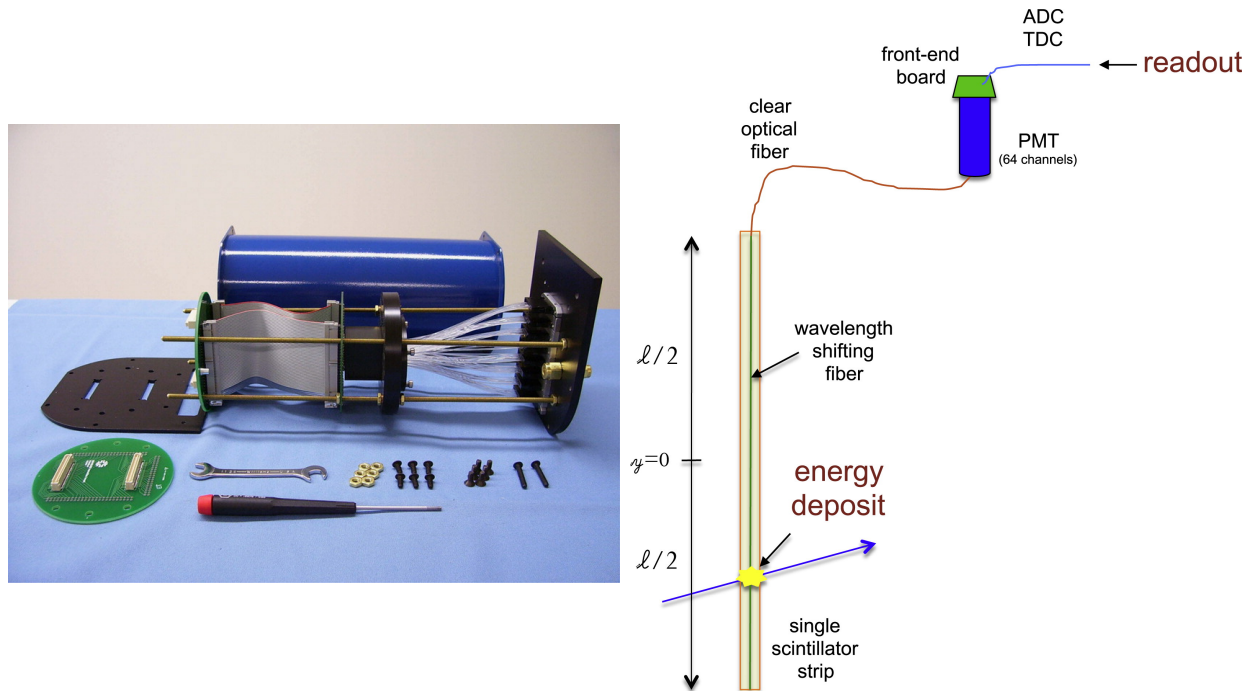


Figure 2.9: Left: optical box assembly, The shield box is at back. Components at the middle (from left to right) are FEB connector board, ribbon cable carrying analog signal, PMT, fibers carrying optical signal, and ODU. Right: schematic view of a readout channel. Figure from [14]

“fired” as well, such that all three ADC configuration measurements are made for all recorded channels at the same time. As a result, one fired discriminator leads to a hit with one timestamp and  $3 \times 32$  charge measurements for 32 optical channels. The three TriP-t chips would enter a 188 ns dead time after recording a hit, so the second hit in one of the 32 channels during the dead time would be lost or significantly attenuated. More details on readout electronics and data acquisition software can be found in [77].



## 2.3 Calibration Chain

The raw hit consists of its time, electronic channels, and ADC counts, which has to be mapped to the physical location and time, as well as deposited energy for physics interpretation. It is not a trivial task because equipment characteristics are not precisely known to us and vary between devices and over time. A set of calibration measurements, both in-situ and ex-situ, are performed to estimate the parameters used in the mapping.

### 2.3.1 Energy Calibration

The first and most complex calibration is energy calibration, which converts ADC counts to energy deposition in scintillators. The mapping is estimated by:

$$E_i = [C(t)S_i(t)\eta_i^{att}e^{l_i/\lambda_{clear}}G_i(t)Q_i(ADC)] \times [ADC_i - Ped_i(t)] \quad (42)$$

where the subscript  $i$  refers to channel  $i$ . There are multiple parameters in this estimator, that account for differences between individual equipment in each physical step, discussed in the following context.

#### 2.3.1.1 FEB Response

The  $Q_i(ADC) \times [ADC_i - Ped_i(t)]$  part of equation 42 is FEB response, converting ADC count to PMT anode charge.  $ADC_i$  is recorded ADC count,  $Ped_i(t)$  is time-dependent pedestal ADC count and  $Q_i(ADC)$  is the ADC-to-charge conversion factor.

$Ped_i(t)$  is measured in-situ by special mixed beam/pedestal subruns that occur once every 32 subruns, about 10.5 hours apart. During such subruns, approximately 750 gates are collected during the beam-absent time for all channels. Readout electronics are open for 16  $\mu$ s each gate and record noise from cosmic rays, radioactivity, electronic sources, and PMT dark current. The  $Ped_i(t)$  is extracted by calculating the mean ADC count in the sample for each channel and stays in effect until the next special subrun. Outliers in the distribution, mostly due to cosmic muons penetrating the detector, are removed by Peirce's

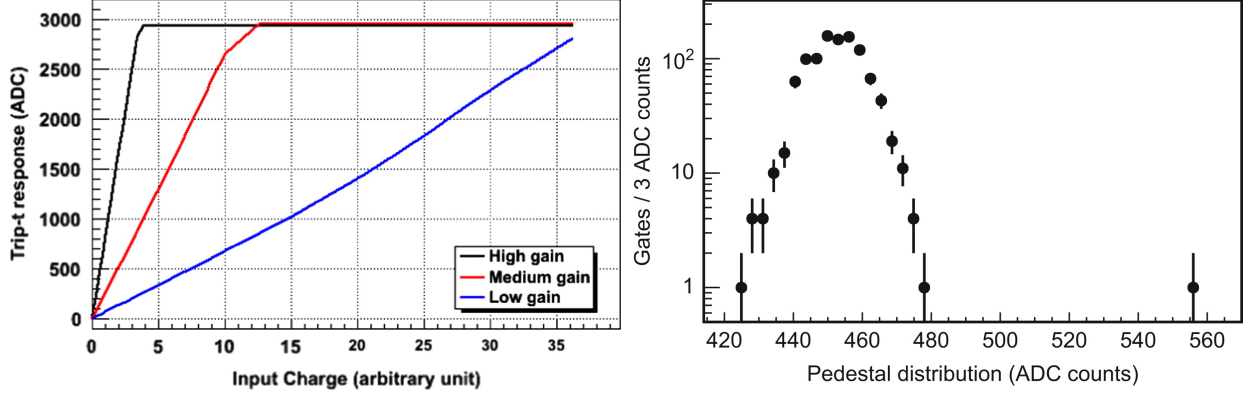


Figure 2.10: Left: Typical FEB response of high, medium, and low gain channels. Right: An example of pedestal measurement with an outlier. Figure from [14]

criterion[86]. The distribution width is interpreted as the uncertainty of the pedestal, which is less than 2%. The pedestal values vary by about 7% across all channels.

$Q_i(ADC)$  is measured by ex-situ charge calibration measurements. External charges generated by pulse generators are fed into input channels and the ADC outputs are calculated as a function of input charges. The high, medium, and low gain channels are each characterized by tri-linear functions, fitted by data from the measurement mentioned above. This response curve parameterization is accurate within 1% over the entire dynamic range.

The measured charge is calculated using the highest gain channel among the channels that ADC counts are under saturation threshold, approximately 2500 ADC counts.

### 2.3.1.2 PMT Response

The PMT responses are characterized by PMT gain,  $G_i(t)$ , which converts anode charge to input photoelectron(PE) count. The gain is determined by in-situ light injection data and modeling of photo statistics. MINERvA has a light injection (LI) system that uses LED to inject a certain amount of light into the optical interface of PMT. The LI system is triggered between beam spills, and the observed charge is recorded and aggregated daily for all optical channels as a sample. The mean and variance of the sample are extracted and the PMT

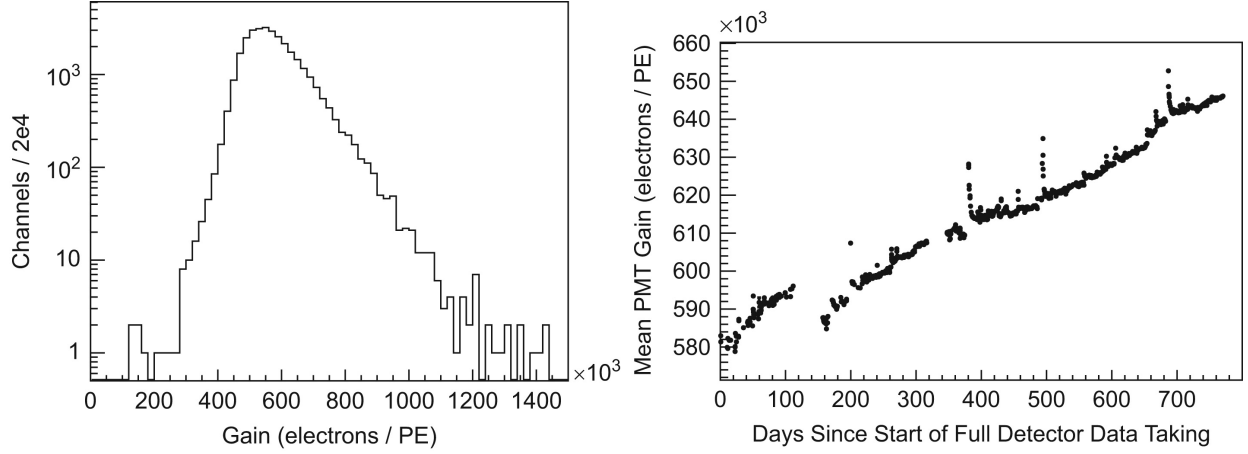


Figure 2.11: Left: measured distribution of PMT gains for all channels, on April 1, 2010. Right: average PMT gain over time. Figure from [14]

gain is determined by solving the following equation:

$$\frac{1}{G} = g = \frac{\sigma^2 - \sigma_p^2}{\bar{Q}(1 + w^2(g))e} \quad (43)$$

where  $g$  is the overall gain of PMT, inverse of  $G_i(t)$ ,  $\bar{Q}$  and  $\sigma^2$  are the mean and variance of anode charge measured in LI triggers,  $\sigma_p$  is the width of pedestal,  $e$  is electron charge, and  $w^2(g)$  is a PMT characteristic parameter can be expressed as a function of overall gain  $g$ . This equation is derived by assuming:

1. the input PEs follow the Poisson distribution.
2. the charge distribution of individual dynode is another Poisson distribution, with  $\lambda_i = g_i * \lambda_{i-1}$ , where  $\lambda_i$  is the mean of Poisson distribution at  $i$ -th dynode, and  $g_i$  is gain of  $i$ -th dynode.
3. the gain of individual dynode ( $g_i$ ) is proportional to  $V^{0.75}$ , where  $V$  is the high voltage[55].
4. the measured charge is smeared by Gaussian noise.

The measured PMT gains are found to be stable within 3% among different channels, and increasing by roughly 0.02% per day on average.

### 2.3.1.3 Scintillator Strip Response

The scintillator strip response is characterized by two attenuation correction terms, accounted for light attenuation as they travel along the WLS fibers ( $\eta_i^{att}$ ) and clear fibers ( $e^{l_i/\lambda_{clear}}$ ). the first term is measured using ex-situ “module mapper” measurements, and the second term is determined by ex-situ fiber measurement.

The “module mapper” measurement is made by scanning two  $^{137}\text{Cs}$  radioactive sources over a detector module and recording the response in readout electronics as a function of illuminated position. Totally 18012 positions are sampled in the inner tracking region, in a 2D grid pattern with 19.05 mm spacing between sampled points. A customized “module mapper” powered by 3 servo motors was built to move the radioactive source to perform the scanning.

The transverse scan (perpendicular to the strip) data is used to determine the maximum response amplitude at a given longitudinal position, extracted from the peak of a Lorentzian function fitted by the measured ADC counts as a function of transverse position. The attenuation response as a function of longitudinal position,  $\eta_i^{att}$ , is then determined by maximum responses at multiple longitudinal positions, parameterized by a double exponential function. Notice that the longitudinal position of a data hit is unknown until track reconstruction<sup>4</sup>, hence all hits are corrected to the center of the strip until the 3D position is reconstructed.

The attenuation in clear fiber,  $e^{l_i/\lambda_{clear}}$ , is an exponential function of fiber length  $l_i$ . The attenuation length,  $\lambda_{clear}$  is measured to be 7.83 m, by sampling 0.5 m, 1.08 m, 1.38 m, and 3.13 m length cables and fit to exponential. The nominal value of fiber length is used in  $l_i$ , which is 1.08 m, 1.38 m, 3.13 m, or 6 m depending on the channel’s position in the detector. Notice that this term is only a normalization factor, which is further calibrated using methods described in section 2.3.1.5 and section 2.3.1.6, hence it doesn’t deserve accurate length measurement.

---

<sup>4</sup>detailed in chapter 4

#### 2.3.1.4 Rock Muon Sample

Rock muons are muons produced by charged current muon neutrino interaction with the rocks between the decay pipe and MINERvA, which are typically few GeV energy muons. The primary energy deposition mechanism in plastic scintillator for muons in this energy range is ionization of atomic electrons, which is known to be a slowly varying function of the muon energy (This behavior is also known as a minimum-ionizing particle, or MIP)[107]. In addition, these muons usually travel in a straight line in MINERvA, making them easy to reconstruct and identify (details in section 4.1). These features make the rock muon sample a standard candle for calibration, hence MINERvA uses rock muons in the various calibration procedures described in the following context.

#### 2.3.1.5 Strip-to-Strip Correction

The remaining normalization variances in responses of scintillator strips are corrected by strip-to-strip correction factors  $S_i(t)$ , which are determined by path length normalized peak energy deposition of through-going rock muons. Fitting the peak energy deposition requires adequate statistics for every single strip, which is not practical since that requires a sample of hundreds of thousands of rock muons. Consequently, two methods are employed to reduce the statistical fluctuations in the procedure. First, the correction factors are recalculated only when hardware changes, and this choice is made to extract correction factors using as much data as possible. Second, The correction factors are calculated by the product of a channel-dependent factor ( $C_j$ ) and plane-dependent factor( $C^j$ ). The strip-dependent part uses truncated mean energy deposition as a proxy of peak energy deposition[22], while the plane-dependent factor uses data from all 127 strips in the same plane to fit the peak properly. The calibration procedure consists of three iterations. First, the truncated mean energy depositions for all channels are measured, and the strip dependent correction factors are calculated by:

$$C_i = \frac{1/x_i}{\frac{1}{N} \sum_{j=1}^N \frac{1}{x_j}} \quad (44)$$

where  $x_i$  is measured truncated mean energy in strip  $i$ , and  $N$  is the number of channels calculated. In addition, a channel is considered dead if

1. it records 0 energy for more than 30% of the time when reconstructed track intersects the channel, or
2. it records extremely low-light for near 100% of the time.

At the second iteration, dead channels are removed and the correction factors are calculated again using the same method. The dead channel removal effectively put an upper bound of about 5 on correction factors. Finally, the plane-dependent correction factors are extracted by:

$$C^j = \frac{\frac{E^j}{p^j}}{\frac{1}{n} \sum_{k=1}^n \frac{E^k}{p^k}} \quad (45)$$

where  $E^j$  and  $p^j$  are truncated mean and peak energy deposition of plane  $j$ , and  $n$  is the number of planes.

### 2.3.1.6 Absolute Energy Scale

All previous calibrations map from ADC counts to the number of PE generated in scintillator strips<sup>5</sup>. The PE count to energy deposition mapping, a.k.a absolute energy scale ( $C(t)$ ), is calibrated using rock muons penetrated MINERvA and recaptured by MINOS, such that the muon momentum can be measured. The muon momentum at the entry point of MINOS is measured by range or curvature. Its momenta at various positions in MINERvA are corrected by expected energy loss in penetrated materials. In addition, a trial energy scale is employed to measure energy depositions of rock muons. On the other hand, the energy depositions in scintillator strips of such muons are simulated using GEANT<sup>6</sup>. The peak region (above half width) of cluster<sup>7</sup> energy distribution is fitted by fifth order polynomial for both data and simulation, and the fitted peak cluster energies are extracted as  $E_{data}$  and  $E_{MC}$ . Finally, the mapping of true and measured energy deposition is fitted to a straight line, and the slope is extracted as  $a$ , such that the absolute energy scale can be

---

<sup>5</sup>Conceptually. The unit is usually arbitrary in practice.

<sup>6</sup>Detailed in section 3.3

<sup>7</sup>Defined in section 4.1.2.

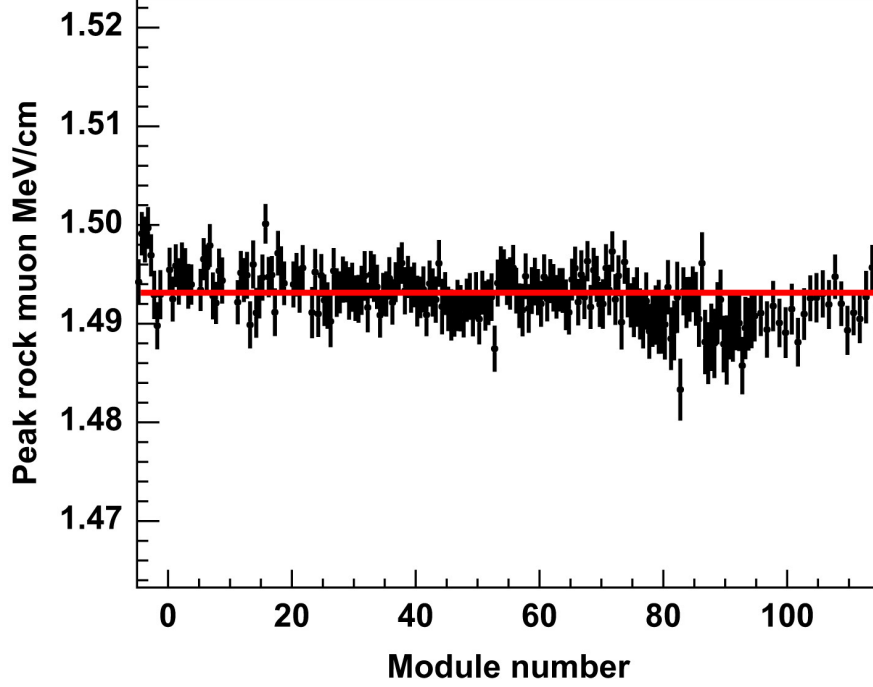


Figure 2.12: Peak energy deposition per unit length for each plane after calibration. Figure from [14]

determined by:

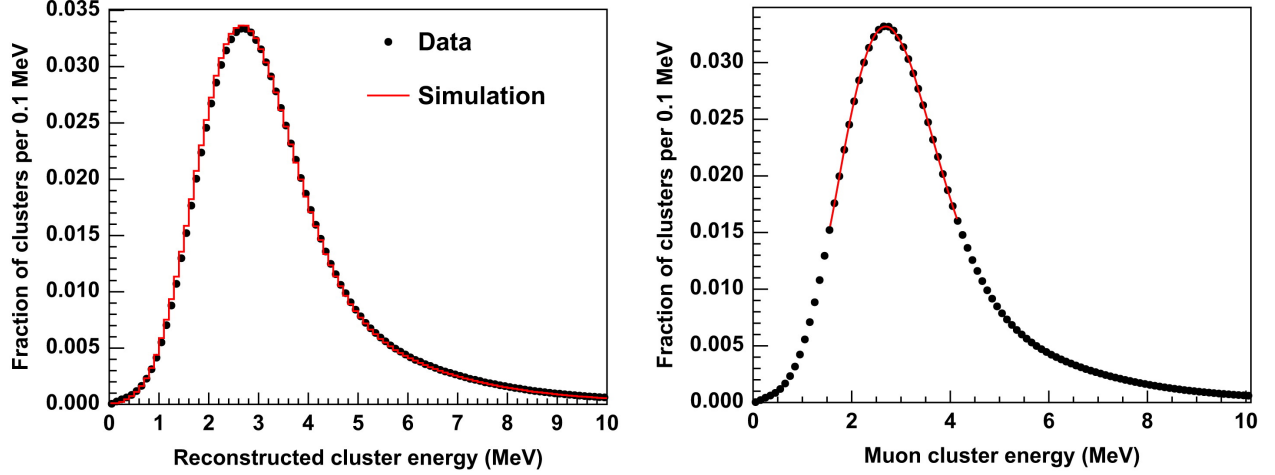
$$C = C_{trial} \frac{E_{MC}}{a} \frac{1}{E_{data}} \quad (46)$$

The absolute energy scale is found to be a function of time, mainly due to scintillator aging. This calibration is performed every two days to ensure the energy scale is constant and consistent with simulation during the entire time MINERvA collects data.

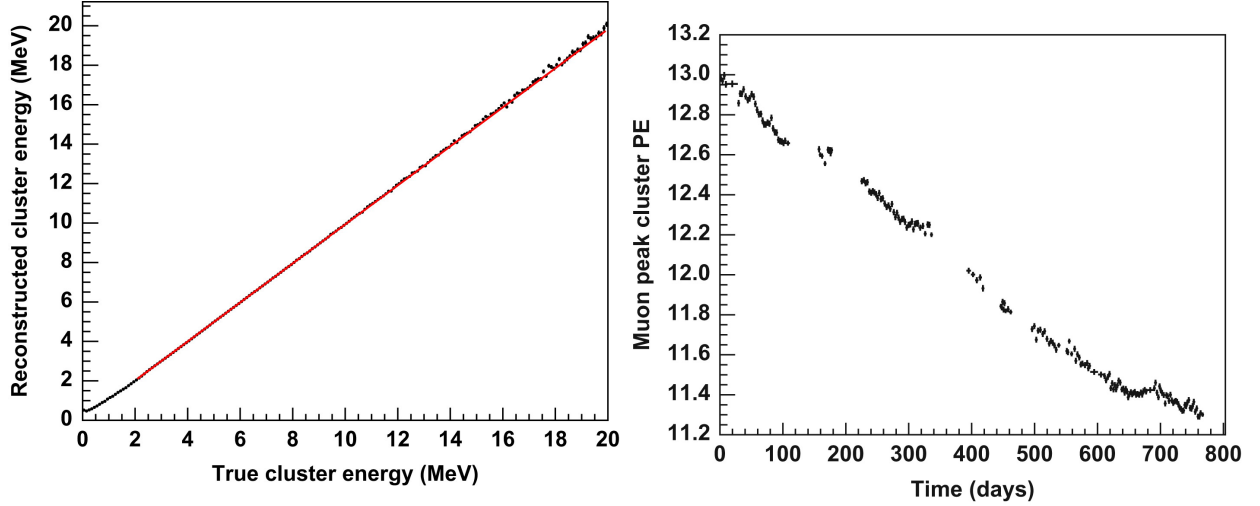
### 2.3.2 Timing Calibration

The raw time recorded in a hit is the time when the discriminator of FEB fires instead of the time scintillator lights. Timing calibration corrects for FEB timing offset and PE-dependent scintillator delay (time slewing), and the rock muon sample is used to calibrate both terms.

The calibration is performed in an iterative way, such that calibration constants are



(a) Simulated and measured cluster energy distribution of rock muon (left), and resulting fit of measured peak (right)



(b) Mapping of reconstructed and generated cluster energy in simulation, as well as the linear fit result. (c) Measured rock muon cluster peak PE as a function of time.

Figure 2.13: Absolution Energy Scale Calibration. Figures from [14]

calculated using constants calculated in the previous iteration until the result converges. At each iteration, the track time is calculated by truncated mean peak hit time of clusters associated with one track. The distribution of hit time relative to track time, corrected by



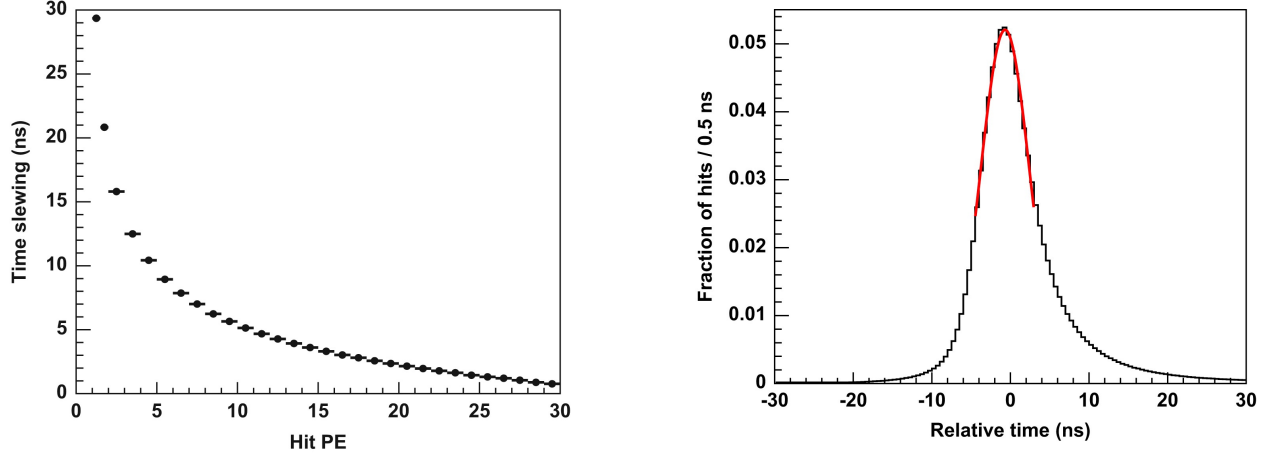


Figure 2.14: Left: measured time slewing. Right: calibrated timing resolution. Figure from [14].

muon time of flight, nominal transport time in fibers, and FEB offsets (referred to as relative hit time in the following context), are binned in several bins of measured number of PEs. The relative hit time distribution in each region is fitted to a Landau-Gauss function, and the peaks of Landau-Gauss functions as a function of  $1/\sqrt{\#PE}$  are fitted to a third-order polynomial. The polynomial gives the most probable delay time given the number of PEs and applied to all hits in the sample. The mean of time slewing corrected relative hit time in a high gain TriP-t chip is extracted as a new FEB timing offset (two per FEB)<sup>8</sup>. The timing calibration is performed every time after a hardware change since the timing offsets of FEBs are changed.

Finally, the timing resolution is determined by the distribution relative hit time after calibration. The peak region is fitted to a Gaussian function and the width is interpreted as the timing resolution, estimated to be 3.0 ns.

<sup>8</sup>The variance of transport time among channels in the same TriP-t Chip is neglected.

### 2.3.3 Alignment Calibration

The MINERvA main detector is built of 120 mechanically independent modules, hence the variations in relative module positions are inevitable. As a result, the mapping of the electronic channel to physical position has to be calibrated as well.

The translation in the measured direction<sup>9</sup> and rotation in the x-y plane are corrected by in situ rock muon samples, extracted in the following way: First, the nominal position, or perfect alignment, is assumed for all planes to fit the muon tracks. Second, the reconstructed intersecting points of muon tracks and the illuminated scintillator strips are calculated. Notice that a muon track is fitted by tens of planes, hence the reconstructed intersecting points are fairly accurate. Third, the hit energies of muon clusters are aggregated in bins of intersecting positions relative to the strip center in the measured direction, and the means are extracted by fitting bi-linear functions. The peak of mean hit energy would be at the strip center if a plane is perfectly aligned because muons would have the largest path length passing the center of the strip. Consequently, the measured peak position off the strip center is the translational alignment correction. Fourth, the hit energy is further binned in translational and longitudinal positions relative to the strip center, such that step 3 is done in 6 different longitudinal positions. The 6 peak hit energy positions are fitted to a straight line, such that the slope represents the x-y plane rotational alignment correction.

The other alignment parameters are found to be insensitive to this measurement, hence remain uncalibrated.

### 2.3.4 Cross-talk Measurements

An illuminated scintillator channel could end up generating an electrical signal in another readout channel, known as “cross-talk”. The energy loss by cross talk would have been compensated by the aforementioned calibration, hence MINERvA identify them and remove them in reconstruction. The primary sources of cross-talk are optical (fiber to PMT) and PMT internal, determined by MINOS study[98]. The cross-talk strength of a PMT is characterized by  $f_{xt,NN}$ , which is the ratio of total cross-talk hit pulse heights in the direct adjacent

---

<sup>9</sup>For example, x direction for X planes defined in section 2.2.1.

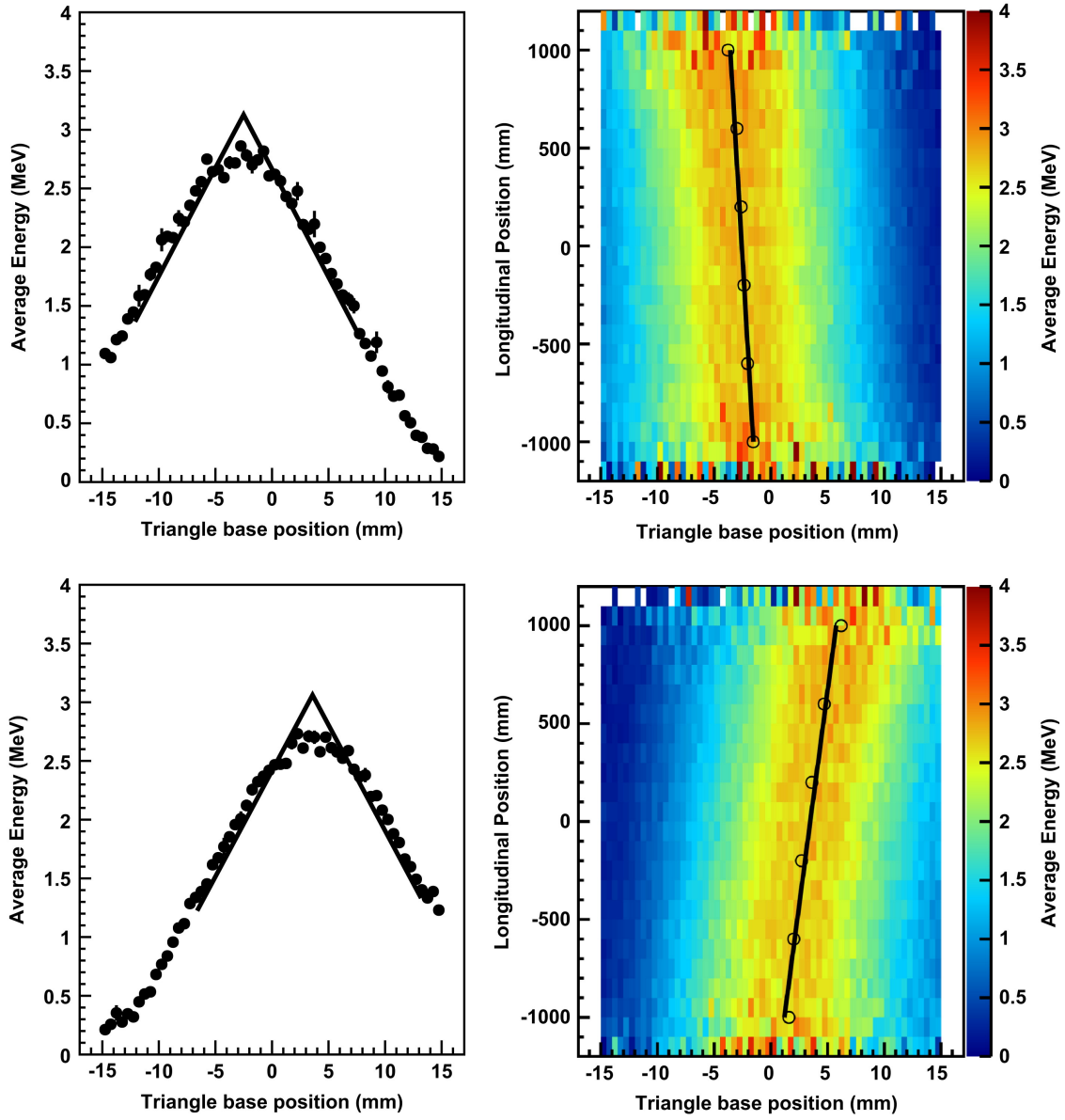


Figure 2.15: 2 examples of alignment calibration, module 50, plane 2 (top) and module 61, plane 1 (bottom). Left: average measured energy as a function of reconstructed triangle base incident position. Right: Fitting the rotational alignment parameter by fitting shifts as a function of longitudinal position. Fig from [14].

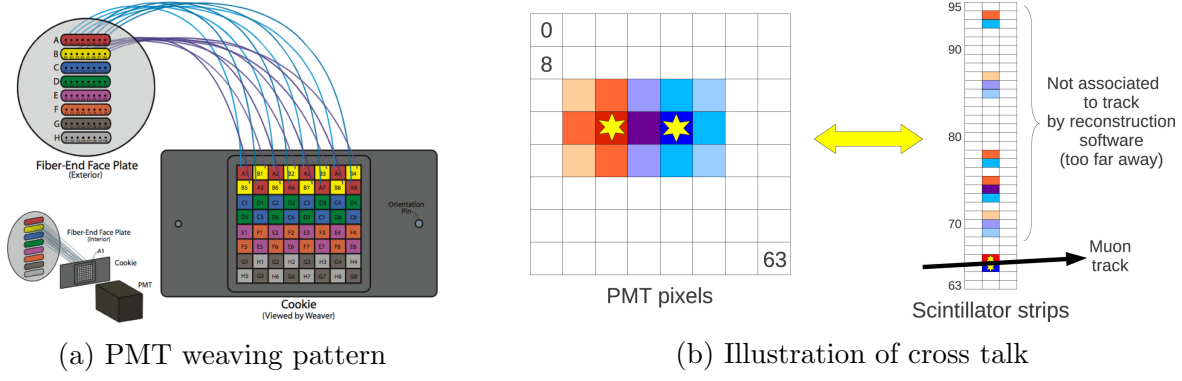


Figure 2.16: The mapping of PMT channels and the physical position of the scintillator strips are arranged such that optical adjacent channels are spatially spread out. Figure from [14].

PMT channels of the source hit to the pulse height of the source hit itself, determined by in-situ measurement using the rock muon sample. This in-situ measurement assumes the hits associated with reconstructed muon tracks are sources, and the stray hits in the same PMT are the cross-talk hits that originated from the muon hit, as shown in figure 2.16, such that the parameter is estimated by average ratio. The measured and simulated  $f_{xt,NN}$  for the inner detector channels are shown in figure 2.17 and used to identify cross-talk candidates in neutrino interaction events, as discussed in section 4.1.2. This measurement only applies to inner detector channels, because tracking in the outer detector is not reliable. As shown in figure 2.17, the simulation doesn't describe cross-talk strength very well, especially outside the 1 - 3.5 PE region. The discrepancy is believed to be a result of some PMTs behaving differently from the majority[98], and not critical to neutrino analyses since low PE cross-talk hits are not likely to fire discriminator, while high PE hits are rare.

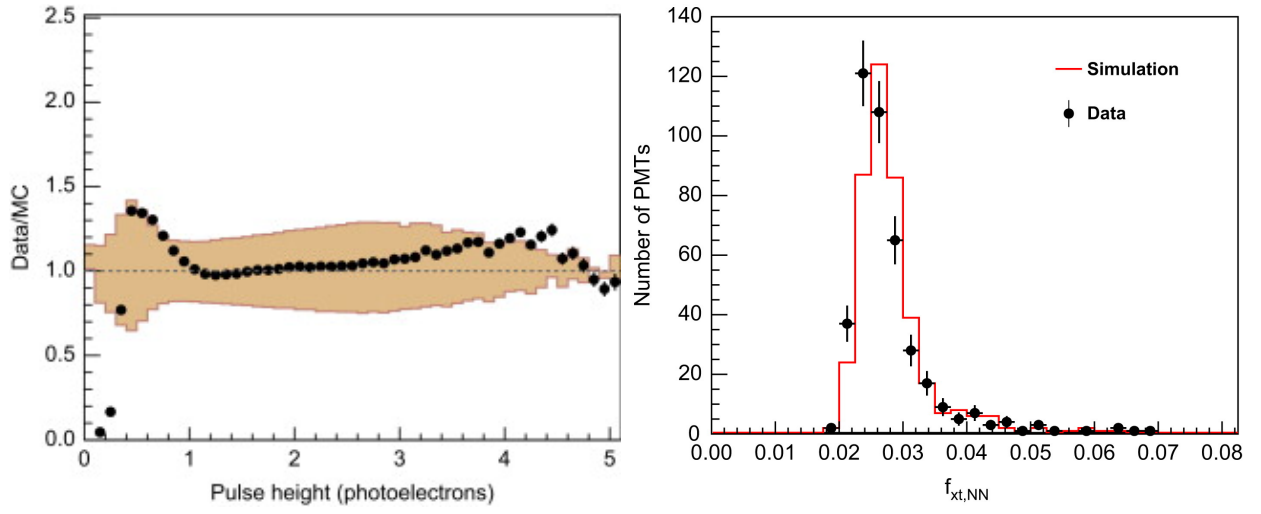


Figure 2.17: Simulated and measured cross-talk strength. Left: data simulation ratio of cross-talk pulse height spectrum. The shaded area is estimated uncertainty. Right:  $f_{xt,NN}$  distribution in data and simulation. Figure from [14].

### 3.0 Simulation in MINERvA

Modern physics experiments use Monte Carlo simulations (MC) to make standard model predictions subjected to detector smearing. The simulation chain MINERvA uses has 3 components: The first one is flux simulation (section 3.1), which predicts neutrino spectrum in MINERvA. The second component is neutrino interaction simulation (section 3.2), which generates neutrino scattering events of various interaction channels and kinematics according to the standard model prediction. The last component is the detector and readout simulation (section 3.3), which predicts the electrical signals that the detector would record given a neutrino scattering event. On top of these three components, there are several post-simulation adjustments applied to simulated events, in order to incorporate simulation developments while reusing the generated sample (section 3.4).

#### 3.1 Flux Simulation

MINERvA uses a modified version of g4numi to simulate neutrino flux[15]. g4numi is a software suite that uses Geant4[11]<sup>1</sup> and geometry model of NuMI beam line equipment to predict the neutrino flux at MINERvA, including simulation of hadron interactions of the 120 GeV proton and NuMI target, as well as the subsequent decay chain. The modifications to g4numi are introduced by ppfx package[16], which provides several hadron production rate corrections based on data inputs from various hadron production measurements.

---

<sup>1</sup>Geant v4.9.2.p03 was used with the FTFP-BERT physics list.

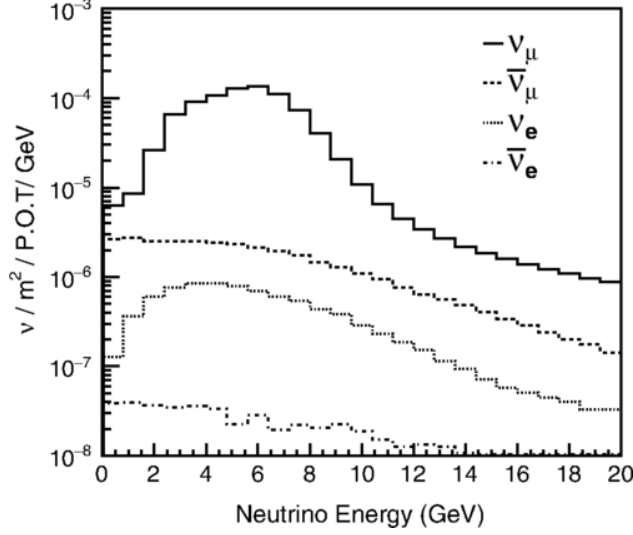


Figure 3.1: Simulated neutrino flux at MINERvA. Figure from [100]

### 3.2 Neutrino Interaction Simulation

Neutrino-nucleus interactions are simulated using GENIE, a Monte Carlo (MC) neutrino interaction event generator[20]<sup>2</sup>. It takes the aforementioned simulated neutrino flux and geometrical model of the MINERvA detector as inputs and generates neutrino interaction events originating in MINERvA inner detector. The elemental composition of materials used in tracker and nuclear target region are listed in table 3.1a and table 3.1b. GENIE simulates multiple neutrino-nucleus interaction channels exclusively, including the three primary channels (CCQE, RES, and DIS) discussed in section 1.3.2, as well as subdominant channels such as charm production and coherent pion production.

The quasi-elastic interactions are simulated using the Llewellyn-Smith formalism[63] with BBBA05 vector form factor modeling[29], where the axial form factor uses the dipole form with an axial mass of  $M_A = 0.99$  GeV. The Rein-Sehgal model[81] with axial mass of  $M_A^{RES} = 1.12$  GeV is employed to simulate resonance productions. DIS interactions are simulated using the leading order model with Bodek-Yang prescription[28]. In addition, 2p2h

---

<sup>2</sup>GENIE v2.12.6

interactions are simulated using the Valencia model[73, 52, 91] and coherent pion production is simulated by the other Rein-Sehgal model[82].

There is an extra complication in simulating coherent pion production. The coherent channel of GENIE doesn't simulate coherent scattering off hydrogen atoms (diffractive pion production). However, LE era MINERvA data showed the contribution of the NC diffractive process is sizable in the sideband region (defined in section 5.4)[102]. In order to simulate this process, the CC diffractive model in GENIE, which is an implementation of the work by Rein[80], is used with two modifications to turn the CC model into an NC model. First, the final state charged lepton is replaced by a neutrino with the same kinematics. Second, the normalization is reduced by a factor of 2 because of CC/NC ratio.

The nucleon initial states are simulated using relativistic Fermi gas model[94] with additional Bodek-Ritchie tail[27] while the FSI is simulated using INTRANUKE-hA package[41], which is a hadronic cascade model.

Neutrino-electron scattering processes, such as inverse muon decay and elastic scattering, are simulated using GENIE as well. The cross sections of these two lepton-lepton processes are well understood, hence MINERvA uses them as standard candle to constraint neutrino flux[74, 100, 88], more details in section 3.4.1.

### 3.3 Detector and Readout Simulation

The detector response is simulated using Geant4[11]<sup>3</sup>, which takes final state particle momenta and the detector model as inputs to predict the fates of final state particles and corresponding energy depositions in active and passive materials. In order to develop and evaluate the reconstruction algorithm using a simulated sample, MINERvA developed software to simulate the electronic responses to the energy depositions, using the parameters extracted from calibration measurements (de-calibrate), such that the reconstruction algorithm applies to data and simulated events in the same way. The remaining unsimulated features in data, such as accidental activities and pile-up of multiple interaction events, are

---

<sup>3</sup>Geant version 4.9.3.p6, with the QGSP BERT physics list



added to the simulated events by the “data overlay” technique. This technique added hits in a data gate on top of a simulated gate, using data gates randomly chosen among the same flux/detector configuration as the simulated gate. There is a truth plausibility veto in the reconstruction algorithm, discussed in section 4.4, to avoid counting a data event overlapped on the simulated gate as the simulated event.

### 3.4 Post-simulation Reweighting

The simulations are constantly improving as new models or data being available. However, generating a simulation sample consumes too many computing resources to run every time a better model is available. As a result, MINERvA uses reweighting technique to approximate the result of a new model using the sample generated by an old model. This is achieved by weighting simulated events using a function of one or more kinematic variables,

| Component | H (%) | C (%) | O (%) | Al (%) | Si (%) | Cl (%) | Ti (%) |
|-----------|-------|-------|-------|--------|--------|--------|--------|
| Strip     | 7.59  | 91.9  | 0.51  | –      | –      | –      | 0.77   |
| Plane     | 7.42  | 87.6  | 3.18  | 0.26   | 0.27   | 0.55   | 0.69   |

(a) Elemental composition of scintillator strip and plane

| Material | Density (g/cm3) | C (%) | Si (%) | Mn (%) | Fe (%) | Cu (%) | Pb (%) |
|----------|-----------------|-------|--------|--------|--------|--------|--------|
| Steel    | 7.83±0.03       | 0.13  | 0.2    | 1.0    | 98.7   | –      | –      |
| Lead     | 11.29±0.03      | –     | –      | –      | –      | 0.05   | 99.95  |
| Graphite | 1.74±0.01       | >99.5 | –      | –      | –      | –      | –      |

(b) Density and elemental composition of nuclear targets.

Table 3.1: Elemental composition of scintillator and nuclear targets. Table from [14].

such that the weighted event distribution in the chosen kinematic variables matches the target model. The kinematic variables are carefully chosen such that the weighted distributions in other variables are close to the new model as well.

### 3.4.1 Flux Reweighting

The neutrino flux in MINERvA is constrained by neutrino-electron elastic scattering (nu+e) measurements[100]. This constraint provides an ensemble of flux universes, each characterized by a neutrino flux spectrum and a posterior probability. The neutrino flux spectra of each universe are simulated using alternative parameters, where the parameters are randomly drawn from Gaussian distributions with mean and variance being nominal value and uncertainty. The posterior probabilities are calculated using Bayes' theorem, assuming the electron energy spectrum of nu+e events is multi-dimensional Gaussian distributed in a given universe. The best estimation of flux after constraint, a.k.a. constrained flux, is calculated by posterior probability-weighted average among the ensemble, which is about a 10% reduction of the nominal flux. The simulated neutrino interaction events are then reweighted by a function of neutrino energy to correct the difference between prior flux (g4numi flux) and constrained flux.

### 3.4.2 Interaction Model Reweighting

There are 3 interaction channels reweighting that are commonly adopted by all MINERvA analyses, RPA reweighting, 2p2h reweighting, and non-resonance pion reweighting. These modifications to GENIE prediction are collectively referred to as “MINERvA Tune-v1”. In addition, this analysis included a resonant pion reweighting on top of “MINERvA Tune-v1”, which is adopted by a number of MINERvA analyses, referred to as “MINERvA Tune-v2”.

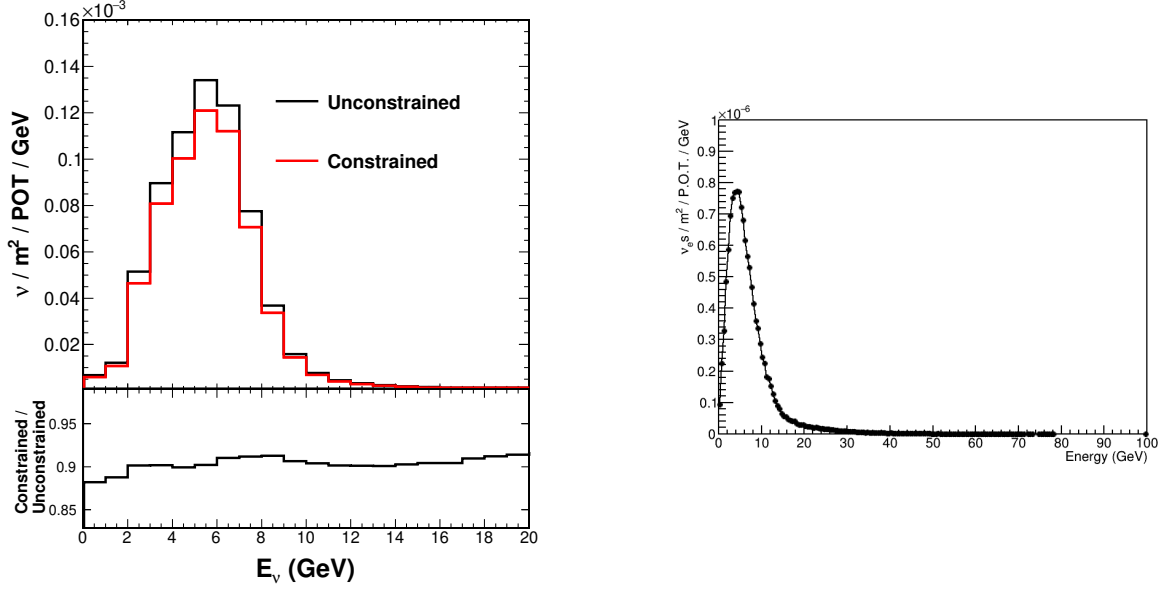


Figure 3.2: Left: prior and constrained  $\nu_\mu$  flux as well as reweighting factors. Right: constrained  $\nu_e$  flux. Figure from [100]

### 3.4.2.1 RPA Reweighting

The Valencia model[72, 54] includes a random phase approximation correction for QE interactions that is not available in the GENIE model at the time of the simulation. MINERvA reweights QE events as a function of 4 momentum transfer  $q = (q_0, |\vec{q}_3|)$ , or  $(q_0, q_3)$  to approximate Valencia model prediction.

### 3.4.2.2 2p2h Reweighting

MINERvA low-recoil analysis found a data excess in the dip region, which is between the peak of QE and resonance interaction in  $(q_0, q_3)$  phase space[83]. MINERvA reweights 2p2h events by a 2D Gaussian function of  $(q_0, q_3)$  to fill in the gap, resulting in roughly 50% increase of simulated 2p2h event rate. The function is given by:

$$w(q_0, q_3) = N \times \exp \left[ -\frac{1}{2(1-C^2)} \left( \frac{(q_0 - \mu_0)^2}{\sigma_0^2} + \frac{(q_3 - \mu_3)^2}{\sigma_3^2} - 2C \frac{(q_0 - \mu_0)(q_3 - \mu_3)}{\sigma_0 \sigma_3} \right) \right] \quad (47)$$

where the parameters are listed in all columns of table 3.2.

### 3.4.2.3 Non-Resonant Pion Reweighting

GENIE assigned large uncertainties for non-resonant pion production cross section parameters because of discrepancies in two bubble chamber data sets, ANL and BNL. A reanalysis[85] found that the discrepancy can be solved by including subdominant channels, and provided a better estimation and reduced uncertainties of related parameters. This leads to a flat 57% reduction of non-resonant single pion production rates.

### 3.4.2.4 Resonant Pion Reweighting

MINERvA measured several pion production cross sections and found tension between data and model predictions. An ad-hoc  $Q^2$  dependent tuning of resonant pion production is proposed to improve the agreement, as an approximation of poor modeled nuclear effects[95].

### 3.4.3 Calorimetry Tuning

MINERvA CC  $\pi^0$  production measurements found that the  $\pi^0$  invariant mass measured

|                  | all       | nn       | np       | QE        |
|------------------|-----------|----------|----------|-----------|
| $N$              | 10.5798   | 8.58724  | 17.0344  | 5.38719   |
| $\mu_0$ (GeV)    | 0.254032  | 0.23626  | 0.289916 | 0.213611  |
| $\mu_3$ (GeV)    | 0.50834   | 0.502603 | 0.532062 | 0.396522  |
| $\sigma_0$ (GeV) | 0.0571035 | 0.072291 | 0.074685 | 0.0496312 |
| $\sigma_3$ (GeV) | 0.129051  | 0.154832 | 0.137321 | 0.125062  |
| $C$              | 0.875287  | 0.789796 | 0.836689 | 0.806659  |

Table 3.2: Parameters of 2p2h reweighting function. The “all” column is used in central value while the others are variations that represent the systematical uncertainty (more information in section 5.8.1)

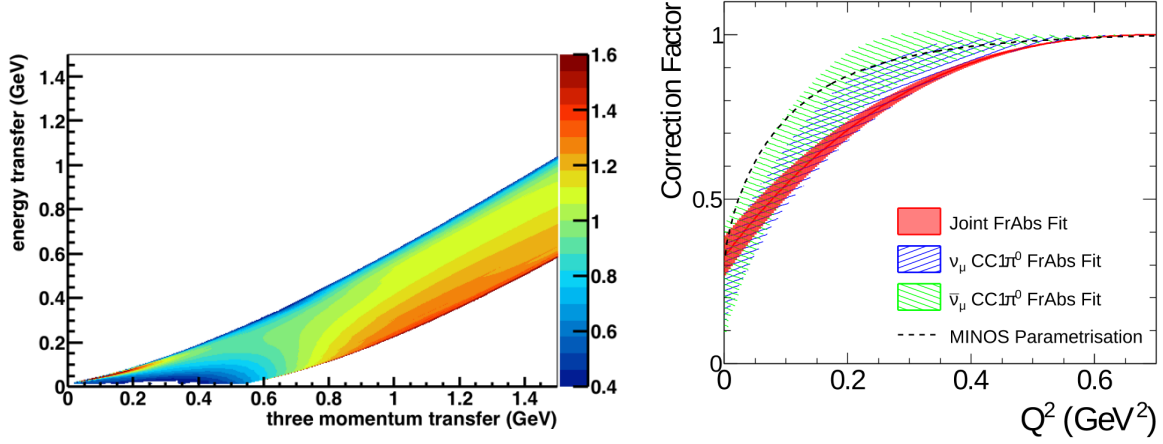


Figure 3.3: Left: RPA reweighting factors. Right: resonant pion reweighting factors. This analysis uses the joint-fit result (red) result. Figure from [54] and [95].

in data is smaller than the nominal 134.97 MeV [17]. MINERvA concluded this is due to the EM energy scale in ECAL being different from what we expected, because  $\pi^0$  invariant mass is a well-measured quantity and decided to reduce the shower energy measured in ECAL by 5.8%.

## 4.0 Reconstruction in MINERvA

Reconstruction is a set of algorithms that process the electrical signal, either simulated or recorded, and infer the nature of physical interaction that happened in the detector. There are two major stages in MINERvA reconstruction: generic reconstruction and analysis unique reconstruction. The generic reconstruction is common to all MINERvA analyses, as suggested by the name, focusing on reconstructing geometry features like tracks and vertices (section 4.1). On the other hand, analysis unique reconstruction performs particle identification and kinematics estimation, together with necessary tracking and/or vertexing on top of generic reconstruction. This separation frees individual analyzers from re-inventing the wheel, but inevitably introduces a bias toward the majority of MINERvA analyses,  $\nu_\mu$  measurements. The reconstruction unique to charged current  $\nu_e$  events consists of two parts, the identification of the final state electron (section 4.2) and calorimetry measurement of final state hadrons (section 4.3). The electron identification in this analysis is essentially the same as MINERvA LE era  $\nu_e$  CCQE measurements[103], while the calorimetry measurement is an analogy to MINERvA LE era  $\nu_\mu$  low recoil analysis[83]. Finally, the truth plausibility veto is a semi-generic part of MINERvA reconstruction: the purpose is generic to all MINERvA analyses, but the implementation is unique to individual analysis ((section 4.4)).

### 4.1 Generic Reconstruction

The generic reconstruction takes the calibrated hits (referred as digits in this section) in the entire  $16\mu\text{s}$  gate as input, splits digits from different interaction events by timing separation and groups digits according to spatial adjacency.

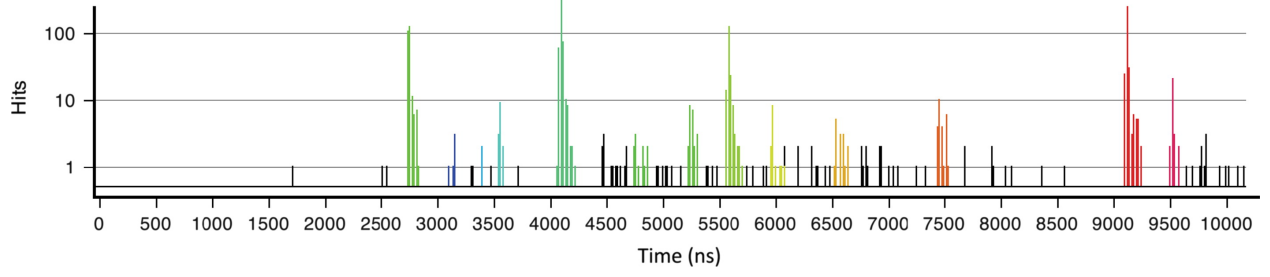


Figure 4.1: Time structure of a typical gate. Each reconstructed time slices are colored in different colors. Figure from [14]

#### 4.1.1 Time Slicing

The start point of generic reconstruction is a collection of calibrated digits. These digits are organized chronologically and sliced into multiple chunks using a peak finding algorithm. This algorithm uses an 80 ns sliding window to scan the gate and identifies peaks, which are time windows with more than 10 photoelectron charges passing the discriminator threshold. Once a peak is identified, the time window is extended forward in time until the peak condition is no longer met in the last 80 ns of the time window. The digits in the entire time window, regardless of exceeding or failing the discriminator threshold, are grouped together as a “Time Slice”. A time slice is usually interpreted as a physical event, unless identified as delayed activity (such as Michel electron) by analysis unique reconstruction.

#### 4.1.2 Cluster Formation

Digits in a time slice that are directly adjacent to each other in the same scintillator plane are further grouped into clusters, which is the basic building block of following reconstruction. MINERvA chooses clusters rather than digits because a single particle trajectory usually intersects two strips per plane, due to the triangular shape of scintillator strips. There are 5 types of clusters, depending on energy and spacial spreading of digits:

1. Low activity clusters, which are clusters with a total energy of less than 1 MeV.

2. Trackable clusters, which are clusters that meet all of these conditions: (a) four or fewer digits, (b) total energy between 1 - 12 MeV, (c) more than one digits have more than 0.5 MeV energy, and these digits must be neighbors.<sup>1</sup>
3. Heavily ionizing clusters, which are clusters that meet condition (a) and (c) of trackable clusters, but have a total energy of more than 12 MeV.
4. Super clusters, which are clusters with more than 4 digits, or more than 1 MeV total energy but are not trackable nor heavily ionizing clusters.
5. Cross-talk clusters, determined by a hypothesis test. Specifically, the null assumption is that all digits in the cluster are cross-talk of adjacent channels. The probability of measuring such pulse height under the null hypothesis (p-value) is calculated using  $f_{xt,NN}$  measurement discussed in section 2.3.4, assuming Poisson distribution. The null hypothesis is rejected when  $p < 0.0001$ [104], otherwise the cluster is tagged as cross-talk.

#### 4.1.3 Track Reconstruction

The next level reconstruction object is the track, which is a collection of clusters that represent a particle traveling in a straight line. There are two steps to reconstruct tracks: the first one is forming 1 view track candidates from track seeds, the second is combining track candidates in multiple views to 3D tracks.

Track seed is defined as 3 trackable or heavily ionizing clusters in 3 consecutive planes of the same view and can be fitted to a 2D line. The seeding method limits the angle of fitted 2D line to be less than 70 degrees with respect to detector z-axis, leading to a similar limit on reconstructed tracks. Track seeds are merged with each other in the same view to construct track candidates. Two track seeds would be merged if they met all of the following conditions:

1. The difference of the fitted slopes between two seeds is within tolerance.
2. They share at least one cluster.
3. They do not contain different clusters in the same plane.

---

<sup>1</sup>In other words, the cluster must not have double peaks.



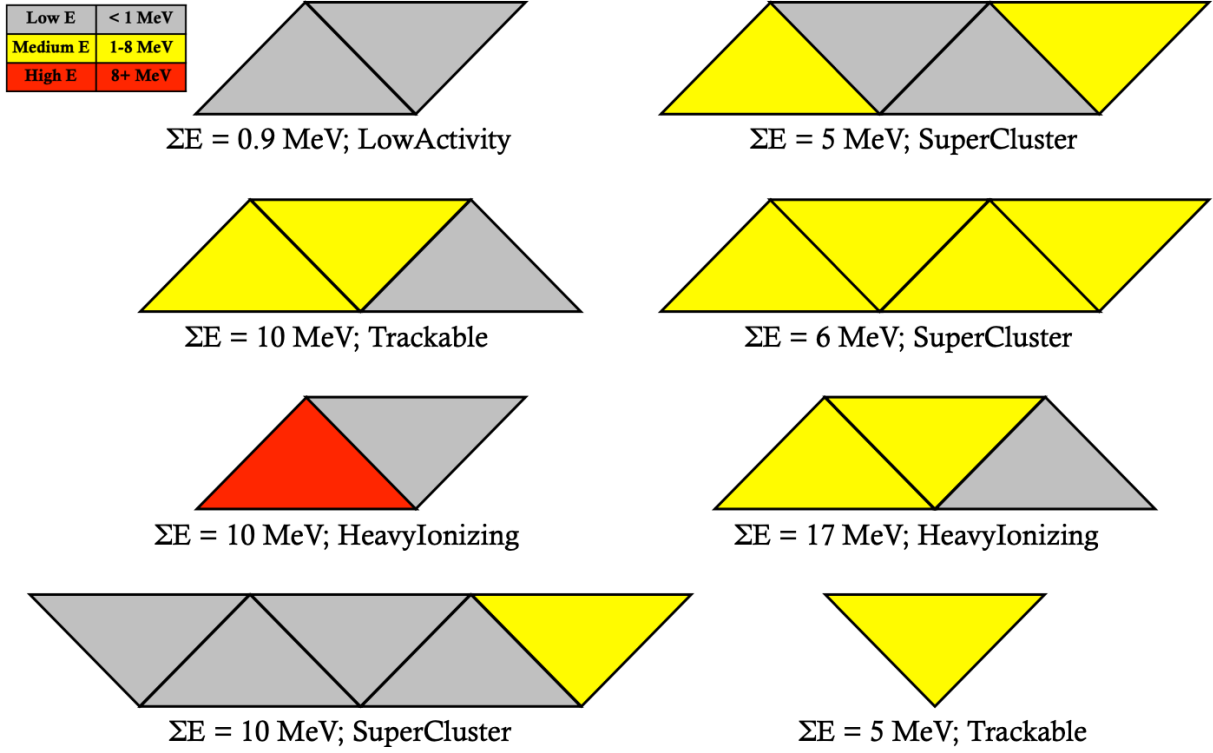


Figure 4.2: Examples of various types of cluster except for cross-talk. Figure from [76]

Once two seeds are merged into a candidate, the algorithm will attempt to merge more seeds in the same direction first, and the seed could only be used by one track candidate. Consequently, the output of this stage depends on the order of merging attempts. This randomness is mitigated by allowing gaps in a track candidate and attempting to merge the same view track candidates after all candidates are built.

The second step, combining track candidates to 3D track, can be accomplished by two methods. The first one is trying to find tracks using track candidates of all three views. This method is more robust because there is a redundant view reducing the chance of mismatching, but is limited to tracks with more the 11 clusters. The first method would try to find as many tracks as possible, and the remainders will be examined by the second method, which requires longitudinal profile matching in any two views. The second method can find tracks as short as 9 clusters, but can't resolve ambiguities if there are multiple matches.

The reconstructed tracks can have gaps or shared clusters at this point due to the choice of track seed, hence an extra step is employed to break clusters and assign proper fraction of clusters to each track. First, all 3D tracks are refined by a Kalman filter fit to get the best estimation of particle trajectory[46]. Second, the intersection point of trajectory and scintillator planes are calculated, such that clusters on the trajectory, including super clusters, are added to the track if not already in the track. Finally, clusters shared by multiple tracks are broken up and assigned fractional ownership to each track according to intersecting point for super cluster or mean energy deposition of the track for other types of clusters.

At this point, if the longest track found has more than 25 clusters, it is assumed to be a muon track and served as an anchor of this event. The interaction point of the event is assumed to be the start point of this track and all tracks except the muon track are discarded, such that their clusters are made available for a second pass of track reconstruction. In addition, clusters that are in the muon track but inconsistent with a minimal ionizing particle are split such that the extra energy is available for the second pass as well. The second pass of the track reconstruction procedure is exactly the same as the first pass, but only tracks that originated from the interaction vertex are kept. The track reconstruction is repeated a third time to find tracks starting from endpoints of existing tracks, in order to keep track of particles re-scattering abruptly in the detector.

After all tracks are reconstructed, the interaction point is re-estimated using all tracks starting from the point with a Kalman filter.[64]

#### **4.1.4 Rock Muon Identification and Removal**

Rock muons can be identified using tracking information. A track is deemed to be rock muon if it meets all of these conditions:

1. It doesn't share a start point with any other track.
2. It is forward going and enters either front or side of MINERvA
3. The average cluster energy of the track is less than 8 MeV.

The mainstream reconstruction tags rock muon clusters as well as clusters that are likely

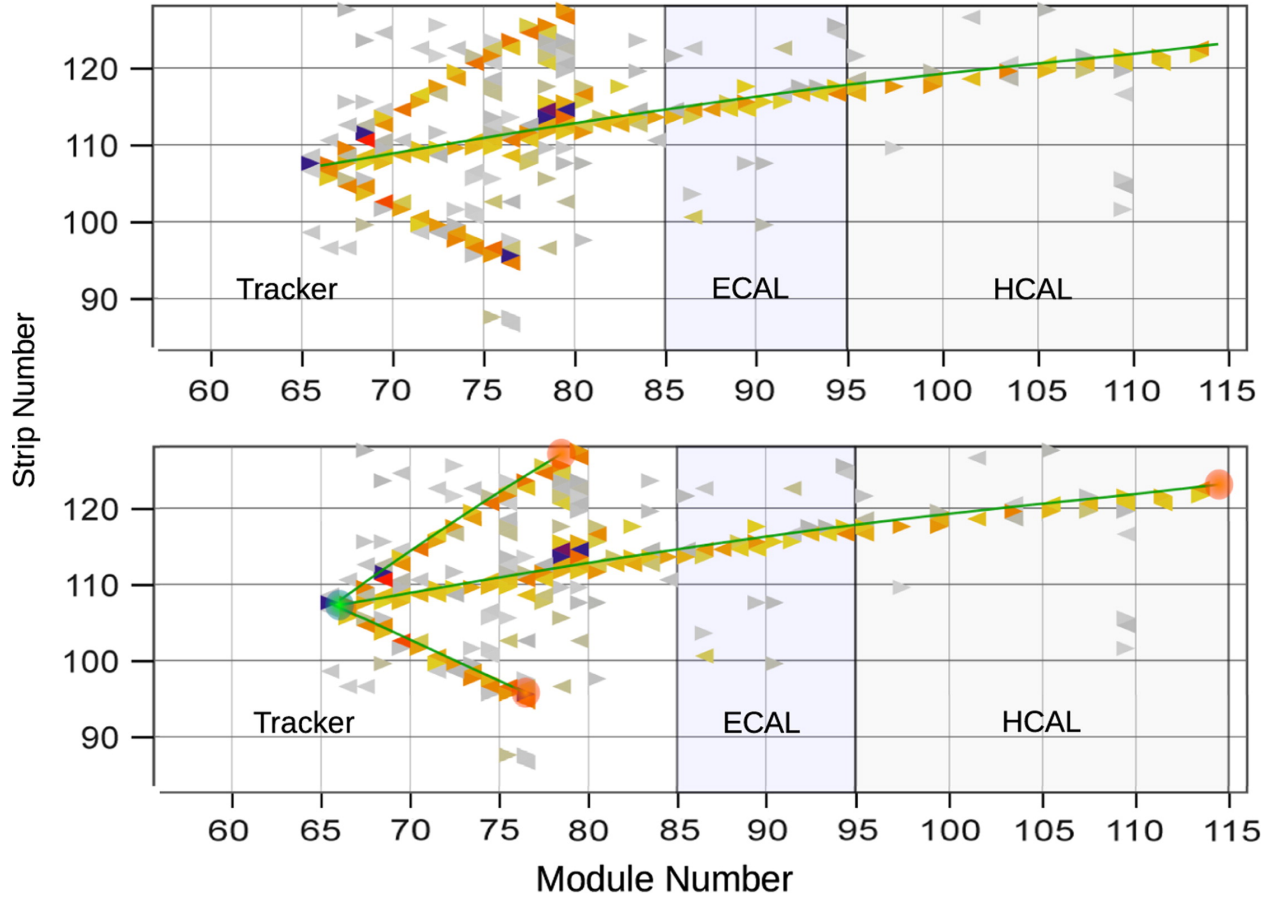


Figure 4.3: Example of track reconstruction. Top plot: the first pass result of track reconstruction. The longest track is selected as the anchor track. Bottom plot: the final result of track reconstruction. Two more tracks are reconstructed from the interaction vertex.

to be shower or cross-talk activities associated with the rock muon and removes them from the event. The reconstruction used in selecting the rock muon sample described in section 2.3.1.4 branches off mainstream reconstruction at this step and saves the rock muon tracks for calibration purposes. The identification of rock muon concludes the generic reconstruction.

## 4.2 Final State Electron Identification

The unique reconstruction of this analysis starts from identifying electrons, and there are three steps in the identification process. First, an electron candidate is constructed for each qualified track. Second, a k-nearest-neighbor (kNN) classifier developed by LE era  $\nu_e$  analyzer[104] is used to evaluate a likelihood score (kNN score), representing the likelihood of the candidate being an electron. Third, the best candidate is chosen among all candidates based on kNN score and reconstructed energy.

### 4.2.1 Characteristics of Electron in MINERvA Detector

The distinguishing feature of electrons at few GeV range passing through a plastic detector is the electromagnetic cascade it initiates. High energy electrons predominately lose energy by bremsstrahlung[107]. At few GeV range, the bremsstrahlung photons are energetic enough to pair produce more electrons, which are still capable of generating more photons, leading to an exponential growth of electrons and photons passing through the detector. This process is referred to as electromagnetic cascades or EM shower. The EM shower terminates when the energy of generated photon fail below the pair-production threshold or ionizing loss dominates generated electron energy loss. Notice that photons with similar energy also initiate EM shower like electrons, but there are two differences between photon and electron-initiated shower in MINERvA:

1. Photon usually leaves no trace in the detector at the beginning of its trajectory, because the mean free path of a photon in plastic is about 20 cm.
2. The beginning of photon-initiated EM shower deposits more energy than electron initiated one because there are two electrons (pair produced electron and positron) rather than one depositing energy to the detector.

Both features are used to distinguish photon (or  $\pi^0$ , which instantly decays to two photons) and electron.

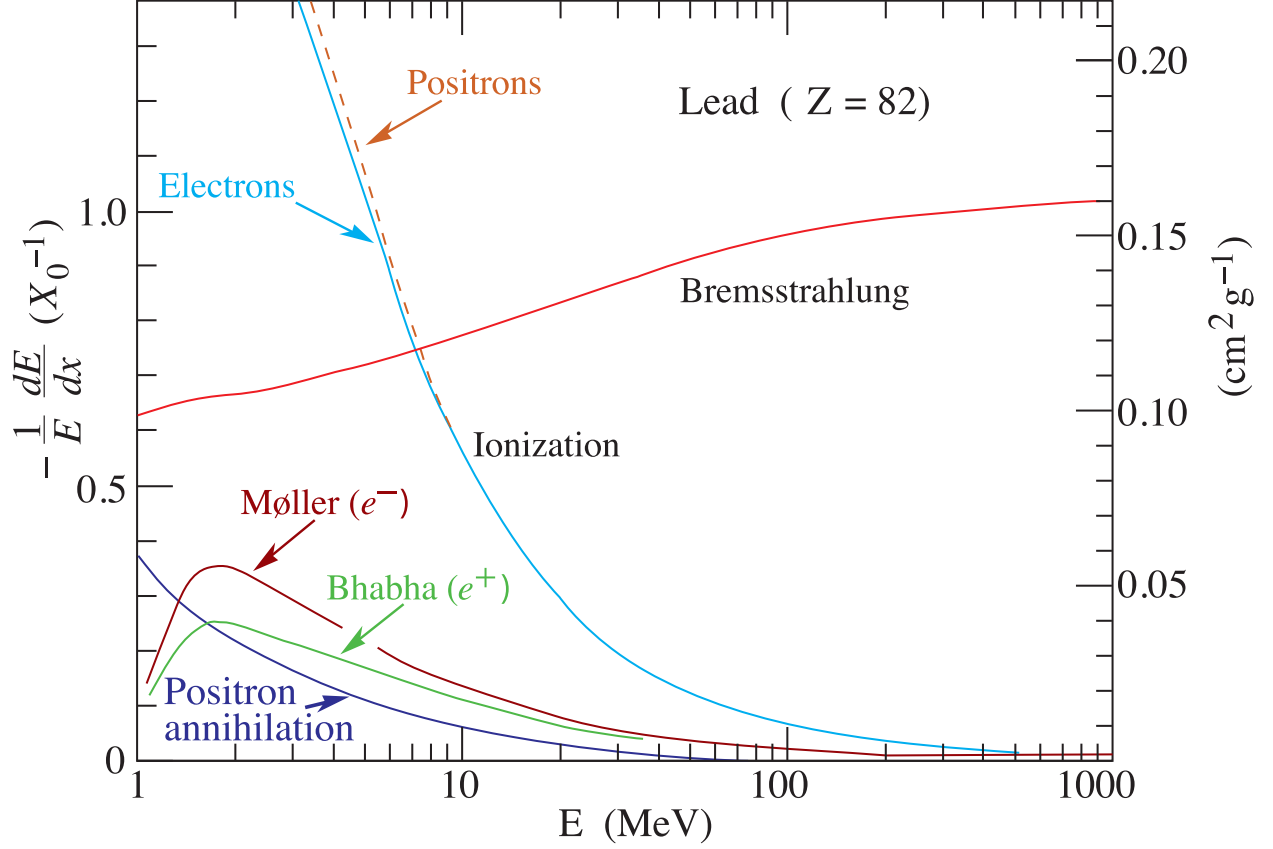


Figure 4.4: Fractional energy loss per radiation length for electron/positron in Lead. Figure from [107].

#### 4.2.2 EM Shower Candidate Formation

The electron EM shower candidates are constructed from reconstructed tracks<sup>2</sup>. A track is considered qualified if it satisfies the following conditions:

1. No track in the same event exits downstream of MINERvA.
2. The starting point of the given track is the most upstream point among all reconstructed tracks.

The first condition removes events with a muon, which are almost certainly CC  $\nu_\mu$  events. The second condition rejects EM shower initiated by a photon, which is likely a decay product

<sup>2</sup>Empirically, the tracking algorithm is capable of reconstructing the beginning of EM shower as a track.

of  $\pi^0$ . For each qualified track, an EM shower region is constructed by the union of a 7.5-degree open angle cone and a cylinder of 50mm radius, using the track direction as axis and the track starting point as apex, as illustrated in figure 4.5.

Next, the algorithm iterates over all pairs of a qualified track and another track (regardless of being qualified track or not), and the clusters of the other track would be absorbed into the qualified track if more than 50% of visible energy are inside the EM shower region of the qualified track. After the iteration, all remaining qualified tracks are likely to represent different particles leaving the interaction point, hence the clusters shared by multiple qualified tracks are re-split according to the average cluster energy of each track. This step removes the bias introduced by assuming the longest track is the muon track during generic reconstruction.

The algorithm then iterates all qualified tracks again to evaluate the kinematics and kNN score. First, isolated clusters<sup>3</sup> inside the EM shower region of a qualified track are absorbed by the qualified track, unless there is a gap of more than 3 radiation lengths between two sets of clusters, in which cases the downstream set of clusters is dropped from the qualified track. Second, the qualified track is refitted using all clusters absorbed, which yields a better estimation of track direction and starting point. The attenuation correction is updated as well since the longitudinal position estimation is updated. Third, the collection of clusters associated with a qualified track is considered an electron candidate, and the kinematics and kNN score are evaluated as described in the following subsections. As a side note, the kNN score evaluation excludes clusters within 25 mm of the cone apex (roughly one module) from variable calculations because the cluster sharing algorithm is not likely to split clusters around the vertex correctly. Finally, the isolated clusters absorbed at the first step of this iteration are made available for consumption on the next qualified track.

### 4.2.3 Electron Candidate Kinematics Reconstruction

The start point and direction of the electron trajectory are estimated by the start point of the qualified track and the direction of the track at the start point. The energy of this

---

<sup>3</sup>Clusters not associated with a track yet

electron candidate is estimated calorimetrically, using the following formula:

$$E^{EM} = \alpha_{scale}(E_T + \alpha_E E_E + (2\alpha_E - 1)E_{SE}^X + (4\alpha_E - 1)E_{SE}^{U,V} + \alpha_H E_H) + \alpha_{EMscale} E_E \quad (48)$$

where the definitions of the variables are listed in table 4.1. This formula is chosen to correct different passive material configurations in different subdetectors, and the parameters except  $\alpha_{EMscale}$  are extracted by fitting to simulated electron sample, detailed in [75], while  $\alpha_{EMscale}$  is determined by calorimetry tuning discussed in section 3.4.3.

#### 4.2.4 kNN Classification

The kNN classifier is trained to distinguish EM shower (either electron or photon initiated) from track-like particles such as protons and charged pions. The training used simulated particle samples, including electron, photon, charged pion, proton, and muon, with initial momenta  $<10$  GeV and initial angle  $<45$  degree with respect to the z-axis.

The variables used by the kNN classifier are:

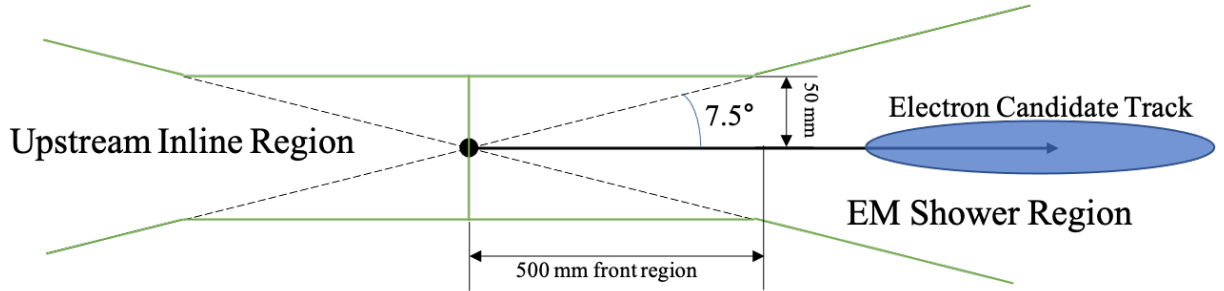


Figure 4.5: Illustration of the EM shower region, where the black arrow represents the electron candidate track. The region enclosed by the green lines on the forward side is the EM shower region, while the backward side is referred to as the upstream inline region, discussed in section 4.3.2. The front dEdX region discussed in section 5.4 is showed as well.

#### 4.2.4.1 Mean dE/dX

The average energy deposition per unit length traversed by a particle ( $\frac{dE}{dx}$ , or dE/dX), which is calculated by dividing estimated EM shower energy by integrated density along the axis of the EM shower region, from the apex to the farthest axis projection point of all clusters. The variable is chosen because EM Showers involve multiple particles, each deposits energy into the detector, leading to higher average dE/dX than track-like particles at the same energy.

#### 4.2.4.2 Endpoint Energy Fraction

The energy deposition at the tail is divided by the energy deposition at the middle of the electron candidate. This variable is calculated by:

1. Calculate the “distance” from each cluster to the cone apex, by the integrated density from the apex to the point of projecting cluster to the axis.
2. Bin clusters per  $10g/cm^2$  density and sum up the cluster energies in each bin.

| Variable           | Description                                | Value                   |
|--------------------|--|-------------------------|
| $\alpha_{scale}$   | Overall Scale (Scintillator)               | 1.326                   |
| $\alpha_E$         | ECAL Scale (Extra Lead)                    | 2.205                   |
| $\alpha_H$         | HCAL Scale (Extra Steel)                   | 9.540                   |
| $\alpha_{EMscale}$ | EM Energy Scale Correction                 | -0.058 (data) or 0 (MC) |
| $E_T$              | Energy in Tracker                          | N/A                     |
| $E_E$              | Energy in DS ECAL                          | N/A                     |
| $E_{SE}^X$         | Energy in Side ECAL (X Configuration)      | N/A                     |
| $E_{SE}^{U,V}$     | Energy in Side ECAL (U or V Configuration) | N/A                     |
| $E_H$              | Energy in HCAL                             | N/A                     |

Table 4.1: Electron Energy Calorimetry Constants and Variables



3. Drop bins with total energy less than 2 MeV.
4. Calculate the ratio of energy in the last bin and the middle bin. The energy of the middle bin is the average of two middle bins if there is an even number of bins.

This variable takes advantage of the difference in the longitudinal energy loss profile of track-like particles and EM shower. Track-like particles deposit more energy at the end of the track than at the middle, which is known as the Bragg peak. On the other hand, EM showers usually deposit less energy in the tail, due to individual particles in the shower falling below the detection threshold.

#### **4.2.4.3 Median Transverse Width**

The median of energy weighted standard deviation of digit position in each scintillator plane. This variable is chosen to separate track-like particles and EM showers by transverse profile. EM shower develops transversely because the secondary particles it generates are energetic enough to travel several planes. On the other hand, track-like particles are less likely to develop transversely because they are most likely to generate low-energy electrons in their vicinity by ionizing. Due to the detector granularity, the width measurement loses sensitivity to the transverse profile when the majority of energy is deposited in two adjacent strips. This is mitigated by merging the two most energetic digits as one pseudo-digit in case they are adjacent to each other.

#### **4.2.5 Choice of The Best Electron Candidate**

An electron candidate passes the selection cut if its likelihood score is greater than 0.7, determined by previous study[104]. There are three scenarios depending on the number of electron candidates passing cut. If there are no candidates selected, the best candidate is the candidate with the highest likelihood score. In order to save computing resources, the event is dropped from further analysis if the best likelihood score is less than 0.6. If there are multiple candidates which pass the cut, the most energetic candidate is chosen as the best electron candidate. This decision is made because the most energetic final state particle is almost certainly the electron in CC  $\nu_e$  scattering events due to interaction kinematics. Finally, the

choice is obvious if there is only one candidate which passed the cut. After the best candidate is chosen, the clusters that were released for evaluating other candidates are re-absorbed, such that only the remaining clusters can be consumed by hadronic reconstruction algorithms. In addition, the event interaction vertex is updated to the refitted electron start point, unless the interaction vertex is determined by multiple tracks in general reconstruction.

### 4.3 Hadron Reconstruction

The hadron reconstruction in this analysis is straightforward: calorimetry. This analysis uses calorimetry measurements in a number of ways<sup>4</sup>, hence we chose to measure several intermediate quantities at this step, such that downstream analysis has the flexibility to combine these quantities for different purposes. These quantities can be categorized in two types: segmented by subdetector or segmented by relative location to the EM shower.

#### 4.3.1 Calorimetry Segmented by Subdetectors

The calorimetry segmented by subdetectors is optimized to measure hadronic energy, including corrections for passive materials. Specifically, the energy of each digit that is not part of the electron candidate is corrected by a strip location dependent scale factor, listed in table 4.2, and summed in 5 subdetector regions, denoted by  $E_{tracker}$ ,  $E_{ECAL}$ ,  $E_{HCAL}$ ,  $E_{OD}$ , and  $E_{nuclear}$ .

#### 4.3.2 Calorimetry Segmented by Relative Location

The calorimetry segmented by relative location to the EM shower region helps separate different neutral current  $\pi^0$  production channels, such that background constraint (discussed in section 5.4) can fit individual channels effectively. The detector is segmented into EM shower region, upstream inline region, and extra region according to the electron candidate location, as illustrated in figure 4.5. The upstream inline energy ( $E_{uie}$ ), the visible electron

---

<sup>4</sup>Detailed in chapter 5

energy ( $E_{vis}$ ), and the extra energy ( $E_{extra}$ ) is defined by the sum of cluster energies in corresponding regions, without passive material correction.

### 4.3.3 Hadron Reconstructions as By-product of Data Preservation Effort

In the data preservation era, MINERvA is actively developing a master reconstruction algorithm that combines the unique reconstructions of all analyses without conflicts. The aforementioned unique reconstruction has been integrated into the master reconstruction algorithm, hence more information about the hadron system, such as proton/pion tracking and identification, are available for data preservation era analyzers. With that being said, this analysis didn't use nor validate the additional information about the hadron system.

## 4.4 Truth Plausibility Veto

This analysis identifies “data overlay” events by the fraction of data digits in reconstructed electron candidate. The event is dropped if data digits in the electron candidate

| Strip Position        | Scale Factor |
|-----------------------|--------------|
| Tracker               | 1.222        |
| Side ECAL X           | 2.805        |
| Side ECAL UV          | 4.388        |
| ECAL                  | 2.013        |
| HCAL                  | 10.314       |
| OD 123                | 21.679       |
| OD 4                  | 42.137       |
| Nuclear Target Region | 1.222        |

Table 4.2: Hadronic Energy Calorimetry Constants

contribute more energy than MC digits in the candidate.

## 5.0 Electron Neutrino Differential Cross Section Measurement

This analysis measures differential cross sections using  $12.1 \times 10^{20}$  P.O.T data in ME FHC configuration, and various MC simulation sample, including  $\sim 4 \times$  data P.O.T general MC simulation, which simulates all major processes in data,  $\sim 30 \times$  P.O.T NC diffractive simulation,  $\sim 16 \times$  P.O.T 2p2h processes simulation up to  $q_3=2.0$  GeV<sup>1</sup>, and  $\sim 42 \times$  P.O.T  $\nu_e$  scattering processes simulation. The differential cross section is measured by the following equation:

$$\left(\frac{d\sigma}{dx}\right)_i = \frac{\sum_j U_{ij}(N_j^{data} - N_j^{bkg})}{\epsilon_i T \Phi (\Delta x)_i} \quad (49)$$

where  $(\frac{d\sigma}{dx})_i$  is the differential cross section as function of  $x$  at bin  $i$ ,  $U_{ij}$  is the unfolding matrix (section 5.5),  $N_j^{data}$  is the measured number of events in bin  $j$  of reconstructed variable  $x$  (section 5.2 to 5.3),  $N_j^{bkg}$  is the predicted number of background events (section 5.4) in bin  $j$ ,  $\epsilon_i$  is estimated acceptance at bin  $i$ ,  $T$  is number of nucleon targets,  $\Phi$  is integrated neutrino flux (section 5.6), and  $(\Delta x)_i$  is bin width normalization of bin  $i$ . The cross section results are presented in section 5.7 and the uncertainties are discussed in section 5.8.

### 5.1 Definition of Signal

We define the signal of this analysis, charged-current  $\nu_e$  nucleus scattering events, by:

- Charged current interaction of an electron neutrino and a nucleus.
- The interaction happens inside the fiducial volume of the MINERvA detector, which is the tracker region defined in detector coordinate by:
  - $5980 \text{ mm} < z < 8422 \text{ mm}$
  - $\text{apothem} < 850 \text{ mm}$

where apothem is apothem of the smallest regular hexagon containing a spatial point  $(x,y,z)$ , centered at  $(0,0,z)$  and aligned with the orientation of MINERvA modules.

---

<sup>1</sup>General simulation uses default GENIE configuration simulates up to  $q_3=1.2$  GeV

- The energy of the final state electron is greater than 2.5 GeV.

The second and third conditions are added to the naive signal definition to avoid extrapolation to regions where the selection efficiency is significantly lower than the average. Specifically, interactions that happen outside of fiducial volume are often poorly reconstructed and not contained by the detector, while the low electron energy region is overwhelmed by misidentified  $\pi^0$  due to the abundance of muon neutrino scattering events.

## 5.2 Sample Selection

### 5.2.1 Selection Cuts

The signal events make up a small fraction of all interaction events happening in the detector, leading to large statistical uncertainty if we naively subtracted predicted background from the data. It is common practice to select events based on several pass/fail conditions (a.k.a cuts) to remove background events from the sample, of course at the cost of worse signal event acceptance.

The selection cuts used in the analysis are inherited from LE CCQE analysis[103] with two modifications: cuts removing non-CCQE events are removed and cuts limiting kinematics phase space are added. There are 4 categories for selection cuts: pre-selection cuts, reconstruction quality cuts, photon rejection cuts, and phase space cuts. The performance of these cuts is estimated using simulation and tabulated in table 5.1.

#### 5.2.1.1 Pre-selection Cuts

Pre-selection cuts are cuts made in the reconstruction stage. We didn't keep information about events removed by these cuts because they are either reconstruction failures or highly unlikely to be signal events. There are three cuts in this category:

1. There is at least one reconstructed track in the event.
2. No reconstructed track leaves downstream of MINERvA.

3. The likelihood score of the best electron candidate is greater than 0.7.

#### 5.2.1.2 Reconstruction Quality Cuts

A “successfully” reconstructed event may not reflect the nature of the event properly because of algorithm failure or hardware limitations. The reconstruction quality cuts remove events that are unlikely to be reconstructed adequately, including the following cuts:

1. Ratio of electron candidate energy in DS HCAL to DS ECAL less than 0.1
2. Ratio of electron candidate energy in OD to Side ECAL less than 0.1
3. No more than 6 reconstructed tracks originated from the electron candidate track starting point.
4. More than 25% of electron candidate digits are first fire digits, which are digits recorded at the first time discriminator fires during a gate.
5. There is no more than 1 dead channel upstream of the electron track.

The first two cuts are containment requirements, making sure the final state electron is contained in the detector. The third cut is a loose quality cut, The granularity of MINERvA limits the capability of multiple tracking, hence high multiplicity vertices are usually due to track seeds merging failure. As a result, the directions of reconstructed tracks are not reliable, hence these events are dropped. The fourth cut intends to remove “ghost” electrons that originated from PMT afterpulsing[55]. PMT afterpulsing is a phenomenon that a secondary weak pulse is observed after a primary pulse, generated by caused by residual gas ions in PMT tubes. These ions are ionized by electrons, return to the photo-cathode, and produced photoelectrons, resulting in afterpulses. A large fraction of not first fire digits indicates the event is likely to be afterpulses of a previous event, because it is uncommon that a channel fires twice during a gate at the event rate observed in MINERvA. The last cut removes events that have a susceptible electron track by requiring the channels upstream of the electron track to be active.

### 5.2.1.3 Electron Selection Cuts

Obviously, we want to select events with an electron and remove those without. The kNN likelihood score does not distinguish electron and photon showers, hence two cuts are introduced to select electron showers. In addition, two more cuts are introduced to further reject track-like particles. This category consists of the following cuts:

1. All reconstructed tracks (except kinked tracks) starts from the same vertex.
2. Front dEdX (defined in following context) less than 2.4 MeV/cm
3. The fraction of energy from trackable clusters is less than 40% of electron energy
4. Transverse spread score (defined in the following context) is greater than 15.

The first cut removes events with multiple start points, which is likely to be  $\pi^0$  production event because of the displaced vertices of photon showers. The second cut also targets rejecting photons, since a photon-initiated EM shower typically has higher dEdX at the front region, as discussed in section 4.2.1. However, the front region of an electron is also the interaction vertex, hence hadronic particles can overlap on the electron track and reduce the sensitivity of these variables. In order to mitigate the impact of vertex activity, the front dEdX is calculated using a 100 mm sliding window across the 500 mm front dEdX region of the electron candidate. The sliding window slides at 25 mm intervals, dEdX is calculated by the sum of cluster energy in the 100 mm region divided by length (100 mm), and the front dEdX used in the cut is the minimal dEdX achieved in the 500 mm region.

The third cut attempts to further reject non-EM shower particles. EM shower consists of a plurality of particles, which creates wide and energetic clusters more often than a single particle traverses the detector. This distinction is captured by the fraction of non-trackable clusters in the electron candidate, as the trackable cluster is defined to represent a single particle transverse the detector.

The fourth cut aims at rejecting track-like particle as well, utilizing the transverse spreading of EM shower. The transverse spread score is calculated in the following way:

1. Calculate the energy weighted mean strip number for each plane  $j$  of the electron candi-



date.

$$\bar{N}_j = \frac{1}{\sum_i E_{i,j}} \sum_i N_{i,j} E_{i,j}$$

where  $N_{i,j}$  and  $E_{i,j}$  are the strip number and energy of  $i$ -th digit on plane  $j$  within EM shower region.

2. Extract the median strip energy for each plane  $j$  as  $\tilde{E}_j$
3. Calculate the spread score for each plane  $S_j$  by:

$$S_j = \frac{1}{\sum_i E_{i,j}} \sum_i |N_{i,j} - \bar{N}_j| |E_{i,j} - \tilde{E}_j|$$

4. Calculate the final transverse spread score by averaging:

$$S = \frac{1}{N_{planes}} \sum_j^{n_{planes}} S_j$$

where  $N_{planes}$  is the number of planes penetrated by the electron candidate.

#### 5.2.1.4 Phase Space Cuts

The phase spaces cut is made inline with signal definitions, including the following cuts:

1. The reconstructed vertex is located in the fiducial volume, defined in section 5.1.
2. The reconstructed electron energy is greater than 2.5 GeV.
3. The reconstructed available energy is less than 2.0 GeV.

| Cuts                  | Data Selected | MC Selected | MC Signal | Efficiency | Purity |
|-----------------------|---------------|-------------|-----------|------------|--------|
| No Cut                | N/A           | N/A         | 445723    | N/A        | N/A    |
| Has Tracks            | 31316700      | 85415550    | N/A*      | N/A*       | 0.00   |
| No BackExiting Tracks | 6124587       | 24737417    | N/A*      | N/A*       | 0.01   |
| kNN Score             | 3664175       | 14960739    | 266164    | 0.60       | 0.02   |
| DSCal VisE            | 3443479       | 14018405    | 260136    | 0.58       | 0.02   |
| ODCal VisE            | 3129646       | 13057179    | 258766    | 0.58       | 0.02   |
| Vertex Track Multi    | 3129585       | 13056868    | 258757    | 0.58       | 0.02   |
| Afterpulsing          | 3117867       | 13053432    | 258714    | 0.58       | 0.02   |
| Dead Time             | 3068545       | 12875995    | 254963    | 0.57       | 0.02   |
| StartPoint Multi      | 1686856       | 7015351     | 190175    | 0.43       | 0.03   |
| Mean Front dEdX       | 503181        | 2059918     | 115448    | 0.26       | 0.06   |
| Non MIP Clus Frac     | 412488        | 1734058     | 115266    | 0.26       | 0.07   |
| Transverse Gap Score  | 287974        | 1303578     | 113868    | 0.26       | 0.09   |
| Vertex Z              | 260703        | 1182464     | 113494    | 0.25       | 0.10   |
| Vertex Apothem        | 207028        | 951776      | 112847    | 0.25       | 0.12   |
| Available Energy      | 116408        | 601121      | 99083     | 0.22       | 0.16   |
| Electron Energy       | 46703         | 252367      | 97898     | 0.22       | 0.39   |

\* These numbers are not available because the reconstruction algorithm doesn't save all events failed pre-selection cuts.

Table 5.1: Selection cuts performance table. Entries are the number of data/simulated events.

### 5.3 Definition of Analysis Variables and Selected Sample Distribution

The differential cross section is measured in the following variables: available energy ( $E_{avail}$ ), three momentum transfer ( $|\vec{q}|$ , or  $q_3$ ), and final state lepton transverse momentum ( $P_{lep}^t$ ). The definitions of the last two quantities are straightforward, while the available energy is defined in the following way as a proxy of energy transfer ( $q_0$ )[83]:

$$E_{avail} = \sum T_p + \sum T_{\pi^\pm} + \sum E_{\pi^0} + \sum (E_s - M_p) + \sum (E_{\bar{b}} + M_p) + \sum E_{others} \quad (50)$$

where  $T_p$  is kinematic energy of final state protons,  $T_{\pi^\pm}$  is kinematic energy of final state charged pions,  $E_{\pi^0}$  is the total energy of final state neutral pion,  $E_s$  is the total energy of final state strange baryons,  $M_p$  is proton mass,  $E_{\bar{b}}$  is total energy of anti-baryons, and finally  $E_{others}$  is the total energy of other final state hadrons except neutron. The main difference between available energy and the energy transfer is that available energy doesn't count neutron kinematic energy and charged pion mass. We chose available energy over energy transfer because these two parts of energy transfer are almost invisible in the MINERvA detector, which leads to a significant model dependence and poor resolution had we measured energy transfer directly.

The reconstruction methods of these variables are described in the following subsections.

#### 5.3.1 Available Energy

We measure available energy in the following way:

$$E_{avail} = \alpha \times \sum_{i=tracker, ECAL} E_i - E_{leakage} \quad (51)$$

$$E_{leakage} = c_{leakage} \times E_{lep} + b$$

where  $E_i$  is the calorimetry energy in subdetector  $i$ , discussed in section 4.3.1,  $\alpha$  is a factor correcting energy losses that are not captured by MINERvA detector, and  $E_{leakage}$  is a correction term accounting for EM shower energy leaked outside of the EM shower region explained in section 5.3.4. MINERvA  $\nu_\mu$  analyses found most activities in nuclear target, OD, and DS HCAL are Beam activities irrelevant to hadronic system[83], hence we only

include tracker, side ECAL, and DS ECAL in this variable. The parameter values in this equation are listed in table 5.2.

### 5.3.2 Lepton Transverse Momentum

Lepton transverse momentum is measured by projecting electron 3 momenta to the the plane perpendicular to the incoming neutrino direction, which is 3.3 degree downward. Reconstruction of electron 4 momentum ( $E_{lep}, \vec{P}_{lep}$ ) is discussed in section 4.2.3.

$$\begin{aligned} P_{lep}^t &= |\vec{P}_{lep}| \sin(\theta_{lep}) \\ \theta_{lep} &= \arccos\left(\frac{\vec{P}_{lep} \cdot \hat{n}_\nu}{|\vec{P}_{lep}|}\right) \end{aligned} \tag{52}$$

where  $\hat{n}_\nu = \cos(\theta_\nu)\hat{z} - \sin(\theta_\nu)\hat{y}$  is the beam direction in detector coordinate with  $\theta_\nu = 3.3$  degree.

| Parameter     | Description                | Value              |
|---------------|----------------------------|--------------------|
| $\alpha$      | Overall scale factor       | 1.17               |
| $c_{leakage}$ | EM energy leakage fraction | 0.008              |
| $b$           | Leakage bias correction    | data: 5 MeV, MC: 0 |

Table 5.2: correction factors for energy reconstruction

### 5.3.3 Three Momentum Transfer

The three momentum transfer is measured using hadronic energy and lepton kinematics:

$$\begin{aligned}
q_3 &= |\vec{q}| = \sqrt{Q^2 + q_0^2} \\
Q^2 &= -q^2 = -(p_{lep} - p_\nu)^2 = 2p_{lep}p_\nu - p_{lep}^2 - p_\nu^2 \\
&\approx 2(E_{lep}E_\nu - |\vec{P}_{lep}|E_\nu \cos(\theta_{lep})) - M_{lep}^2 \\
&= 2E_\nu(E_{lep} - |\vec{P}_{lep}| \cos(\theta_{lep})) - M_{lep}^2 \\
E_\nu &= E_{lep} + q_0 \\
q_0 &= f_s\left(\sum_i (E_i)\right)
\end{aligned} \tag{53}$$

where  $f_s(x)$  is a first order spline function<sup>2</sup> defined by anchor points listed in table 5.3, and  $\sum_i (E_i)$  is the sum of calorimetry energy in all subdetectors. The anchor points of the spline functions are extracted from simulated  $\nu_\mu$  inclusive sample by correcting the difference between  $\sum_i (E_i)$  and  $q_0$ , resulting in an unbiased estimator of  $q_0$ .

### 5.3.4 Leakage Correction

EM shower energy will leak out of the EM shower region because shower development is stochastic and the shower region is conservative. This energy leakage leads to an overestimation of available energy, especially when hadronic energy is relatively small. We estimated

|         |         |         |         |         |         |         |
|---------|---------|---------|---------|---------|---------|---------|
| x (GeV) | 0       | 1.05282 | 1.41762 | 1.89408 | 2.38637 | 2.88095 |
| y (GeV) | 0       | 1.5788  | 2.1649  | 2.9304  | 3.6923  | 4.4445  |
| x (GeV) | 3.37431 | 5.07854 | 10.6784 | 15.931  | 25.6898 | 50      |
| y (GeV) | 5.1995  | 7.8079  | 16.296  | 24.104  | 38.788  | 75.662  |

Table 5.3: Anchor points of  $q_0$  spline function

---

<sup>2</sup>Functions defined by connecting anchor points by straight lines.

the energy leakage by simulating electrons-initiated showers with various energy and angle, and estimated that 0.8% of electron energy is leaked. Next, we compared the simulation with the data in order to check if there is any difference between data and simulation. We selected a sub-sample of neutrino-electron elastic scattering ( $\nu + e$ ) events and measured the available energy distribution. Since the hadronic energy is 0 for  $\nu + e$  events by definition, this measurement is an in-situ measurement of EM shower energy leakage. This sub-sample is selected by adding two more cuts that MINERvA  $\nu + e$  analysis[100] used in addition to the selection cuts employed by this analysis:

1.  $Q_{QE}^2 < 0.02 \text{ GeV}^2$
2.  $E_e \theta_e^2 < 0.0032 \text{ GeV}$

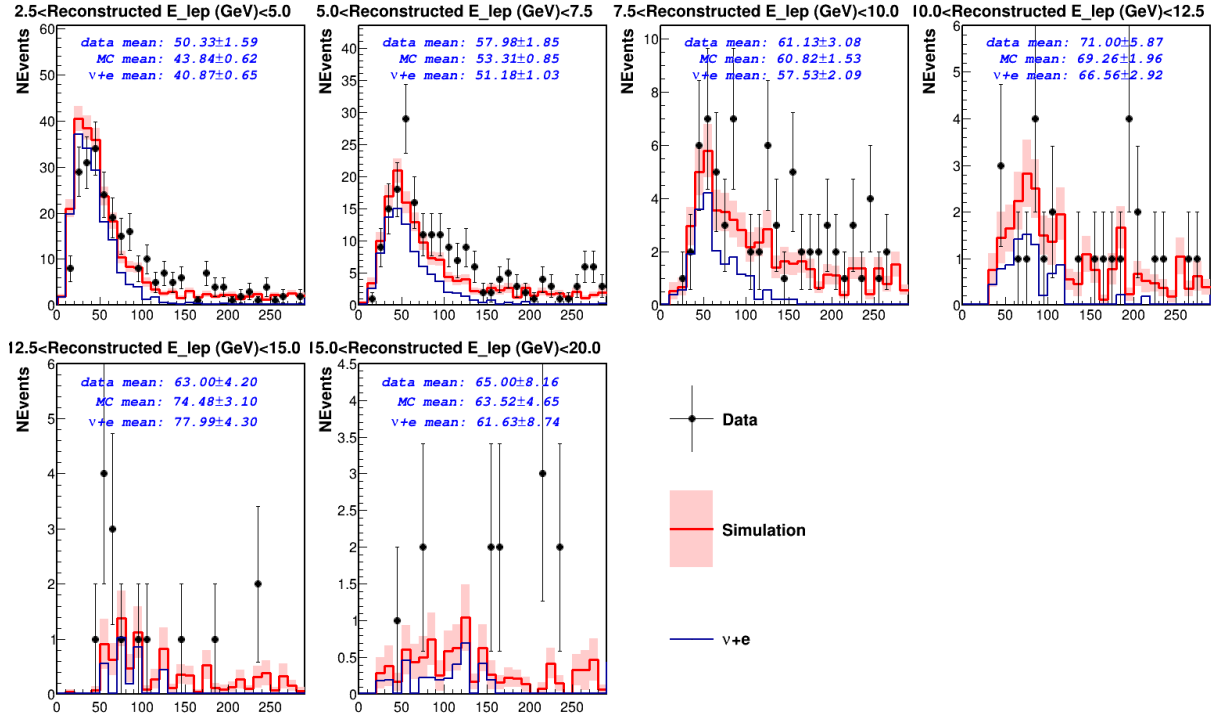


Figure 5.1: Available energy distribution sliced by lepton energy of  $\nu + e$  sub-sample. Data shows the simulation under-predicted the energy leakage of EM showers.

where  $Q_{QE}^2$  is calculated based on CCQE assumption using lepton kinematics alone:

$$\begin{aligned} E_\nu^{QE} &= \frac{M_n E_e - m_e^2/2}{m_n - E_n + p_e \cos(\theta_e)} \\ Q_{QE}^2 &= 2m_n(E_\nu^{QE} - E_e) \end{aligned} \tag{54}$$

The result is plotted in figure 5.1. We concluded the simulation underestimates the energy leakage by  $5 \pm 2$  MeV based on the two top-left plots, since the other energy regions are statistically limited.

Finally, the estimated EM shower energy leakage is removed from available energy, as described in equation 50.

### 5.3.5 Selected Data and MC Samples

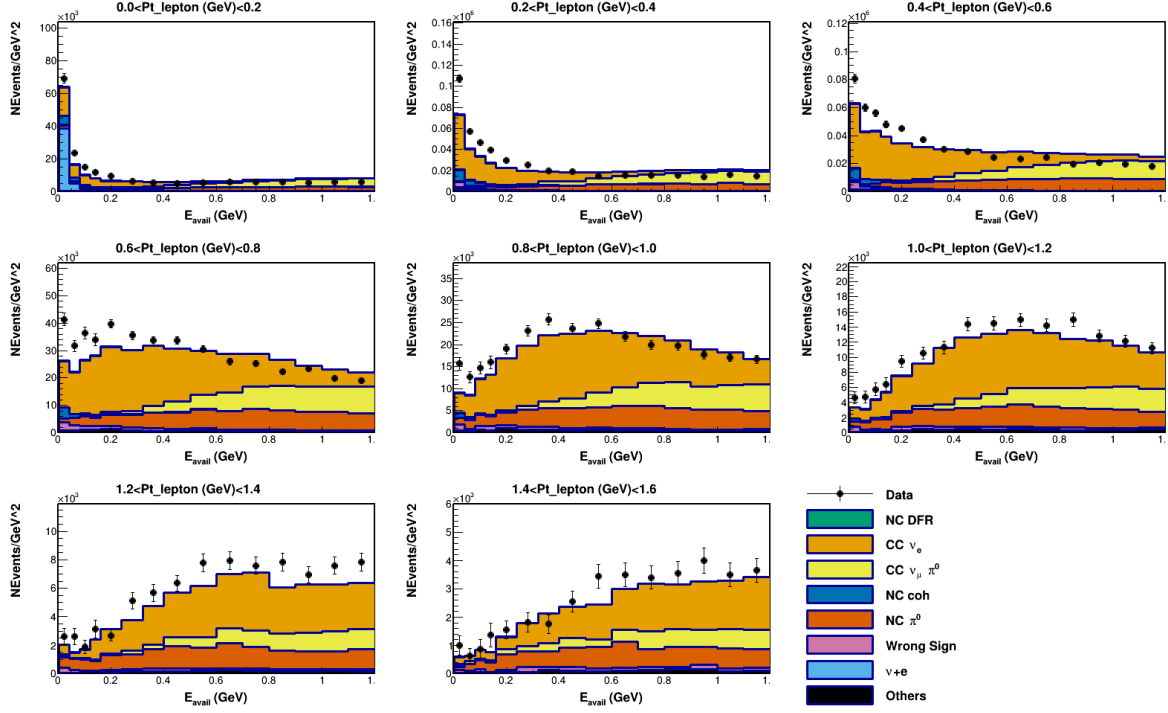
The selected data and MC sample are shown as sliced histograms, as a function of available energy and lepton transverse momentum, or available energy and three momentum transfer in figure 5.2. The MC sample includes the aforementioned generic MC sample<sup>3</sup>, NC diffractive sample, and 2p2h processes sample, normalized to data POT. The data sample is shown as points with statistical uncertainties, while the MC sample is shown as stacked histograms.

The categories used in stacked histograms are defined as follows:

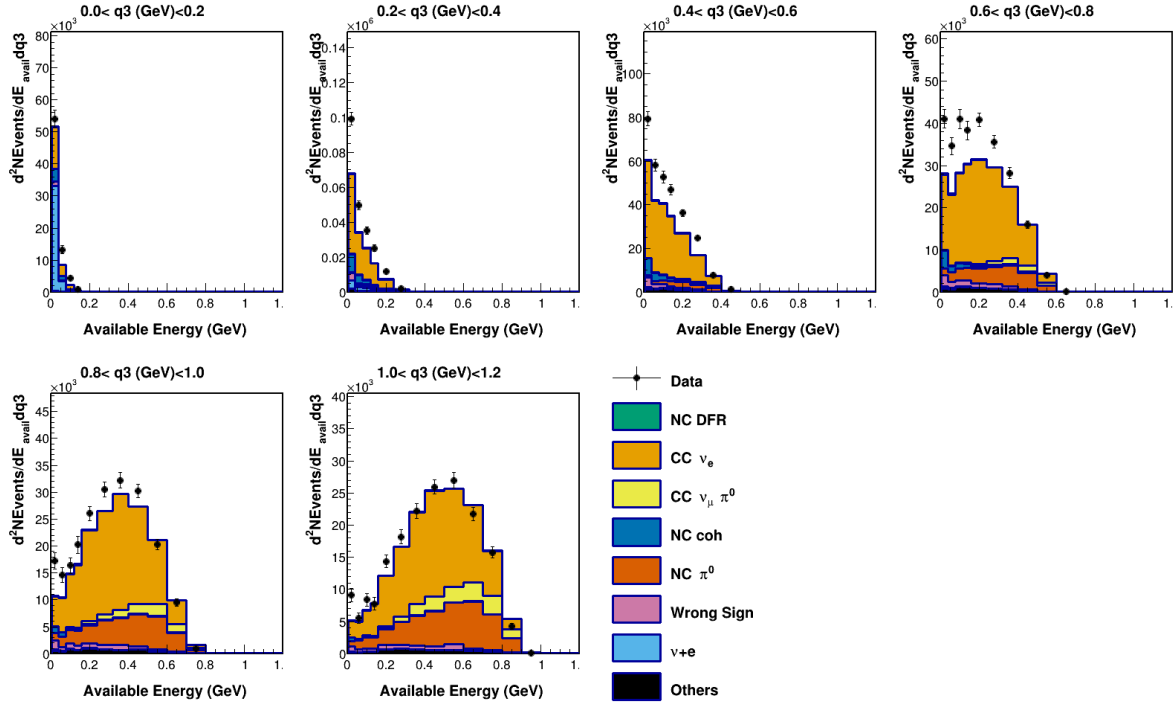
- NC DFR: neutral-current diffractive production of  $\pi^0$  off the proton.
- CC  $\nu_e$ : the signal processes as defined in section 5.1.
- CC  $\nu_\mu \pi^0$ : charged-current  $\nu_\mu$  scattering events that produced a final state  $\pi^0$ .
- NC coh: neutral-current coherent production of  $\pi^0$ .
- NC  $\pi^0$ : neutral-current non-coherent production of  $\pi^0$ .
- Wrong sign:  $\bar{\nu}_e$  scattering events. MINERvA is not magnetized, hence not able to distinguish electron from positron.
- $\nu+e$ : neutrino electron elastic scattering events.

---

<sup>3</sup>Without 2p2h components



(a) Selected sample in  $E_{avail} - P_{lep}^t$  space



(b) Selected sample in  $E_{avail} - q_3$  space

Figure 5.2: Selected sample distributions



- Others: any events that passed selection cuts but not one of the aforementioned types of events. The majority of them are  $\nu_e$  scattering events failed fiducial volume or kinematics requirements.

The sample shows that the background contribution is relatively small, dominated by misidentified  $\pi^0$ s, either from NC or CC interactions. There are significant contribution from neutrino-electron elastic scatterings in the lowest available energy bin. The simulation describe the  $P_T$  distribution of data relatively well, but not the available energy shape. The simulation under-predicted data in low available energy region and over-predicted in the high available energy region. The  $Q_3$  distribution tells a similar story that data favors more low-recoil events. This is not a surprise because the data of hadronic system is limited compared to the lepton kinematics.

## 5.4 Background Constraint

The background prediction provided by simulation is not trustworthy most of the time, because they are neutrino interactions too. The background constraint is a technique to make better background predictions by making measurements of background processes using data in regions that are background rich and adjacent to the sample region (sideband regions). The data MC discrepancies in sideband regions are usually corrected by fitting a set of scale factors, which modify the normalization and/or shape of background processes. These scale factors are applied to the background prediction in the signal region, resulting in a more accurate prediction. In addition to the data in sideband regions, this analysis also uses RHC data from a companion study in order to better constrain some subdominant backgrounds. The companion study is a CC  $\bar{\nu}_e$  cross section measurement using the RHC sample, done by Sarah Henry.

The vast majority of background events in this analysis are  $\pi^0$  productions events, as a result of photons misidentified as electrons, seconded by  $\nu + e$  events and CC  $\bar{\nu}_e$  scattering (wrong sign) events. The  $\pi^0$  background is constrained using sideband data and RHC data, discussed in section 5.4.1, while the wrong sign background is constrained by RHC data

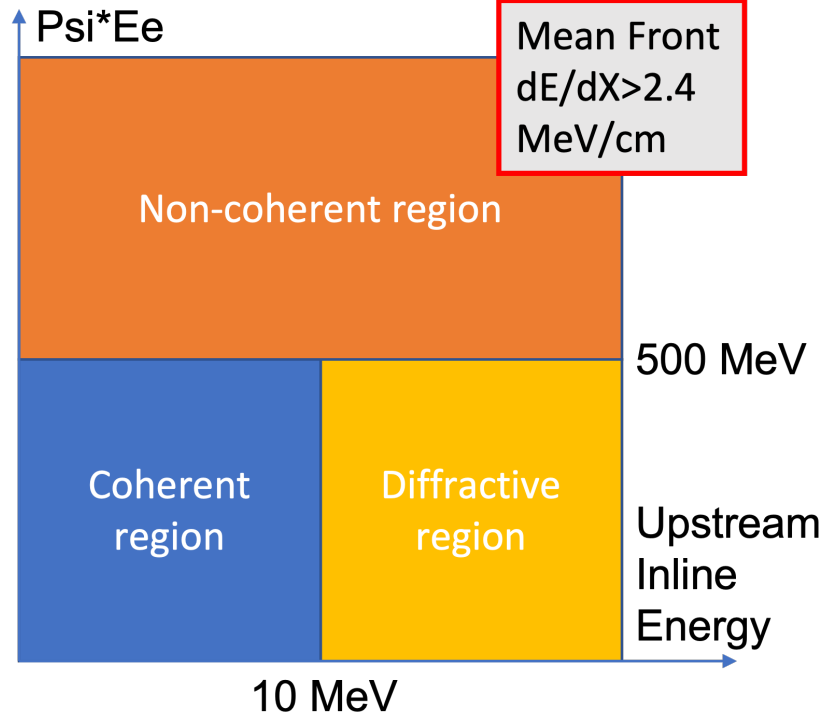


Figure 5.3: Illustration of sideband definition. The entire region requires front  $dE/dX$  greater than  $2.4 \text{ MeV/cm}$ , hence not included in the selected sample.

alone, discussed in section 5.4.2. On the other hand,  $\nu + e$  events are not further constrained in this analysis because this lepton-lepton interaction is well understood and constrained by flux reweighting.

#### 5.4.1 $\pi^0$ Background Constraint with Sideband

The data in high front  $dE/dX$  region, which consists of events failed and only failed the front  $dE/dX$  cut among all sample selection cuts, are chosen to constrain  $\pi^0$  background. Furthermore, the high front  $dE/dX$  region are subdivided into three regions using to separate 4 different  $\pi^0$  production channel. Two variables are used to separate these three regions: upstream inline energy  $E_{uie}$  and extra energy  $\Psi E_{EM}$ , where  $\Psi$  is an ancillary variable defined

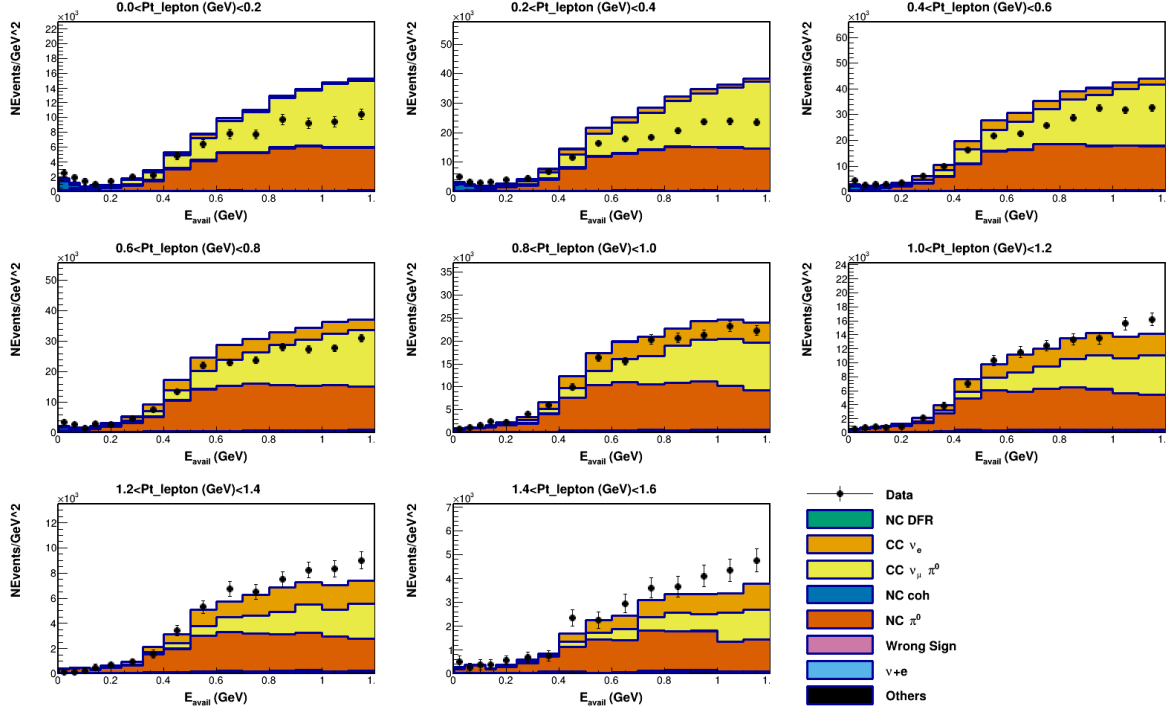
by the visible energy ratio of non-electron clusters and electron clusters:

$$\Psi = \frac{E_{extra} + E_{uie}}{E_{vis}} \quad (55)$$

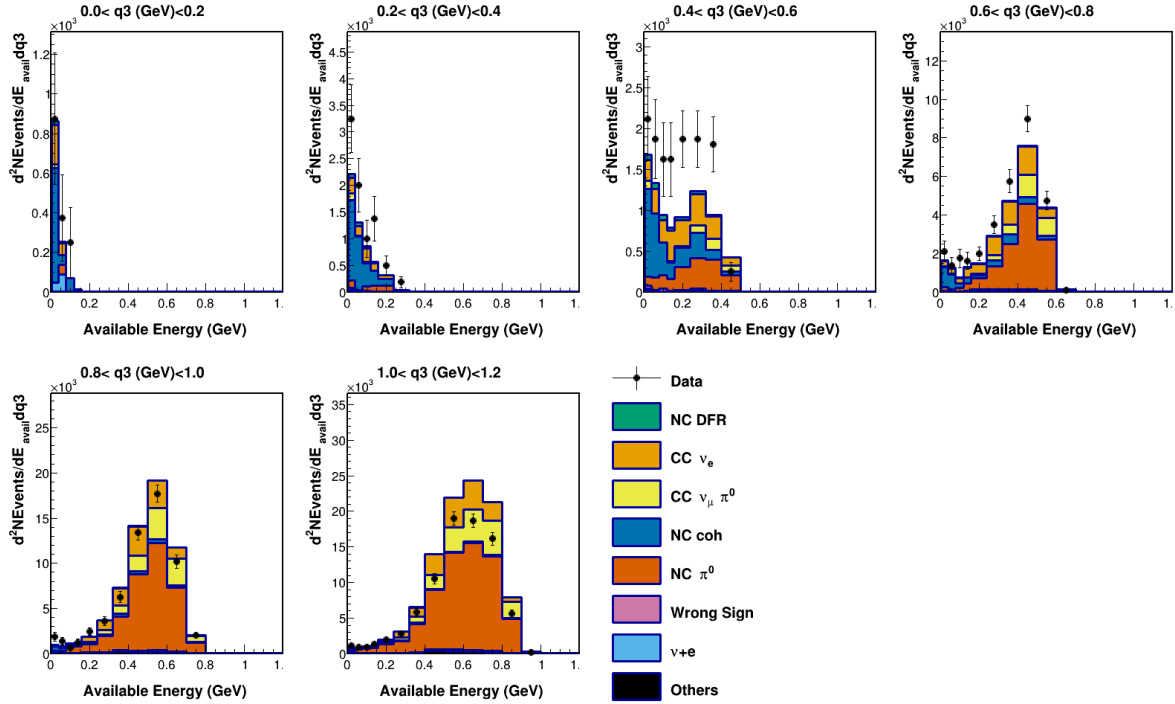
$E_{uie}$ ,  $E_{extra}$ , and  $E_{vis}$  are defined in section 4.3.2 and  $E_{EM}$  is defined in section 4.2.3. The division of sideband regions is listed and illustrated in figure 5.3:

- Non-coherent region, defined by  $\Psi E_{EM} > 500 MeV$ , targets to constrain NC and CC non-coherent  $\pi^0$  production.
- Coherent region, defined by  $\Psi E_{EM} < 500 MeV$  and  $E_{uie} < 10 MeV$ , targets to constrain NC coherent  $\pi^0$  production from carbon target.
- Diffractive region, defined by  $\Psi E_{EM} < 500 MeV$  and  $E_{uie} > 10 MeV$ , target to constrain NC diffractive  $\pi^0$  production.

The data and simulated sideband sample distributions are plotted in figure 5.4- 5.6, and the result supports the statement we made above: the simulation doesn't predict the data in background rich regions. The non-coherent  $\pi^0$  region is over-predicted while the coherent and diffractive regions are under-predicted. We concluded the discrepancy in the non-coherent region is due to mismodeling of NC and CC non-coherent  $\pi^0$  productions, and decided to apply scale factors to non-coherent  $\pi^0$  production as a function of  $P_{lep}^t$  to correct the discrepancy. However, it is hard to address the data excess in diffractive and coherent regions using the FHC sample because of the non-coherent contribution in the sideband samples. Luckily, MINERvA has a RHC sample that is more suitable for the constraint because it features less non-coherent contributions. An extensive study was done by Sarah Henry using the RHC sample and briefed in appendix C. The conclusion is that the excess is due to mismodeling of NC coherent and NC diffractive  $\pi^0$  productions (which leads to the division of sideband regions as well). The study also leads to the decision that the data/MC discrepancy in both FHC and RHC samples should be corrected by applying a single set of scale factors to coherent and diffractive  $\pi^0$  contributions as function of  $E_{EM}$ , extracted from RHC sample.

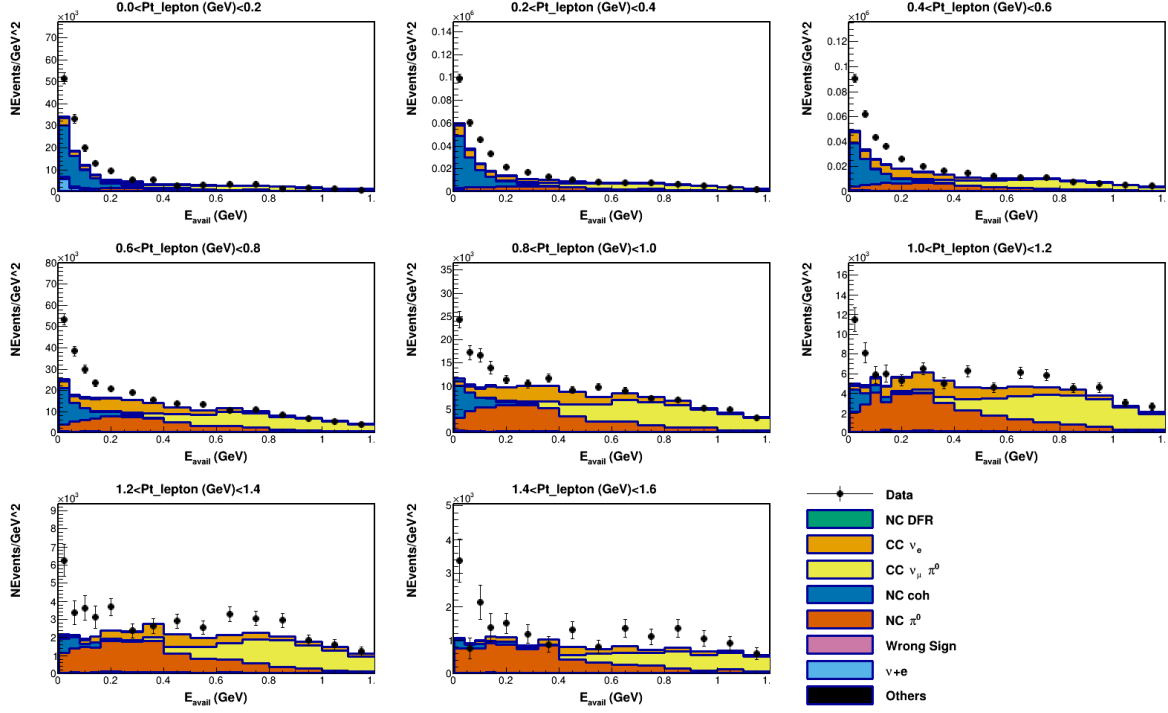


(a) Non-coherent sideband in  $E_{avail} - P_{lep}^t$  space

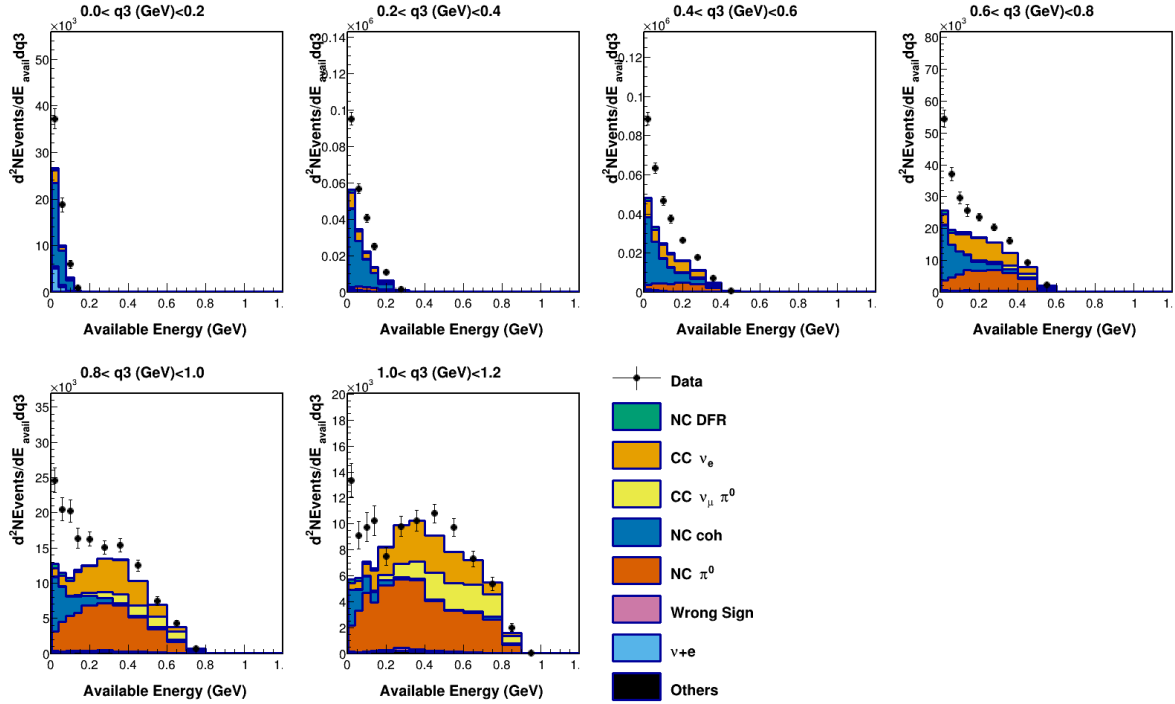


(b) Non-coherent sideband in  $E_{avail} - q_3$  space

Figure 5.4: Non-coherent sideband sample distributions before constraint

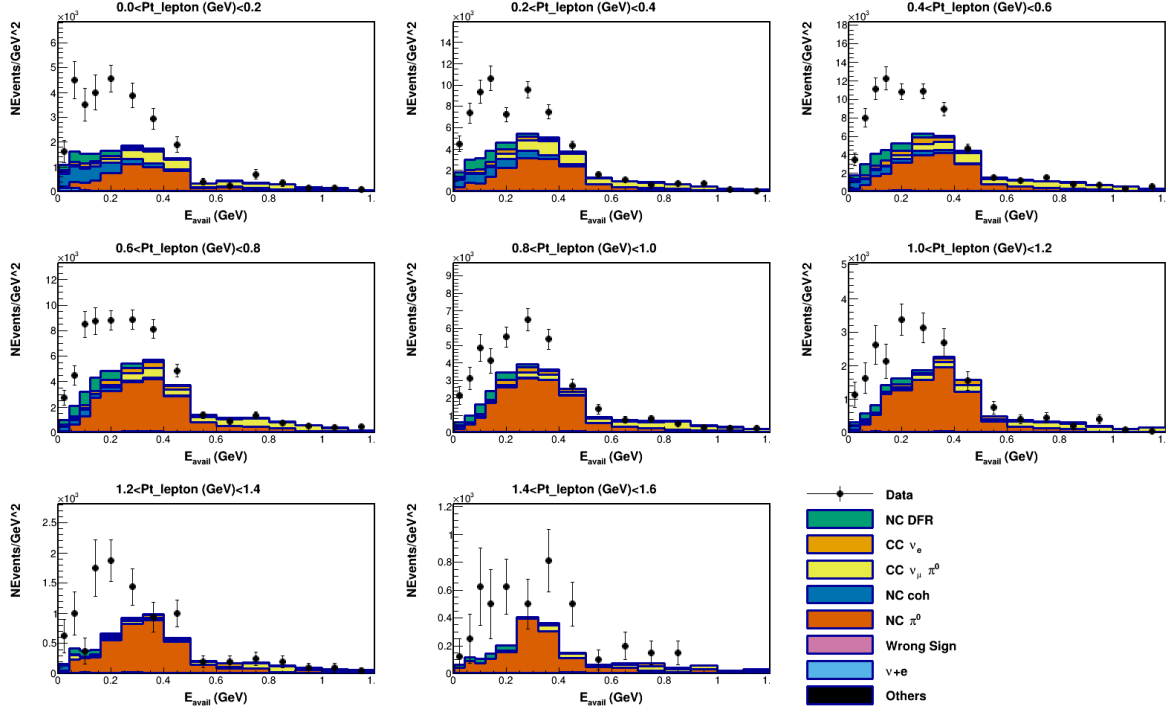


(a) Coherent sideband in  $E_{avail} - P_{lep}^t$  space

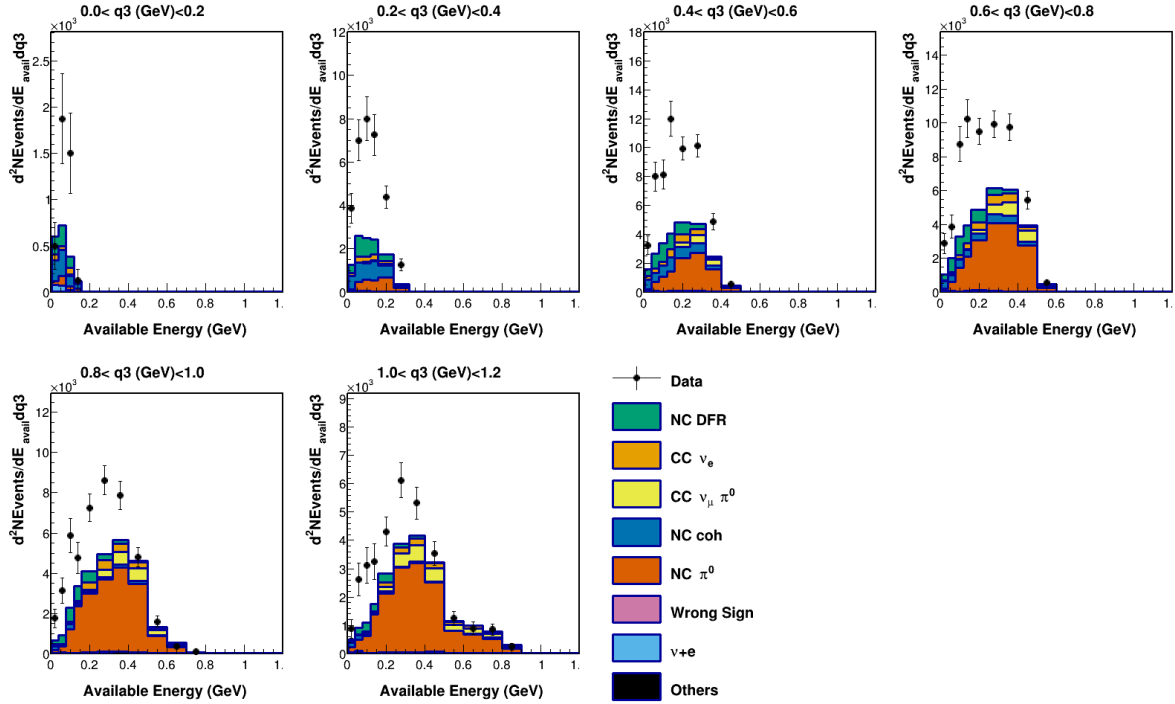


(b) Coherent sideband in  $E_{avail} - q_3$  space

Figure 5.5: Coherent sideband sample distributions before constraint



(a) Diffraction sideband in  $E_{avail} - P_{lep}^t$  space



(b) Diffraction sideband in  $E_{avail} - q_3$  space

Figure 5.6: Diffraction sideband sample distributions before constraint

The scale factors are extracted by minimizing regulated negative log-likelihood assuming Poisson distribution:

$$-\log \mathcal{L}(\alpha_j) = \sum_i (-N_i^{data} \log(N_i^{pred}(\alpha_j)) + N_i^{pred}(\alpha_j)) + \sum_j \lambda(\alpha_j - 1)^2 \quad (56)$$

where  $N_i^{data}$  is the measured data event rate in bin  $i$ ,  $\alpha_j$  are the scale factors,  $N_i^{pred}(\alpha_j)$  is the scaled predicted event rate in bin  $i$ , and  $\lambda$  is regulating parameter, which is set to  $0.01^4$ . Data in both signal and sideband regions are used in minimization to provide a joint-fit because all processes have sizable contributions in more than one regions. In addition, the minimization has to be conducted in two steps because of the scale factors depends on two variables: the scale factors for coherent and diffractive  $\pi^0$  processes first and then the scale factors for non-coherent  $\pi^0$  production. The first step uses RHC data in  $\Psi E_{EM}$  and  $E_{EM}$  bins, and floats scale factors for coherent and diffractive  $\pi^0$  as well as normalization of signal and non-coherent  $\pi^0$  processes. The background predictions of coherent and diffractive processes are updated before the second step by applying scale factors event-by-event, such that the correlation of  $E_{EM}$  and other variables are preserved. The second step uses FHC data in  $E_{avail}$  and  $P_{lep}^t$  bins, and floats scale factors for non-coherent  $\pi^0$  and normalization of signal processes. Again, the scale factors of non-coherent  $\pi^0$  are applied event-by-event to make the final background prediction.

| $E_{EM}$ (GeV)      | [2.5,5) | [5,7.5) | [7.5,10) | [10,12.5) | [12.5,15) | [15,20) |
|---------------------|---------|---------|----------|-----------|-----------|---------|
| Diffractive $\pi^0$ | 3.385   | 7.413   | 9.535    | 15.95     | 23.21     | 9.807   |
| Coherent $\pi^0$    | 1.970   | 2.258   | 2.936    | 2.614     | 2.018     | 5.363   |

| $P_{lep}^t$ (GeV)    | [0,0.2) | [0.2,0.4) | [0.4,0.6) | [0.6,0.8) | [0.8,1.0) | [1.0,1.2) | [1.2,1.6) |
|----------------------|---------|-----------|-----------|-----------|-----------|-----------|-----------|
| Non-coherent $\pi^0$ | 0.6897  | 0.6945    | 0.7659    | 0.8151    | 0.9229    | 1.014     | 1.151     |

Table 5.4: Scale factors applied to  $\pi^0$  production processes

<sup>4</sup>The regulating term is negligible unless simulation predicts 0 events in certain region.

The applied scale factors are listed in table 5.4 and the constrained background distributions are showed in section 5.4.3. There is a residual data MC discrepancy in diffractive rich region for  $0.2 \text{ GeV} < E_{avail} < 0.5 \text{ GeV}$ , and there are two possible explanations for this:

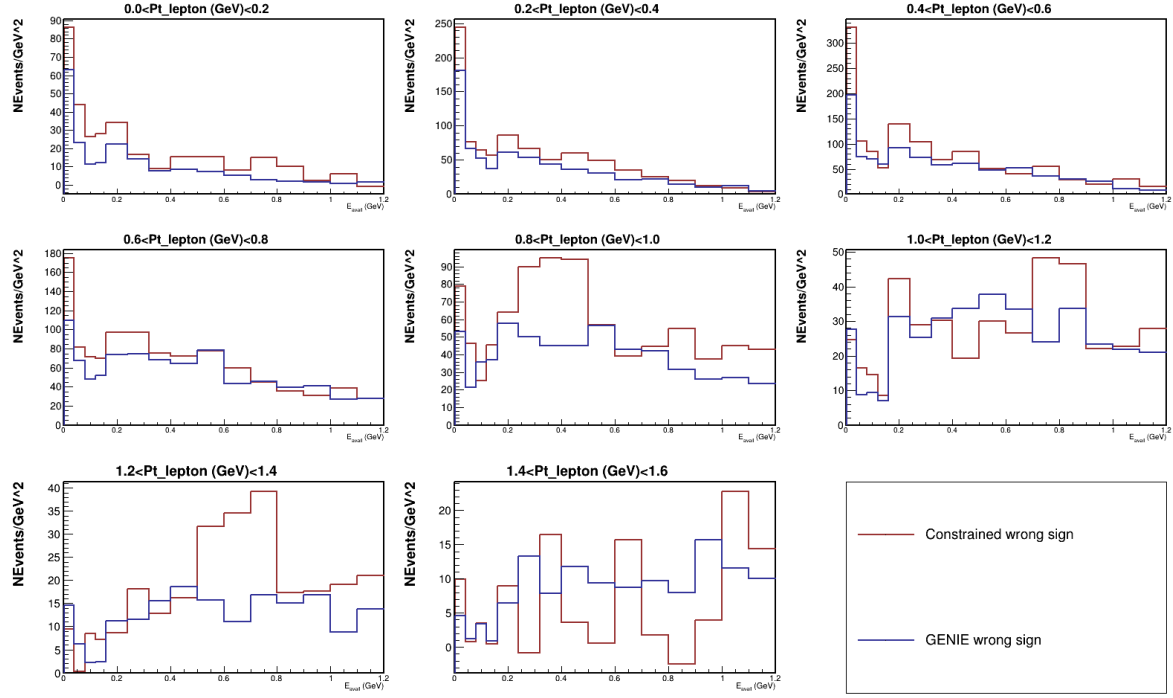
- The modified diffractive model is not identical in FHC and RHC.
- The non-coherent  $\pi^0$  contribution is wrong, a subset of this process has to be enhanced by a factor of  $\sim 2$ .

Neither of them is satisfying: the first is disfavored because they are the same processes with subtle flux difference, while the second is not supported by data in non-coherent sideband. As a result, we decided to add a systematical uncertainty to quantify the effect of this tension by two alternative background constraint methods, detailed in section 5.8.4.

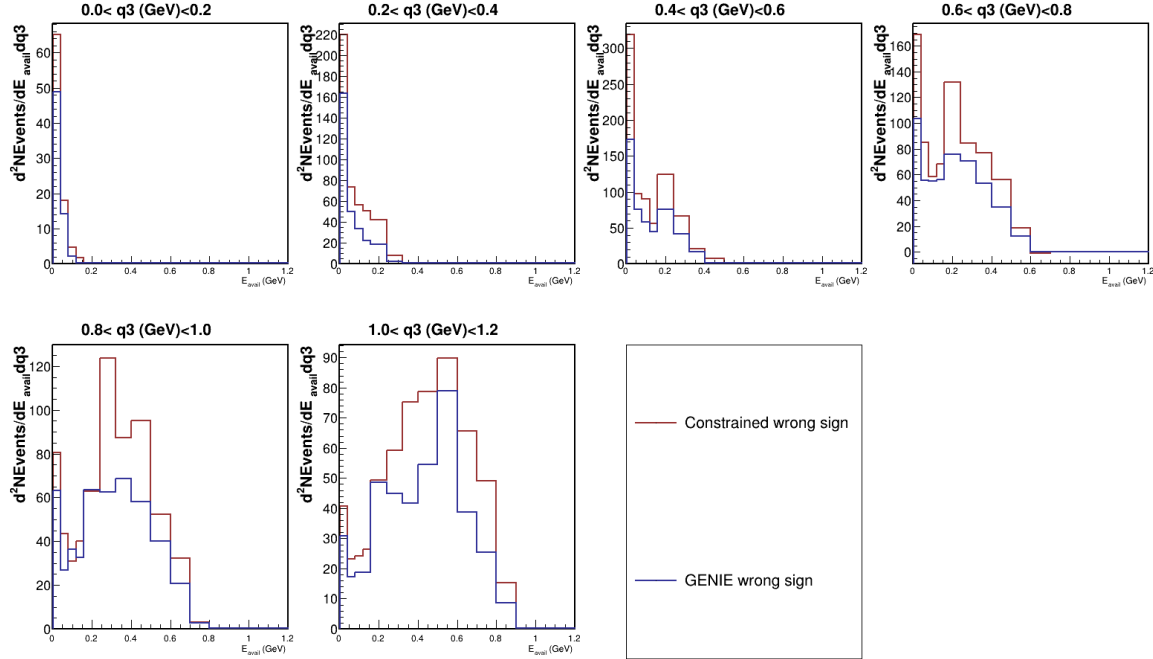
#### 5.4.2 Wrong Sign Background Constraint

Since the MINERvA detector can't distinguish an electron from a positron, the only way to constrain the wrong sign background is by the RHC sample. Sarah Henry developed and validated an iterative procedure to make an FHC (RHC) wrong sign prediction by RHC (FHC) sample, which takes flux difference into account. Using  $\nu_e$  prediction in RHC sample as an example, there are four steps to get a constrained  $\nu_e$  prediction in the RHC sample starting from a  $\bar{n}u_e$  prediction in the FHC sample. First, start with the  $\bar{\nu}_e$  prediction and constrain  $\pi^0$  backgrounds as described by section 5.4.1. Second, find the ratio of simulated neutrino energy for selected  $\nu_e$  events between RHC and FHC samples. Third, weight data and simulated events by the RHC/FHC ratio according to reconstructed neutrino energy. As a result, the weighted distribution approximates the event rates measured in RHC flux. Finally, the  $\nu_e$  prediction in the RHC sample is given by subtracting backgrounds ( $\pi^0$ ,  $\bar{\nu}_e$  and others) from data. The  $\bar{\nu}_e$  prediction in FHC sample can be then made by following the same procedure with the new  $\nu_e$  prediction in RHC and the procedure can be repeated until the predictions converge. The final wrong sign prediction used in this analysis is shown in figure 5.7 and compared to the unconstrained prediction.





(a) Wrong sign prediction in  $E_{avail} - P_{lep}^t$  space



(b) Wrong sign prediction in  $E_{avail} - q_3$  space

Figure 5.7: Wrong sign prediction in signal region

### 5.4.3 Constrained Background Predictions

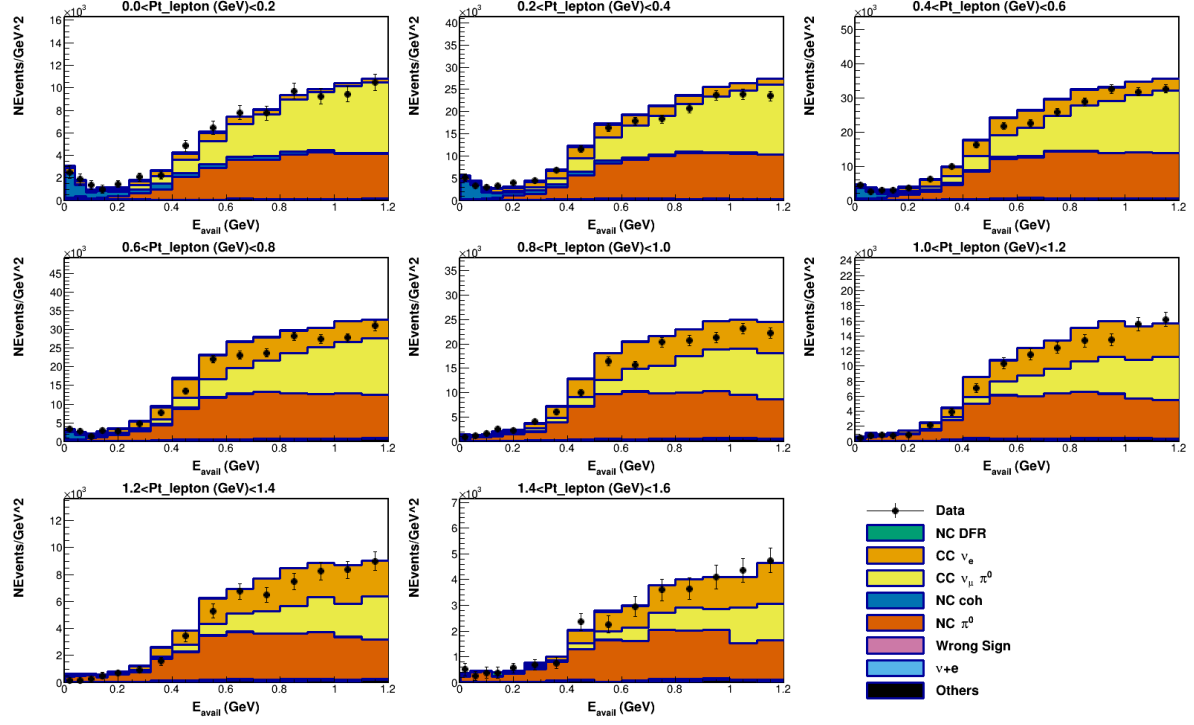
The constrained MC predictions are plotted in figure 5.8- 5.11. Notice that the signal contributions in these plots are scaled by a factor of 1.157 as a result of floating signal normalization in the constraining procedure. This scale factor is discarded in the following cross section extraction.

## 5.5 Unfolding

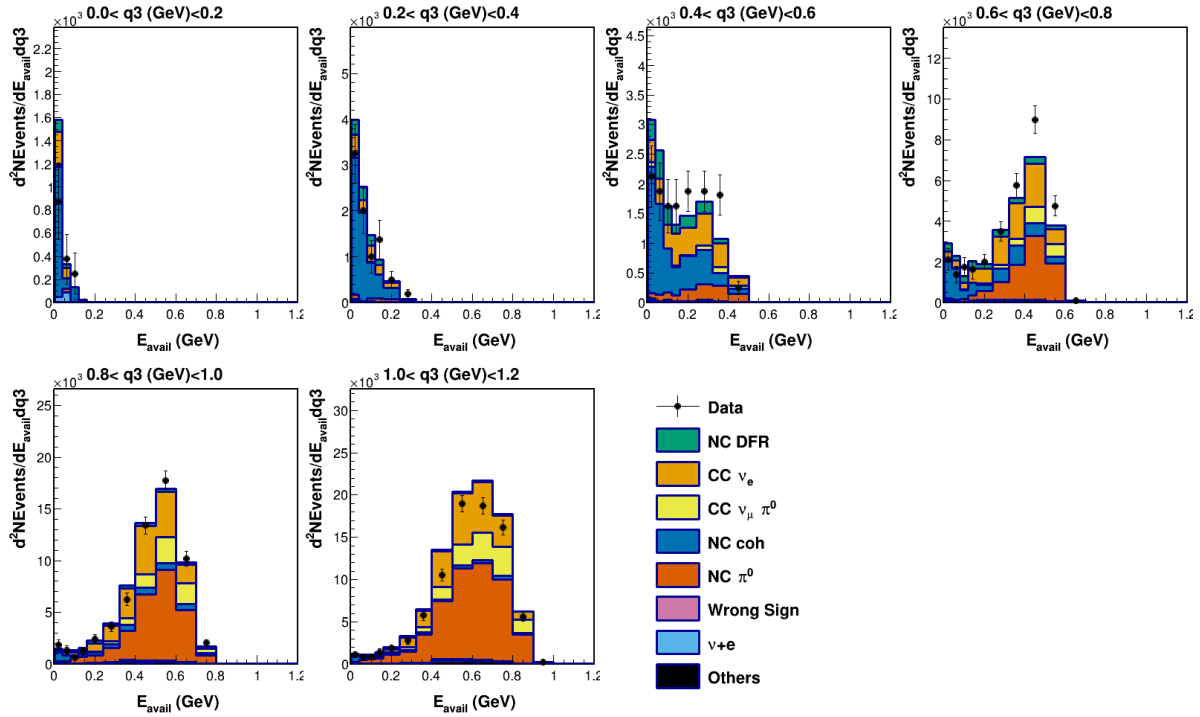
The measurement of the physical variables are usually smeared and shifted from the true value, because of detector limitation and the stochastic nature of underlining physics processes. It would make cross experiment comparisons hard if we leave it alone, since different experiments have different smearing characteristics. The de-smearing procedure is called unfolding, and MINERvA analyses use D’Agostini unfolding[40] by conversion. D’Agostini unfolding is an iterative procedure taking 3 inputs, migration matrix, prior distribution, and measured event rate histogram (reconstructed histogram). At each iteration, the estimated true event rate is given by:

$$\begin{aligned}
 n(C_i) &= \sum_j M_{ij} n(E_j) = \sum_j M_{ij} (N_j^{data} - N_j^{bkg}) \\
 M_{ij} &= \frac{P(E_j|C_i)P_0(C_i)}{\sum_l P(E_j|C_l)P_0(C_l)} \\
 P_0^{next}(C_i) &= \frac{n(C_i)}{\sum_i n(C_i)}
 \end{aligned} \tag{57}$$

where  $n(C_i)$  is event rate in true kinematic bins,  $n(E_j)$  is estimated signal event rate in reconstructed bins,  $P(E_j|C_i)$  is probability of a event in true bin  $i$  being reconstructed in bin  $j$  (a.k.a. migration matrix), and  $P_0(C_i)(P_0^{next}(C_i))$  is the prior distribution of true kinematics at current (next) iteration. The number of iterations serves as a regulation parameter, controlling the bias-variance trade-off: each additional iteration reduces the bias (less sensitive to prior distribution) but increases the variance (more sensitive to measured distribution).

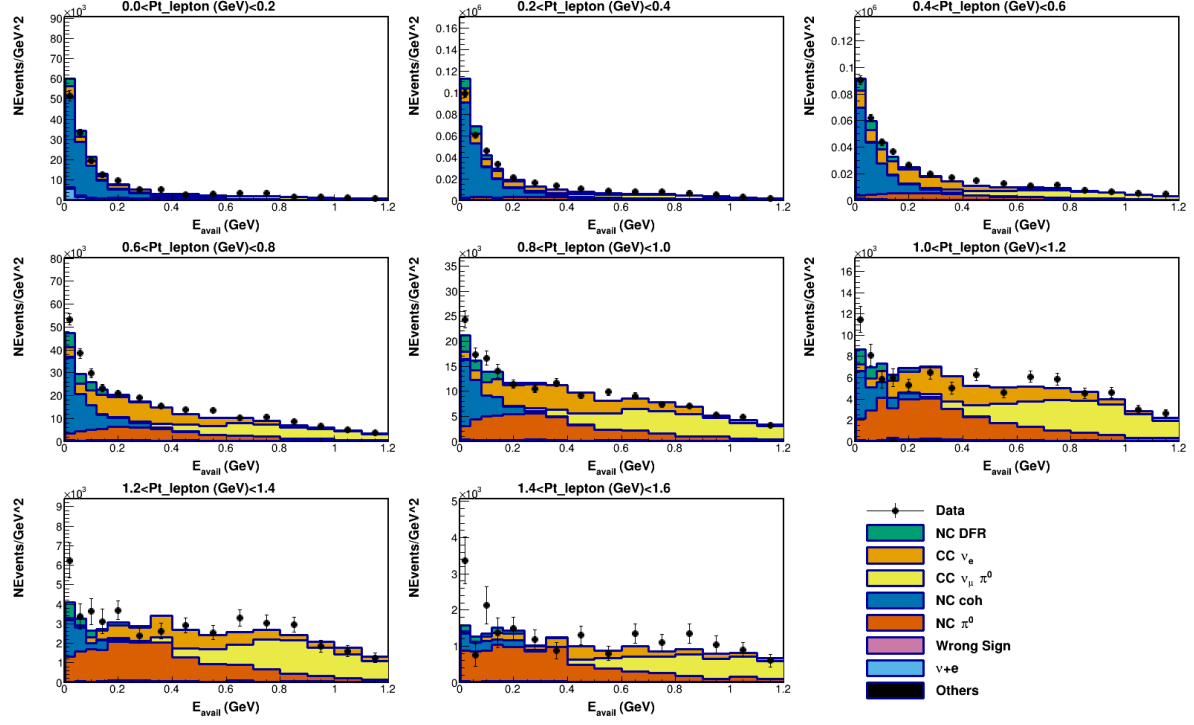


(a) Non-coherent sideband in  $E_{avail} - P_{lep}^t$  space

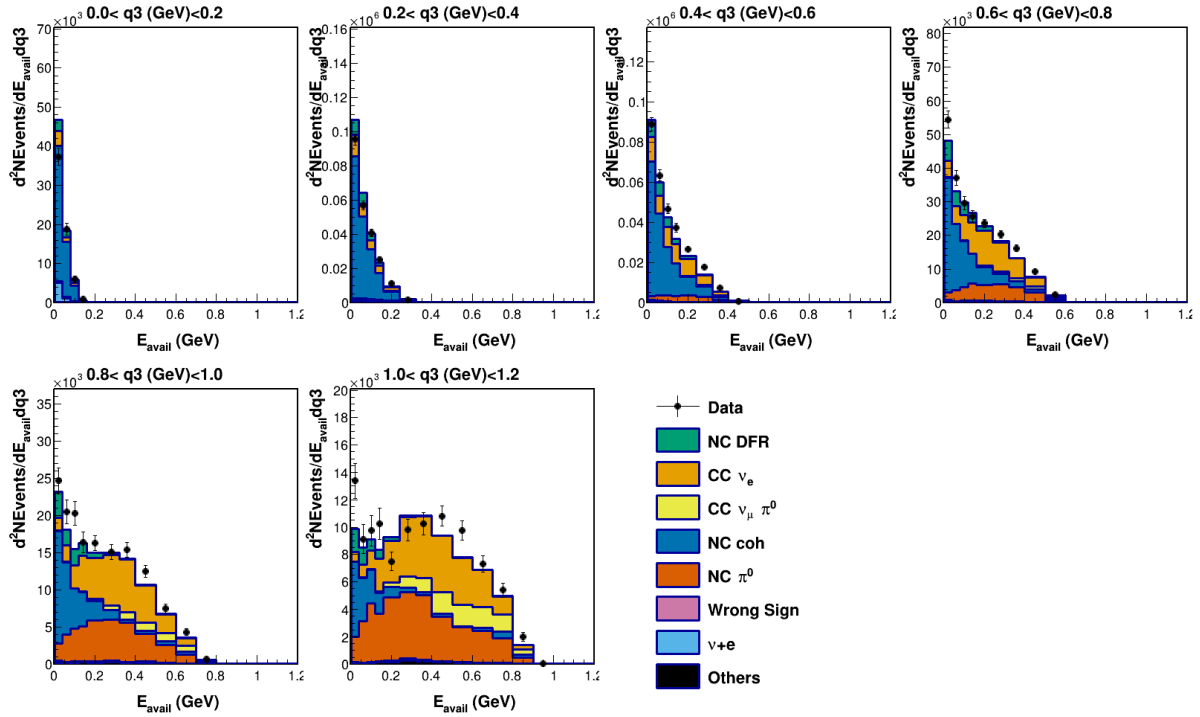


(b) Non-coherent sideband in  $E_{avail} - q_3$  space

Figure 5.8: Non-coherent sideband sample distributions after constraint

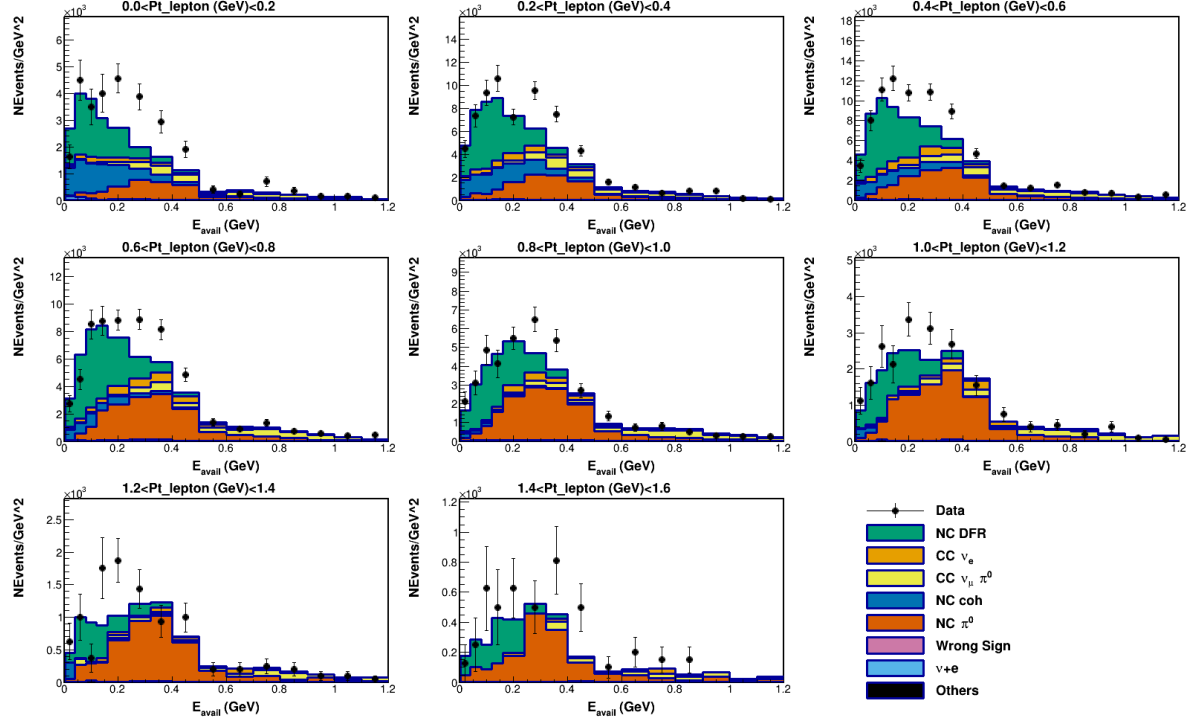


(a) Coherent sideband in  $E_{avail} - P_{lep}^t$  space

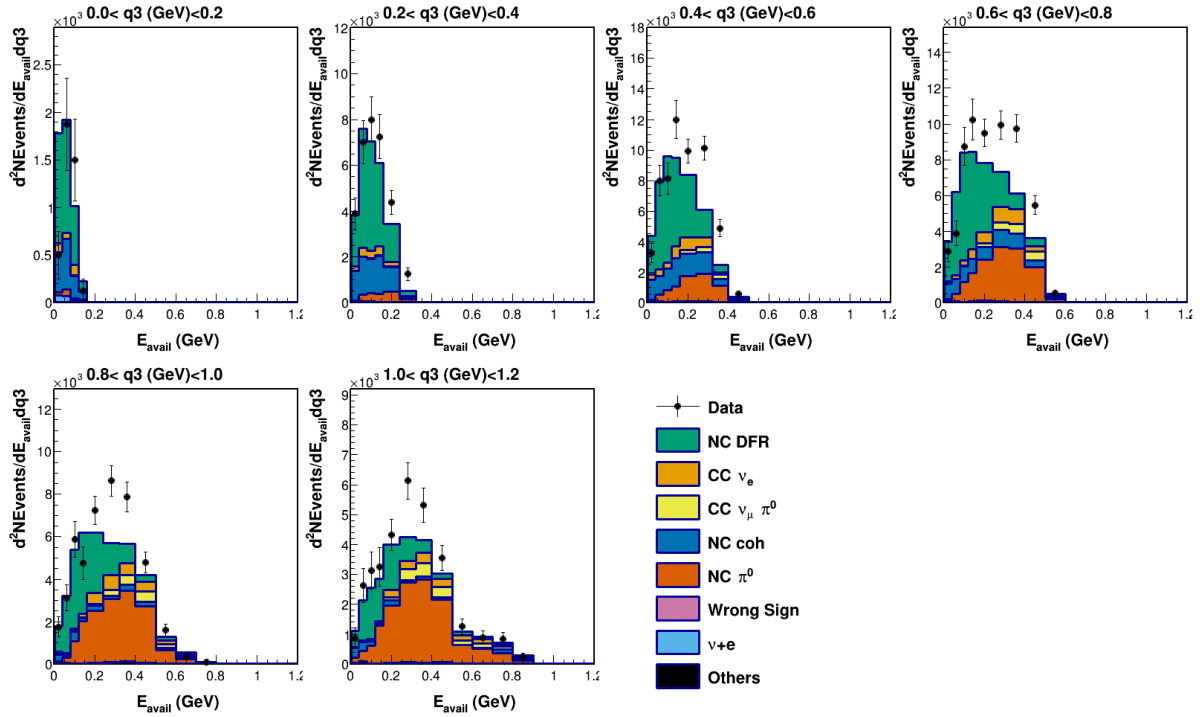


(b) Coherent sideband in  $E_{avail} - q_3$  space

Figure 5.9: Coherent sideband sample distributions after constraint

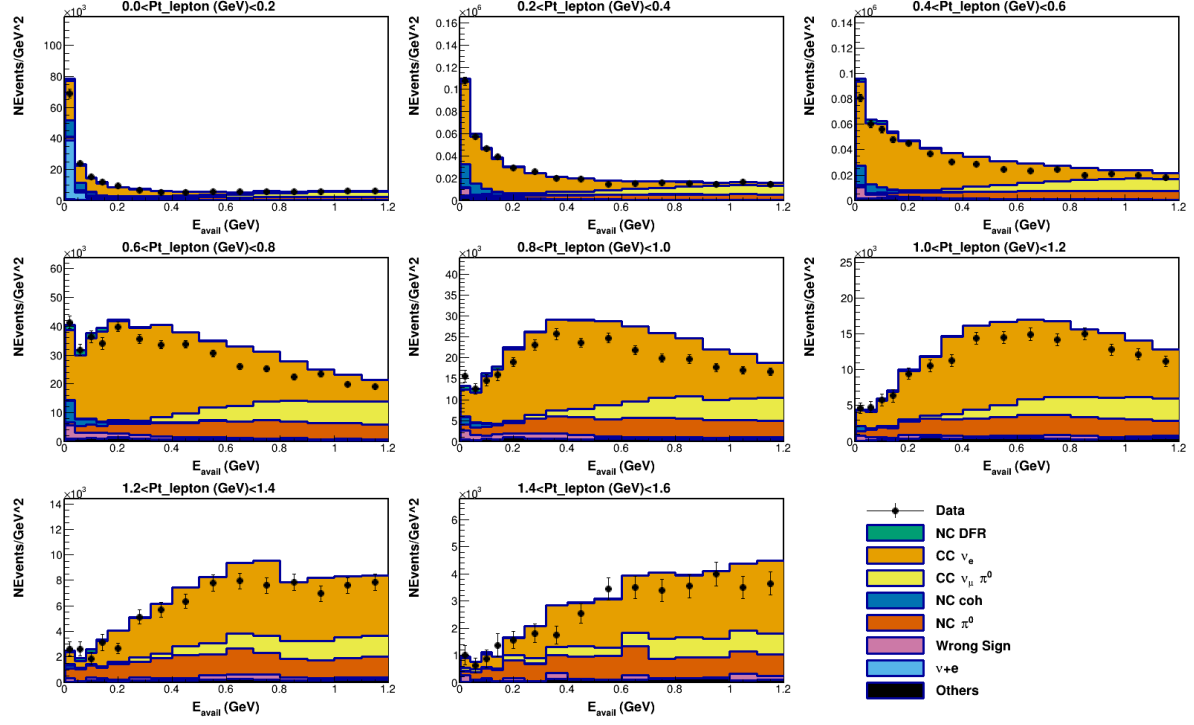


(a) Diffraction sideband in  $E_{avail} - P_{lep}^t$  space

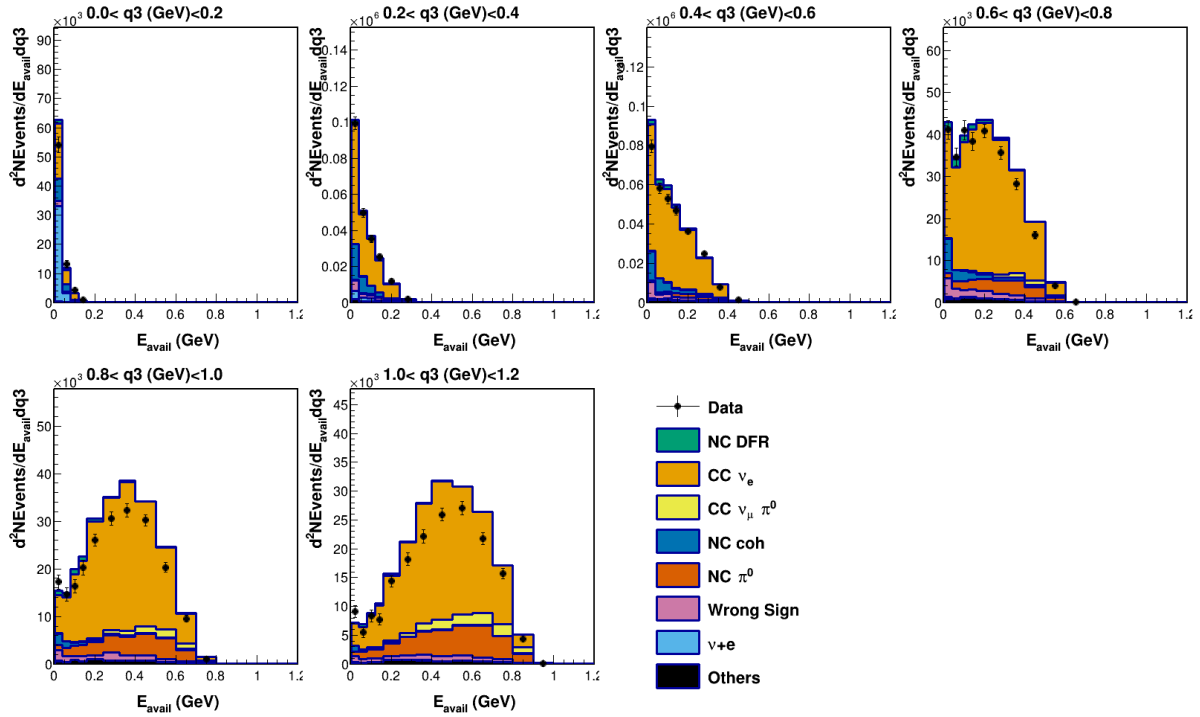


(b) Diffraction sideband in  $E_{avail} - q_3$  space

Figure 5.10: Diffraction sideband sample distributions after constraint

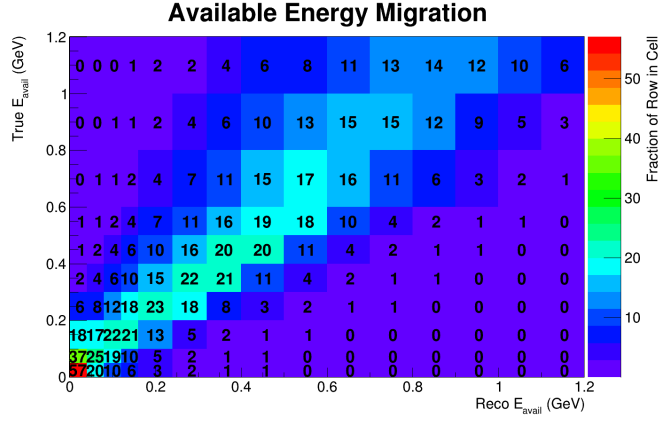


(a) Selected sample in  $E_{avail} - P_{lep}^t$  space

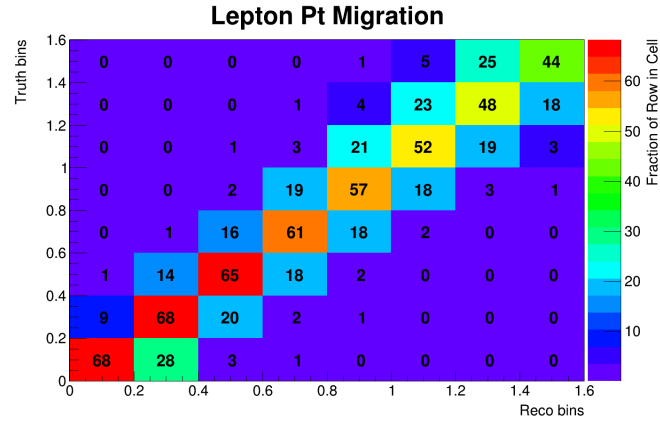


(b) Selected sample in  $E_{avail} - q_3$  space

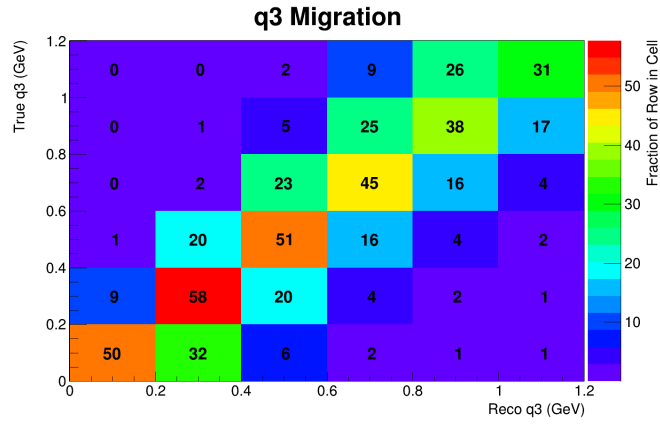
Figure 5.11: Selected sample distributions after background constraint



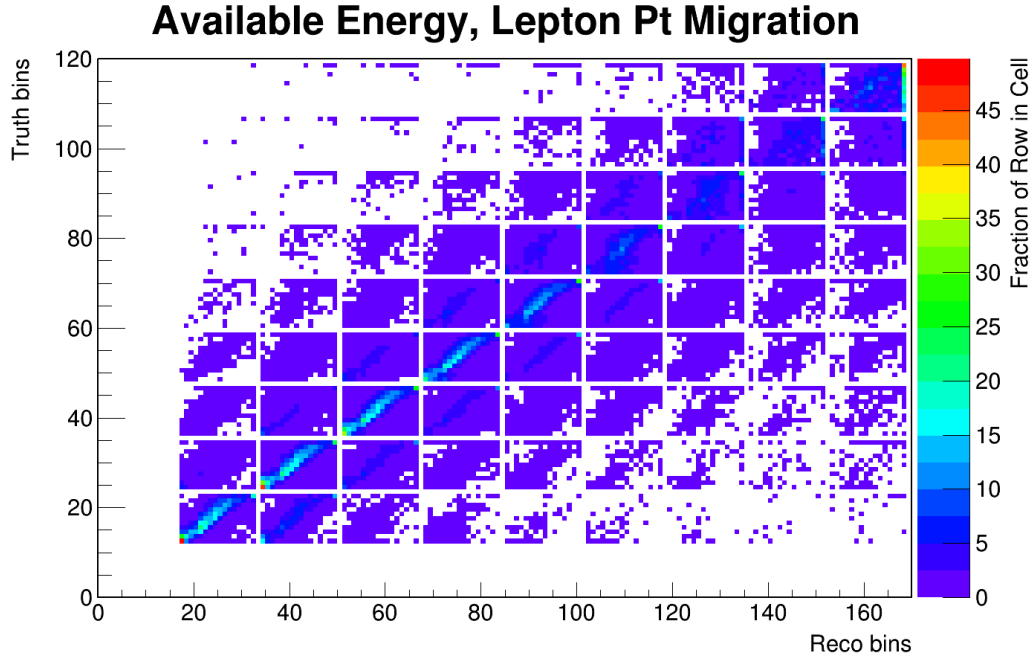
(a)  $E_{\text{avail}}$  migration



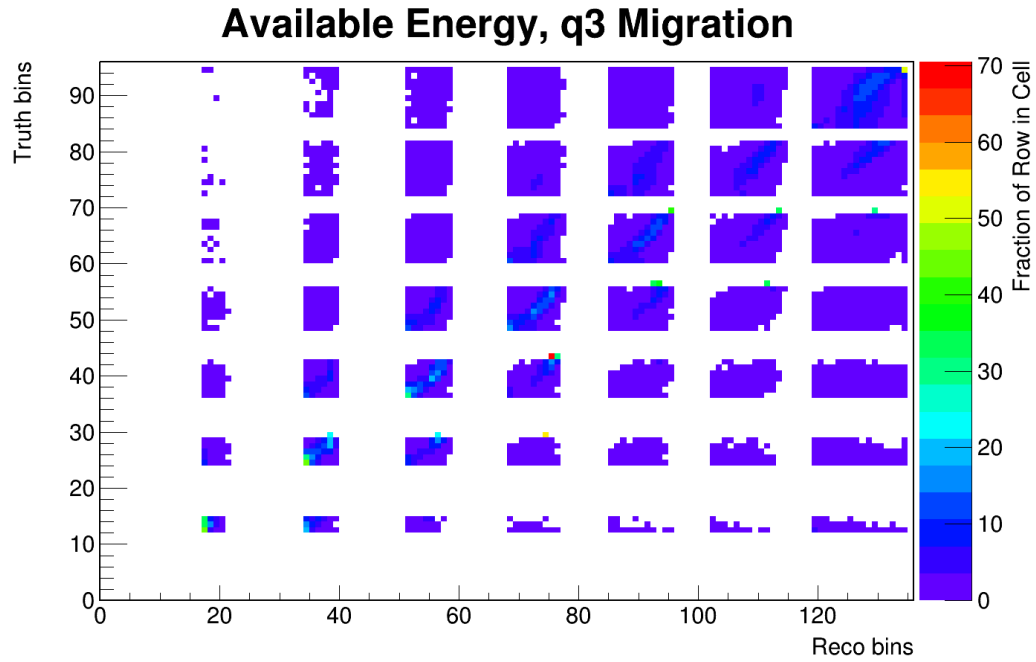
(b)  $P_{\text{lep}}^t$  migration



(c)  $q_3$  migration



(d)  $E_{avail}-P_{lep}^t$  migration in encoded bin space.



(e)  $E_{avail}-q_3$  migration in encoded bin space.

Figure 5.12: Migration matrices



The migration matrices are estimated using the  $\sim 42 \times$  POT  $nu_e$  scattering simulation sample in order to estimate the migration matrix with adequate statistics, plotted in figure 5.12. The prior distribution is simply chosen to be the default GENIE prediction and the number of iterations is chosen to be 10 for  $E_{avail} - P_{lep}^t$  distribution and 15 for  $E_{avail} - q_3$  distribution, determined by warping tests (see Appendix B).

## 5.6 Acceptance and Target Normalization

The acceptance corrects the inefficiency of selection cuts. It is necessary for a similar reason to unfolding, that different experiments may not have the same acceptance. The acceptance is estimated using the  $\nu_e$  scattering sample, as a function of measured variables:

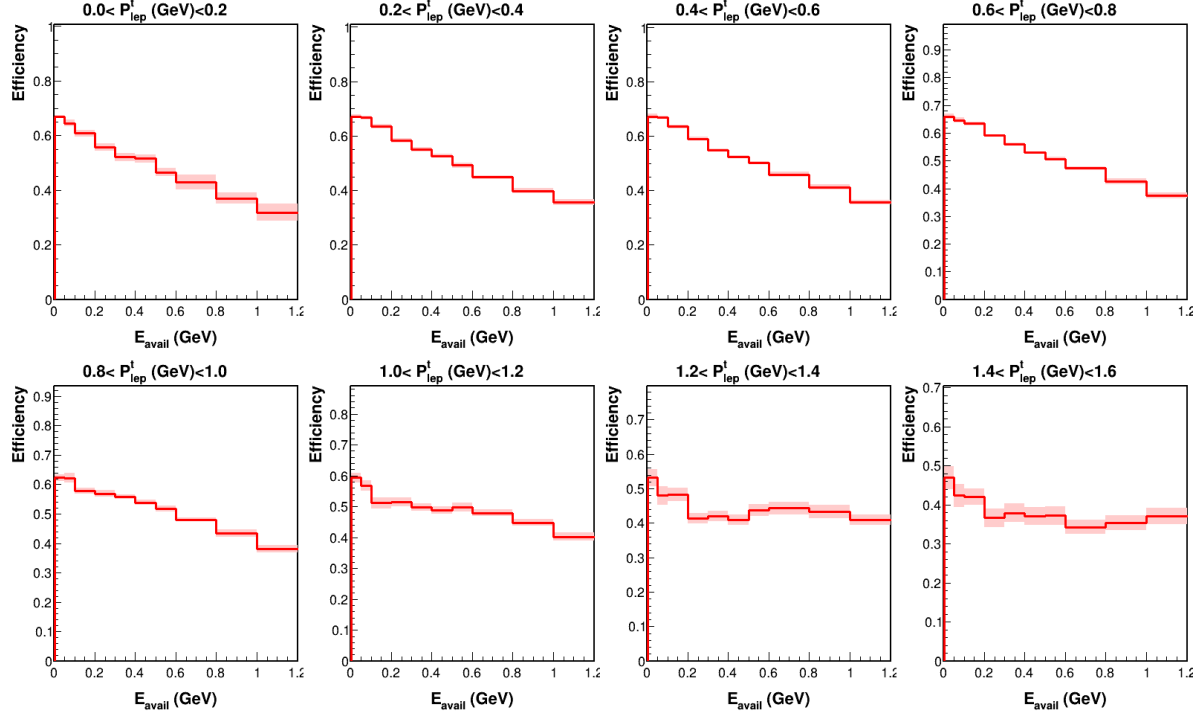
$$\epsilon_i = \frac{N_i^s}{N_i^t} \quad (58)$$

where  $N_i^{s(t)}$  are number of selected (simulated) signal events in bin  $i$ . In addition, a few bins at the edge of phase spaces suffer from limited statistics, leading to large statistical uncertainty. This is mitigated by pseudo count technique:

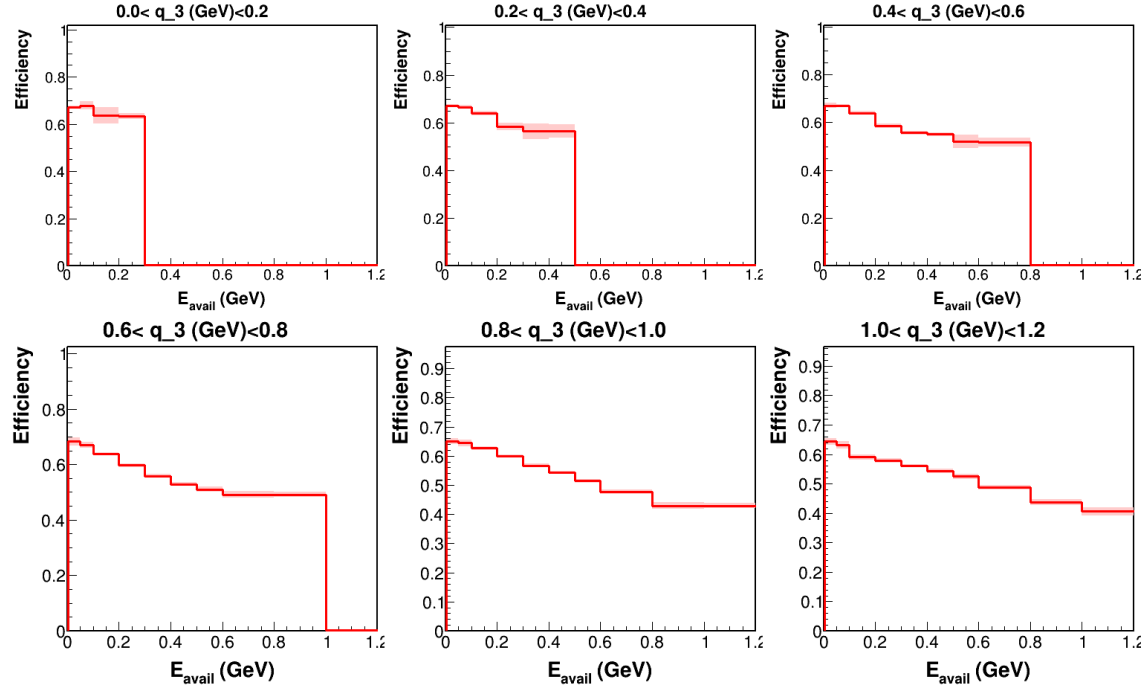
$$\epsilon_i = \frac{N_i^s + N_{i-1}^s}{N_i^t + N_{i-1}^t} \quad \text{for } N_i^t < 100 \quad (59)$$

where  $N_{i-1}^{s(t)}$  are number of selected (simulated) events in the left adjacent bin (same  $q_3$  or  $P_{lep}$ , smaller  $E_{avail}$ ). In other words, the acceptance in the low statistics bins are estimated by the average of adjacent bins. The acceptance is shown in figure 5.13. The inefficiency of high  $E_{avail}$  events is due to the overlapping of EM shower and hadronic activities, such that the tracking algorithm can't reconstruct a proper track candidate and/or front dEdX exceeds the threshold.

The last two ingredients of cross section are integrated flux and the target number normalization. The integrated flux is estimated by simulation, corrected by the flux constraint described in section 3.4.1, leading to  $\Phi = 6.7 \pm 0.2 \times 10^{11} \text{ } \nu/cm^2$ . The number of targets is measured by the number of nuclei, using the chemical analysis result[14], leading to  $T = 3.23 \pm 0.05 \times 10^{30}$  nucleons.



(a) Acceptance in  $E_{avail} - P_{lep}^t$  space



(b) Acceptance in  $E_{avail} - q_3$  space

Figure 5.13: Estimated acceptance

## 5.7 Cross Section Result

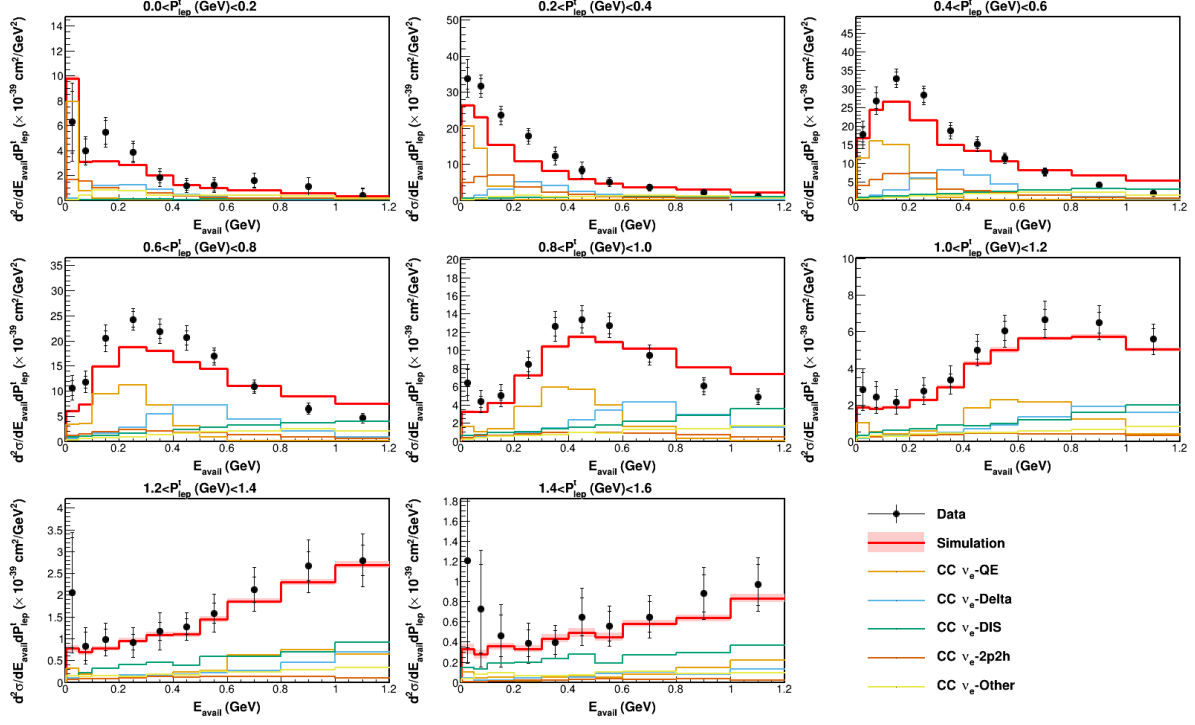
The cross section result compared to MnvTune v2 simulation is plotted in figure 5.14. The error bars are statistical and total uncertainties. The simulated contribution from various channels are plotted as well, including CCQE (CC  $\nu_e$ -QE), Delta resonance (CC  $\nu_e$ -Delta), DIS (CC  $\nu_e$ -DIS), 2p2h (CC  $\nu_e$ -2p2h), and others (CC  $\nu_e$ -Other, dominated by higher resonance).

## 5.8 Uncertainties

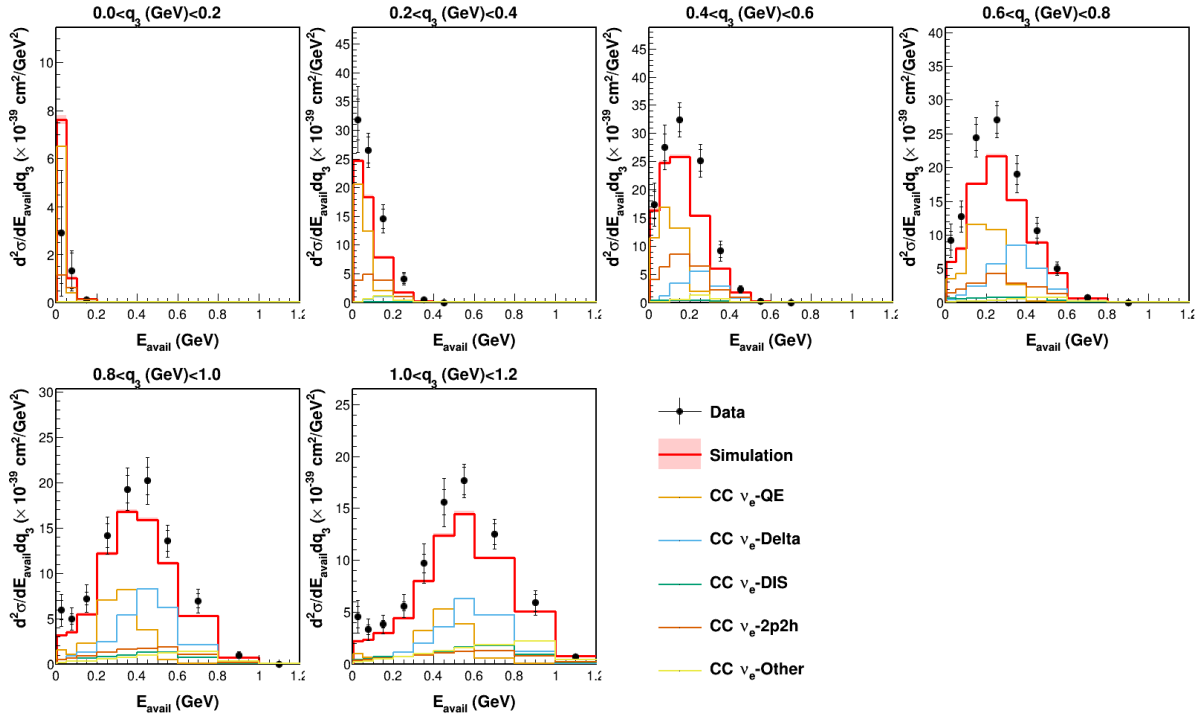
The uncertainties of this measurement consist of two parts, statistical and systematical uncertainties, and uncertainty summary is plotted in figure 5.15.

The statistical uncertainty comes from three sources: measured data, estimated background, and efficiency estimation, while the statistical uncertainty of the migration matrix is neglected because of the sample size. The bin contents of measured data ( $N_j^{data}$ ) and estimated background histograms ( $N_j^{bkg}$ ) are assumed to be independently Poisson distributed, hence the statistical uncertainties are  $\sqrt{N_j^{data}}$  and  $\sqrt{N_j^{bkg}}$  respectively. The statistical uncertainty of efficiency estimation is evaluated by assuming  $N_i^s$  follows a binomial distribution  $B(N_i^t, \epsilon_i)$  and calculating the second derivative of log-likelihood function of  $\epsilon_i$ [42]. These statistical uncertainties are then propagated to cross section with first order approximations.

On the other hand, the systematical uncertainty, which comes from imperfections of the simulations, is estimated using many-universe method[67]. A number of parameters used in simulations different from the real detector, due to measurement limitation or ignorance of physics, resulting in deviations from the true cross section. For example, the active mass of MINERvA could be different from the number used in simulation by 1%, which leads to different estimation of background rate and target number normalization, hence different cross section results. The concept of the many-universe approach is evaluating systematical uncertainty by extracting cross section in an ensemble of simulations (universes), where simulation parameters are shifted randomly according to their uncertainties. In practice,

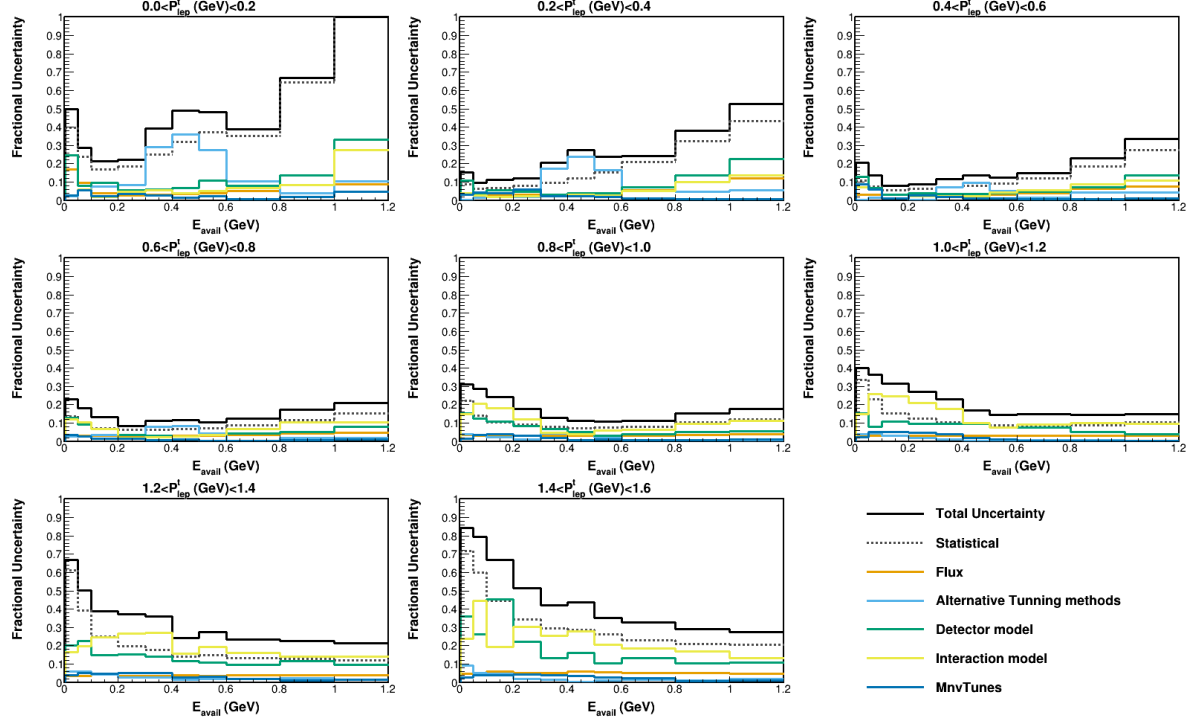


(a) Measured differential cross section in  $E_{avail} - P_{lep}^t$  space

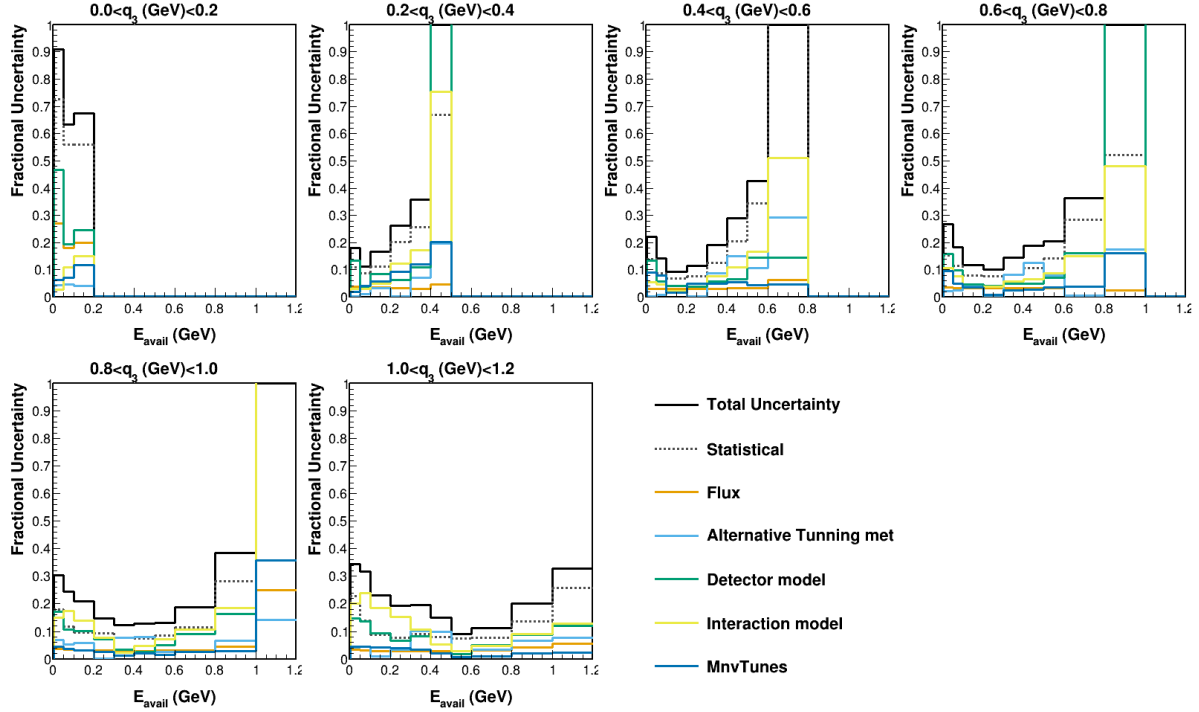


(b) Measured differential cross section in  $E_{avail} - q_3$  space

Figure 5.14: Measured differential cross section



(a) Fractional uncertainties in  $E_{avail} - P_{lep}^t$  space



(b) Fractional uncertainties in  $E_{avail} - q_3$  space

Figure 5.15: Fractional uncertainties of measured differential cross section

there are a number of approximations.

1. Only one parameter is shifted at a time and the uncertainties from different sources are summed in quadrature. This is equivalent to assuming no correlation between uncertainty sources.
2. Only three variations are used for one parameter: center value and  $\pm 1\sigma^5$ .
3. The variant results are achieved by weighting simulated events or modifying simulated variables, rather than actually re-simulating.

There are several ways of determining the uncertainties of individual parameters. First, the simulation may provide uncertainties on the parameters, such as GENIE uncertainties. Second, MINERvA may have measured, directly or indirectly, some parameters used in simulation, and the differences are interpreted as uncertainty. Lastly, in case the measured data simulation difference was corrected, the uncertainty of measurement would be used as uncertainty.

We evaluated 4 types of systematical uncertainty in this analysis.

### 5.8.1 Interaction Model Uncertainties

Interaction model uncertainties are uncertainties of physical models in interaction simulation, which consists of 3 categories: primary interaction, final state interaction, and MINERvA tunes. The interaction event generator, GENIE, provides a set of weights corresponding to shifting model parameters by  $1\sigma$  for the first two categories. The full list of shifted parameters are listed in table 5.5 and 5.6[20].

#### 5.8.1.1 MINERvA Tune Uncertainties

The interaction model reweighting applied in this analysis comes with  $1\sigma$  shift weights as well. The 2p2h reweighting uncertainty is evaluated by changing the weighting method to three variances, leading to new weights to replace the default weight[84]. The default weight weights up both nn or np initial stats, while variants 1 and 2 weight up either nn

---

<sup>5</sup>Unless stated otherwise in the following context

or np pair. Variant 3 only weights up QE processes, which is assuming the data excess is indeed a mismodeling of QE processes.

The RPA reweighting uncertainty is evaluated by approximating the parameter uncer-

| Symbol                             | Description                          | Uncertainty                   |
|------------------------------------|--------------------------------------|-------------------------------|
| NC elastic model                   |                                      |                               |
| MaNCEL                             | Axial mass                           | $\pm 25\%$                    |
| EtaNCEL                            | Strange axial FF parameter $\eta$    | $\pm 30\%$                    |
| CCQE model                         |                                      |                               |
| MaCCQE                             | Axial mass                           | $+25\% / -15\%$               |
| VecFFCCQEShape                     | Vector form factor model             | BBBA $\leftrightarrow$ dipole |
| CCQEPauliSupViaKF                  | Pauli-blocking momentum cutoff       | $\pm 30\%$                    |
| Resonance model                    |                                      |                               |
| MaRES                              | Axial mass                           | $\pm 20\%$                    |
| MvRES                              | Vector mass                          | $\pm 20\%$                    |
| NormCCRES                          | CC normalization                     | $\pm 20\%$                    |
| NormNCRES                          | NC normalization                     | $\pm 20\%$                    |
| Non-resonant pion production model |                                      |                               |
| Rvn1pi/Rvp1pi                      | Normalization of $1\pi$ final states | $\pm 5\%(50\%)*$              |
| Rvn2pi/Rvp2pi                      | Normalization of $2\pi$ final states | $\pm 50\%$                    |
| DIS model                          |                                      |                               |
| AhtBY                              | Bodek-Yang parameter $A_{HT}$        | $\pm 25\%$                    |
| BhtBY                              | Bodek-Yang parameter $B_{HT}$        | $\pm 25\%$                    |
| CV1uBY                             | Bodek-Yang parameter $C_{V1u}$       | $\pm 30\%$                    |
| CV2uBY                             | Bodek-Yang parameter $C_{V2u}$       | $\pm 30\%$                    |

\* The default GENIE uncertainty is 50%, but the MINERvA reweighting introduced in section 3.4.2.3 reduced the uncertainty to 5%.

Table 5.5: GENIE uncertainties: primary interactions

tainties of RPA model[53]. The author evaluated the uncertainty differently in high and low  $Q^2$  regions, because the overall modification is suppressive in the low  $Q^2$  region and enhance in the high  $Q^2$  region.

| Symbol                            | Description  | Uncertainty                      |
|-----------------------------------|--|----------------------------------|
| Nucleon fates                     |  |                                  |
| FrAbs_N                           | Nucleon absorption probability                         | $\pm 20\%$                       |
| FrCEX_N                           | Nucleon charge exchange probability                    | $\pm 50\%$                       |
| FrElas_N                          | Nucleon elastic scattering probability                 | $\pm 30\%$                       |
| FrInel_N                          | Nucleon inelastic scattering probability               | $\pm 40\%$                       |
| FrPiProd_N                        | Nucleon $\pi$ -production probability                  | $\pm 20\%$                       |
| MFP_N                             | Nucleon mean free path                                 | $\pm 20\%$                       |
| Pion fates                        |  |                                  |
| FrAbs_pi                          | Pion absorption probability                            | $\pm 20\%$                       |
| FrCEX_pi                          | Pion charge exchange probability                       | $\pm 50\%$                       |
| FrElas_pi                         | Pion elastic scattering probability                    | $\pm 10\%$                       |
| FrInel_pi                         | Pion inelastic scattering probability                  | $\pm 0\%(40\%)*$                 |
| FrPiProd_pi                       | Pion $\pi$ -production probability                     | $\pm 20\%$                       |
| MFP_pi                            | Pion mean free path                                    | $\pm 20\%$                       |
| Hadronization and resonance decay |  |                                  |
| RDecBR1gamma                      | Branching ratio for radiative resonance decays         | $\pm 50\%$                       |
| Theta_Delta2Npi                   | Pion angular distribution in $\Delta \rightarrow N\pi$ | isotropic $\leftrightarrow$ R.S. |
| AGKYxF1pi                         | Pion Feynman x in for $N\pi$ states in AGKY            | $\pm 20\%$                       |

\* This uncertainty is not evaluated because of large anti-correlation with other FSI parameters.

Table 5.6: GENIE uncertainties: final state interactions



## 5.8.2 Detector Model Uncertainties

The detector model uncertainties reflect our ignorance of the detector simulation, including the uncertainty of modeling particles passage in the detector and the imperfections of the physical model of the detector. The majority of them are evaluated by shifting the reconstructed physical quantity by some amount, usually the difference between simulation and data when we believe the discrepancy is due to mismodeling of the detector.

### 5.8.2.1 Angular Resolution

The electron angle is determined by the track direction, which has 1 mrad resolution, determined by rock muon tracks[14]. This uncertainty is evaluated by an ensemble of 100 universes, each shifted reconstructed electron angle by a random amount drawn from a Gaussian distribution  $\mathcal{N}(0, 1\text{mrad})$ .

### 5.8.2.2 Beam Angle

The Beam angle used in the simulation (3.3 degrees) has an uncertainty determined by neutrino electron scattering measurement, which is 1 mrad at x direction and 0.9 mrad at y direction[99]. This uncertainty is evaluated by 4 universes, shifting the  $\hat{\nu}$  by 1(0.9) mrad in the x(y) direction.

### 5.8.2.3 EM Energy Scale

The scale factors used in estimating electron energy (tabulated in table 4.1) have uncertainties determined by CC  $\pi^0$  measurment[17]. This measurement concluded that the EM energy scale has 1.5% uncertainty in ECAL and 5% uncertainty in HCAL. Four universes are used in evaluating the uncertainty, shifting reconstructed electron energy by  $\pm 1.5\%(5\%)$  of contributions from ECAL (HCAL).

#### 5.8.2.4 Calorimetry Responses

The calorimetry uncertainty is similar to EM energy scale uncertainty, reflecting the calorimetry difference between data and simulation, but different in the method of uncertainty determination, which are measured by test beam measurements[35]. This measurement built a mini-MINERvA detector and place it in beamline of various particles, such as proton and pion. The difference between measured and simulated responses is interpreted as the hadron response uncertainty of a given particle type. In addition, this measurement determined the cross-talk uncertainty as well, listed in table 5.7

The uncertainty is evaluated by universes that shift the calorimetry measurements described in section 4.3.2 by  $\pm 1\sigma$  of the amount contributed by the given source.

#### 5.8.2.5 Hadron Re-interaction Rate

The uncertainty of GEANT detector simulation mostly comes from the hadron re-interaction cross section, in which MINERvA found a 10% difference between ex-situ data and simulation. This uncertainty is evaluated by universes that reweighting events according to the path length between re-interactions such that it mimics the effect of shifting GEANT

| Source               | Fractional Uncertainty |
|----------------------|------------------------|
| Proton               | 3.5%                   |
| Meson (mostly pions) | 5%                     |
| Electromagnetic      | 3%                     |
| Cross Talk           | 20%                    |
| Others               | 20%                    |

Table 5.7: Calorimetry uncertainties

cross section by 10%. In summary, the weight is given by:

$$w = A_{norm} \prod_{segments} w(L, \rho) = \prod_{segments} \frac{P_f(L, \rho, \sigma')}{P_f(L, \rho, \sigma)} \quad (60)$$

$$P_f(L, \rho, \sigma^{(i)}) = \begin{cases} e^{-\rho L \sigma_{total}^{(i)}} & \text{if no re-interaction} \\ (1 - e^{-\rho L \sigma_{total}^{(i)}}) \frac{\sigma_i^{(i)}}{\sigma_{total}^{(i)}} & \text{if re-interacted in channel } i \end{cases}$$

where  $A_{norm}$  is a normalization factor,  $P_f$  is the probability of a hadron undergo some fate in given segment,  $\rho$  is density of material,  $\sigma_{total}^{(i)}$  is central value (shifted) total interaction cross section of given hadron, and  $\sigma_i^{(i)}$  is center value (shifted) interaction cross section of exclusive channel  $i$ , which is elastic or inelastic. The normalization factor  $A_{norm}$  is a function of final state kinematics, such that this reweighting doesn't change neutrino interaction cross section.

#### 5.8.2.6 Leakage Estimation

We estimated 2 MeV uncertainty on the EM shower energy leakage estimation, based on the data/MC difference described in section 5.3.4. Two universes are constructed in order to evaluate this uncertainty, each shifts the leakage estimation by  $\pm 2$  MeV.

#### 5.8.2.7 Target Mass

The target mass uncertainty is determined by chemical analysis as stated in section 5.6. This uncertainty is evaluated by universes that shift the normalization (by weighting) of all simulated events by  $\pm 1\sigma$  and change the target number normalization by the same amount.

### 5.8.3 Flux Uncertainty

The flux reweighting discussed in section 3.4.1 naturally provides an ensemble of universes for evaluating flux uncertainty. The top 200 most probable (posterior probability) universes are chosen, and events are reweighted according to simulated neutrino energy to resemble the result simulated by the alternative flux.

#### 5.8.4 Background Constraint Method

As mentioned in section 5.4.1, this uncertainty is evaluated by two alternative background constraint methods. Both methods attempt to address the residual discrepancy in the diffractive region, and hopefully, the true answer is covered between these two methods.

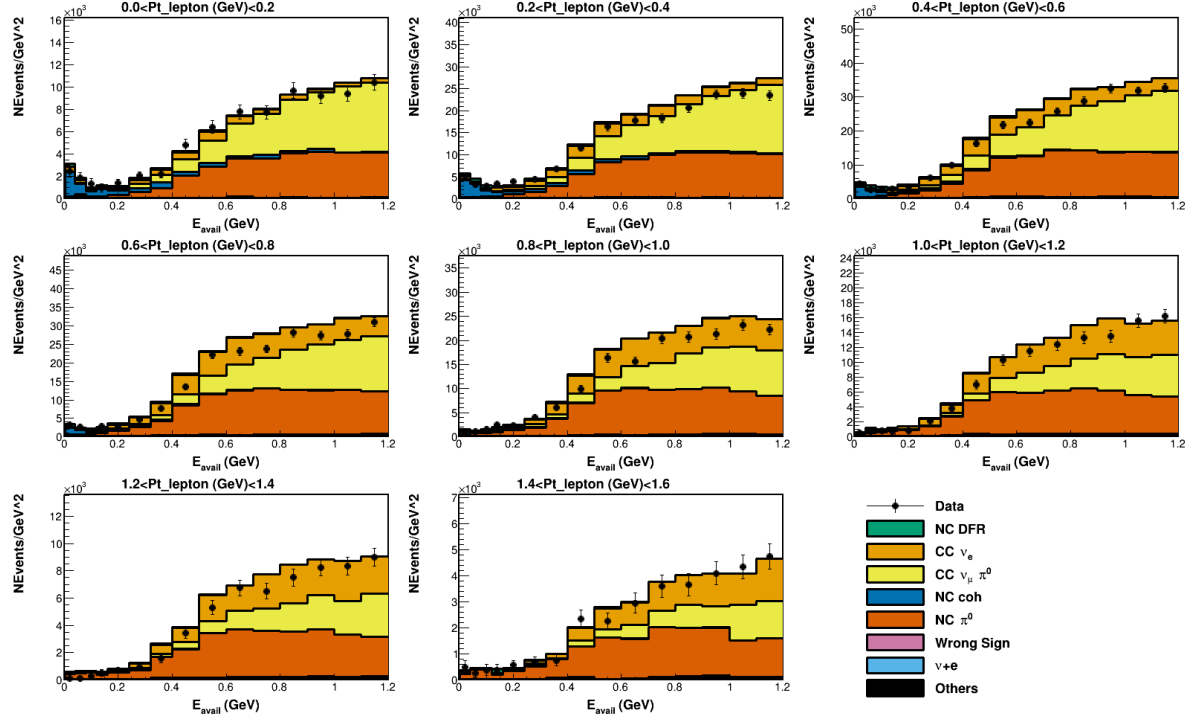
Method 1 floats the normalization of NC diffractive and coherent contribution when joint-fitting non-coherent  $\pi^0$  contribution using FHC data. This method attempts to reduce the size of residual discrepancy without changing the  $|t|$  shape of both processes. The result increases the diffractive normalization by 31.6%, reduces coherent normalization by 2.7%, and reduces non-coherent contribution by about 1% depending on  $P_{lep}^t$ . The variant MC distributions in sideband regions are plotted in figure 5.16- 5.18.

Method 2 applies additional scale factors to non-coherent  $\pi^0$  contribution in the region of data/MC discrepancy:  $0.2 \text{ GeV} < E_{avail} < 0.5 \text{ GeV}$  and  $P_{lep}^t < 1 \text{ GeV}$ . The scale factor is extracted by minimizing the negative log-likelihood in the discrepancy region, leading to 45% to 9.6% enhancement of non-coherent  $\pi^0$  contribution depending on  $P_{lep}^t$ . The variant MC distributions in sideband regions are plotted in figure 5.19- 5.21.

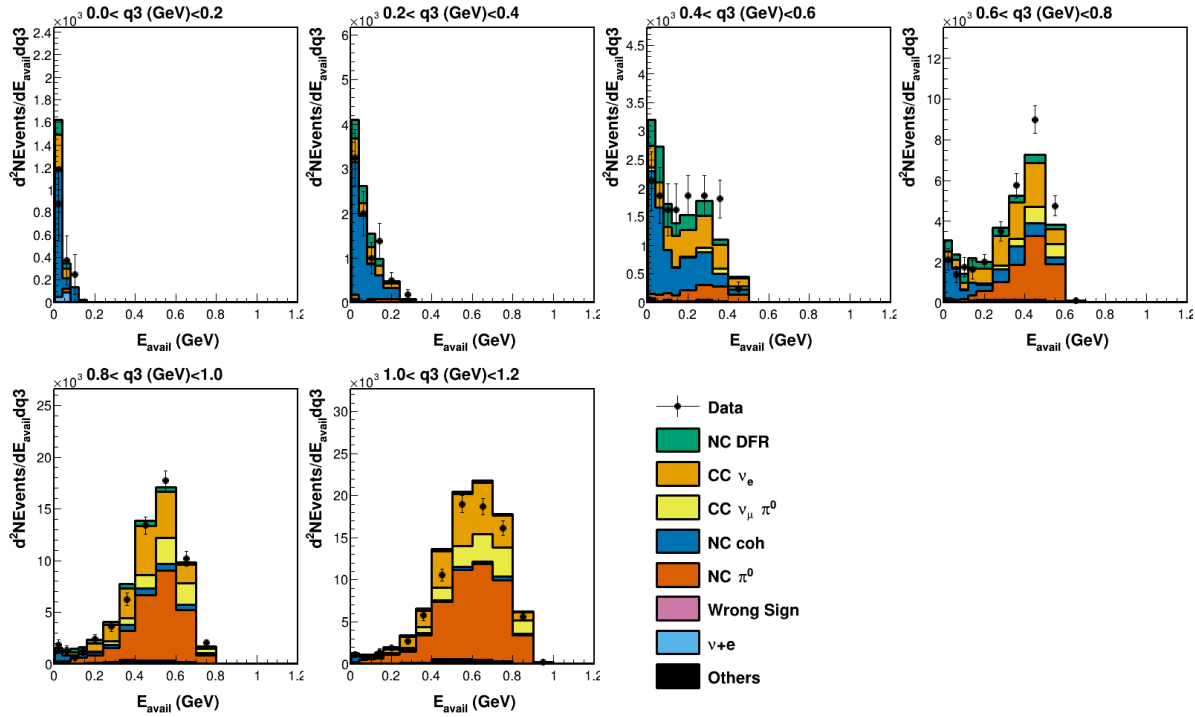
The differences of these two methods to the CV methods are summed in quadrature and interpreted as the background constrain method uncertainty.

### 5.9 Direct Comparison with Published $\nu_\mu$ Measurements

It is natural to compare this result with MINERvA  $\nu_\mu$  low recoil measurements[83, 21] because lepton universality predicts  $\nu_e$  and  $\nu_\mu$  cross sections being almost identical, and the deviation is driven by the lepton mass term. However, there are a few constraints driving the  $\nu_e$  and  $\nu_\mu$  result from being identical in practice. There are mainly three differences between this  $\nu_e$  and MINERvA  $\nu_\mu$  analyses. First, the flux of  $\nu_e$  and  $\nu_\mu$  is different, and showed in figure 3.1. Second, the signal definition is not identical.  $\nu_\mu$  results require the lepton scattering angle less than 20 degrees and momentum greater than 1.5 GeV, while  $\nu_e$  analysis requires lepton energy greater than 2.5 GeV and no scattering angle requirement. This

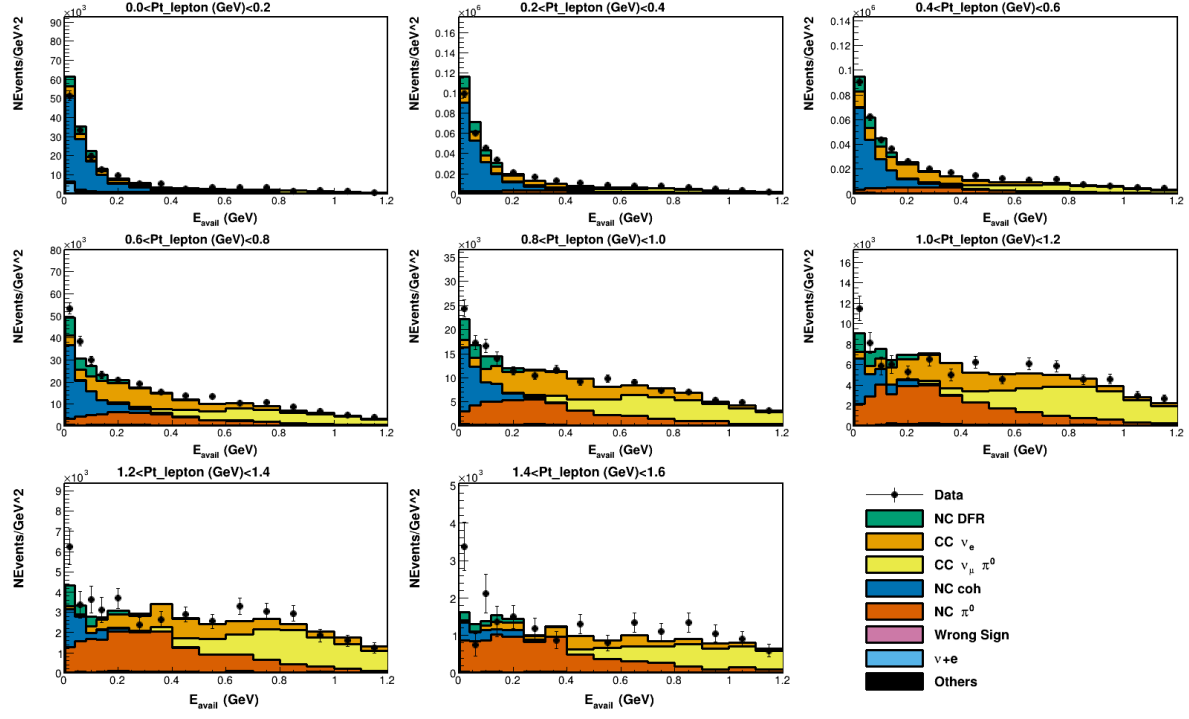


(a) Non-coherent sideband in  $E_{avail} - P_{lep}^t$  space

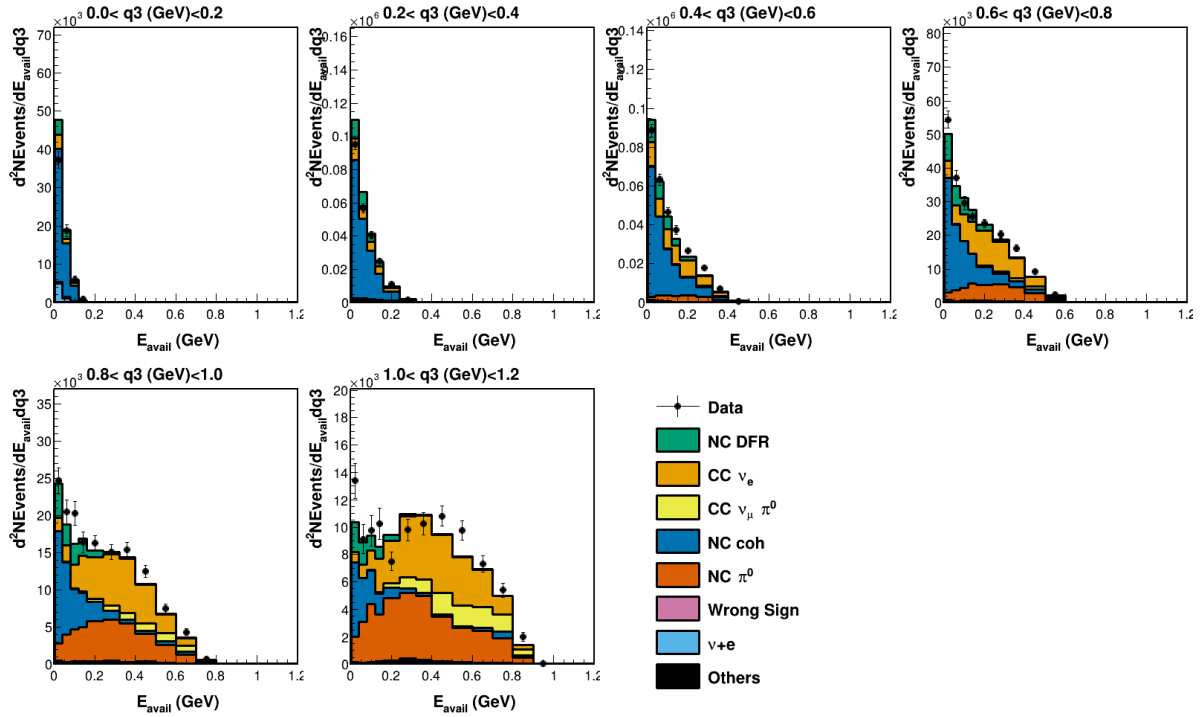


(b) Non-coherent sideband in  $E_{avail} - q_3$  space

Figure 5.16: Non-coherent sideband sample distributions constrained by alternative method

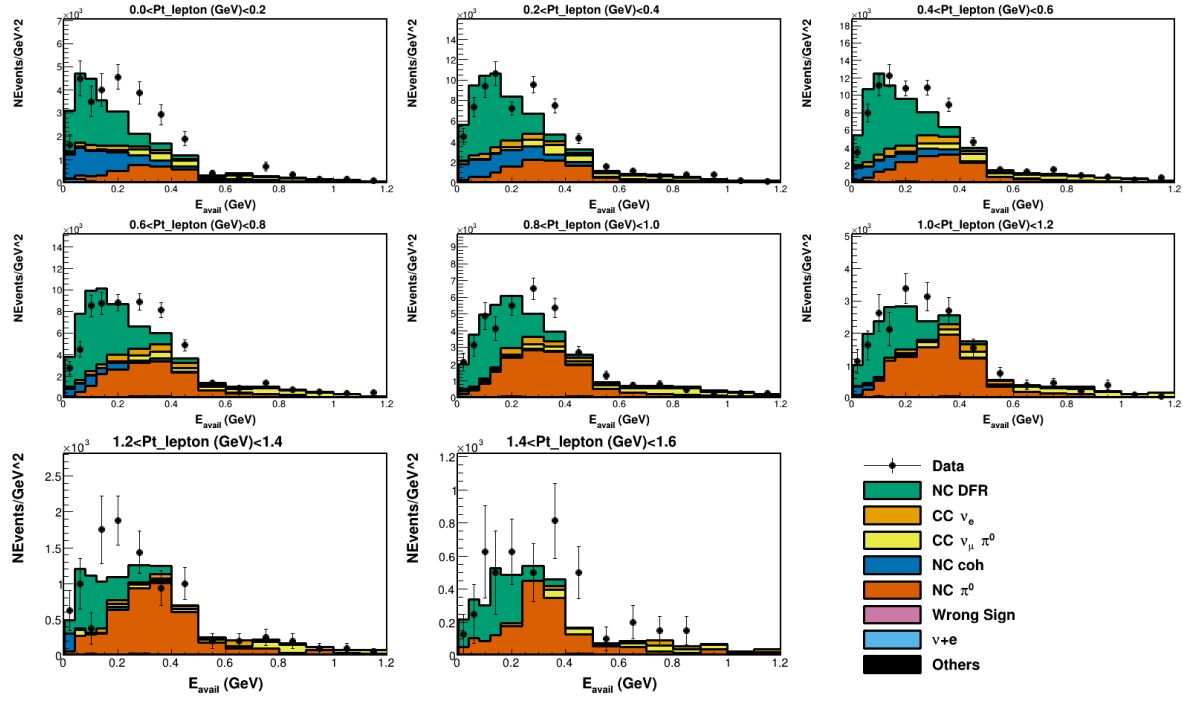


(a) Coherent sideband in  $E_{avail} - P_{lep}^t$  space

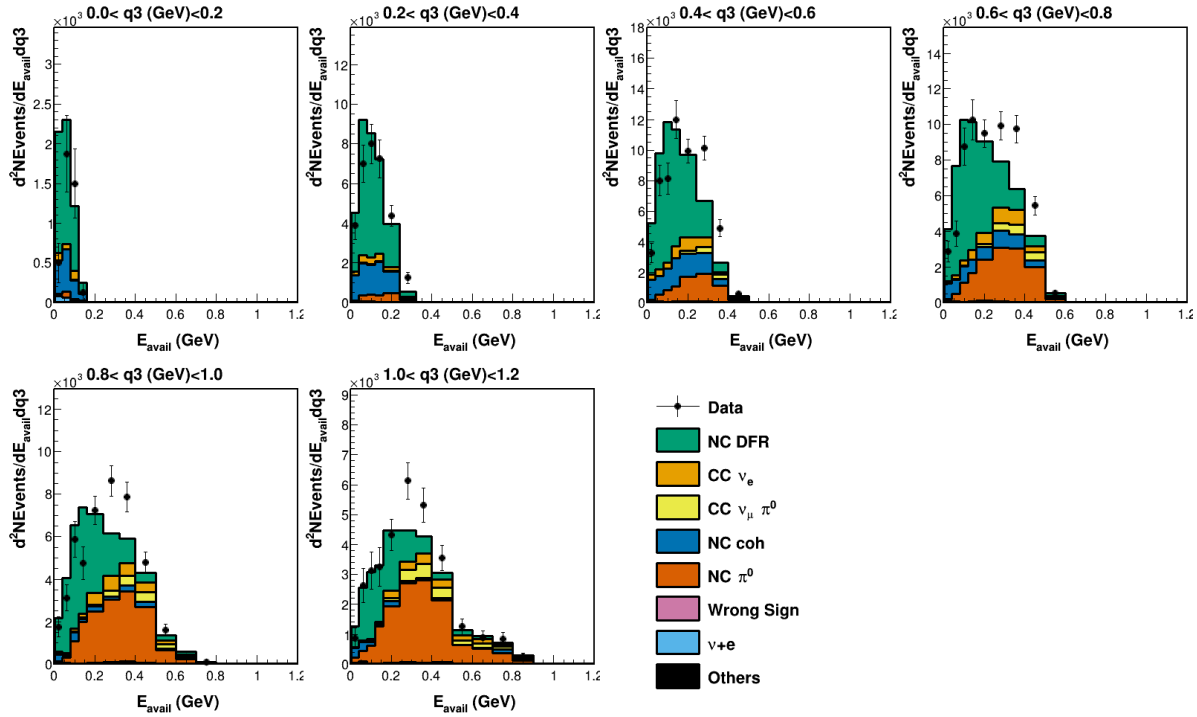


(b) Coherent sideband in  $E_{avail} - q_3$  space

Figure 5.17: Coherent sideband sample distributions constrained by alternative method 1

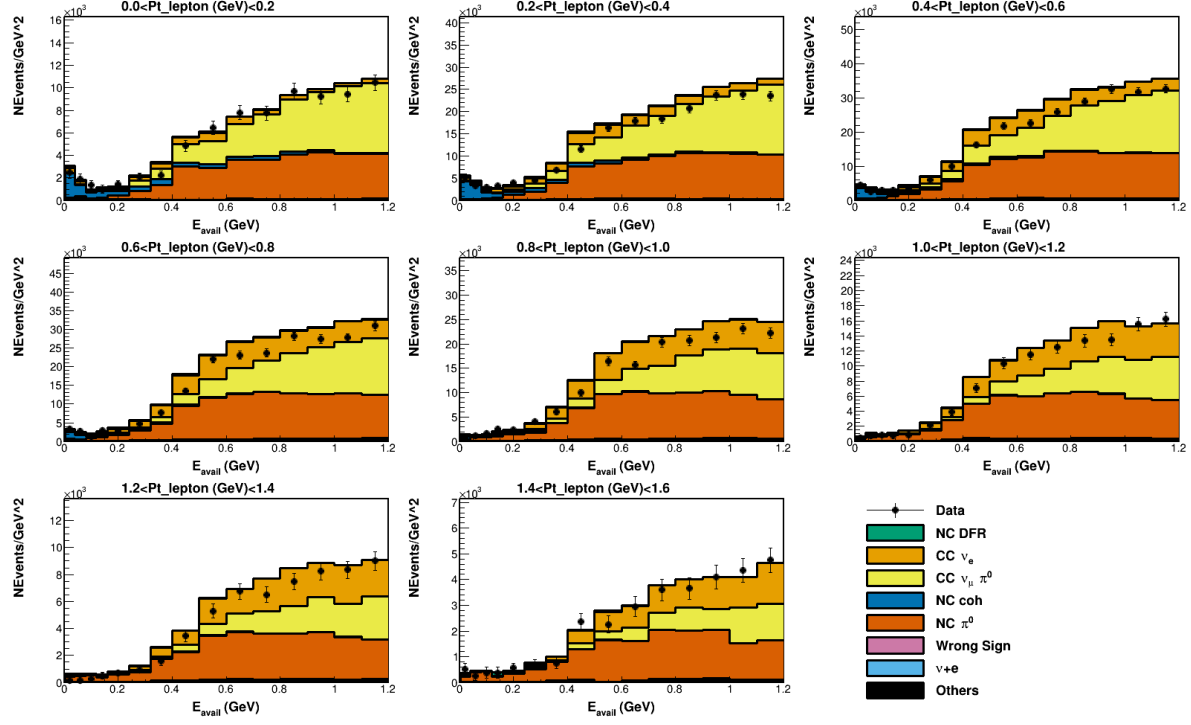


(a) Diffraction sideband in  $E_{avail} - P_{lep}^t$  space

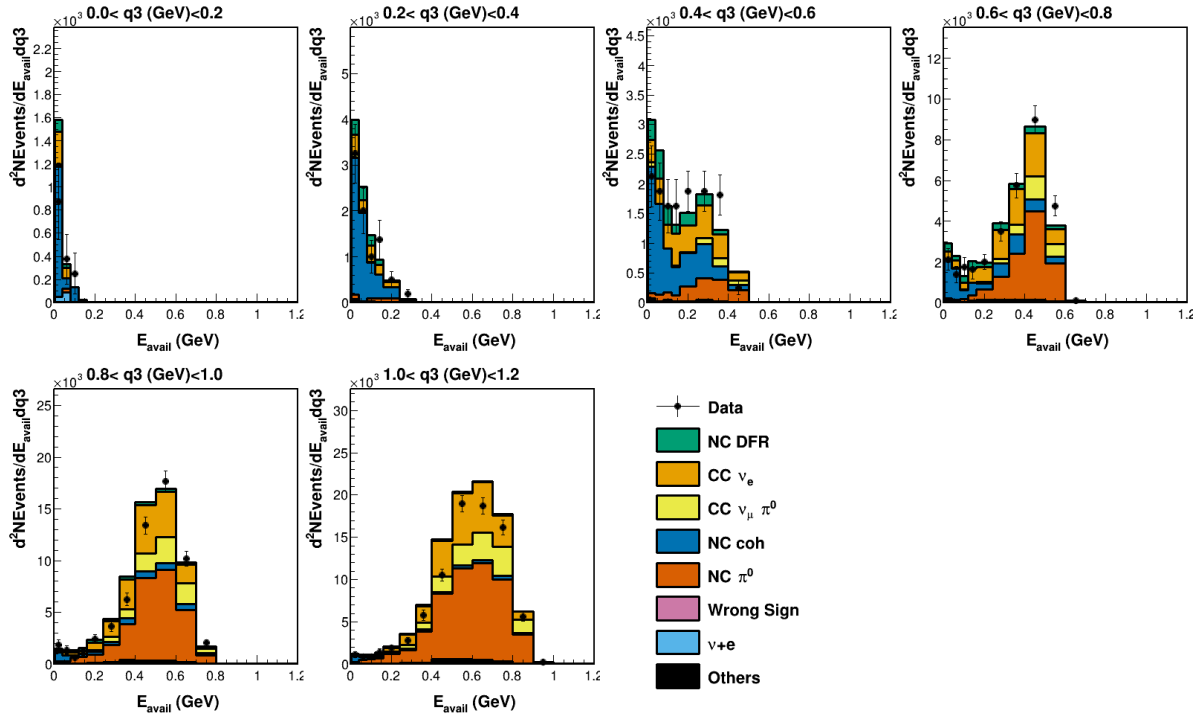


(b) Diffraction sideband in  $E_{avail} - q_3$  space

Figure 5.18: Diffraction sideband sample distributions constrained by alternative method 1



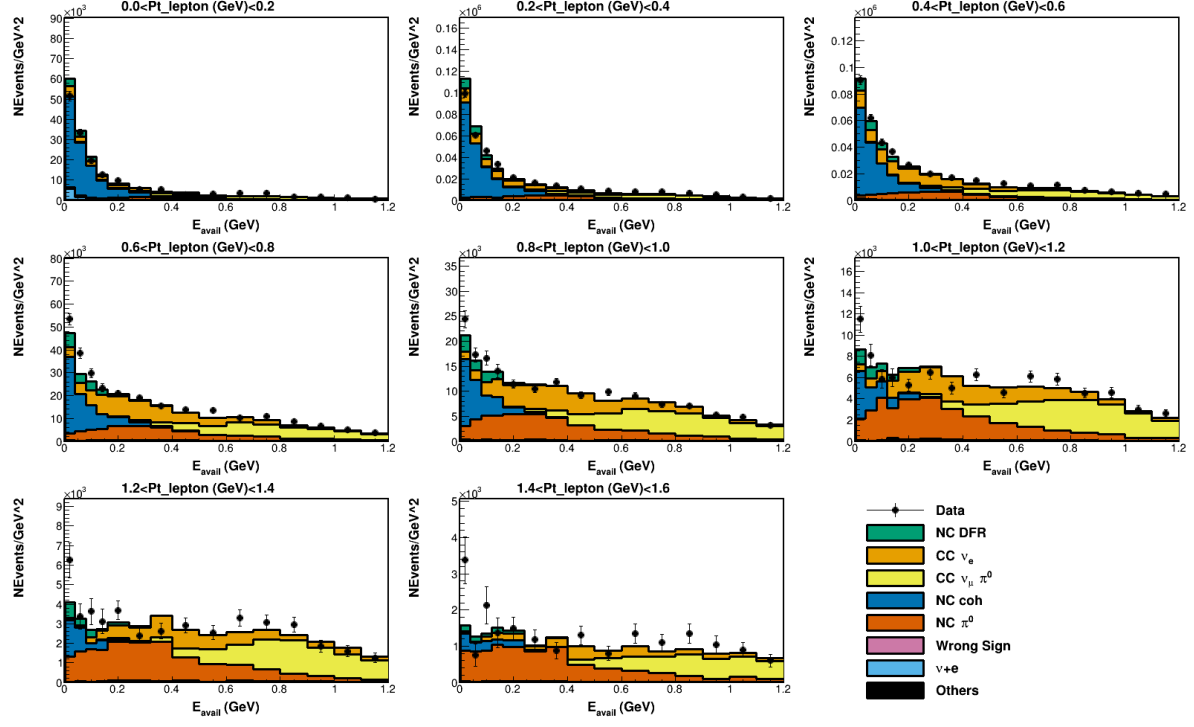
(a) Non-coherent sideband in  $E_{avail} - P_{lep}^t$  space



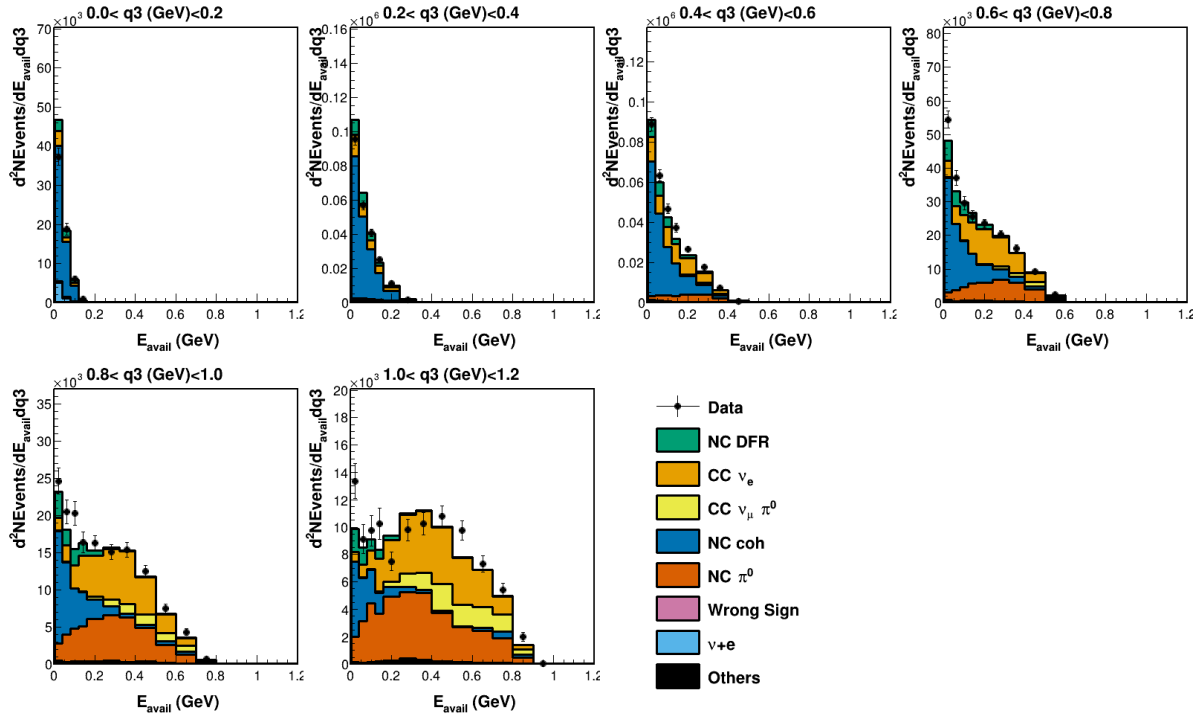
(b) Non-coherent sideband in  $E_{avail} - q_3$  space

Figure 5.19: Non-coherent sideband sample distributions constrained by alternative method



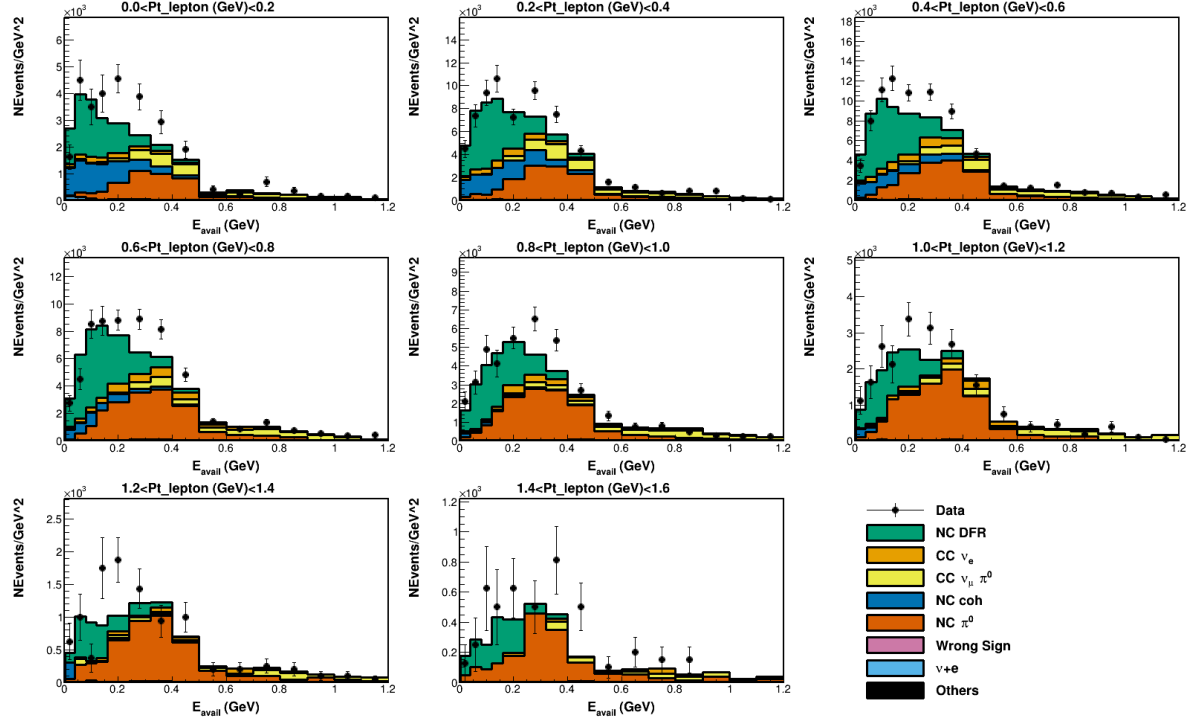


(a) Coherent sideband in  $E_{avail} - P_{lep}^t$  space

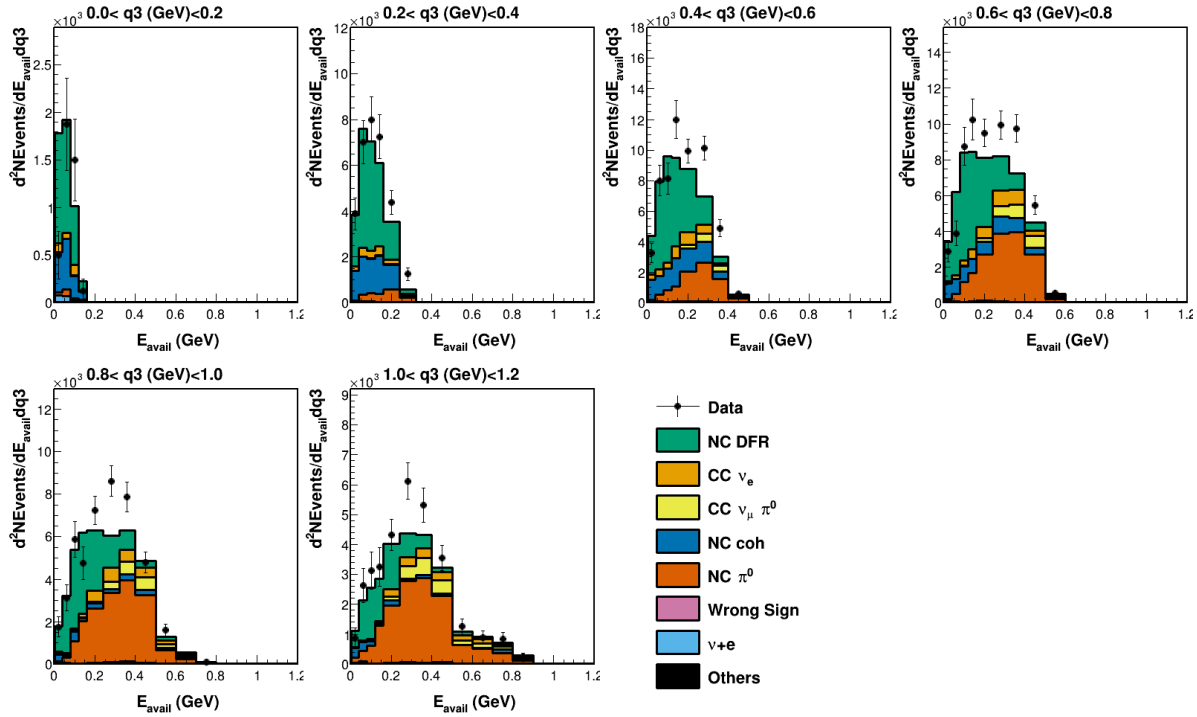


(b) Coherent sideband in  $E_{avail} - q_3$  space

Figure 5.20: Coherent sideband sample distributions constrained by alternative method 2



(a) Diffractive sideband in  $E_{avail} - P_{lep}^t$  space



(b) Diffractive sideband in  $E_{avail} - q_3$  space

Figure 5.21: Diffractive sideband sample distributions constrained by alternative method 2

difference is a result of detector limitations since high angle muon can't be reconstructed and low energy electron is overwhelmed by  $\pi^0$  background. In addition, the LE  $\nu_\mu$  measurement requires neutrino energy between 2 GeV and 6 GeV, which is dropped because we believe it introduces additional model dependence. Third,  $\nu_e$  and  $\nu_\mu$  analysis made different choices in unfolding histograms due to sampling size.  $\nu_\mu$  analysis chose a fine binning and a small number of iterations, while  $\nu_e$  analysis chose a coarse binning and a large number of iterations.

Keeping these differences in mind, the cross section measurement results of ME era electron neutrino and muon neutrino samples are shown in figure 5.22. The LE era analysis is left out because the flux and neutrino interaction model are substantially different. We concluded this result is qualitatively consistent with  $\nu_\mu$  results, as predicted by lepton universality, except the lowest  $q_3$  and  $E_{avail}$  bin, where measured  $\nu_e$  cross section is significantly smaller than  $\nu_\mu$  cross section. Unfortunately we can't calculate statistical consistency because of the binning differences.

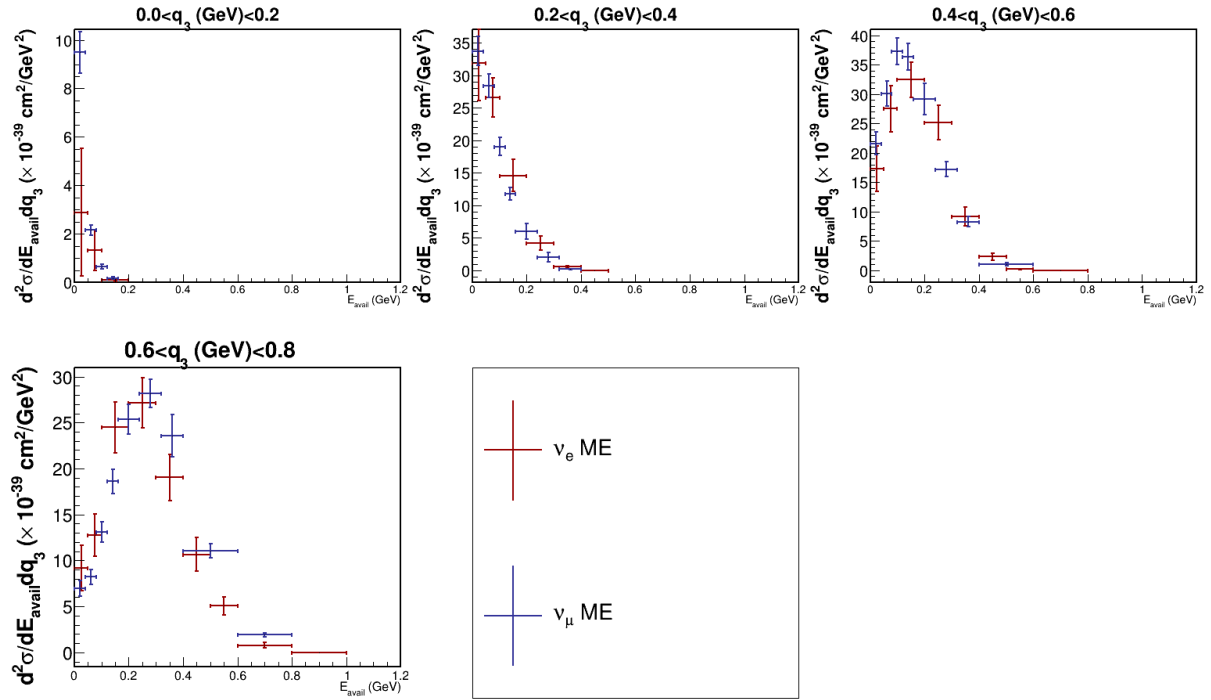


Figure 5.22: Comparison with published MINERvA  $\nu_\mu$  measurements

## 6.0 Conclusion

We have presented the first double-differential cross section measurement of electron neutrino in the low recoil region. This measurement is compared to two similar measurements for the muon neutrino using the same detector but with different energy spectra. We found them to be qualitatively consistent, as predicted by lepton universality. The agreement between MINERvA tuned GENIE model and data is mediocre because of the shape of  $E_{avail}$ . The data suggests enhancement in the low hadronic energy region and suppression in the high hadronic energy region, which is the same trend observed by muon neutrino measurements done by MINERvA.

We also reproduced the excess of photon-like events observed in LE era data[102] using the coherent and diffractive sideband samples, illustrated in figure 5.5 and 5.6. We concluded that NC diffractive and coherent processes are responsible for this data excess, but this conclusion is in tension with other CC and NC coherent measurements[69, 6]. Consequently, further studies are necessary to resolve the tension.

## Appendix A Closure Tests

A closure test is a fake data test that ensures the correctness of the analysis code. MINERvA developed a tool independent from individual analysis software that extracts flux integrated cross section from GENIE spline. The cross section extraction software is expected to reproduce this GENIE cross section if the measured data is exactly the same as GENIE predicts, which is done by feeding the simulated sample as data to the software. By convention, the difference is expected to be less than 0.1%, because the statistical fluctuations are avoided by using one simulation sample for everything. However, this analysis used two simulation samples, one for background prediction (standard sample) and the other for unfolding and efficiency estimation (signal rich sample), hence the statistical fluctuation can not be avoided entirely.

We decided to do the closure test in two ways. First, the conventional closure test, in which test we refrain from using the signal-rich sample and aim at the same threshold as conventional closure tests. It turns out this analysis has a 0.08% normalization disagreement (showed in figure A1), which passed the test. Second, we extract the cross section twice, one uses the signal-rich sample for unfolding and efficiency estimation, and the other uses a standard MC sample for those two steps. The first method aligns with the method used in the main context, while the second is the same as the first closure test. The test result is shown in figure A2. We concluded that the two results are statistically compatible by eye.

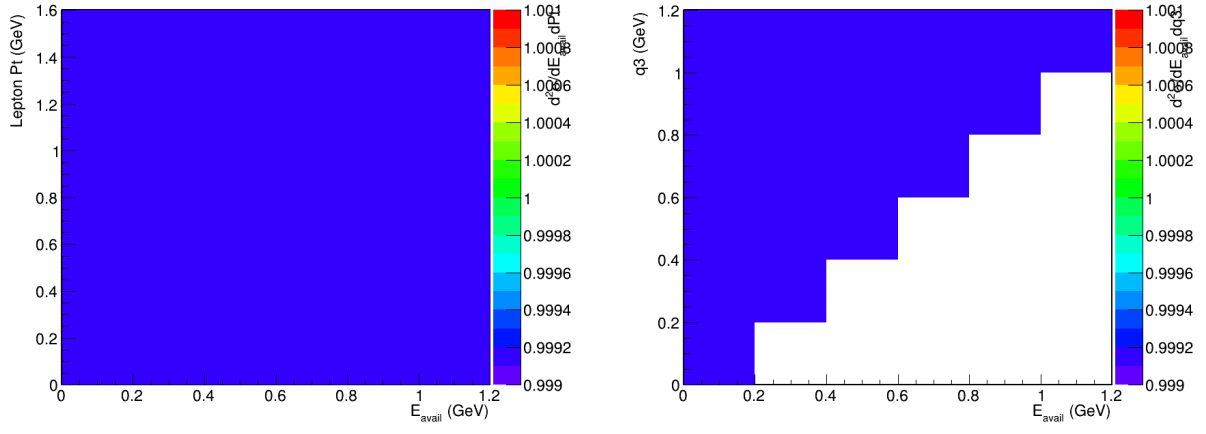


Figure A1: Ratio of cross section extracted by this analysis and the MINERvA tool using the conventional method. Left:  $E_{\text{avail}}-P_{\text{lep}}^t$ , right:  $E_{\text{avail}}-q_3$ .

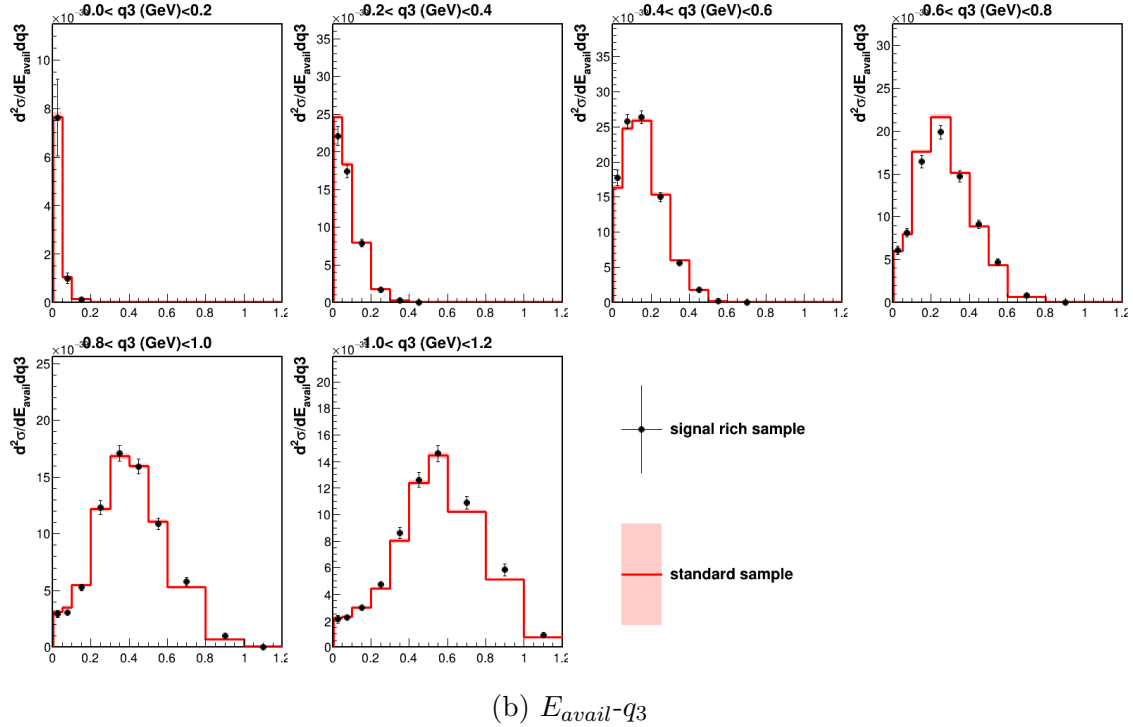
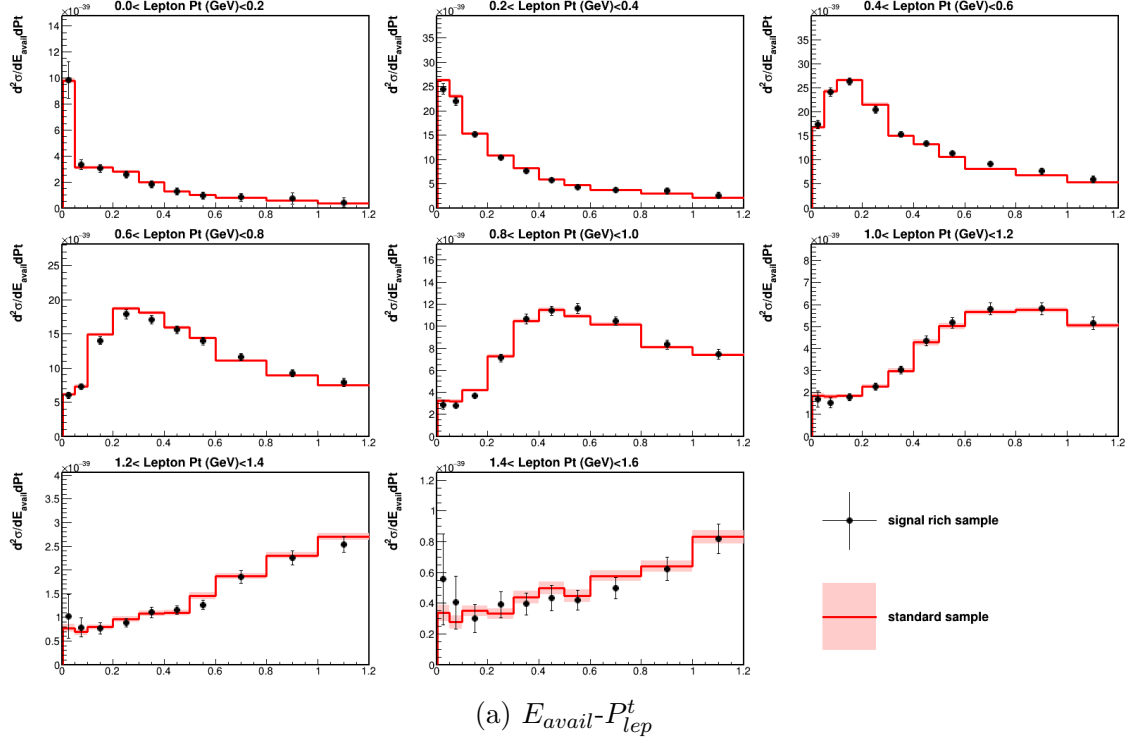


Figure A2: Comparison of cross section extracted by the described procedure and conventional procedure. Error bars are statistical.



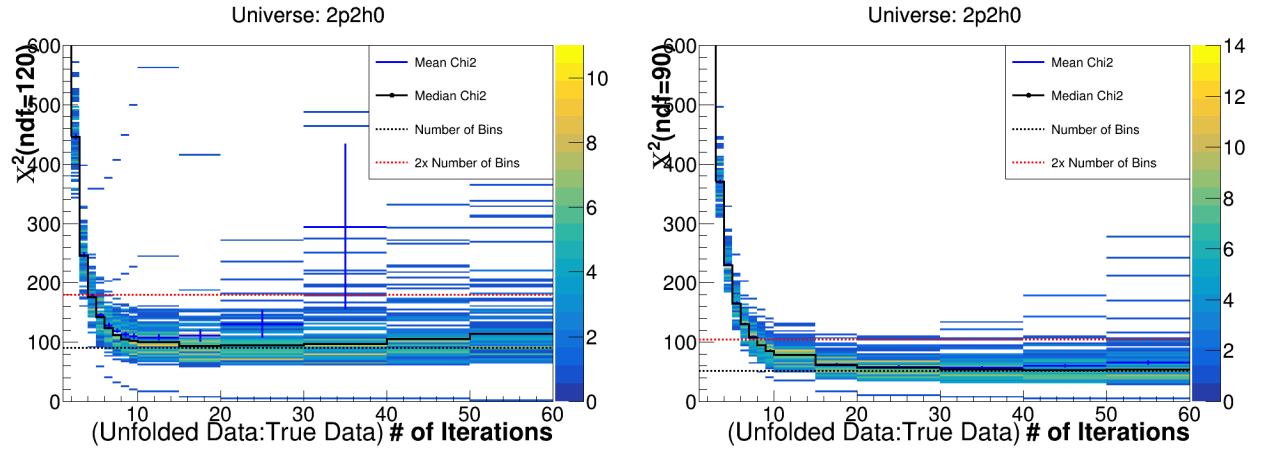
## Appendix B Warping Tests

MINERvA uses warping tests to determine the number of iterations. The warping test is a fake data test, which evaluates the bias and variance by unfolding an ensemble of measured histogram resulted from a true distribution that is known but different from the prior distribution. The simulation provides a measured true histogram pair, and the ensemble is generated by replacing the bin contents of the measured histogram by random numbers, using a Poisson distribution of  $\lambda = \text{original bin contents}$ . The  $\chi^2$  of unfolded distribution and true distribution calculated in the following way is the metric we use.

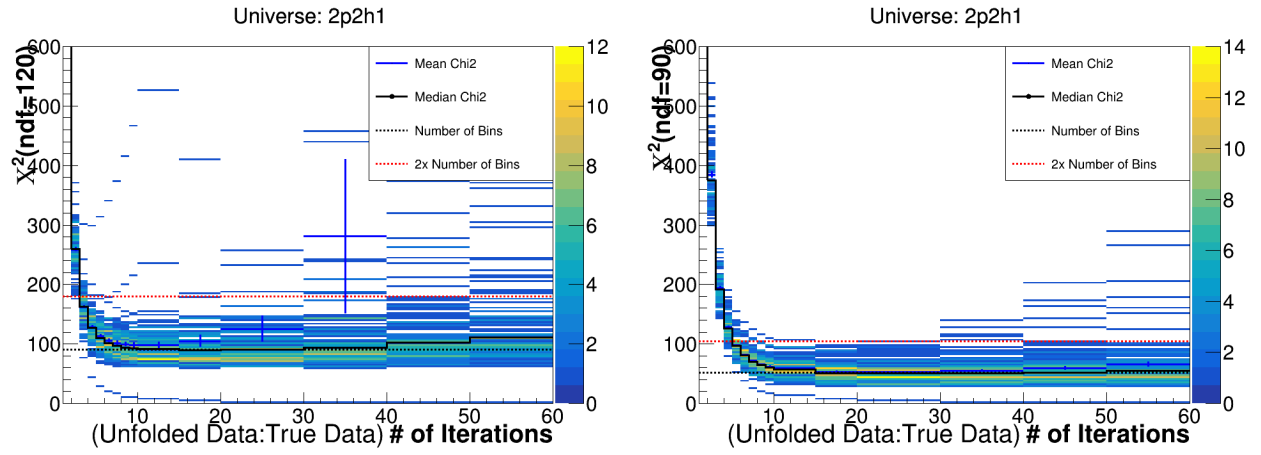
$$\begin{aligned}\chi^2 &= \sum_{ij} (x_i^u - x_i^t) V_{ij} (x_j^u - x_j^t) \\ V_{ij} &= \sum_{k,l} M_{ik} \text{cov}(n(E_k), n(E_l)) M_{lj} = \sum_k M_{ik} n(E_k) M_{kj}\end{aligned}\tag{61}$$

where  $x_i^u(x_i^t)$  are the unfolded (true) event rate histograms. This calculation assumes the bin contents in the measured histogram are mutually independent Poisson distributions, and the statistical uncertainty of migration matrix is negligible compared to the measured histogram. The mean (or median) value of  $\chi^2$  represents the bias since it measures the difference between unfolded histogram and true histogram, while the variance of  $\chi^2$  distribution represents the variance, as it measures the variance due to statistics alone. A “good” number of iterations should be large enough to reduce the mean  $\chi^2$  to statistically consistent with the correct model, while small enough to avoid uncertainty blow up. However, this may not always be achievable.

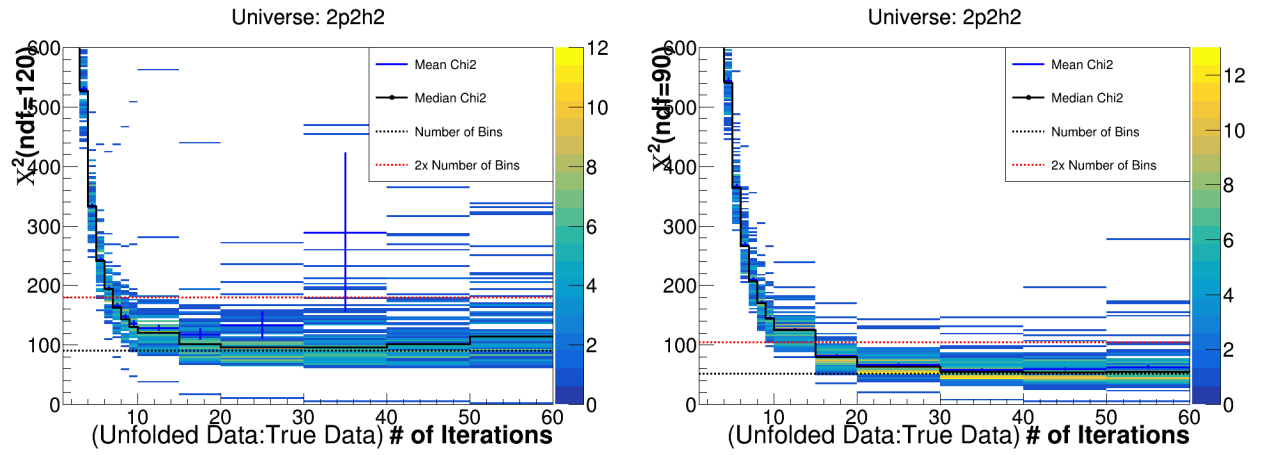
The  $\chi^2$  as functions of the number of iterations for various fakes data inputs are plotted in figure B1. Notice that any bin less than 5 is excluded from the  $\chi^2$  calculation because the bin content distribution is far from gaussian and adds a significant penalty to  $\chi^2$ . The heatmaps represent the chi2 distribution as a function of iterations, and the median and mean of chi2 as a function of iterations is plotted as well. The dashed line denotes the statistical limits: the black dash line is the expected mean chi2 value when the the unfolded model has converged to the true model, while the red dash line is an empirical threshold when the unfolded model is close enough to the true model.



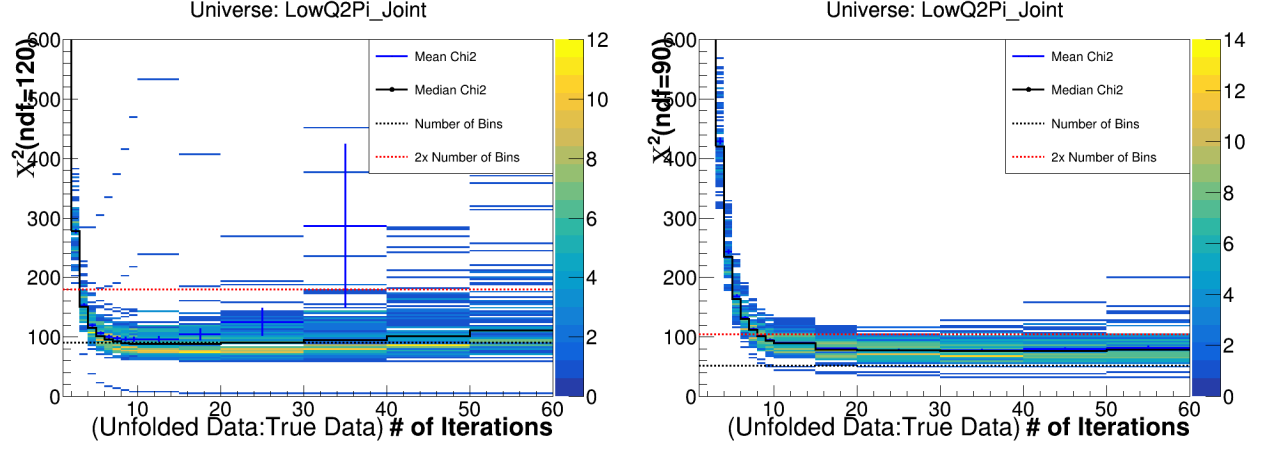
(a) Fake Data Model: MINERvA 2p2h Tune Variant: nn pair



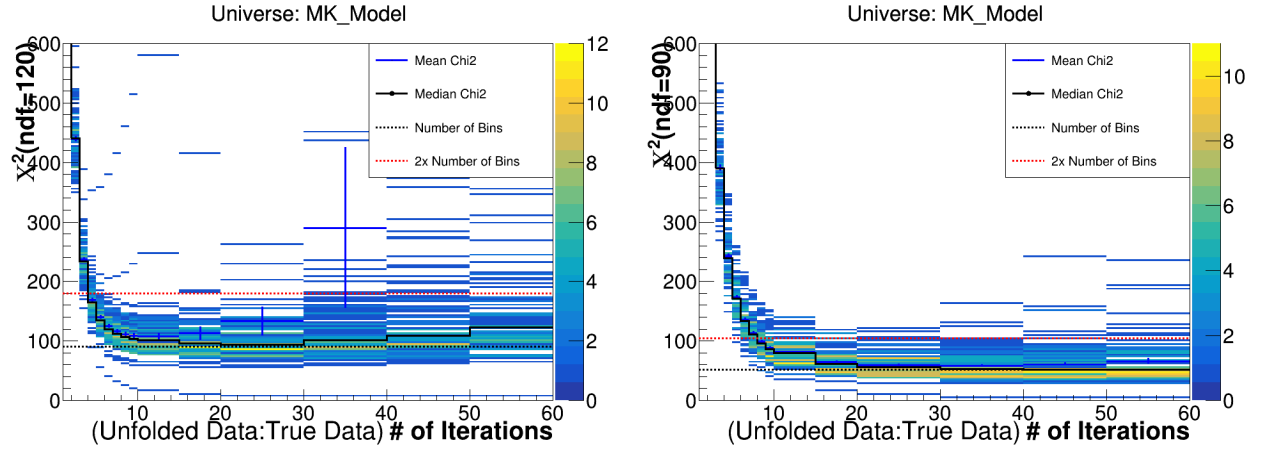
(b) Fake Data Model: MINERvA 2p2h Tune Variant: np pair



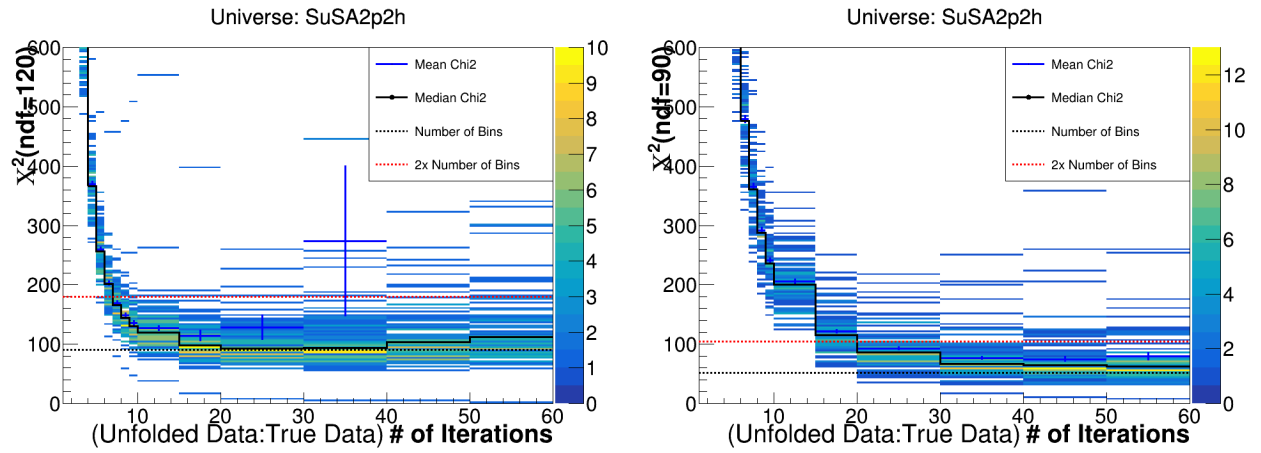
(c) Fake Data Model: MINERvA 2p2h Tune Variant: QE



(d) Fake Data Model: MINERvA Tune v1



(e) Fake Data Model: MK model



(f) Fake Data Model: SuSA 2p2h model

Figure B1: Warping tests results. Left:  $E_{avail}-P_{lep}^t$ . Right:  $E_{avail}-q_3$

## Appendix C Data Excess Studies

The data excess (or the excess) refers to a large model under-prediction in high dEdX and small non-EM-Shower energy deposition region observed in this analysis, as shown in figure C1. The data excess studies are mostly done by Sarah Henry, who did a  $\bar{\nu}_e$  low recoil analysis using RHC data. A brief summary is presented here and more details can be found in her thesis.

Previous MINERvA analyses looking for final state electrons observed similar excesses in photon-rich regions as well, including neutrino-electron elastic measurements[100] and LE  $\nu_e$  CCQE analysis[103]. MINERvA drew the conclusion using LE data that the excess is contributed by NC diffractive processes[102], which was not simulated in the LE era. We simulated its contribution and studied the excess again using ME FHC and RHC data.

The excess was observed in both ME FHC and RHC samples and had very similar shape in multiple reconstructed variables in the excess region[96]<sup>1</sup>. As a result, we concluded the source of the excess is the same in FHC and RHC samples, and the RHC sample is

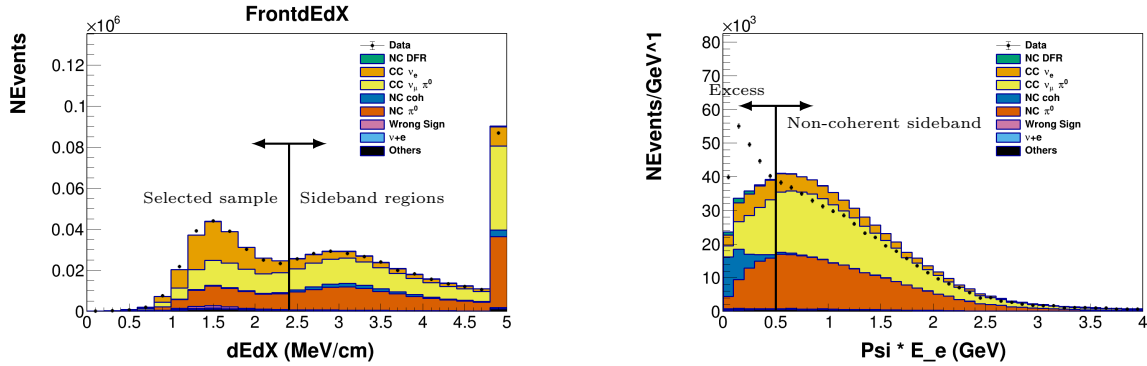


Figure C1: Left: Front dEdX distribution. The last bin is overflow bin that includes all events with  $dEdX > 4.8$  MeV/cm. Right:  $\Psi E_{EM}$  distribution in sideband regions. The Excess region is the union of coherent and diffractive sideband regions.

<sup>1</sup>The excess region was defined by Front  $dEdX > 2.4$  MeV/cm and  $\Psi < 0.1$ .

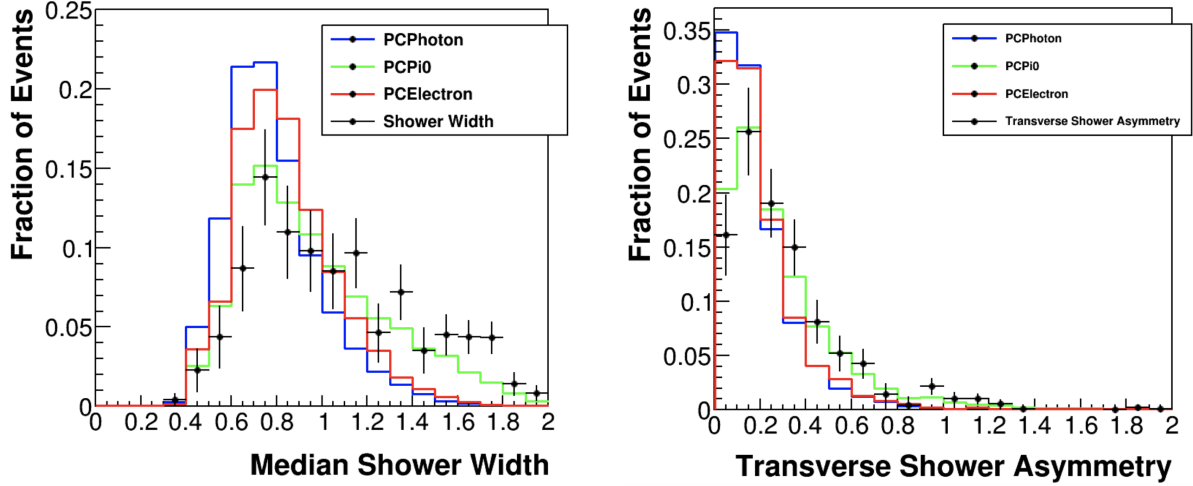


Figure C2: Excess region shower shape study. Left: median shower width. Right: Transverse Asymmetry. Figure shared by Sarah.

more suitable to study the excess shape because the RHC sample has less non-coherent contamination than the FHC sample.

### C.1 Excess Characterization

We tested three hypotheses of the particle content in the EM shower: electron, photon, and  $\pi^0$ . We simulated the detector response for these types of particles that originated at the center of the MINERvA detector with 0-10 GeV energy and 0-30 degree angle (with respect to detector z-axis). Two shower shape variables, median shower width and transverse shower asymmetry, are evaluated and compared to the data<sup>2</sup>, as shown in figure C2. The ME data still favors  $\pi^0$  initiated shower like the LE data. Next, we tested coherent and non-coherent  $\pi^0$  hypotheses by comparing  $E_{\pi^0}\theta_{\pi^0}^2$ ,  $\Psi$  variables and etc., as plotted in figure C3. It is obviously that ME data favors coherent  $\pi^0$  production processes. Finally, we tested the diffractive and coherent  $\pi^0$  hypotheses by looking at upstream inline energy  $E_{uie}$ , which

<sup>2</sup>Definition of both variables can be found in [104].

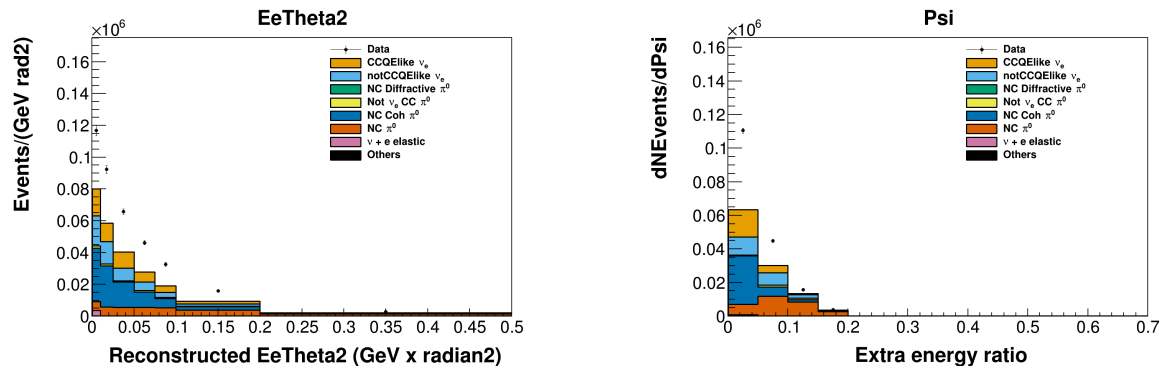


Figure C3: Left:  $E_{\pi^0}\theta_{p\pi^0}^2$  distribution. Right:  $\Psi$  distribution. The excess shape is similar to NC coherent  $\pi^0$  production. Figure shared by Sarah.

captures vertex activities in case of NC  $\pi^0$  processes since the shower cone points back to the interaction vertex. The vertex energy is correlated with the energy of recoil proton or nucleus, which is related to the  $|t|$  variable in coherent pion production processes, defined by:

$$|t| = -|p_{p(A),f} - p_{p(A),i}|^2 = 2m_{p(A)}(E_{p(A),f} - m_{p(A)}) = 2m_{p(A)}T_{p(A)} \quad (62)$$

The most popular diffractive and coherent models are Rein-Sehgal models[80, 82], which predict the  $|t|$  distribution follows exponential distribution  $\exp(-\frac{1}{3}R_0^2A^{2/3}|t|)$ , where  $A$  is number of nucleons and  $R_0 \approx 1$  fm is the nuclear length scale. Consequently, the diffractive model predicts higher  $E_{uie}$  than coherent model because of smaller  $A$  and  $m$ . The upstream inline energy distribution is plotted in figure C4.

We observed that:

1. NC diffractive contribution is the only known process filling high  $E_{uie}$  region without blowing up low  $E_{uie}$  region.
2. NC coherent contribution also has to be increased to fill the low  $E_{uie}$  region.

Hence we concluded that the excess is due to under-prediction of NC diffractive and coherent  $\pi^0$  production. We knew the conclusion was not the most satisfying answer because it is in tension with other measurements of CC and NC coherent processes, such as[69, 6],

which found good data/MC agreements. How to resolve the tension is beyond the scope of this analysis because the predicted contribution in the signal region is relatively small.

## C.2 Creating an Excess Model

Given that GENIE's diffractive and coherent models do not predict the data well, we have to create an ad hoc excess model by a data-driven approach. We decided to scale the model predictions as a function of  $E_{EM}$ , because:

1. The  $E_{EM}$  dependence of the diffractive model doesn't agree with the data.
2. Both diffractive and coherent models do not predict pion energy dependence, hence

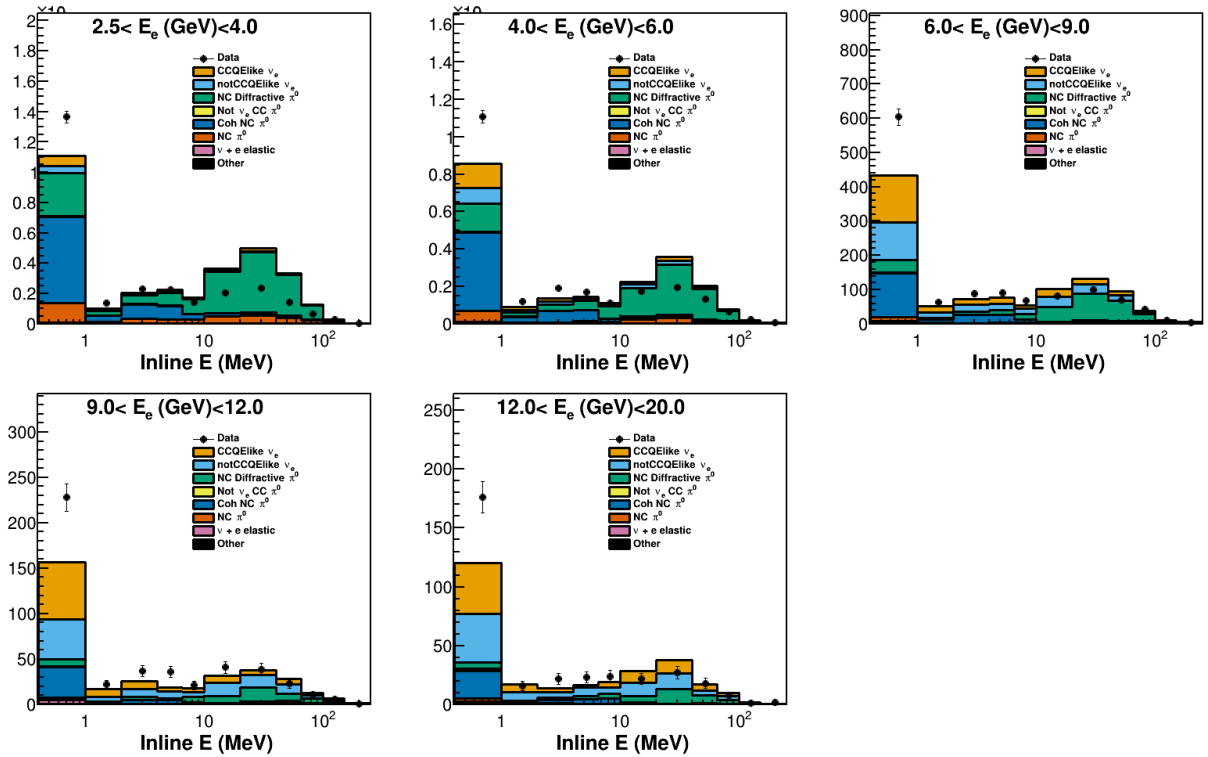


Figure C4: Upstream inline energy in bins of  $E_{EM}$  in the excess region. NC diffractive  $\pi^0$  contribution is scaled up by 12x. Figure shared by Sarah.

changing the shape won't break the physics of the models.

In addition, the excess region is split into high and low  $E_{uie}$  regions in order to separate diffractive and coherent rich regions. Fitting the scale factors to RHC data yields the scale factors listed in table 5.4, which agree with FHC data fairly well.



## Bibliography

- [1] M G Aartsen et al. Icecube-gen2: the window to the extreme universe. *Journal of Physics G: Nuclear and Particle Physics*, 48(6):060501, Apr 2021. ISSN 1361-6471. doi: 10.1088/1361-6471/abbd48. URL <http://dx.doi.org/10.1088/1361-6471/abbd48>.
- [2] K. Abe et al. Measurement of the inclusive electron neutrino charged current cross section on carbon with the t2k near detector. *Physical Review Letters*, 113(24), Dec 2014. ISSN 1079-7114. doi: 10.1103/physrevlett.113.241803. URL <http://dx.doi.org/10.1103/PhysRevLett.113.241803>.
- [3] B. Abi et al. Deep underground neutrino experiment (dune), far detector technical design report, volume i: Introduction to dune, 2020.
- [4] A. G. Abramov et al. Beam optics and target conceptual designs for the NuMI project. *Nucl. Instrum. Meth. A*, 485:209–227, 2002. doi: 10.1016/S0168-9002(01)02112-X.
- [5] P. Abratenko et al. First measurement of inclusive electron-neutrino and antineutrino charged current differential cross sections in charged lepton energy on argon in micro-boone. *Phys. Rev. D*, 105:L051102, Mar 2022. doi: 10.1103/PhysRevD.105.L051102. URL <https://link.aps.org/doi/10.1103/PhysRevD.105.L051102>.
- [6] M. A. Acero et al. Measurement of neutrino-induced neutral-current coherent  $\pi^0$  production in the NOvA near detector. *Physical Review D*, 102(1), jul 2020. doi: 10.1103/physrevd.102.012004. URL <https://doi.org/10.1103/PhysRevD.102.012004>.
- [7] Mario A. Acero, Carlo Giunti, and Marco Laveder. Limits on  $\nu_e$  and  $\bar{\nu}_e$  disappearance from gallium and reactor experiments. *Physical Review D*, 78(7), Oct 2008. ISSN 1550-2368. doi: 10.1103/physrevd.78.073009. URL <http://dx.doi.org/10.1103/PhysRevD.78.073009>.
- [8] P. Adamson et al. Neutrino and antineutrino inclusive charged-current cross section measurements with the minos near detector. *Phys. Rev. D*, 81:072002, Apr 2010. doi: 10.1103/PhysRevD.81.072002. URL <https://link.aps.org/doi/10.1103/PhysRevD.81.072002>.
- [9] P. Adamson et al. The numi neutrino beam. *Nuclear Instruments and Methods in Physics Research Section A: Accelerators, Spectrometers, Detectors and Associated Equipment*, 806:279–306, 2016. ISSN 0168-9002. doi: <https://doi.org/10.1016/j.nima.2015.08.063>. URL <https://www.sciencedirect.com/science/article/pii/S016890021501027X>.

- [10] Stephen L. Adler. Tests of the conserved vector current and partially conserved axial-vector current hypotheses in high-energy neutrino reactions. *Phys. Rev.*, 135:B963–B966, Aug 1964. doi: 10.1103/PhysRev.135.B963. URL <https://link.aps.org/doi/10.1103/PhysRev.135.B963>.
- [11] S. Agostinelli et al. Geant4—a simulation toolkit. *Nuclear Instruments and Methods in Physics Research Section A: Accelerators, Spectrometers, Detectors and Associated Equipment*, 506(3):250–303, 2003. ISSN 0168-9002. doi: [https://doi.org/10.1016/S0168-9002\(03\)01368-8](https://doi.org/10.1016/S0168-9002(03)01368-8). URL <https://www.sciencedirect.com/science/article/pii/S0168900203013688>.
- [12] A. Aguilar, L. B. Auerbach, R. L. Burman, D. O. Caldwell, E. D. Church, A. K. Cochran, J. B. Donahue, A. Fazely, G. T. Garvey, R. M. Gunasingha, R. Imlay, W. C. Louis, R. Majkic, A. Malik, W. Metcalf, G. B. Mills, V. Sandberg, D. Smith, I. Stancu, M. Sung, R. Tayloe, G. J. VanDalen, W. Vernon, N. Wadia, D. H. White, and S. Yellin. Evidence for neutrino oscillations from the observation of  $\bar{\nu}_e$  appearance in a  $\bar{\nu}_\mu$  beam. *Physical Review D*, 64(11), Nov 2001. ISSN 1089-4918. doi: 10.1103/physrevd.64.112007. URL <http://dx.doi.org/10.1103/PhysRevD.64.112007>.
- [13] Q. R. Ahmad et al. Direct evidence for neutrino flavor transformation from neutral-current interactions in the sudbury neutrino observatory. *Physical Review Letters*, 89(1), Jun 2002. ISSN 1079-7114. doi: 10.1103/physrevlett.89.011301. URL <http://dx.doi.org/10.1103/PhysRevLett.89.011301>.
- [14] L. Aliaga et al. Design, calibration, and performance of the minerva detector. *Nuclear Instruments and Methods in Physics Research Section A: Accelerators, Spectrometers, Detectors and Associated Equipment*, 743:130–159, 2014. ISSN 0168-9002. doi: <https://doi.org/10.1016/j.nima.2013.12.053>. URL <https://www.sciencedirect.com/science/article/pii/S0168900214000035>.
- [15] L. Aliaga et al. Neutrino flux predictions for the numi beam. *Phys. Rev. D*, 94:092005, Nov 2016. doi: 10.1103/PhysRevD.94.092005. URL <https://link.aps.org/doi/10.1103/PhysRevD.94.092005>.
- [16] Leonidas Aliaga Soplin. *Neutrino Flux Prediction for The Numi Beamline*. PhD thesis, William-Mary Coll., 2016.
- [17] O. Altinok et al. Measurement of  $\nu_\mu$  charged-current single  $\pi^0$  production on hydrocarbon in the few-gev region using minerva. *Phys. Rev. D*, 96:072003, Oct 2017. doi: 10.1103/PhysRevD.96.072003. URL <https://link.aps.org/doi/10.1103/PhysRevD.96.072003>.
- [18] J. E. Amaro, M. B. Barbaro, J. A. Caballero, T. W. Donnelly, A. Molinari, and I. Sick. Using electron scattering superscaling to predict charge-changing neutrino cross sections in nuclei. *Phys. Rev. C*, 71:015501, Jan 2005. doi: 10.1103/PhysRevC.71.015501. URL <https://link.aps.org/doi/10.1103/PhysRevC.71.015501>.

- [19] Fengpeng An et al. Neutrino physics with juno. Journal of Physics G: Nuclear and Particle Physics, 43(3):030401, Feb 2016. ISSN 1361-6471. doi: 10.1088/0954-3899/43/3/030401. URL <http://dx.doi.org/10.1088/0954-3899/43/3/030401>.
- [20] C. Andreopoulos, A. Bell, D. Bhattacharya, F. Cavanna, J. Dobson, S. Dytman, H. Gallagher, P. Guzowski, R. Hatcher, P. Kehayias, A. Mereaglia, D. Naples, G. Pearce, A. Rubbia, M. Whalley, and T. Yang. The genie neutrino monte carlo generator. Nuclear Instruments and Methods in Physics Research Section A: Accelerators, Spectrometers, Detectors and Associated Equipment, 614(1):87–104, 2010. ISSN 0168-9002. doi: <https://doi.org/10.1016/j.nima.2009.12.009>. URL <https://www.sciencedirect.com/science/article/pii/S0168900209023043>.
- [21] M. V. Ascencio et al. Measurement of inclusive charged-current  $\nu\mu$  scattering on hydrocarbon at  $\langle E\nu \rangle \sim 6$  GeV with low three-momentum transfer. Phys. Rev. D, 106(3):032001, 2022. doi: 10.1103/PhysRevD.106.032001.
- [22] P.S. Auchincloss et al. A study of the energy dependence of the mean, truncated mean, and most probable energy deposition of high-energy muons in sampling calorimeters. Nuclear Instruments and Methods in Physics Research Section A: Accelerators, Spectrometers, Detectors and Associated Equipment, 343(2):463–469, 1994. ISSN 0168-9002. doi: [https://doi.org/10.1016/0168-9002\(94\)90225-9](https://doi.org/10.1016/0168-9002(94)90225-9). URL <https://www.sciencedirect.com/science/article/pii/0168900294902259>.
- [23] Ch. Berger and L. M. Sehgal. Lepton mass effects in single pion production by neutrinos. Physical Review D, 76(11), dec 2007. doi: 10.1103/physrevd.76.113004. URL <https://doi.org/10.1103/physrevd.76.113004>.
- [24] A. J. Bevan et al. The physics of the b factories. The European Physical Journal C, 74(11), Nov 2014. ISSN 1434-6052. doi: 10.1140/epjc/s10052-014-3026-9. URL <http://dx.doi.org/10.1140/epjc/s10052-014-3026-9>.
- [25] S M Bilenky. The history of neutrino oscillations. Physica Scripta, T121:17–22, Jan 2005. ISSN 1402-4896. doi: 10.1088/0031-8949/2005/t121/001. URL <http://dx.doi.org/10.1088/0031-8949/2005/T121/001>.
- [26] J Blietschau, H Deden, FJ Hasert, W Krenz, D Lanske, J Morfin, M Pohl, K Schultze, H Schumacher, H Weerts, et al. Total cross sections for  $\nu e$  and  $\bar{\nu} e$  interactions and search for neutrino oscillations and decay. Nuclear Physics B, 133(2):205–219, 1978.
- [27] A. Bodek and J. L. Ritchie. Further studies of fermi-motion effects in lepton scattering from nuclear targets. Phys. Rev. D, 24:1400–1402, Sep 1981. doi: 10.1103/PhysRevD.24.1400. URL <https://link.aps.org/doi/10.1103/PhysRevD.24.1400>.
- [28] Arie Bodek, Inkyu Park, and Un ki Yang. Improved low  $q^2$  model for neutrino and electron nucleon cross sections in few gev region. Nuclear Physics B - Proceedings Supplements, 139:113–118, 2005. ISSN 0920-5632. doi: <https://doi.org/10.1016/j.nuclphysbps.2004.11.208>. URL <https://www.sciencedirect.com/science/article/pii/S0920563204001120>.

- com/science/article/pii/S0920563204007492. Proceedings of the Third International Workshop on Neutrino-Nucleus Interactions in the Few-GeV Region.
- [29] R. Bradford, A. Bodek, H. Budd, and J. Arrington. A new parameterization of the nucleon elastic form factors. Nuclear Physics B - Proceedings Supplements, 159:127–132, 2006. ISSN 0920-5632. doi: <https://doi.org/10.1016/j.nuclphysbps.2006.08.028>. URL <https://www.sciencedirect.com/science/article/pii/S0920563206005184>. Proceedings of the 4th International Workshop on Neutrino-Nucleus Interactions in the Few-GeV Region.
  - [30] D. Casper. The nuance neutrino physics simulation, and the future. Nuclear Physics B - Proceedings Supplements, 112(1):161–170, 2002. ISSN 0920-5632. doi: [https://doi.org/10.1016/S0920-5632\(02\)01756-5](https://doi.org/10.1016/S0920-5632(02)01756-5). URL <https://www.sciencedirect.com/science/article/pii/S0920563202017565>.
  - [31] Bruce T Cleveland, Timothy Daily, Raymond Davis Jr, James R Distel, Kenneth Lande, CK Lee, Paul S Wildenhain, and Jack Ullman. Measurement of the solar electron neutrino flux with the homestake chlorine detector. The Astrophysical Journal, 496(1):505, 1998.
  - [32] ALEPH Collaboration et al. Electroweak measurements in electron–positron collisions at w-boson-pair energies at lep. Physics Reports, 532(4):119–244, Nov 2013. ISSN 0370-1573. doi: 10.1016/j.physrep.2013.07.004. URL <http://dx.doi.org/10.1016/j.physrep.2013.07.004>.
  - [33] DUNE Collaboration. Long-baseline neutrino facility (lbnf) and deep underground neutrino experiment (dune) conceptual design report volume 2: The physics program for dune at lbnf, 2016.
  - [34] MINERvA collaboration. The minerva technical design report. MINERvA DocDB, 2008.
  - [35] MINERvA Collaboration. Minerva neutrino detector response measured with test beam data, 2015.
  - [36] MiniBooNE Collaboration. A combined  $\nu_\mu \rightarrow \nu_e$  and  $\bar{\nu}_\mu \rightarrow \bar{\nu}_e$  oscillation analysis of the miniboone excesses, 2012.
  - [37] Planck Collaboration. Planck 2018 results. vi. cosmological parameters. Astronomy & Astrophysics, 641:A6, sep 2020. doi: 10.1051/0004-6361/201833910. URL <https://arxiv.org/abs/1807.06209>.
  - [38] The ALEPH Collaboration et al. Precision electroweak measurements on the z resonance. Physics Reports, 427(5–6):257–454, May 2006. ISSN 0370-1573. doi: 10.1016/j.physrep.2005.12.006. URL <http://dx.doi.org/10.1016/j.physrep.2005.12.006>.

- [39] W. N. Cottingham and D. A. Greenwood. An Introduction to the Standard Model of Particle Physics. Cambridge University Press, 2 edition, 2007. doi: 10.1017/CBO9780511791406.
- [40] G. D’Agostini. A Multidimensional unfolding method based on Bayes’ theorem. Nucl. Instrum. Meth. A, 362:487–498, 1995. doi: 10.1016/0168-9002(95)00274-X.
- [41] Steven Dytman. Neutrino event generators. AIP Conference Proceedings, 896(1): 178–184, 2007. doi: 10.1063/1.2720468. URL <https://aip.scitation.org/doi/abs/10.1063/1.2720468>.
- [42] William Templeton Eadie, Daniel Drijard, and Frederick E James. Statistical methods in experimental physics. Amsterdam: North-Holland, 1971.
- [43] Ivan Esteban, M.C. Gonzalez-Garcia, Michele Maltoni, Thomas Schwetz, and Albert Zhou. The fate of hints: updated global analysis of three-flavor neutrino oscillations. Journal of High Energy Physics, 2020(9), Sep 2020. ISSN 1029-8479. doi: 10.1007/jhep09(2020)178. URL [http://dx.doi.org/10.1007/JHEP09\(2020\)178](http://dx.doi.org/10.1007/JHEP09(2020)178).
- [44] RP Feynman and M Gell-Mann. Feynman 1958. Phys. Rev, 109:193, 1958.
- [45] J. A. Formaggio and G. P. Zeller. From  $\nu_e$  to  $\bar{\nu}_e$ : Neutrino cross sections across energy scales. Rev. Mod. Phys., 84:1307–1341, Sep 2012. doi: 10.1103/RevModPhys.84.1307. URL <https://link.aps.org/doi/10.1103/RevModPhys.84.1307>.
- [46] R. Frühwirth. Application of kalman filtering to track and vertex fitting. Nuclear Instruments and Methods in Physics Research Section A: Accelerators, Spectrometers, Detectors and Associated Equipment, 262(2):444–450, 1987. ISSN 0168-9002. doi: [https://doi.org/10.1016/0168-9002\(87\)90887-4](https://doi.org/10.1016/0168-9002(87)90887-4). URL <https://www.sciencedirect.com/science/article/pii/0168900287908874>.
- [47] Y. Fukuda et al. Evidence for oscillation of atmospheric neutrinos. Phys. Rev. Lett., 81:1562–1567, Aug 1998. doi: 10.1103/PhysRevLett.81.1562. URL <https://link.aps.org/doi/10.1103/PhysRevLett.81.1562>.
- [48] A. Gando et al. Search for majorana neutrinos near the inverted mass hierarchy region with kamland-zen. Physical Review Letters, 117(8), Aug 2016. ISSN 1079-7114. doi: 10.1103/physrevlett.117.082503. URL <http://dx.doi.org/10.1103/PhysRevLett.117.082503>.
- [49] Carlo Giunti and Chung W. Kim. Fundamentals of Neutrino Physics and Astrophysics. OUP Oxford, 2007. ISBN 978-0-19-850871-7.
- [50] Carlo Giunti and Marco Laveder. Statistical significance of the gallium anomaly. Physical Review C, 83(6), Jun 2011. ISSN 1089-490X. doi: 10.1103/physrevc.83.065504. URL <http://dx.doi.org/10.1103/PhysRevC.83.065504>.

- [51] Tomasz Golan, Cezary Juszczak, and Jan T. Sobczyk. Effects of final-state interactions in neutrino-nucleus interactions. *Phys. Rev. C*, 86:015505, Jul 2012. doi: 10.1103/PhysRevC.86.015505. URL <https://link.aps.org/doi/10.1103/PhysRevC.86.015505>.
- [52] R. Gran, J. Nieves, F. Sanchez, and M. J. Vicente Vacas. Neutrino-nucleus quasi-elastic and 2p2h interactions up to 10 gev. *Phys. Rev. D*, 88:113007, Dec 2013. doi: 10.1103/PhysRevD.88.113007. URL <https://link.aps.org/doi/10.1103/PhysRevD.88.113007>.
- [53] Richard Gran. Model uncertainties for valencia rpa effect for minerva, 2017. URL <https://arxiv.org/abs/1705.02932>.
- [54] Richard Gran. Model uncertainties for valencia rpa effect for minerva, 2017.
- [55] Toshikazu Hakamata, H Kume, K Okano, K Tomiyama, A Kamiya, Y Yoshizawa, H Matsui, I Otsu, T Taguchi, Y Kawai, et al. Photomultiplier tubes: basics and applications. *Hamamatsu Photonics KK Electron Tube Division, Hamamatsu City*, 2006.
- [56] D. Hanneke, S. Fogwell Hoogerheide, and G. Gabrielse. Cavity control of a single-electron quantum cyclotron: Measuring the electron magnetic moment. *Physical Review A*, 83(5), may 2011. doi: 10.1103/physreva.83.052122. URL <https://doi.org/10.1103%2Fphysreva.83.052122>.
- [57] M. Kabirnezhad. Single pion production in neutrino-nucleon interactions. *Phys. Rev. D*, 97:013002, Jan 2018. doi: 10.1103/PhysRevD.97.013002. URL <https://link.aps.org/doi/10.1103/PhysRevD.97.013002>.
- [58] P. R. Karns, D. S. Bollinger, and A. Sosa. Recent operation of the final magnetron h- ion source. *AIP Conference Proceedings*, 2017. ISSN 0094-243X. doi: 10.1063/1.4995775. URL <http://dx.doi.org/10.1063/1.4995775>.
- [59] Lord Kelvin. I. nineteenth century clouds over the dynamical theory of heat and light. *The London, Edinburgh, and Dublin Philosophical Magazine and Journal of Science*, 2(7):1–40, 1901.
- [60] Lev Landau. On the conservation laws for weak interactions. *Nuclear Physics*, 3(1): 127–131, 1957.
- [61] C. Lazzeroni et al. Precision measurement of the ratio of the charged kaon leptonic decay rates. *Physics Letters B*, 719(4):326–336, 2013. ISSN 0370-2693. doi: <https://doi.org/10.1016/j.physletb.2013.01.037>. URL <https://www.sciencedirect.com/science/article/pii/S0370269313000786>.
- [62] Tsung D Lee and Chen Ning Yang. Parity nonconservation and a two-component theory of the neutrino. *Physical Review*, 105(5):1671, 1957.

- [63] C.H. Llewellyn Smith. Neutrino reactions at accelerator energies. Physics Reports, 3(5):261–379, 1972. ISSN 0370-1573. doi: [https://doi.org/10.1016/0370-1573\(72\)90010-5](https://doi.org/10.1016/0370-1573(72)90010-5). URL <https://www.sciencedirect.com/science/article/pii/0370157372900105>.
- [64] Rolf Luchsinger and Christoph Grab. Vertex reconstruction by means of the method of kalman filtering. Computer Physics Communications, 76(3):263–280, 1993. ISSN 0010-4655. doi: [https://doi.org/10.1016/0010-4655\(93\)90055-H](https://doi.org/10.1016/0010-4655(93)90055-H). URL <https://www.sciencedirect.com/science/article/pii/001046559390055H>.
- [65] Pedro A. N. Machado, Ornella Palamara, and David W. Schmitz. The short-baseline neutrino program at fermilab. Annual Review of Nuclear and Particle Science, 69(1), 10 2019. doi: 10.1146/annurev-nucl-101917-020949.
- [66] Kendall Mahn, Chris Marshall, and Callum Wilkinson. Progress in measurements of 0.1-10 gev neutrino-nucleus scattering and anticipated results from future experiments. Annual Review of Nuclear and Particle Science, 68(1):105–129, 2018. doi: 10.1146/annurev-nucl-101917-020930. URL <https://doi.org/10.1146/annurev-nucl-101917-020930>.
- [67] Ben Messerly, Rob Fine, and Andrew Olivier and. An error analysis toolkit for binned counting experiments. EPJ Web of Conferences, 251:03046, 2021. doi: 10.1051/epjconf/202125103046. URL <https://doi.org/10.1051%2Fepjconf%2F202125103046>.
- [68] D.G. Michael, P. Adamson, T. Alexopoulos, W.W.M. Allison, G.J. Alner, K. Anderson, C. Andreopoulos, M. Andrews, R. Andrews, C. Arroyo, and et al. The magnetized steel and scintillator calorimeters of the minos experiment. Nuclear Instruments and Methods in Physics Research Section A: Accelerators, Spectrometers, Detectors and Associated Equipment, 596(2):190–228, Nov 2008. ISSN 0168-9002. doi: 10.1016/j.nima.2008.08.003. URL <http://dx.doi.org/10.1016/j.nima.2008.08.003>.
- [69] A. Mislivec et al. Measurement of total and differential cross sections of neutrino and antineutrino coherent  $\pi^\pm$  production on carbon. Physical Review D, 97(3), feb 2018. doi: 10.1103/physrevd.97.032014. URL <https://doi.org/10.1103%2Fphysrevd.97.032014>.
- [70] MissMJ. Standard model of elementary particles, 2022. URL [https://en.wikipedia.org/wiki/File:Standard\\_Model\\_of\\_Elementary\\_Particles.svg](https://en.wikipedia.org/wiki/File:Standard_Model_of_Elementary_Particles.svg). [Online; accessed 06-April-2022].
- [71] Hiroki Nakamura and Ryoichi Seki. Quasi-elastic neutrino-nucleus scattering and spectral function. Nuclear Physics B - Proceedings Supplements, 112(1):197–202, 2002. ISSN 0920-5632. doi: [https://doi.org/10.1016/S0920-5632\(02\)01771-1](https://doi.org/10.1016/S0920-5632(02)01771-1). URL <https://www.sciencedirect.com/science/article/pii/S0920563202017711>.

- [72] J. Nieves, J. E. Amaro, and M. Valverde. Erratum: Inclusive quasielastic charged-current neutrino-nucleus reactions [phys. rev. c 70, 055503 (2004)]. Phys. Rev. C, 72: 019902, Jul 2005. doi: 10.1103/PhysRevC.72.019902. URL <https://link.aps.org/doi/10.1103/PhysRevC.72.019902>.
- [73] J. Nieves, I. Ruiz Simo, and M. J. Vicente Vacas. Inclusive charged-current neutrino-nucleus reactions. Phys. Rev. C, 83:045501, Apr 2011. doi: 10.1103/PhysRevC.83.045501. URL <https://link.aps.org/doi/10.1103/PhysRevC.83.045501>.
- [74] J. Park et al. Measurement of neutrino flux from neutrino-electron elastic scattering. Phys. Rev. D, 93:112007, Jun 2016. doi: 10.1103/PhysRevD.93.112007. URL <https://link.aps.org/doi/10.1103/PhysRevD.93.112007>.
- [75] Jaewon Park. Neutrino-Electron Scattering in MINERvA for Constraining the NuMI Neutrino Flux. PhD thesis, U. Rochester, 2013.
- [76] Gabriel N. Perdue. Minerva reconstruction from 1,000 feet. MINERvA DocDB entry 10017-v2, 2014.
- [77] G.N. Perdue et al. The minerva data acquisition system and infrastructure. Nuclear Instruments and Methods in Physics Research Section A: Accelerators, Spectrometers, Detectors and Associated Equipment, 694:179–192, 2012. ISSN 0168-9002. doi: <https://doi.org/10.1016/j.nima.2012.08.024>. URL <https://www.sciencedirect.com/science/article/pii/S0168900212008844>.
- [78] Michael E. Peskin and Daniel V. Schroeder. An Introduction to quantum field theory. Addison-Wesley, Reading, USA, 1995. ISBN 978-0-201-50397-5.
- [79] B Pontecorvo. Servation of lepton charge. JETP, 5:1297, 1957.
- [80] Dieter Rein. Diffractive pion production in neutrino reactions. Nuclear Physics B, 278(1):61–77, 1986. ISSN 0550-3213. doi: [https://doi.org/10.1016/0550-3213\(86\)90106-9](https://doi.org/10.1016/0550-3213(86)90106-9). URL <https://www.sciencedirect.com/science/article/pii/0550321386901069>.
- [81] Dieter Rein and Lalit M Sehgal. Neutrino-excitation of baryon resonances and single pion production. Annals of Physics, 133(1):79–153, 1981. ISSN 0003-4916. doi: [https://doi.org/10.1016/0003-4916\(81\)90242-6](https://doi.org/10.1016/0003-4916(81)90242-6). URL <https://www.sciencedirect.com/science/article/pii/0003491681902426>.
- [82] Dieter Rein and Lalit M. Sehgal. Coherent  $\pi^0$  production in neutrino reactions. Nuclear Physics B, 223(1):29–44, 1983. ISSN 0550-3213. doi: [https://doi.org/10.1016/0550-3213\(83\)90090-1](https://doi.org/10.1016/0550-3213(83)90090-1). URL <https://www.sciencedirect.com/science/article/pii/0550321383900901>.
- [83] P. A. Rodrigues et al. Identification of nuclear effects in neutrino-carbon interactions at low three-momentum transfer. Phys. Rev. Lett., 116:071802, Feb 2016.



- doi: 10.1103/PhysRevLett.116.071802. URL <https://link.aps.org/doi/10.1103/PhysRevLett.116.071802>.
- [84] P.A. Rodrigues et al. Empirical constraint on the multi-nucleon component in neutrino-carbon reactions. MINERvA DocDB, 2018.
  - [85] Philip Rodrigues, Callum Wilkinson, and Kevin McFarland. Constraining the genie model of neutrino-induced single pion production using reanalyzed bubble chamber data. *The European Physical Journal C*, 76(8):474, 2016. doi: 10.1140/epjc/s10052-016-4314-3. URL <https://doi.org/10.1140/epjc/s10052-016-4314-3>.
  - [86] Stephen M Ross et al. Peirce’s criterion for the elimination of suspect experimental data. *Journal of engineering technology*, 20(2):38–41, 2003.
  - [87] Paul Rubinov. AFEII Analog Front End Board Design Specifications. Technical report, Fermi National Accelerator Lab. (FNAL), Batavia, IL (United States), 4 2005.
  - [88] D. Ruterbories et al. Constraining the numi neutrino flux using inverse muon decay reactions in minerva, 2021.
  - [89] Abdus Salam. On parity conservation and neutrino mass. *Il Nuovo Cimento (1955-1965)*, 5(1):299–301, 1957.
  - [90] J. Schechter and J. W. F. Valle. Neutrino masses in  $su(2) \otimes u(1)$  theories. *Phys. Rev. D*, 22:2227–2235, Nov 1980. doi: 10.1103/PhysRevD.22.2227. URL <https://link.aps.org/doi/10.1103/PhysRevD.22.2227>.
  - [91] J. Schwehr, D. Cherdack, and R. Gran. Genie implementation of ific valencia model for qe-like 2p2h neutrino-nucleus cross section, 2017.
  - [92] Aldo M. Serenelli, W. C. Haxton, and Carlos Peña-Garay. Solar models with accretion. i. application to the solar abundance problem. *The Astrophysical Journal*, 743(1): 24, Nov 2011. ISSN 1538-4357. doi: 10.1088/0004-637x/743/1/24. URL <http://dx.doi.org/10.1088/0004-637X/743/1/24>.
  - [93] A Yu Smirnov. The MSW effect and matter effects in neutrino oscillations. *Physica Scripta*, T121:57–64, jan 2005. doi: 10.1088/0031-8949/2005/t121/008. URL <https://doi.org/10.1088/0031-8949/2005/t121/008>.
  - [94] R.A. Smith and E.J. Moniz. Neutrino reactions on nuclear targets. *Nuclear Physics B*, 43:605–622, 1972. ISSN 0550-3213. doi: [https://doi.org/10.1016/0550-3213\(72\)90040-5](https://doi.org/10.1016/0550-3213(72)90040-5). URL <https://www.sciencedirect.com/science/article/pii/0550321372900405>.
  - [95] P. Stowell et al. Tuning the genie pion production model with minerva data. *Phys. Rev. D*, 100:072005, Oct 2019. doi: 10.1103/PhysRevD.100.072005. URL <https://link.aps.org/doi/10.1103/PhysRevD.100.072005>.

- [96] Hang Su. nue update – rhc/fhc comparison. MINERvA DocDB, 2020.
- [97] Ennackal CG Sudarshan and RE Marshak. Chirality invariance and the universal fermi interaction. Physical Review, 109(5):1860, 1958.
- [98] N. Tagg, A. De Santo, A. Weber, A. Cabrera, P.S. Miyagawa, M.A. Barker, K. Lang, D. Michael, R. Saakyan, and J. Thomas. Performance of hamamatsu 64-anode photomultipliers for use with wavelength—shifting optical fibres. Nuclear Instruments and Methods in Physics Research Section A: Accelerators, Spectrometers, Detectors and Associated Equipment, 539(3):668–678, 2005. ISSN 0168-9002. doi: <https://doi.org/10.1016/j.nima.2004.11.003>. URL <https://www.sciencedirect.com/science/article/pii/S0168900204023460>.
- [99] E. Valencia. Neutrino-electron scattering in me angle beam alignment 2.0. MINERvA DocDB entry 11550-v2, 2015.
- [100] E. Valencia et al. Constraint of the MINERvA medium energy neutrino flux using neutrino-electron elastic scattering. Phys. Rev. D, 100:092001, Nov 2019. doi: 10.1103/PhysRevD.100.092001. URL <https://link.aps.org/doi/10.1103/PhysRevD.100.092001>.
- [101] C. Wilkinson. Overview of neutrino-nucleus interaction physics. 17th International Workshop on Next Generation Nucleon Decay and Neutrino Detectors, 2017. URL [https://indico.cern.ch/event/657167/contributions/2677886/attachments/1547560/2429424/NNN\\_xsec\\_summary.pdf](https://indico.cern.ch/event/657167/contributions/2677886/attachments/1547560/2429424/NNN_xsec_summary.pdf).
- [102] J. Wolcott et al. Evidence for neutral-current diffractive  $\pi^0$  production from hydrogen in neutrino interactions on hydrocarbon. Phys. Rev. Lett., 117:111801, Sep 2016. doi: 10.1103/PhysRevLett.117.111801. URL <https://link.aps.org/doi/10.1103/PhysRevLett.117.111801>.
- [103] J. Wolcott et al. Measurement of electron neutrino quasielastic and quasielasticlike scattering on hydrocarbon at  $\langle E_\nu \rangle = 3.6$  GeV. Phys. Rev. Lett., 116:081802, Feb 2016. doi: 10.1103/PhysRevLett.116.081802. URL <https://link.aps.org/doi/10.1103/PhysRevLett.116.081802>.
- [104] Jeremy Wolcott. Measurement of the Charged-Current Quasi-Elastic Cross-Section for Electron Neutrinos on a Hydrocarbon Target. PhD thesis, Rochester U., 2015.
- [105] C. S. Wu, E. Ambler, R. W. Hayward, D. D. Hoppes, and R. P. Hudson. Experimental test of parity conservation in beta decay. Phys. Rev., 105:1413–1415, Feb 1957. doi: 10.1103/PhysRev.105.1413. URL <https://link.aps.org/doi/10.1103/PhysRev.105.1413>.
- [106] Tsutomu Yanagida. Horizontal Symmetry and Masses of Neutrinos. Progress of Theoretical Physics, 64(3):1103–1105, 09 1980. ISSN 0033-068X. doi: 10.1143/PTP.64.1103. URL <https://doi.org/10.1143/PTP.64.1103>.

- [107] P.A. Zyla et al. Review of Particle Physics. PTEP, 2020(8):083C01, 2020. doi: 10.1093/ptep/ptaa104.